University of Strathclyde

Department of Physics

A simulation study of simple ionic liquids near charged walls: The melting of the electric double layer and structural transitions at the interface

by

Kathleen Kirchner

A thesis presented in fulfilment of the
requirements for the degree of

Doctor of Philosophy

2013

This thesis is the result of the author's original research. It has been composed by the author and has not been previously submitted for examination which has led to the award of a degree.

Signed: K. Kirchner Date: April 24, 2013

Acknowledgements

I wish to thank Professor Maxim V. Fedorov for giving me the opportunity to perform research at the German Max-Planck-Institute for Mathematics in the science and the Institute of Physics at the University of Strathclyde, the British University of the Year 2012/13. My gratitude is offered for his guidance and scholarship. I also wish to thank Professor Frank Endres for stimulating discussions and the possibility, to combine my simulation results with the real world. Special thanks goes to Professor Philippe Bopp for introducing me to the field of computer simulations of ion effects and his guidance during my first project in the group and to Dr. Babak Minofar for his explicit help during my first steps in the field of ionic liquids and molecular simulations with Gromacs.

I also have to thank the members of my Viva Voce committee, Professor Frank Endres, Professor Paul Mckenna and Dr. David McKee for the memorable examination, that I found to be a highlight of my academic research.

I thank my colleagues Andrey Frolov, Nikolaj Georgi, Vladislav Ivaništšev, Ekaterina Ratkova, Anastasia Romanova and Volodymyr Sergiievskyi for fruitful discussions.

This work wouldn't have been possible without super computing facilities. I acknowledge the supercomputing support from the von Neumann-Institut für Computing, FZ Jülich (Project ID ESMI11) and from the facilities of HECToR, the UK's national high-performance computing service, which is provided by UoE HPCx Ltd at the University of Edinburgh, Cray Inc and NAG Ltd, and funded by the Office of Science and Technology through EPSRC's High End Computing Programme. Additional computing power was provided by the Academic and Research Computer Hosting Industry and Enterprise in the West of Scotland, ARCHIE-WeSt. Moreover I thank the Max Planck Institut für Mathematik in den Naturwissenschaften for hospitality during the stay there and for access to the local computing facilities, especially Ronald Kriemann for his support. This work was supported by Grant FE 1156/2-1 of the Deutsche Forschungsgemeinschaft (DFG), which I have to acknowledge for the high standards of maternity rights and the support they provide.

Most of all, I wish to thank my husband Tom for all of his support throughout my PhD and my son Sebastian for the countless hours of joy during days and nights.

Abstract

The temperature dependence of the electrical double layer (EDL) capacitance of high and low temperature ionic liquids (IL) is under excited debates within experimental, theoretical & computational communities for decades. Using a coarse-grain model of ILs with asymmetric sized ions we studied the EDL behaviour of ILs at an electrified interface to gain understanding in the temperature-effect. We improved the accuracy of the capacitance calculations by increasing the overall simulation time by an order of magnitude compared to former publications and discussed possible error sources. The analysis of different temperatures from 250 K to 500 K revealed a voltage dependent temperature-effect on the differential capacitance. To our opinion, the temperature dependence can be attributed to the formation of well ordered structures of the EDL at low temperatures, that are 'melted' at higher temperatures. The results provide an explanation for the contradicting experimental results published in the past years.

By systematically analysing number density profiles, a charge induced structural transition has been revealed. At most surface charge densities under study, the electric double layer forms a multilayered structure. At transition points, a hexatic (also termed as Moiré-like) monolayer structure is formed by the counterions. These findings correlate very well with experimental observations on room temperature ionic liquids and metal melts by Freyland and co-workers (Phys. Chem. Chem. Phys., 2008, 10, 923-936). The ions of the hexatic layer screen the electrode charge completely, thereby annihilating the interaction between electrode and subsequent bulk ionic liquid. Moreover we can report the formation of herring-bone structures at higher surface charge densities, that form as the superposition of two hexatic layers.

Graphical abstract

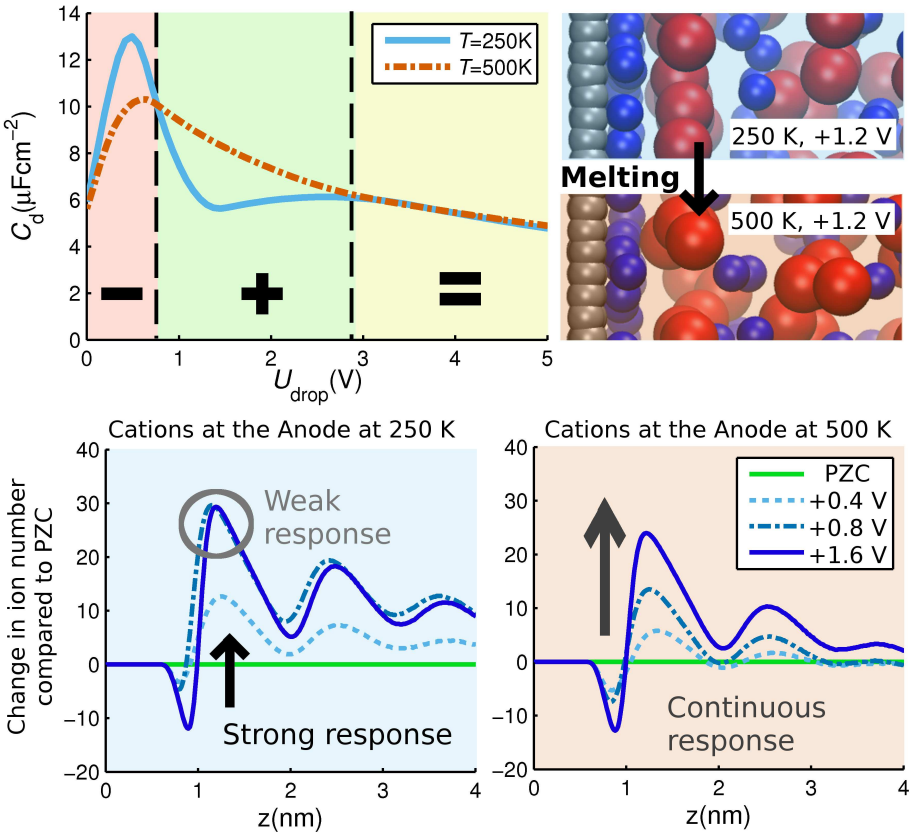

Differential capacitance of ionic liquids: temperature vs. voltage

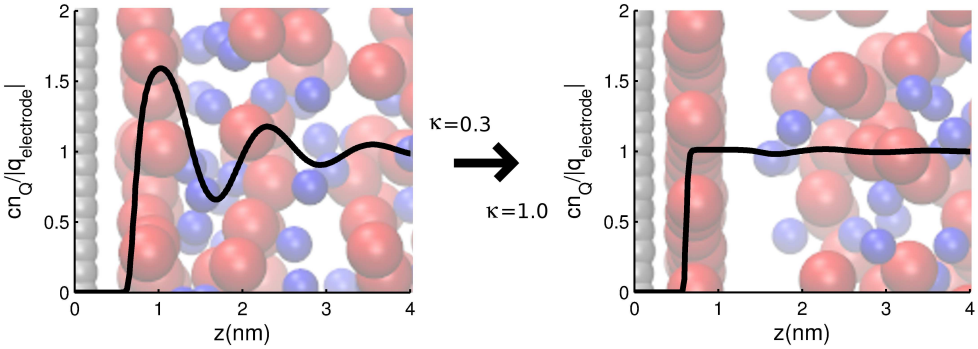

Electrical double layer in ionic liquids: structural transitions from multilayer to monolayer structure at the interface

Contents

List of Figures

List of Tables

Chapter 1

Introduction

1.1 Research motivation

A vast number of observations in the fields of physics, chemistry and biology are based on particle-particle correlations through electrostatic potentials [1]. Electrostatic correlations form our molecular picture of Coulombic fluids [2], such as liquid metals, plasmas, molten salts, ionic liquids and charged colloidal suspensions [3, 4, 5].

To name some examples: Phase transitions in two component plasma containing positive and negative ions are caused by positional correlations between the ions [1]. In confined geometries, colloids are known to form layers or micelles in the fluid [5]. Phenomena based on electrostatic interactions such as screening effects and charge oscillations are characteristic for ionic liquids [6, 7, 8, 9, 10, 11]. The study of the fundamental ion-ion correlations in these fluids gives rise to a broader understanding of physical phenomena of liquids in general [12, 13, 14, 15, 16].

Leading scientists in the field considered ionic liquids, especially room temperature ionic liquids (RTILs) consisting of organic charged particles [17] as highly important for the electrochemical nanotechnology [18, 19, 20, 21, 22, 23, 2]. The high charge density of ions in RTILs changes the nature of common phenomena at electrified interfaces. New perspectives in galvanic deposition, etching, corrosion science, electro-catalysis and other branches of applied electro-chemistry are

revealed. Despite the huge interest in electrochemical properties of RTILs and structuring of RTILs at neutral and electrified interfaces, there are still many effects not understood.

The temperature effect on the properties of the electrical double layer (EDL) in ionic liquids is a long standing question. Since the 60-70s there have been intensive debates on the nature of the temperature dependence of the double layer capacitance in high temperature ionic liquids (e.g. molten alkali halides) within experimental [24] and theoretical & computational communities [25, 26, 27]. However, due to a number of experimental problems related with electrochemical measurements in high temperature molten salts, there was no general agreement in the literature about the true character of this dependence.

The recent wave of interest to electrochemical applications of room temperature ionic liquids (RTILs) provoked a series of new experimental [28, 29, 30, 31, 32, 33, 34] and computational [35, 36, 37] studies on the temperature effects on EDL properties in ionic liquids. Nevertheless, a review of the published results on the temperature dependence of the EDL differential capacitance, C_d, in RTILs shows that this question remains to be controversial.

Weakly solvated ions, such as SO_4^{2-}, Cl^-, Br^-, I^-, are known to form ordered adlayers at the interface between electrode and aqueous electrolyte. The formation of such adlayers is originated in the partial striping of the solvation shell and direct adhesion to the electrode surface. An absence of solvent molecules in RTILs implies that the factors determining the ordering in aqueous electrolytes must be different from those in ionic liquids. However, Pan and co-workers [38] observed similar ordering in the ionic liquid 1-butyl-3-methylimidazolium hexafluorophosphate ([BMIm][PF_6]) at the Au(111) surface.

As has been reported by Aal et al [39] and Drüschler et al [31], the Au(111) surface reconstructs upon charging within some RTILs. The reconstruction appears as the formation of a herring bone super structure, that is not yet explained. Waldmann et al [40] resolved STM images of pyrrolidinium cations at the Au(111) surface on a molecular level. Ordered molecular structure were found only at low temperatures (210 K). At room temperature the mobility of the ions appeared to be too high to preserve the same structure, instead making STM images blur [41, 42, 43].

Experimentalists are approaching rapidly new ionic liquids in various environments and surface topologies, however the molecular effects causing the observed phenomena are still under discussion. While experimental methods are mostly affected by the assumptions made during the data evaluation procedure and pos-

sible pollutions of the system, computer simulations on an atomistic level can lead to a deeper understanding of molecular behaviour. As Schatz [44] mentions, experiments on nano-scale objects are often fraught with uncertainty due to the difficulty of fabricating and manipulating these objects. Many devices that hold or measure the nano-scale structure can produce irreversible degradation. Electron microscopy can produce defects in the structure being measured, optical measurements on the smallest metal nano-particles are subject to serious heating effects that can melt or destroy the particle, and atomic force microscopy studies of soft materials often lead to structural reorganization. In addition, the highest resolution measurements of structure, such as electron microscopy measurements, require that the nano-structure be removed from its natural environment, such as from solution, and placed on a grid under circumstances where aggregation and restructuring can occur. The need of theory for "filling in the gaps" in our understanding of phenomena at the nano-scale, and to predict new properties and phenomena, is quite important. Computational results aid to analyse the structures and visualize the important intermolecular interactions [45].

Using molecular dynamics (MD) simulations [46, 47] of a model coarse grain ionic liquid (IL) we provide insights into the structural organization of ionic liquids at the electrified interface under various temperatures.

The given scope of the research tasks requires an advanced methodology for the data handling or *data mining* [48, 49]. However, concepts for efficiently storing and analysing large files in conjunction with graphical visualization and numerical data processing of thousands of small files are hardly developed in the scientific community [50, 51]. The need for flexible, reusable, maintainable and well documented scientific software increases steadily as the performance of computing facility and data accessibility improves [52]. The current work makes an attempt to improve the standards in scientific computing by distributing a documented script collection that allows reproducing all simulations and analysis results presented in this work.

1.2 Research contributions

The research presented in this thesis pertains to the academic fields of electro chemistry, ionic liquids and computational physical chemistry. The principle contributions made by this thesis are:

1. Using a coarse-grain model of ionic liquids (ILs) within molecular dynamics simulations we studied interfacial phenomena of ILs at electrified interfaces.

Despite the simplicity of the chosen model, it seems capable of catching important effects observed in room temperature ILs:

a) [**Temperature-effect on the differential capacitance**]
The analysis of different temperatures from 250 K to 500 K revealed a voltage dependent temperature-effect on the differential capacitance. To our opinion, the temperature dependence can be attributed to the formation of well ordered structures, that are 'melted' at higher temperatures.

b) [**Structural transition at the interface**]
By systematically analysing number density profiles of ionic species near the electrodes, a structural transition at the interface from multilayer to monolayer structure has been revealed. At most surface charge densities under study, the electric double layer forms a multilayered structure. At transition points, a hexatic (also termed as Moiré-like) monolayer structure is formed by the counter-ions.

2. [**NaRIBaS**]
A unix-based preparation and analysis toolbox for "**N**anomaterials **a**nd **R**oom Temperature **I**onic Liquids in **B**ulk **a**nd **S**lab" using bash scripts, Gromacs tools and Matlab functions, has been created and made available for a broader scientific audience. The toolbox is to be understood as a scripting framework rather than a black-box software. User input like physical properties or simulation parameter and task lists like analysis steps and plotting routines are considered as independent blocks hold together by a linking function.

The publications that have resulted from this thesis are:

Kirchner, K., Kornyshev, A., & Fedorov, M. V. (In preparation). Differential capacitance - Temperature vs. Voltage.

Kirchner, K., Kirchner, T., Ivaništšev, V., & Fedorov, M. V. (Preprint version 2013, Electrochimica Acta). Electrical double layer in ionic liquids: structural transitions from multilayer to monolayer structure at the interface.

Kirchner, K., & Fedorov, M. V. (2013). NaRIBaS - A scripting framework for computational modelling of Nanomaterials and Room Temperature Ionic Liquids in Bulk and Slab. Open source, `http://sourceforge.net/projects/naribas/`.

1.3 Thesis outline

This thesis is organised into ten chapters with Chapter 1 being the current introduction.

In Chapter 2 we define the electric double layer and describe the reaction of a solute on electrode charging. The need for a method capable of bridging theoretical models and experimental observations is emphasized.

To gain insights into the electric double layer structuring on a fundamental level, we chose a model for ions and electrode, which will be discussed in conjunction with a collection of electrochemical properties of room temperature ionic liquids in Chapter 3. Before starting our research, we discuss in Chapter 4 state-of-the art methods for enhanced sampling and comment on their usability for our tasks. Thereby estimations of costs in terms of computational effort and human time are included.

In Chapter 5 we describe the final simulation methodology including the force field and system configuration and simulation parameter. We comment on the computational costs. Moreover, we justify the system geometry by calculating ion-ion correlations in the centre of the simulation box to assure proper separation of the electrodes.

The temperature dependence of the differential capacitance over voltage is described in Chapter 6. The calculation of the differential capacitance based on the structural ordering of ions close to the surface requires an advanced smoothing algorithm with assumptions about boundary conditions. Chapter 7 provides an explanation of the temperature dependence of the differential capacitance by the melting of the electric double layer.

Within Chapter 8 we discuss phenomena of ionic liquids at electrified interfaces, such as alternated layering and charge compensation. Surprisingly, we find a co-ionic enrichment at the anode.

The detailed analysis of number density profiles and interfacial structures of single ion layers made a structural transition at the electrode interface apparent, shown in Chapter 9.

The primary conclusions drawn from the results in this thesis are summarised in Chapter 10. Shortcomings of the simulation approach are noted. Ideas for further work are outlined.

The appendix contains three chapters that cover the influence of the temperature coupling on the simulation results and provide additional methodological descriptions and figures. Lastly the scripting framework NaRIBaS is introduced including the implementation of the iterator pattern.

Chapter 2

Ionic liquids at electrified interfaces: The theory of the Electric Double-Layer

The structure of electrolytic solutions at interfaces is a classic, highly investigated system in experiment and theory [53, 54, 55, 56, 18, 57, 58, 59, 60, 7, 61, 62, 8]. The early theories that aimed to describe the electric double-layer (EDL) were based on the spatial distribution of infinitely small, non-interacting charged species along the interface. The theoretical predictions worked well for diluted ion solutions, however the occurrence of dense Coulombic fluids such as ionic liquids pointed out the severe lack in the ion description. We will provide a definition of the electric double-layer and introduce theoretical models for the description of the solute reaction on electrode charging. Furthermore, we provide a pathway for calculating the differential capacitance in numerical simulations based on the Poisson equation.

2.1 The electrode-solution interface

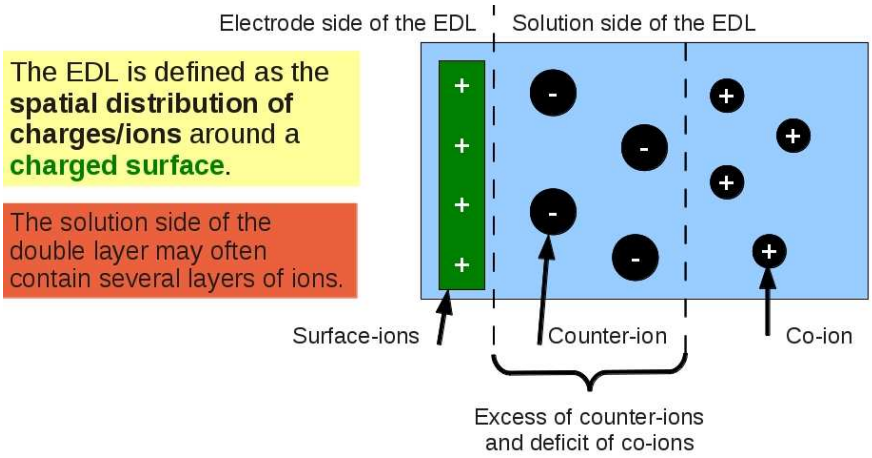

Figure 2.1: Principal definition of the electric double-layer (EDL) according to the IUPAC Technical Report on measurements and interpretation of electrokinetic phenomena [63].

According to the IUPAC Technical Report on measurements and interpretation of electrokinetic phenomena [63], the EDL is defined as the spatial distribution of charges/ions around a charged surface. Basically the term is already applicable to the simple picture of a particle or solid surface in contact with a solution. Upon charging the surface or particle, a diffusely distributed layer of charged particles will form within the solution in contact with the surface. Within this layer an excess of ions with opposite sign compared to the surface-charge (called counter-ions) is found in conjunction with a deficit of ions with the same sign compared to the surface-charge (called co-ions).

As explained by Bard and Faulkner [18], distinguishing between the electrode side and solution side of the double layer is reasonable. It is important to note, that usually the solution side of the double layer is thought to contain *several layers* of ions. A summary of the terminology is shown in Fig. 2.1.

We note that – using the same terminology as in the IUPAC report [63] – an ion/electrode model with a repulsive van-der-Waals interaction potential is considered to contain *indifferent adsorbing ions*, which adsorb purely through Coulomb forces on the surface. Furthermore, the charged electrode atoms are called *surface ions*.

2.2 Reaction of a solute on electrode charging

A description of theories and models for the double-layer structure can be taken from recent text books on electro chemistry, see for example Bard and Faulkner [18] or Izutsu [64] or Schmickler and Santos [65]. We provide a short overview of the most important models. We note, that all historical publications of the electrochemical theories are available through the online database project "Electrochemical Science and Technology Information Resource (ESTIR)" by Zoltan Nagy [66].

Helmholtz model Helmholtz [67, 68] was among the first to propose a model for the electric double layer. He assumed an attraction of counter-ions from the solution by the electrode charge. Thereby counter-ions move towards the electrode surface to screen the charge. Helmholtz defined a distance d between the surface and the counter-ion layer. If the surface charge on the electrode is located on the outer surface of the electrode, the distance d is characterized by the ion size. If the ions do not strip of their solvation shell, the distance d is characterized by the size of the solvation shell.

The configuration electrode/counter-ion-layer can be considered as a parallel-plate capacitor with a surface charge density σ

$$\sigma = \frac{\varepsilon\varepsilon_0}{d} \cdot U.$$

U is the potential drop, ε and ε_0 the dielectric constant and the permittivity of free space. The differential capacitance C_d is found to be

$$\frac{\partial\sigma}{\partial U} = C_d = \frac{\varepsilon\varepsilon_0}{d} = \text{const.}$$

Gouy-Chapman theory Gouy [69, 70] and Chapman [71] developed independently from each other a different theory. They suggested a thick *diffuse* ion layer as the reaction on a surface charge. The highest ion concentration would occur nearest to the electrode and then diminish with increasing distance. The reason for the spatially distributed ion layer lies in the thermal disturbance of the layer and a finite concentration of the electrolyte.

The thermal disturbance is introduced by a Boltzmann weighting:

$$\rho(z) = \rho_0 \cdot \exp\left(\frac{-qU}{k_\mathrm{B}T}\right),$$

with $\rho(z)$ being the ion density at distance z from the electrode, ρ_0 the bulk ion density, q the ion charge, U the electrostatic potential and $k_\mathrm{B}T$ the Boltzmann factor. An increased ion concentration leads to a smaller average distance between ions and electrode surface.

The distance dependent potential $U(z)$ is expressed as:

$$\frac{\mathrm{d}U(z)}{\mathrm{d}z} = -\left(\frac{8k_\mathrm{B}T\rho_o}{\varepsilon\varepsilon_0}\right)^{1/2} \cdot \sinh\left(\frac{qU}{2k_\mathrm{B}T}\right).$$

Using the Debye-length λ_D

$$\frac{1}{\lambda_\mathrm{D}} = \sqrt{\frac{2\rho_0 q^2}{\varepsilon\varepsilon_0 k_\mathrm{B}T}}$$

the expression for the potential can be simplified for small surface charges to

$$U(z) = U_0 e^{-z/\lambda_\mathrm{D}}.$$

The last equation results from the Debye-Hueckel theory [72].

In the Gouy-Chapman theory the differential capacitance decreases with the temperature, increases with the electrolyte concentration and the potential drop. This dependence reflects several phenomena observed in experiments but still fails at other important points. Thus, the Gouy-Chapman theory is unable to explain the occurrence of capacitance maxima. At least some of the discrepancies to experimental observations in real systems arise from the fact, that the ions are treated as infinitely small. The ions are able to move arbitrarily close to the electrode surface and can be compressed unlimited, namely, $\rho(z)$ can grow to infinity.

Stern model Stern [73] tried to correct one of the shortcomings of the Gouy-Chapman theory, namely the missing restriction for the distance between ions and electrode. The Stern theory combines the Gouy-Chapman model with the Helmholtz model by introducing a *compact ion layer* closest to the electrode surface in addition to the *diffuse layer*. The two layers behave like two capacitors in series

$$\frac{1}{C_d} = \frac{1}{C_H} + \frac{1}{C_D}.$$

The Gouy-Chapman-Stern model gives reasonable predictions for many real systems. However ion structuring in the compact layer, saturation effects, differences for the anionic and cationic excess are not taken into account as well as ion-ion correlations. With the discovery of room temperature ionic liquid, all these effects

gain importance resulting in severe discrepancies between the model predictions and results from real experiments.

Mean field lattice-gas model Limitations of the local ion concentration have also been introduced in the mean field lattice-gas model for the description of the electric double-layer [59]. Attempts of improvements of the theory are promising [74, 8]. Still, a comparison of experiments [75, 76, 29], theories incorporating ion correlations [77] and numerical simulations [78, 79, 7, 80, 81, 82] is crucial for the proof of the mean field theory.

2.3 The differential capacitance obtained in numerical simulations through the Poisson equation

The total electrostatic potential ϕ_t between two electrodes of distance L calculates as

$$\phi_t(z) = \phi_\sigma(z) + \phi_{\text{dielectric}}(z)$$

with z being the distance coordinate normal to the electrode surface, ϕ_σ the potential of external electric field created by the charge density on the electrodes and $\phi_{\text{dielectric}}$ the potential of the electric field created by the dielectric in response to the external electric field.

The electrodes are assumed to have a surface charge density σ that is homogeneously distributed across the surface. The potential of external field thus reads

$$\phi_\sigma(z) = -\frac{4\pi\sigma}{\varepsilon^*} z.$$

An effective dielectric constant ε^* may be introduced to account for the fast electronic polarisability of ions.

The potential caused by the response of the ionic liquids on the surface charge density is calculated using the Poisson equation

$$\phi_{IL}(z) = -\frac{4\pi\sigma}{\varepsilon^*} \int_0^z (z - z')\rho_{\text{ion}}(z')\mathrm{d}z'$$

taking into account the charge density profile of the ions $\rho_{\text{ion}}(z)$ averaged over z.

For calculating the differential capacitance C_d of our system

$$C_d = \frac{\mathrm{d}\sigma}{\mathrm{d}U_{\mathrm{drop}}}$$

we are interested in the potential drop U_{drop} between the electrode and the bulk liquid. This potential drop equals the total potential at the position of the electrode $\phi_t(0)$ minus the total potential at the middle between anode and cathode $\phi_t(L/2)$, where the dielectric should behave as bulk liquid without 'feeling' the electrodes any more. The potential drop calculates as follows

$$\begin{aligned}
U_{\mathrm{drop}} &\equiv \phi_t(0) - \phi_t(L/2) \\
&= \phi_\sigma(0) - \phi_\sigma(L/2) + \phi_{IL}(0) - \phi_{IL}(L/2) \\
&= \frac{4\pi\sigma}{\varepsilon^*}\left[0 - \left(-\frac{L}{2}\right) + \left(-\int_0^0 (-z')\rho_{\mathrm{ion}}(z')\mathrm{d}z'\right) - \left(-\int_0^{L/2}\left(\frac{L}{2} - z'\right)\rho_{\mathrm{ion}}(z')\mathrm{d}z'\right)\right] \\
&= \frac{4\pi}{\varepsilon^*}\left[0 + \sigma\frac{L}{2} + 0 + \frac{L}{2}\left(\int_0^{L/2}\rho_{\mathrm{ion}}(z')\mathrm{d}z'\right) - \left(\int_0^{L/2} z'\rho_{\mathrm{ion}}(z')\mathrm{d}z'\right)\right] \\
&= \frac{4\pi}{\varepsilon^*}\left[0 + \sigma\frac{L}{2} + 0 + \frac{L}{2}(-\sigma) - \left(\int_0^{L/2} z'\rho_{\mathrm{ion}}(z')\mathrm{d}z'\right)\right] \\
&= -\frac{4\pi}{\varepsilon^*}\int_0^{L/2} z'\rho_{\mathrm{ion}}(z')\mathrm{d}z'.
\end{aligned}$$

The dielectric has to compensate the surface charge introduced on the electrode. Thus the charge density integrated over the distance between one electrode and the middle of both electrodes equals the negative surface charge density given on the electrode. The potential drop U_{drop} then equals the negative integral of the charge density profile $\rho_{\mathrm{ion}}(z)$ multiplied by z. On a positively charged electrode, anode, we will find an enrichment of anions which are negatively charged. The integral over the charge density profile will be negative. Therefore a positive surface charge density σ corresponds to a positive potential drop U_{drop},

$$\sigma = -\int_0^{L/2}\rho_{\mathrm{ion}}(z')\mathrm{d}z' > 0 \quad \rightarrow \quad U_{\mathrm{drop}} > 0$$

and

$$\sigma = -\int_0^{L/2}\rho_{\mathrm{ion}}(z')\mathrm{d}z' < 0 \quad \rightarrow \quad U_{\mathrm{drop}} < 0.$$

Potential of zero charge The ideal capacitance curve has a parabolic shape with a minimum value equal to the so called potential of zero charge. In molecular simulations this potential equals the potential drop that is observable at neutral electrodes.

A potential drop between the uncharged electrode surface and the bulk might occur due to spontaneous adsorption of ions on the electrode surface. This potential drop might be explained by two phenomena:

1. Pure entropy: In case of asymmetric ion pairs (e.g. anions smaller than cations) the smaller ions are statistically favoured to come closer to the electrode surface and thus filling voids between the electrode surface and the larger specie.

2. Adsorption: If the electrode atoms are modelled including an attractive potential, the ions are likely to adsorb on the electrode surface. Depending on the actual van der Waals potential, either cations or anions will show a preference to adsorption and thus increase or decrease the potential of zero charge.

A negative potential of zero charge corresponds to the favoured adsorption of anions at the surface or a smaller anionic size, a positive potential drop to the favoured adsorption of cations or a smaller cationic size.

2.4 Conclusion: Numerical simulations are required to enhance the understanding of the Electric Double-Layer as current theories fail

The well developed theories for small dissolved and diluted electrolytes are not applicable to the class of ionic liquids. The great variety and high charge density of ionic liquids hold many challenges for theoreticians. Properties of Coulombic fluids and highly charged systems not yet included in theoretical models are

- ion size and ion shape,
- structural transitions and phase transitions,
- polarization effects and
- electrode types and shapes.

For filling the current gab between experimental results and theoretical models we are able to perform simulations on a molecular level [83]. Following the recent advances by [78, 79, 7, 80, 81, 82], we aim to understand the electric double layer formation and resulting capacitance by molecular simulations of room temperature ionic liquids.

Chapter 3

Electrochemical properties of room-temperature ionic liquids in experiment and simulation

Within this chapter we aim to provide a non-exhaustive overview of physicochemical properties of room-temperature ionic liquids (RTILs). Specific emphasis is set on properties that are discussed in conjunction with electrochemical applications. We start with the definition of common abbreviations of typical cations and anions, including their molar mass and effective size. For every property a short conclusion is provided whether it is accessible in molecular dynamics simulations of ionic liquids. We summarize experimental methods applied to ionic liquids at electrified interfaces and provide insights into recent results of molecular dynamics simulations of RTILs at interfaces. We conclude the necessity to perform computer simulations for a fundamental understanding of underlying phenomena. Lastly we comment on the force field choice for the model ionic liquid/electrode under study in terms of reproducing important features of RTILs at electrified interfaces.

3.1 Introduction: Common anions and cations

Room temperature ionic liquids (RTILs) gain more and more attention as designer solvents in electro-chemistry due to their properties. RTILs are environmentally friendly and non-volatile [84], and sustain higher voltages without decomposition [85]. Because of their large electrochemical windows (up to +/- 5-6 V, wider than any aqueous solutions), RTILs are very promising materials for electrochemical capacitors [86]. As has been stated by several authors in the past years, ionic liquids will have a bright future due to their unique combination of properties [87, 88, 89].

Table 3.1 and 3.2 contain names, common abbreviations and chemical formulas of some typical cations and anions that are used as constituents of RTILs. As can be seen from the tables, for the given ions there is no uniform naming convention. The origin is found in the historical development of this new material class. Thus the knowledge of the common abbreviations proves useful for subsequent literature research.

Table 3.1: The names, common abbreviations and chemical formulas of some typical cations, constituents of room temperature ionic liquids. Non substituted, non functionalised cations. Effective size at 289 K and 1 bar, taken from [90].

Full name	Abbreviation	Chemical formula	Molar mass M (g / mol)	Effective size V^* (cm^3/mol)
		Cations		
Imidazolium				
1-Ethyl-3-methyl-imidazolium	[emim] [C_2Mim]	$C_6H_{11}N_2$	111.17	99.2
1-Butyl-3-methyl-imidazolium	[bmim] [C_4Mim]	$C_8H_{15}N_2$	139.22	133.6
1-Hexyl-3-methyl-imidazolium	[hmim] [C_6Mim]	$C_{10}H_{19}N_2$	167.27	168.0
Ammonium				
Tetraethyl-ammonium	[TEA] [N2222]	$C_8H_{20}N$	130.25	
Phosphonium				
Trihexyl-tetradecyl-phosphonium	[P666,14] [$(C_6)_3C_{14}P$]	$C_{32}H_{68}P$	483.87	556.6
Pyrrolidinium (Cyclic Ammonium)				
N,N-dimethyl-pyrrolidinium	P11	$C_6H_{14}N$	100.18	
Pyridinium				
N-Butyl-pyridinium	[C_4py] [Bpy]	$C_9H_{14}N$	136.22	287.4
1-Butyl-3-methyl-pyridinium	[bmpy] [C_4-$3C_1$pyr]	$C_{10}H_{16}$	150.24	304.6

Table 3.2: The names, common abbreviations and chemical formulas of some typical anions, constituents of room temperature ionic liquids. Effective size at 289 K and 1 bar, taken from [90].

Full name	Abbreviation	Chemical formula	Molar mass M (g / mol)	Effective size V^* (cm^3/mol)
		Anions		
Chloride	[Cl]	Cl	35.45	25.9
Bromide	[Br]	Br	79.9	27.8
Tetrafluoroborate	[BF4]	BF_4	86.80	53.4
Hexafluorophosphate	[PF6]	F_6P	144.96	73.7
Trifluoromethanesulfonate	[otf] [OTf] [TfO]	CF_3O_3S	149.07	
Bis-((trifluoromethyl)-sulfonyl)imide	[ntf] [TFSI] [TF2N]	$[NTf_2]$ $C_2F_6NO_4S_2$	280.15	158.7
Methylsulfonate / Mesylate	[mso] [MeSO3] [mesy]	CH_3O_3S	95.10	66.5
Methylsulfate	[msu] [MeSO4]	CH_3O_4S	111.10	73.6
Ethylsulfate	[esu] [EtSO4]	$C_2H_5O_4S$	125.12	91.7
Dicyanamide	[dca]	C_2N_3	66.04	55.2

3.2 Electrochemical properties of typical room temperature ionic liquids

The properties of typical RTILs composed of some of the above listed ions are provided in this section. Emphasis is set on RTILs, that appear to be frequently used in the studies of electrical double layer and various applications. Main reviews of RTIL properties are provided in the following works:

- Zhang et al [91]: Physical Properties of Ionic Liquids: Database and Evaluation. Including Phase Transition Temperature: Melting Point, Glass Transition Point, Decomposition Point, Freezing Point, and Clearing Point, Density, Viscosity, and Surface Tension, Conductivity, Polarity and the Electrochemical Window.

- Subsequent publication of Zhang et al [92]: A handbook of physico-chemical properties of ionic liquids.

- A series of three paper from Tokuda et al [93, 94, 95] containing physical properties of RTILs and discussion of the influence of the anionic specie, the cationic structure and for RTILs with imidazolium cations the variation of the alkyl chain length.

Some sources provide an overview over specific properties not covered here. They will be summarized below:

- The molecular volumes and radii as well as the solvent-accessible surface and the different enthalpies calculated with COSMO-RS [96].

- Temperature-dependent viscosities and conductivities of [TFSI]-ILs by Bulut et al [97], accessible through [98].

- Kamlet-Taft solvent parameters, α (hydrogen bond donor), β (hydrogen bond acceptor), and π^* (polarisability) for solvents [99] and for RTILs [100]. See also Jessop et al [101].

- Solubility of four ionic liquids in water by Shvedene et al [102].

- Surface tension of ionic liquids and ionic liquid solutions by Tariq et al [103].

- Solubility constants of inorganic salts in several ionic liquids by Endres et al [104] (Page 65, Table 3.12).

3.2.1 Density, melting temperature, decomposition temperature and electrochemical window

RTILs, as suggested by their name, are ionic liquids with a melting temperature slightly above or below 300 K. They contain densely packed ionic species, with each compound carrying a net-charge. In the introduction we referred to the low probability of vaporisation of RTILs. Instead of evaporating, ionic liquids rather decompose at higher temperatures. Thus, the decomposition temperature T_d is of relevance for industrial applications. For electrochemical applications, the electro-chemical window is of special interest. Table 3.3 contains a summary of density, melting temperature, decomposition temperature and electro-chemical window for some typical RTILs.

Table 3.3: Density at 293 K (taken from [105]), melting temperature, decomposition temperature (taken from [92]) and E tlectro-chemical window (taken from the reference as stated in the table).

Cation/Anion abbreviation	Density ρ (g/cm^3)	Melting Temperature T_m (K)	Decomposition Temperature T_d (K)	Electrochemical Window (V) [Working Electrode]
[emim][BF4]	1.28	287.57	718.64	4.4 [Pt] [104] / 4.55-5.2 [92]
[emim][TFSI]	1.518	256.15	690	6.3 [104] / 4-4.6 [92]
[bmim][Cl]	1.10	314.15	527.15	
[bmim][BF4]	1.17	192.15	708.15	4.7 [Pt] [106]
[bmim][PF6]	1.36	212.15	663.15	4.7 [Pt] [106]
[bmim][TFSI]	1.43	271.15	675.15	4.8 [Pt] [106]
[bmim][TfO]	1.29	289.55		3.8 [Pt] [104] / 4.9 [Pt] [106]
[bmpy][BF4]	1.220			
[bmpy][TFSI]	1.449			
[C4py][TFSI]	1.453 [92]	299	677	
[P666,14][TFSI]	1.065 [92]		673.15 [92]	5.0 [Pt] [106] / 6.5 [92]

Advanced procedures for the calculation of melting points and thermodynamic stability exist [107], however their usage is still not widely applied. Tian et al [108] presented a comprehensive overview of computational methods for calculating the electrochemical window of RTILs with varying degrees of approximation, computational costs and accuracy.

3.2.2 Dynamic properties: Viscosity, diffusion coefficient, conductivity

Dynamic properties of RTILs are still of considerable scientific interest due to their obscure nature [95, 109]. For example, experimental results of ionic mobility show for small anions a reduced mobility compared to their larger counter-parts, the cations [95, 110, 111]. Table 3.4 and 3.5 provide an overview of dynamic properties of common RTILs.

In computer simulations, transport or dynamic properties are hard to calculate due to the slow dynamics of most IL systems [109]. Without specific adjustments of the underlying models or force fields, the discussion of diffusion coefficients, viscosity and ionic conductivity is not reasonable [112, 113]. Kowsari et al [114] determined one major factor for the magnitude of the self-diffusion as the geometric shape of the anion of the ionic liquid.

Table 3.4: Dynamic properties. The diffusion coefficients from reference [104] are provided at 303 K. High temperature molten salts NaCl and CsCl are given as reference in the last lines of the table. Properties measured at conditions near the melting point for NaCl ($T_m = 1081\,\mathrm{K}$) and CsCl ($T_m = 918\,\mathrm{K}$).

Cation/Anion abbreviation	Viscosity η_D ($1\,\mathrm{cP} = 1\,\mathrm{mPa}\cdot\mathrm{s}$)	Ion diffusion coefficient D ($10^{-11}\,\mathrm{m}^2/\mathrm{s}$)		Conductivity σ (mS/cm)	Molar conductivity Λ ($\mathrm{S\,cm}^2/\mathrm{mol}$)
		Cation	Anion		
[emim][BF4]	25 [105]	5.0 [2]	4.0 [2]	2.2 [105], 13.6 [104]	2.1 [104]
[emim][TFSI]	23 [105]	6.2 [104]	3.7 [104]	7.4 [105], 5.7-9.0 [104]	1.5-2.3 [104]
[bmim][Cl]					
[bmim][BF4]	233 [105]	1.8 [104]	1.8 [104]	0.17 [105]	
[bmim][PF6]	312 [105]	0.89 [104]	0.71 [104]	0.14 [105]	
[bmim][TFSI]	52 [105]	3.4 [104]	2.6 [104]	3.9 [105]	
[bmim][TfO]	90 [105]	2.2 [104]	1.6 [104]	3.7 [105]	
[bmpy][BF4]	90 [105]			0.33 [105]	
[bmpy][TFSI]	40 [105]			0.30 [105]	
[P666,14][TFSI]	450 [106]				
[C4py][TFSI]	58.3 [115]	2.8 [104]	2.2 [104]	3.21 [115]	0.92 [115]
NaCl	1.43 [2]	962 [2]	673 [2]	3610 [2]	
CsCl	1.60 [2]	350 [2]	380 [2]	1090 [2]	

Table 3.5: Kinematic viscosity over temperature of [HMIM][TFSI] taken from Santos et al [116]. Capillary tube (Ostwald; Ubellohde) method. Note: This property is seldom described, the large overview from Zhang et al [92] reports in total only 11 values from over 7000 quantities.

Temperature T (K)	Kinematic Viscosity η_K ($10^{-5}\,\mathrm{m}^2/\mathrm{s}$)
298.149	5.062
303.151	4.039
313.156	2.698
323.149	1.897
333.153	1.392
343.150	1.059

3.2.3 Static dielectric constant

Ionic liquids are conductive, which makes the measurement of the dielectric constant of RTILs challenging [100]. Usually experimental values are based on microwave dielectric relaxation spectroscopy including sophisticated extrapolation schemes. Either the macroscopic, static dielectric constant ε or the Kamlet-Taft dipolarity/polarisability parameter π^* is used for discussing the electrostatic solute-solvent interactions.

As shown by Schroder et al [117], the computational calculation of the dielectric spectrum of ILs is strongly dependent on the application of a polarisable model. In the words of the authors, "the inclusion of polarizable forces is more than a mere numerical improvement [...] In fact, it is essential to account for the correct collective dynamics."

Table 3.6: Static dielectric constant. Taken from [118]. Comprehensive list also given by Kobrak [100]. Values reported there for a wider range of cations vary between $\varepsilon = 8.9$ and $\varepsilon = 27.9$.

Cation/Anion abbreviation	Dielectric constant ε
[emim][TfO]	15.2
[emim][BF4]	12.8
[bmim][BF4]	11.7
[bmim][PF6]	11.4
[hmim][PF6]	8.9

3.2.4 Surface tension of the liquid/vapour interface

The discussion of the surface tension is in general plausible due to the wide applicability of this macroscopic quantity. The measurement of the surface tension of ionic liquids is an effective way to access intrinsic energies, that are involved in the interactions between the ions, as explained by Tariq et al [103] in their critical review analysis. Due to nature of ionic liquids, the surface tension is an important quantity also in terms of structural processes. At the surface, the internal anisotropy of ILs becomes apparent, moreover types of segregation/orientation and influence of the interaction with other molecules can be studied [103].

Within computer simulations, the simulation of the liquid/vapour interface is possible [119], however a number of considerations are known to affect the results [103]. Among the difficulties are the adequacy of long range corrections and influence of finite-size effects [120, 121].

Table 3.7: Surface tension of the liquid/vapour interface σ_{lv} near their respective melting points. Taken from [2].

Cation/Anion abbreviation	Surface tension σ_{lv} (mJ/m^2)
[bmim][Cl]	47.5
[bmim][PF6]	43.5
NaCl	1138
KCl	98
$BiCl_3$	73

3.2.5 Electrode materials and experimental accessible electrode charge densities

A summary of types of electrodes that have been used in conjunction with RTILs is given by Endres et al ([104], page 301, table 11.1).

The determination of experimentally accessible electrode charge densities is rather difficult [1]. For ions in aqueous solutions, surface charge densities between -40 to $+80\,\mu$C/cm^2 have been reported [122]. Upon considering the area under an experimentally measured capacitance/potential-curve starting from the potential of zero charge, a rough approximation of the surface charge density can be obtained. For the spherical ion PF_6^- at a Au(111) electrode, the surface charge density can be estimated to be approximately $+30$ to $+40\,\mu$C/cm^2 [30].

[1] The author thanks V. Ivaništšev for useful insights in this topic.

3.3 Electrochemical studies of room temperature ionic liquids: Experimental methods and molecular simulations

We discussed in the previous section the accessibility of properties of room temperature ionic liquids in molecular dynamics simulations. Yet, we are not only interested in the physical properties in bulk liquids, but aim to understand the capacitance of a model capacitor filled with an ionic liquid and the interfacial structuring at the electrodes. Experimental methods applied to ionic liquids at electrified interfaces range from electrochemical impedance spectroscopy (EIS) and cyclic voltametry (CV) to a variety of spectroscopic methods. A short overview of experimental methods applied to room temperature ionic liquids at electrified interfaces is provided Tab 3.8 including selected references.

Table 3.8: Electro-chemical studies of room temperature ionic liquids: experimental methods.

Property	Experimental method	Selected references
Differential capacitance and cyclic voltammograms	Electrochemical impedance spectroscopy (EIS)	[33] [28] [30] [32] [123] [31] [124]
	Cyclic voltammetry (CV)	[28] [106] [30] [42]
Interfacial structure	Scanning tunnelling microscopy (STM)	[30] [39] [42] [41]
	Atomic force microscopy (AFM)	[125] [42] [41]
	Distance tunnelling spectroscopy (DTS)	[42] [41]
	Sum frequency generation spectroscopy	[126] [127]
	Ultraviolet photoelectron spectroscopy (UPS)	[128]
Thin film structure	Transmission electron microscopy (TEM)	[129]
	Surface Force Apparatus (SFA)	[16]
	Angle-resolved X-ray photoelectron spectroscopy (ARXPS)	[130] [131]
Structural transitions and phase behaviour	Transmission electron microscopy (TEM)	[129]
	Raman spectroscopy	[132]

We note, that Drüschler et al [31] reported experimental results on the influence of temperature on the differential capacitance for the extremely pure ionic

liquid 1-butyl-1-methylpyrrolidinium tris(pentafluoroethyl)-trifluorophosphate at an Au(111) electrode. The authors performed careful analysis of broadband capacitance spectra of the electrode/RTIL interface by combining electrochemical impedance spectroscopy combined with in situ STM and in situ AFM techniques. The interfacial dynamics were found to be dependent on processes taking place on significant different time scales. Thus, artefacts might potentially occur through single-frequency experiments on the temperature dependence of the interfacial capacitance.

Molecular dynamics simulations of RTILs proofed in a variety of recent studies capable of providing insights into the differential capacitance as well as structural properties of RTIL/electrode combinations, see Tab. 3.9. The listed references are far from being all-encompassing, however the references provided by the respective authors can be considered as source for further reading.

From the provided collection of computational studies and experimental methods, we draw the following conclusions:

1. A variety of experimental methods is applied to RTILs at electrified interfaces. Especially the combination of voltammetry/electrochemical impedance spectroscopy and interfacial structure analysis by scanning tunnelling microscopy or atomic force microscopy provides basic insights in the origin of physical phenomena.

2. Molecular dynamics simulations are capable of providing informations on atomistic and molecular structuring, charge ordering and thus potential drop and capacitance within the same experimental setup. Thus, the influence of molecular ordering on the capacitance can be analysed without the risk of artificial variation of the environmental conditions.

3. Although molecular structuring is accessible through experiments, molecular dynamics simulations are capable of providing an atomistic resolution and thoroughgoing definition of environmental details.

The combination of experimental and computational studies is a powerful path to enable fundamental understanding of the underlying physical and chemical phenomena demonstrated by recent publications in the field [141, 138, 142, 143]. Especially the surface chemistry of ionic liquids requires attention from both, experimentalists and theoreticians [144, 145].

Table 3.9: Selected electrochemical studies of room temperature ionic liquids by molecular dynamics simulations.

Author & Year	Ref.	System under study	Selected results
Structure and capacitance of the EDLs			
Kislenko 2010	[133]	[BMIM][PF6] at graphite, influence of temperature	Magnitudes of density peaks of anions near the surface decrease with increasing temperature while in the case of cations anomalous temperature behaviour of the density profile is observed: the magnitude of the second peak of cations increases with the increase of temperature.
Feng 2011	[134]	Neat RTILs and in RTILs mixed with different mass fractions of organic solvents	The description of ions as *ion pairs* proved useful for describing the relationship between EDL structure and capacitance.
Structure and potential of mean force			
Fedorov 2012	[135]	[dmim][Cl] at a neutral graphene surface	Enrichment of cations at the surface leads the formation of several distinct solvation. A non-zero potential drop results.
Influence of the electrode (e.g. roughness, curvature)			
Vatamanu 2012	[136]	[C(n)mim][TFSI], n = 2, 4, 6, and 8 at basal (flat) and prismatic edge face (rough) graphite electrodes	The differential capacitance depends on the potential dependent structure and composition of the interfacial electrolyte layer. The ability of ions to rearrange/reorient charge-caring groups is important for maximization of the counterion number charge near the surface.
Feng 2012	[137]	Onion-like carbon (OLC) electrode surface	Capacitance of EDLs on OLCs increases with the curvature, explained by dominance of charge overscreening and increased ion density per unit area of electrode surface.
McDonough 2012	[138]	Carbon onions in acetonitrile with 1 M [TEA][BF4] or [TBA][BF4]	The larger alkyl chains of the $[TBA]^+$ cation compared to $[TEA]^+$ results in better separation of ions and counter-ions at the charged OLC surface, which allow for better charge screening and results in a larger capacitance.
Merlet 2012	[139]	Microporous carbon electrodes	Not the large surface area but the separation of positive and negative ions inside the porous disordered carbons causes a high capacitance.
Mendonca 2012	[140]	Alkylammonium cations and alkylsulfonate anions on a flat iron surface	Anions and cations are in the interfacial layer. Alkyl chains of the ions interact with the surface: Butyl chains of sulfonate anions tend to be directed away from the surface, whereas butyl chains of ammonium cations lie parallel to the surface.

3.4 Reviewing the force field for the model ionic liquid

For modelling ionic liquids in molecular dynamics simulations, a variety of force fields has been developed and applied in the last years [146, 147, 148, 149] ranging from non-polarisable full atomistic models [150, 151, 152, 153, 154, 145, 155, 156, 140] over united-atom approaches [157, 158, 159, 160] to simplifying coarse grain models [161, 121]. Force fields with implementation of polarization effects are discussed in [162, 163, 164, 165, 166].

The choice of a model reflects the aims of a certain study. A model might be capable of reproducing the dissolution of carbon dioxide, but might fail completely if the ionic mobility is discussed. In this study, we are specifically interested in the structuring of ions at a charged interface. Thereby we want to understand size effects and the influence of the temperature on the ion structuring. Furthermore we want to study the origin of experimentally reported effects on a fundamental level. These constraints lead to the choice of an extremely simplified force field model for the ionic liquid and electrodes.

As has been reported by Fumino et al [167], ionic liquids do not only form through a subtle balance between Coulomb forces and dispersion forces, but also hydrogen bonds play a considerable role. A tuned balance between these interaction force is necessary to assure the correct reproduction of real melting points, viscosities and enthalpies of vaporization. By simplifying a model to a coarse grain form, we immediately neglect such subtle connections. However, drawing conclusions on the origin of observations becomes straightforward if the number of possible reasons is reduced.

As is explained in more detail in Chapter 5, we describe the ions and electrode atoms as slightly soft spheres by a repulsive Lennard-Jones potential. The ions and electrode atoms are only allowed to interact via Coulombic attraction/repulsion and steric repulsion. No attractive potential is included except for the Coulomb potential between oppositely charged ions. To include polarization effects, we apply charge scaling.

In the following sections, we comment on the choice of the ion sizes and justify the charge scaling approach. The results of the calculation of the liquid/vapour surface tension of the chosen model are reported. The phase diagram of a comparable restricted primitive model with asymmetric sized ions is described. The discussed properties should allow a refined picture of the model including its advantages and drawbacks.

3.4.1 Ion sizes are comparable with room temperature ionic liquids

In a recent work by Costa et al [90] the effective ion size of several cation and anion species of ionic liquids are given. This work allows us to make a rough estimation whether the ion size chosen for this coarse grain model is comparable to "real" ionic liquids.

The spherical volumes of our coarse grain model ionic liquids are for the cations

$$V_{\text{Cation}} = 4/3\pi r^3_{\text{Cation}} = 4/3\pi 0.5^3\,\text{nm}^3 = 0.52\,\text{nm}^3 = 313\,\text{cm}^3/\text{mol}$$

and for the anions

$$V_{\text{Anion}} = 4/3\pi r^3_{\text{Anion}} = 4/3\pi 0.25^3\,\text{nm}^3 = 0.065\,\text{nm}^3 = 39.2\,\text{cm}^3/\text{mol}.$$

Sample room temperature ionic liquid compounds with the same effective molar volumes are $[\text{C6pyr}]^+$ ($318.8\,\text{cm}^3/\text{mol}$) and $[NO_3]^-$ ($39.1\,\text{cm}^3/\text{mol}$). Similar size ratios for anions and cations are found for $[C_8\text{mim}]^+$ ($202.3\,\text{cm}^3/\text{mol}$) and $[\text{Cl}]^-$ ($25.9\,\text{cm}^3/\text{mol}$) or $[(C_6)_3C_14P]^+$ ($556.6\,\text{cm}^3/\text{mol}$) and $[PF_6]^-$ ($73.7\,\text{cm}^3/\text{mol}$). Notations for the ions and values are taken from [90].

3.4.2 Inclusion of polarization effects by charge scaling

Under current discussion in the scientific community is the importance or the necessity, to include polarization effects into the force field models describing ionic liquids [149, 168]. As Schröder discussed recently [168], classical molecular dynamics simulations often overestimate charge ordering effects found in ionic liquids and underestimate the ionic mobility. He explains the drawbacks of classical molecular dynamics simulations by the missing or insufficient inclusion of polarization effects. Polarization effects are found to have a considerable influence on the immediate neighbourhood of a molecular ion, thereby critically influencing the diffusion coefficients and short-ranged ordering of the ions.

Two separate methods are currently present to include polarization effects in a molecular dynamic model, namely scaling of partial charges by a factor between 0.7 and 0.9, and the inclusion of polarization forces. The charge scaling approach is constituted within the electronic continuum model requiring introduction of an effective dielectric constant [169]. As polarization forces in general lead to more accurate results on all length scales, the charge scaling concept is especially

reliable for the collective level, but might fail on the local or short-range level.

However polarisable force field models contain the drawback of a large increase of computational costs, which proved incompatible with the requested amount of independent simulation setups and the coarse grain character of the model under study. In conclusion, we decided upon the usage of a charge scaling approach for the inclusion of polarization effects. We expect that in future research the influence of different polarization strategies for electrode atoms and ions will to be considered in more detail thereby following the work of Vatamanu et al [36, 170] and Merlet et al [171].

3.4.3 The liquid/vapour surface tension is not well reproduced by pure Coulombic attraction

So far, we discussed the quality of our model based on the reasonability of ion size, size ratio and ion charge. To understand the applicability of the model, a comparison of physical properties of the model ionic liquid with real target properties is advisable. Therefore, we chose the surface tension as a macroscopic property, that allows considerable insights into the ionic interactions [103]. Merlet et al [120, 121] proved a simulation scheme for calculating the surface tension for a coarse grain model ionic liquid comparable to the model under study. The authors performed extensive tests on the effect of box size, therefore we feel confident to apply the same routine as presented in [120] [2].

The resulting surface tension of the model under study was found to be in the region of 0.5-1 mN/m for temperatures between 250 K and 350 K. At higher temperatures, vaporisation increased considerably. The surface tension is thus found to be much lower than experimental references for RTILs (e.g. 43.5 mN/m for [bmim][PF6] [2]). Also Merlet et al [120] report higher surface tensions. The model of Merlet et al contains an attractive Lennard-Jones potential between the ions. We expect the reduced attraction between the ions the key for the low surface tension. Pure Coulombic attraction is not sufficient to reproduce the surface tension of RTILs accurately.

[2] We note an unexpected difficulty when simulating the liquid/vapour interface using the simulation software Gromacs. If the position of the interface is chosen to be close to the boundary of the simulation box, the calculated surface tension exhibits large fluctuations. Moreover, ion chains are formed between subsequent interfaces. While avoiding the overlapping of the liquid slab and the box boundaries, few ions leave the liquid phase as expected and the surface tension can be calculated without extensive fluctuations.

3.4.4 A comment on the phase diagram of the model ionic liquid

The knowledge of the phase diagram of liquids is usually of practical and fundamental importance [172]. However, for ionic liquids we severely lack understanding of the critical behaviour and coexistence of phases [173]. In the recent years, attempts have been made to characterize the phase diagram of Coulombic fluids by describing the restricted primitive model and its variations [174]. To allow a comparison of the model under study in this work and reported results for the restricted primitive model, we have to transfer all units to their reduced forms as they are used by the community.

The concept of reduced units

On characterizing the model system and comparison with other experimental and theoretical concepts, reduced units are widely used. Alternatively to the characterization of a model system in SI units, one can easily develop a set of reduced units taking into account the length σ_{LJ} and the energy ε_{LJ}. Both parameter correspond to the range and strength of the intermolecular forces [13]. According to Hansen and McDonald [13] a common reduction of physical quantities can be done by reducing the number density $\rho_N = N/V$ to

$$\rho^* = N\sigma_{LJ}^3/V,$$

with N being the number of ions, V being the volume and σ_{LJ} being the particle diameter [3]. The temperature T can be reduced using $T^* = k_B T/\varepsilon_{LJ}$, with k_B being the Boltzmann constant. For the liquid region of the phase diagram both values, reduced number density ρ_N^* and reduced temperature T^*, are expected to be in order of unity. A general rule is the reduction of energy units by $k_B T$ and the reduction of any length by σ_{LJ}.

The considerations about reduced units are basically simple for the hard sphere model, also termed "primitive restricted model" (RPM) [176, 175, 177, 178]. Two deviations from the classic RPM appear in the model system under study in this work: (i) the particles are not completely hard spheres, but contain

[3] Definitions of the number density vary between the authors, as one might either consider the number of ion pairs $\rho_N = N_{\text{ion pairs}}/V = N_{\text{co-ions}}/V = N_{\text{counter-ions}}/V$ or the number of (combined) ions $\rho_N = N_{\text{ions}}/V = N_{\text{co-ions}}/V + N_{\text{counter-ions}}/V$. For example Hynninen et al. defined the total reduced number density as $\rho_t^* = (N_+ + N_-)/V \cdot \sigma_{LJ}^3$ [175]. We will later calculate all possibilities.

a certain softness defined by the repulsive Lennard-Jones potential used

$$U_{LJ}^{ij} = 4\varepsilon_{LJ}\left(\frac{\sigma_{LJ}^{i}+\sigma_{LJ}^{j}}{r}\right)^{12} = 2k_BT\left(\frac{\sigma_{LJ}^{i}+\sigma_{LJ}^{j}}{r}\right)^{12};$$

(ii) cations and anions are not equally shaped but have a size asymmetry of $\lambda = \sigma_{LJ}^{+}/\sigma_{LJ}^{-} = 2$, which is a model referred to as size-asymmetric primitive model (SAPM) [178][4]. Yan et al. [178] defined in the context of the SAPM a mean diameter $\sigma_{LJ}^{\pm} = (\sigma_{LJ}^{+} + \sigma_{LJ}^{-})/2$ to account for the ionic size asymmetry. However, as in this work interfacial properties are studied, it is reasonable to avoid mixing the ionic size and consider for anions and cations some physical quantities - like surface charge density - independent from each other.

Application of the concept of reduced units to the model under study

The coarse grain IL in reduced units In comparison with the given literature, it is possible to understand the system studied in this work as size-asymmetric primitive model electrolyte with high density within a medium with a dielectric constant $\varepsilon = 2$. Both, co-ions and counter-ions, carry a charge with magnitude $|q| = 1\,e$ but varying sign. Using this assumption, we can compare the primitive hard sphere models with our model with slightly soft balls. Basically results are not expected to differ much.

The simulation setup with charged walls contains a slit pore with diameter $L_z = 24\,\mathrm{nm}$ corresponding to a reduced wall-distance of $L_z^{*+} = 24$, $L_z^{*-} = 48$ and $L_z^{*\pm} = 32$ for cations, anions and the combined liquid, respectively.

With the given particle parameter, we can reduce the physical properties to obtain a set of reduced quantities as used in the literature, see Tab. 3.10 and 3.11. The bulk ion density is constant for all temperatures, namely $\rho_{N0} = 0.365\,\mathrm{ionpairs/nm^3}$. The reduced cation number density reads $\rho_{N0\mathrm{Cation}}^{*} = 0.365$, the reduced anion number density $\rho_{N0\mathrm{Anion}}^{*} = 0.0456$. Using the definition given by Yan and Pablo [178], the total reduced number density in the system should be considered with $\rho_{total}^{*} = (N_+ + N_-)/V \cdot (\sigma_{LJ}^{\pm})^3 = 0.308$.

The Bjerrum length λ_B is defined as the distance at which the electrostatic interaction between two elementary charges is comparable in magnitude to the thermal energy k_BT. It is considered to appear for the RPM as $\lambda_B = q^2/(4\pi\varepsilon\varepsilon_0 k_BT) = \sigma_{LJ}/T^{**}$, with ε_0 being the vacuum permittivity [175]. Again, we consider a size-asymmetric primitive model electrolyte with high density within a medium with

[4]The results for $\lambda = \sigma_{LJ}^{+}/\sigma_{LJ}^{-} = 2$ are equal to the results obtained for $\lambda = \sigma_{LJ}^{+}/\sigma_{LJ}^{-} = 0.5$.

Table 3.10: Reduced temperatures under study. Comparison of several possible reductions used in literature. (i) Reduction by the Lennard-Jones softness parameter ε_{LJ}: $T^* = k_B T/\varepsilon_{LJ}$. (ii) Reduction by the electrostatic interaction energy of two ions in contact $T^{**} = (4\pi\varepsilon\varepsilon_0 k_B T \cdot \sigma_{LJ})/q^2$, with ε_0 being the vacuum permittivity. This reduction depends on the ion interaction parameter σ_{LJ}, which is given below. The ions are considered to be dissolved in a medium with dielectric constant $\varepsilon = 2$.

T (K)	T^*	T^{**}		
		$\sigma^+_{LJ} = 1.0\,\text{nm}$	$\sigma^-_{LJ} = 0.5\,\text{nm}$	$\sigma^\pm_{LJ} = 0.75\,\text{nm}$
250	1.11	0.030	0.015	0.023
300	1.33	0.036	0.018	0.027
350	1.56	0.042	0.021	0.032
400	1.78	0.048	0.024	0.036
450	2.00	0.054	0.027	0.041
500	2.22	0.060	0.030	0.045

Table 3.11: Reduced surface charge $\sigma^* = \sigma \cdot \sigma^2_{LJ}/e$ under study, with σ being the "real" surface charge density, σ_{LJ} being the diameter of the ion and $e = 1.602 \cdot 10^{-19}\,\text{C}$ being an elementary charge. Surface charges under study are ranging from 0.00 to 50.0 μC/cm^2

σ (μC/cm^2)	Reduced surface charge σ^*		
	Cation $\sigma^+_{LJ} = 1.0\,\text{nm}$	Anion $\sigma^-_{LJ} = 0.5\,\text{nm}$	Ions $\sigma^\pm_{LJ} = 0.75\,\text{nm}$
0.25	0.0156	0.0039	0.0088
1.00	0.0624	0.0156	0.0351
5.00	0.312	0.0780	0.181
16.0	1.00	0.250	0.563
24.0	1.50	0.375	0.844
50.0	3.12	0.780	1.755

a dielectric constant of $\varepsilon = 2$. Both, co-ion and counter-ion, carry a charge with magnitude $|q| = 1\,e$, but varying sign.

Table 3.12: Bjerrum length $\lambda_B = q^2/(4\pi\varepsilon\varepsilon_0 k_B T)$ and its reduction by σ_{LJ}: $\lambda_B^* = \lambda_B/\sigma_{LJ}$.

T (K)	Bjerrum length			
	λ_B (nm)	Cationic λ_B^{*+}	Anionic λ_B^{*-}	Ionic $\lambda_B^{*\pm}$
250	33.3	33.3	66.6	44.4
300	27.8	27.8	55.6	37.1
350	23.8	23.8	47.6	31.7
400	20.8	20.8	41.6	27.7
450	18.5	18.5	37.0	24.7
500	16.7	16.7	33.4	22.3

The capacitance C or differential capacitance C_d can be reduced by $C^* = C \cdot \sigma_{LJ}/(4\pi\varepsilon\varepsilon_0)$ as given by Reszko-Zygmunt et al [177].

Analysing the asymmetric sized primitive model (ASPM) phase diagram: Results for the system under study For the ASPM Yan and Pablo [178] estimated the critical point for the gas-liquid transition, finding for $\lambda = 0.5$ a critical temperature $T_c = 0.0475$ and a critical density of $\rho_c = 0.070$. Moreover they present in their Figure 1 the simulated binodal curves. A comparison of the model under study in this work with a fixed reduced number density of $\rho^*_{total} = 0.308$ and the given binodal curves - thereby disregarding the minor deviations in the model force field - indicates a fluid phase for the highest temperatures under study ($T = 450\,\mathrm{K} \mathrel{\hat{=}} T^* = 0.041$ and $T = 500\,\mathrm{K} \mathrel{\hat{=}} T^* = 0.045$), a coexistence of liquid and vapour phase for $T = 250\,\mathrm{K} \mathrel{\hat{=}} T^* = 0.023$, $T = 300\,\mathrm{K} \mathrel{\hat{=}} T^* = 0.027$, $T = 350\,\mathrm{K} \mathrel{\hat{=}} T^* = 0.032$, $T = 400\,\mathrm{K} \mathrel{\hat{=}} T^* = 0.036$. However, direct correlations should be avoided, as even tiny changes in the force field may result in large deviations as it has been shown / will be shown in the upcoming analysis. As Panagiotopoulos and Fischer have shown, the phase behaviour of an asymmetric sized hard sphere model depends strongly on the size ratio of the ions thereby contradicting available theories [179].

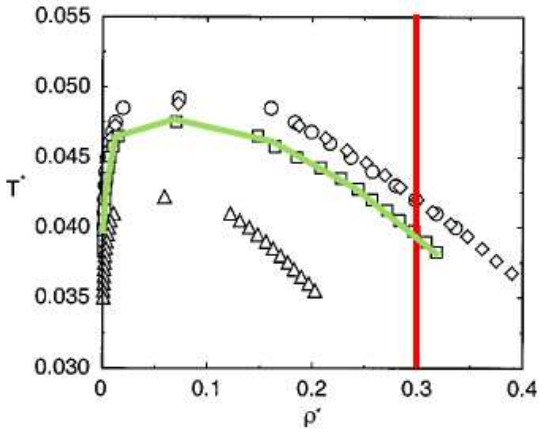

FIG. 1. Simulated binodal curves for size-asymmetric electrolyte systems with different λ. Circles: λ=1; diamonds: λ=0.75; squares: λ=0.5; triangles: λ=0.25.

Figure 3.1: Simulated binodal curves for size-asymmetric electrolyte systems taken from Yan et al [178]. Red and green lines added to guide the eye. The red line corresponds to the reduced density of the system under study in this work $\rho^*_{total} = 0.308$.

3.4.5 On the choice of surface charge densities and electrode model

Driven by the discussion of experimentally accessible surface charge densities, we conclude the usage of a charge density interval between -50 and $+50\,\mu\mathrm{C/cm^2}$. Whereas experimentalists mostly provide potential drops, the calculation of the dependence of the surface charge density on electrode potential remains a challenge in MD simulations. Yet, factors that influence the surface charge/potential-dependence are under debate. For example, attractive ion-surface interactions [180] and the electrode polarization [171] might drastically influence the surface charge/potential-dependence.

We note, that the chosen electrode model is designed to be as simplest as possible without any polarisation effects or charge transfer. Furthermore, the electrode atoms are purely repulse to assure that only steric effects and Coulombic interaction influence the adsorption of ions.

3.5 Conclusion: Are we confident with our model? What are the drawbacks?

We want to study the origin of experimentally reported effects of ionic liquids at electrified interfaces on a fundamental level by only including steric effects and Coulombic interaction in our model. These constraints lead to the choice of an extremely simplified force field model for the ionic liquid and electrodes.

Upon judging the force field we draw the following conclusions:

- \- The model is non-atomistic and non-polarisable. We do not include quantum effects and charge transfer.

+ \+ Ion sizes are in the region of room temperature ionic liquids.

+ \+ We integrated polarization effects by charge scaling. The method is considered as "the poor man's way" of introducing polarisability, however Fedorov and Kornyshev [7] used the model successfully.

- \- The ionic liquid model does not allow the reproduction of experimental surface tensions.

? \? The ionic liquid model under the given conditions might be in a state of liquid and vapour coexistence.

- \- We do not model metal electrodes, our electrode model is non-polarisable. We do not consider quantum effects and charge transfer for the electrodes.

+ \+ Surface charge densities under study are comparable to experiments.

Naturally, any chosen model contains drawbacks that should be discussed and possibly eliminated in upcoming studies. However, we expect, that the structural analysis of the ion distribution at the electrode surfaces will provide us with physical meaningful results.

Chapter 4

Advanced sampling methods

In the following chapter we introduce the concepts of advanced sampling methods within molecular dynamics and Monte Carlo simulations. Emphasis is set on the possible application of advanced sampling methods for the simulation of ionic liquids at electrified interfaces.

4.1 Introduction

Limitations in length and time scales within molecular dynamics (MD) and Monte Carlo (MC) simulations are a driving factor for the development of advanced sampling methods. Systems with *rugged* or *frustrated* energy landscapes, meaning numerous deep local minima, are usually difficult to sample as hopping between minima in the energy landscape is similar to simulating rare events. The most famous and most widely studied system that belongs to this category are protein-folding problems where information of a wide conformational space is required [181, 182, 183, 184]; the number can be increased by the following systems [185, 186]:

1. Biomolecular systems (proteins and lipids),
2. Macromolecular and polymeric systems,
3. Self-organizing or self-structuring systems (e.g. micelles and bilayers),
4. Systems with strong electrostatic interactions,
5. Fluids of strongly orientation-dependent interactions (e.g. dipoles and hydrogen bonds),
6. Supercooled liquids and amorphous systems at very low temperatures.

Among these systems, molten salts and room temperature ionic liquid, could be affiliated to number 4, 5 and 6, showing the importance to understand advanced sampling techniques as well as their limitations. Is it possible to use and benefit from advanced sampling techniques while modelling ionic liquids at electrified interfaces?

The following chapter will be split into a description of the theoretical basis and a collection of advanced sampling methods. The collection should not be understood as complete in all terms, but provide the interested reader with the ideas that stand behind the methods and a number of publications that allow continued reading on the topic. After the description of the sampling methods we will discuss the problems that encounter by sampling of the phase space using

"brute-force" independent replicas. Two ideas to improve sampling and understand the free energy landscape based on replica exchange molecular dynamics and metadynamics will be seized on. We would like to smooth the way for further research on that topic by providing pre-calculations and giving hints on possible implementations in advanced simulation tools.

4.2 Theoretical basis

Ergodicity A basic requirement for computer simulations of many-body systems is the so-called ergodicity of the system [186]. A system is called ergodic, if the probability to reach any point in phase space converges to a unique limiting value as $T \to \infty$ such that the time average of a quantity is equal to its ensemble average

$$\lim_{T\to\infty} f(q_0, p_0) = \langle f \rangle.$$

This assumption is also called *ergodic hypothesis*. Resulting from the ergodic hypothesis any sufficiently long trajectory of a multi-body system will (i) allow the evaluation of statistically averaged properties and (ii) time-averaged properties become independent of the initial conditions.

The ergodicity is the foundation of statistical mechanics developed by Boltzmann and Maxwell.

Energy concepts Following Boltzmanns law, not all possible configurations of a system have the same probability to occur. Which configuration is preferred depends on external limits, as there are fixed temperature or fixed pressure. All possible configurations in these limits are called ensemble. The ensemble is commonly named after physical properties, that are kept constant; e.g. a set of configurations with a fixed number of particles N, pressure P and temperature T is called a NPT ensemble.

For every ensemble, an energy can be defined, for which the probability of a configuration in inversely dependent to the named energy. Or in other words, the system will tend to the configuration with the smallest energy. For the NPT ensemble, the energy is called the Gibbs free energy, for the NVT ensemble, the Helmholtz free energy.

Upon stating the usage of free energy landscapes we still haven't defined what exactly the free energy is. The free energy of a system is the energy that can be used to perform work.

Based on the thermodynamic laws, the heat Q is given as change of entropy

S and temperature T written as

$$Q = \mathrm{d}(TS) = \mathrm{d}(U + pV - \mu N),$$

where U means the internal energy, p the pressure, V the volume, μ the chemical potential and N the particle number. The free energies for several ensembles are defined in Table 4.1.

Table 4.1: Definitions of the free energies

Name	Formula	Ensemble	Absolute & Difference
Entropy	S	(N, V, E)	$S = E/T + PV/T - \mu N/T$
			$\mathrm{d}S = \mathrm{d}E/T + P\mathrm{d}V/T - \mu\mathrm{d}N/T$
Internal Energy	E, U	(N, V, S)	$E = TS - PV + \mu N$
			$\mathrm{d}E = T\mathrm{d}S - P\mathrm{d}V + \mu\mathrm{d}N$
Helmholtz	A, F	(N, V, T)	$A = E - TS = -PV + \mu N$
			$\mathrm{d}A = -S\mathrm{d}T - P\mathrm{d}V + \mu\mathrm{d}N$
Grand	Φ	(μ, V, T)	$\Phi = A - \mu N = -PV$
			$\mathrm{d}\Phi = -S\mathrm{d}T - P\mathrm{d}V - N\mathrm{d}\mu$
Gibbs	G	(N, P, T)	$G = A + PV = \mu N$
			$\mathrm{d}G = -S\mathrm{d}T + V\mathrm{d}P + \mu\mathrm{d}N$
Enthalpy	H	(N, P, S)	$H = E + PV = TS + \mu N$
			$\mathrm{d}H = T\mathrm{d}S + V\mathrm{d}P + \mu\mathrm{d}N$

4.3 Collection of advanced sampling methods

Advanced sampling methods are based on the construction of artificial dynamics in the systems that accelerate convergence towards equilibrium. Using advanced sampling methods, we will barely be able to make conclusions about kinetic properties of the systems, but we might be able to increase the confidence in the calculation of thermodynamic properties as we can hope to sample the whole free energy landscape.

4.3.1 Multi-canonical algorithm and simulated tempering

A canonical Monte Carlo simulation in which the temperature changes randomly is called simulated tempering [187, 188]. The standard Monte Carlo approach on energy fluctuation moves including

- single-particle displacements and

- orientational displacements

is extended by temperature fluctuation moves, which means

- periodically increasing or decreasing of the temperature by fixed amounts so that the temperature of the system is set to one temperature value from the interval

$$[T_{min}, T_{min} + \Delta T, T_{min} + 2\Delta T, \ldots, T_{max}] .$$

The acceptance criterion for a random temperature perturbation $T_2 = T_1 + \Delta T$ is given by

$$P_{12}^{accepted} = \min \left[1, e^{-(\beta_2 - \beta_1)U + \eta(T_2) - \eta(T_1)}\right]$$

with $\eta(T)$ being a weighting function in temperature that accounts for the introduced temperature dependence of the micro-state

$$\wp(\boldsymbol{r}^N, T) \propto e^{-\beta U(\boldsymbol{r}^N) + \eta(T)}.$$

Simulated tempering mimics a free random walk in temperature space, thereby belonging to a method called multi-canonical algorithm. The multi-canonical algorithm performs a free 1-dimensional random walk in energy space based on non-Boltzmann probability weight factors. As random walks allow the simulation to pass any energy barrier, a wider phase space can be sampled than by conventional methods. During a multi-canonical simulation, the global minimum-energy state as well as thermodynamic quantities as a function of temperature for a wide temperature range can be obtained by monitoring the energy for every time step.

The main drawbacks of simulated tempering are the expensive computation of free energies at every temperature in order to sample all temperatures properly and a possible extremely long simulation time as the system needs to traverse the full temperature range several times.

Note: The term *simulated annealing* should not be confused with *simulated tempering*. The first one refers to a gradually increase and decrease of the temperature in a given simulation setup to overcome energy barriers of the initial configuration once. Simulated tempering refers to a continuous temperature perturbation over the whole length of the trajectory that is statistically solved.

4.3.2 Replica exchange MD (REMD): Temperature and Hamiltonian REMD

The replica exchange method was originally devised by Swendsen [189]. The very first report of an advanced sampling method (replica exchange molecular dynamics, REMD, parallel tempering) is dated back to 1999 by Sugita and Okamoto [181]. For a review article, see Earl and Deem [182].

The general mechanics of the replica exchange method can be summarized as follows [185]:

1. J simulations ("replicas" or walkers) of the same system are performed simultaneously at different temperatures T_j or different energy states (e.g. bound state and unbound state)

2. Each simulation is evolved independently, either through MD or MC methods, at the corresponding temperature

3. At set intervals, replica swap moves are performed between adjacent temperature replicas. In a swap move, the instantaneous configurations are exchanged between the two temperatures.

There is in general no fundamental requirement on the exchange scheme; anything (temperature T, Hamiltonian λ, charge q etc.) can be exchanged.

One main advantage of the method is that not only properties at a given temperature can be calculated, but an average at any arbitrary temperature between the minimum and maximum temperature can be computed. The histograms of each potential energy visited in each temperature can be collected during a REMD simulation. By using reweighting equations to compute the free energies and configurational weights at each temperature, the average of any property can be calculated [190].

For a discussion of convergence and sampling efficiency in replica exchange simulations of peptide folding in explicit solvent, see [191].

Note: Buchete and Hummer [192] developed a method for recovering some kinetic information even within replica exchange simulations. Rates of protein folding and unfolding can be extracted by analysis of the brief and continuous trajectory segments between replica exchanges. Buchete and Hummer constructed a master equation by estimating short-time propagators in conformation space.

Temperature replica exchange or parallel tempering

During temperature replica exchange molecular dynamics simulations several replicas of a system are simulated at different temperatures in parallel allowing for exchange between replicas at frequent intervals. By analysis of the free energy histograms, most often done by temperature weighted histogram analysis (TWHAM) [193], the sampling from all temperatures can be combined [182].

The method was recently applied to investigate freezing of mixtures confined in silica nano-pores by grand canonical Monte Carlo simulations for Lennard-Jones Ar/Kr mixtures confined in a silica cylindrical nano-pore [194].

More details on the method are explained in the sections below on the usage of REMD in Gromacs.

Hamiltonian REMD (HREMD) and other variants

Hamiltonian-REMD methods can be specifically designed to enhance the sampling of specific conformations (e.g. for proteins and nucleic acids) by applying various levels of biasing potentials for each replica run. The potential energy function itself is modified thereby reducing its roughness. One example is the systematically scaling of partial charges from zero to full value as one moves from replica to replica.

Two-dimensional replica exchange with differing in both temperature and chemical potential or pressure have been performed already. An interesting new approach is given in Heating and flooding: A unified approach for rapid generation of free energy surfaces by Ming Chen, Michel A. Cuendet, and Mark E. Tuckerman [195].

On the convergence of replica exchange molecular dynamics

Usually the convergence of REMD compared to long-time MD results is considered to be excellent as several studies have shown extensively [196]. However, such speed-ups do not occur for all systems [197].

4.3.3 Metadynamics

Metadynamics can been metaphorically described as “filling the free energy wells with computational sand”. The algorithm assumes that the system can be described by a few collective variables. The free energy landscape is flattened by inserting a time dependent potential, that depends on the history of the system's

trajectory [198, 199]. When all energy minima are sampled ("filled"), the free energy profile can be reconstructed from the final potential.

Bussi et al [200] described the a method to combine temperature REMD with metadynamics, which is already used successfully [201, 202, 203]. Smiatek and Heuer [204] presented a combined approach of histogram reweighting and metadynamics.

The solid-liquid interface free energy obtained through metadynamics simulations is discussed by Angioletti-Uberti and co-workers [205].

Orlandini et al [206] used restrained MD and temperature REMD to study the stability of amorphous vs. crystalline Si nano-particles. Further applications of the metdadynamics approach have been recently performed by Giacomello et al [207] and Savoy et al [208]. Giacomello et al [207] investigated the wetting of a surface decorated with one nanogroove by a bulk Lennard-Jones liquid at various temperatures and densities.

Among the methods that are connected with metadynamics, one finds accelerated MD [209], conformational flooding [195] and hyperdynamics [210, 211, 212].

Despite the increased interest in the metadynamics approach in the community, the application to systems not similar to solvated proteins is still difficult. The reason is explained by Bussi et al [200]: the error in the free-energy estimation is related to the choice of the collective variable and the diffusion coefficient in the collective variables dynamics. If the dynamics are to slow, the free energy estimate will contain a huge error. The same situation occurs if an important collective variable is missing in the description.

4.3.4 Jarzynski-equation based steered MD

Jarzynski-equation based steered MD and Steered molecular dynamics (SMD) can be used as synonyms for the whole number of force probe simulations [213, 214, 215]. These simulations apply forces to a particle or protein in order to manipulate its structure by pulling it along desired degrees of freedom. Pull codes work either with the velocity held constant or with the applied force hold constant.

4.3.5 Umbrella sampling

With Umbrella sampling Torrie and Valleau [216] made a successful attempt to overcome the shortcomings of the usage of Boltzmann-weighted sampling distributions, which are extremely inefficient in many cases. The usage of arbitrary

sampling distributions has been tested successfully on the Lennard-Jones system and is used widely in the scientific community these days [217, 218]. A popular method of computing the potential of mean force is through the weighted histogram analysis method (WHAM), which analyses a series of umbrella sampling simulations.

4.4 Problem description: Sampling of the phase space using independent replicas

A method for exploring a specific temperature range and assuring better sampling is more and more frequently used in the computational scientific community. The method is called temperature replica exchange MD (T-REMD) and will be described in detail below. We want to understand whether it is possible to use T-REMD in our case and to which extent we can profit from the advantages of advanced sampling compared to the brute force modelling of independent replicas. Basically, we want to consider the following questions:

1. How are the total energies of each system distributed? Do energy distributions overlap for the given set of temperatures?

2. How can we construct a temperature interval that allows to do temperature replica exchange MD (T-REMD)?

3. Upon analysing the energy distributions, do we find any evidence of several stable structures?

4. If we find evidence of several stable structures - do they switch between each other within the given observation time? What are the frequencies?

4.4.1 Pre-calculations: Results from the classical simulations

Time evolution of the total energy and resulting energy distributions

To answer the given questions, we plotted the time evolution of the total energy for the systems discussed in this thesis. Details are given in Fig. 4.1, 4.2, 4.3 and 4.4.

While reaching intermediate and high surface charges, the energy distributions of the replicas do not overlap any more. This observation indicates several stable states for the system at the given conditions. Figure 4.1 shows a simulation setup ($T = 450\,\mathrm{K}$ and $\sigma = 30.00\,\mu\mathrm{C/cm^2}$), where two well distinguishable states are visible. For the different replicas a snapshot of the cathodic interfacial layer is presented. Interestingly, one snapshot shows 157 counter-ions in the interfacial layer whereas the snapshots for all other replicas contain only 150 counter-ions in the interfacial layer. Thereby a correlation between structuring in the interfacial layer and total energy could be discussed.

In Fig. 4.2 and 4.3 non-overlapping energy distributions are associated with number density profiles. Again, different energy distributions belong to different interfacial structures. Moreover a slow structural change becomes apparent upon discussing the time evolution of the number density profiles.

Figure 4.4 shows the time evolution of the total energy for one simulation where a swap between different states has been explored.

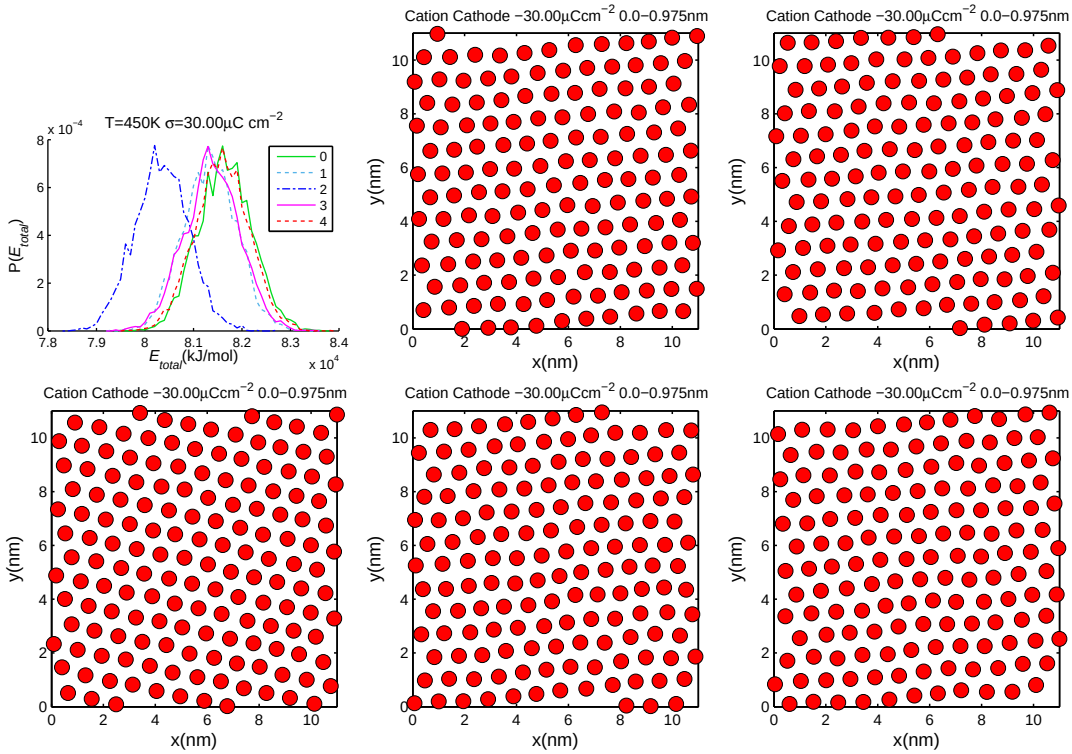

Figure 4.1: Energy distribution in conjunction with interfacial structures for the simulations at 450 K and $\sigma = 30.00\,\mu\mathrm{C/cm^2}$. The energy distributions for the replicas show two different configurations with a mean total energy of 8.0 and 8.16×10^4 kJ/mol. The outlying energy distribution appeared in replica 2. From left to right and top to bottom five snapshots for the different replicas are shown. The (BOTTOM-LEFT) figure belongs to replica 2. Interestingly, the snapshot shows 157 counter-ions in the interfacial layer whereas the snapshots for all other replicas contain only 150 counter-ions in the interfacial layer. Thereby a correlation between structuring in the interfacial layer and total energy could be discussed.

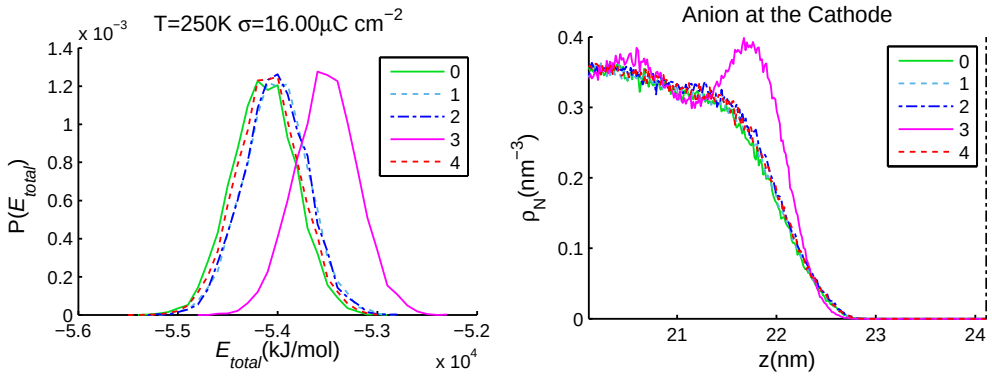

Figure 4.2: (LEFT) Energy distribution in conjunction with (RIGHT) the number density profile of anions at the cathode (vertical dot-dashed line) for the simulations at 250 K and $\sigma = 16.00\,\mu\mathrm{C/cm^2}$. The energy distributions for the replicas show a deviation between replica 3 (solid magenta line) and all other replicas. Similar the number density profiles shows overlap of all replicas except replica 3.

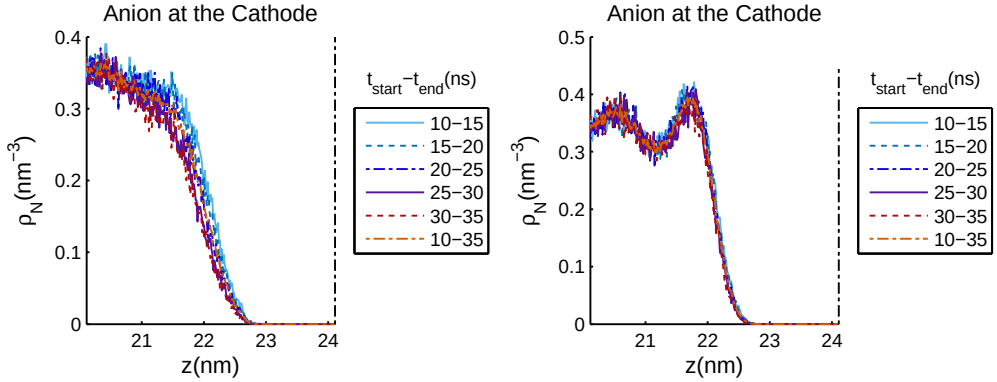

Figure 4.3: Number density profile evolution with time for five different time intervals of 5 ns length each for anions at the cathode (vertical dot-dashed line). The simulation has been carried out at $T = 250\,\mathrm{K}$ and $\sigma = 16.00\,\mu\mathrm{C/cm^2}$. (LEFT) Replica 0 and (RIGHT) replica 3, compare with Fig. 4.2. Whereas the number density profile of anions at the cathode in replica 3 shows no time dependence, a time evolution is clearly visible in replica 0.

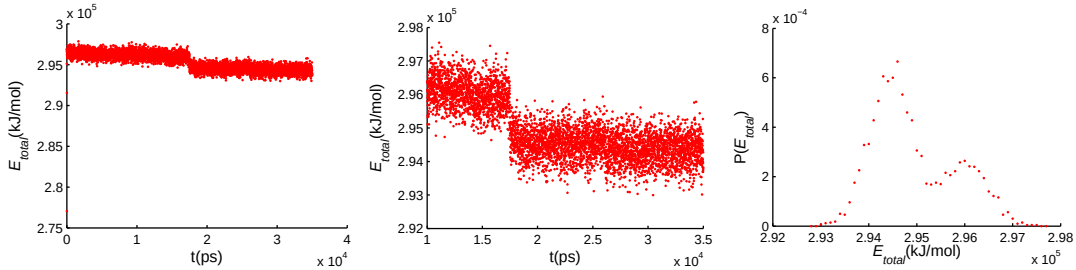

Figure 4.4: (LEFT) Time evolution of the total energy, (MIDDLE) Close-up of the time evolution of the total energy and (RIGHT) resulting energy distribution for $T = 350\,\mathrm{K}$ and $\sigma = 46.00\,\mu\mathrm{C/cm^2}$. During the simulation time the system clearly moves to another state. This is 1 of 2 simulations from 1020 where we found such a transition during a simulation.

Energy distributions for different temperatures

Figure 4.5 shows the energy distributions for three different temperatures at a specific surface charge. The energy distributions do not overlap. As a rough estimate we make a relation between the width of the distributions and the distance between the energy distributions for each temperature. Thereby, we assume that approximately ten temperatures between 450 K and 500 K should be sufficient to obtain exchange rates between 0.3 and 0.5 when performing T-REMD. It is usually suggested that the temperatures should follow an exponential distribution to assure that exchange rates between all neighbouring temperatures are nearly equal. However the larger temperatures 400 K, 450 K and 500 K do show nearly equidistant distances between the distributions. Therefore we suggest a 5 K interval for the temperature choice.

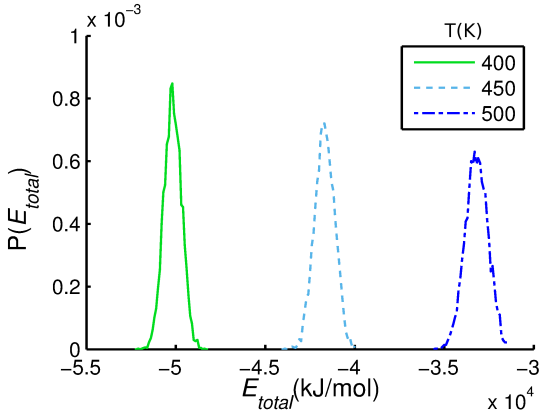

Figure 4.5: Distribution of the total energy for three different temperatures (400 K, 450 K and 500 K) at the surface charge density of $\sigma = 8.00\,\mu\mathrm{C/cm^2}$.

4.4.2 Conclusions

The results shown in this section indicate indeed a rugged energy landscape with several minima for the system under study. The energy barriers for conformational changes seem rather high as changes have been observed only two times among all simulations that have been performed.

For the application of advanced sampling methods, we see basically two promising options:

1. To reduce the equilibration time, we suggest the usage of temperature replica exchange MD (T-REMD).

   As it is possible to use the Gromacs implementation for REMD simulations, we will perform a couple of tests on this method. Details for the system preparation and application are given above during the discussion of former simulations and will be extended below. Apart from simulating different temperatures, we also want to consider the variation of the surface charge density between different replicas. This approach is so far not documented anywhere else.

2. To analyse the free energy landscape of simulations at higher surface charges, where especially interfacial configurations seem to play an important role, we suggest the usage of metadynamics. With given tools and advanced thoughts on the collective variables that should be used, a deeper understanding of the interfacial structuring could be obtained.

   As came apparent by the literature review, the metadynamics approach requires a detailed understanding of the underlying variables. We will provide below a list of suggestions for collective variables and possible implementations using Gromacs simulation software and the free energy tool PLUMED. A rigorous calculation of these variables in a classical simulation is necessary, to obtain a "first guess" for the metadynamics simulations.

4.5 Replica exchange molecular dynamics in Gromacs

As the Gromacs molecular dynamics package [219] includes a variety of analysis tools and interfaces to other software, we concentrate on the application of advanced sampling methods in Gromacs.

4.5.1 Implementation

The Gromacs implementation of REMD is based on the article of Hukushima and Nemoto [220]. A basic introduction to the usage of the REMD algorithm is given in [221].

4.5.2 System preparation: Finding a suitable setup

The following collections of hints for the system preparation of a replica exchange MD simulation are taken from various sources:

- Daniel Weinstock: Replica Exchange Molecular Dynamics. Simulations in Computational Biophysics in Spring 2010, February 11, 2010. (Presentation online available, see [222].)
- Jianhan Chen: Replica Exchange Sampling. MMTSB/CTBP Workshop in August 4-9, 2009, Kansas State University. (Presentation online available, see [223].)
- Gromacs web-page [221].
- Zhang [196]: Convergence of replica exchange molecular dynamics.

Temperature range and distribution The temperature distribution for systems with constant heat capacity can be made exponentially. The lowest temperature is often the temperature of interest, the highest temperature is less obvious to define, but a critical parameter.

Number of replicas = number of intermediate temperatures The number of replicas depends on a variety of system properties like the system size and the temperature range. The average exchange probability between each replica is again determined by the system, number of replicas, range of temperature space and the distribution of temperatures.

An optimal exchange acceptance ratio should be around 0.2-0.3, but 0.5 is also not uncommon. Also the exchange attempt frequency is important, as it should be fast but no too fast. An exchange every 1-2 ps proved reasonable for solvated proteins, but reported exchange frequencies range from 0.02 to 5 ps. More generally, an exchange should take place after the systems temperature is stabilized again. Large systems require a longer relaxation time after replica exchange. If temperatures are close to one another, more frequent exchanges are possible.

Note: We found several hints that implicit solvent is not only particularly suitable for replica exchange methods, but also explicit solvent simulations are barely reasonable when using REMD. However, there was no proof or detail given within the above collected sources.

Length of simulation The longer the better. Convergence can be tricky to judge, as a plateau in some quantity does not necessarily mean a convergence. It is better to judge on several physical quantities. Even for REMD it is reasonable to produce multiple independent simulations for testing convergence.

How to quantify "sampling" A number of ideas can help to quantify the sampling quality: autocorrelation analysis, statistical tests, conformational space analysis, thermodynamics properties, transition events and effective sample size through structural distribution analysis [224].

4.5.3 Difficulties / Drawbacks / Questions

1. The system, number of replicas, range of temperature space and the distribution of temperatures determine the average exchange probability between each replica. Thus the method needs to be tested extremely thoroughly to assure proper exchange rates.

2. There is no discussion about the frequency of trajectory storage. Does it matter? What happens if we want to analyse structural parameters at on specific temperature but store only high or low energy configurations as the storing frequency correlates with the exchange attempt frequency?

3. There is a rapid increase of the replica number with increasing system size to cover a desired temperature range.

4. How does the collective variable needs to be chosen in regions of non-constant heat capacity? What happens along the phase diagram?

4.5.4 A general route for the usage of REMD with ILs at electrified interfaces

To collect ideas for the possible application of replica exchange to our specific setup:

Temperature replica exchange MD (T-REMD) The application of temperature replica exchange requires a basic iterative process, that will probably be the most time consuming (both, computational and human time):

1.a Define a minimum and a maximum temperature

1.b Define the number of replicas (intermediate temperatures)

1.c Equilibrate the simulation box according to the given temperatures

2.a Run replica exchange (at least 100 ps for solvated proteins, unknown for ionic liquids)

2.b Check the exchange rate and decide if it is (i) within the desired range (e.g. 0.2-0.5) and (ii) equal for all intermediate temperatures

→ If one of the requirements from 2.b fails, start over at 1.b. In the worst case if several iterations fail, start again at 1.a

If finally the desired temperature range and the exchange range fit together, the next evaluation process can start:

3.a Choose the exchange frequency which correlates with the number of time steps necessary for relaxation after an exchange

3.b Choose the output frequency

3.c Choose the simulation length

4.a Run replica exchange with the defined properties

4.b Analyse (which?) properties to assure proper equilibration and sampling

→ If one the requirements from 4.b fail, start over at 3.a

According to our knowledge, the analysis of structural parameters at a specified temperature should be straightforward. However the analysis of further physical properties might need the usage of advanced statistical methods like weighted histogram analysis.

Surface charge replica exchange MD (Sigma-REMD) The variation or perturbation of a physical quantity of the system apart from the temperature is termed Hamiltonian REMD.

On the one hand one could try to use Gromacs build-in replica exchange technique and collect a number of equilibrated simulations with different surface charges - similar to the simulation of different temperatures. However a test of this approach showed even for systems with non-overlapping energy distribution, the exchange probability between the replicas is always 100 %. A solution might be provided by Mu et al [225], who implemented a recalculation of the exchange probability for Hamiltonian-REMD.

On the other hand PLUMED could be used as described in the following section (with probably more overall control). However extensive testing is required for PLUMED and any self-made extension.

4.6 Metadynamics applied to ionic liquids at electrified interfaces: Concepts

As it is described above, the metadynamics approach is based on the assumption, that a change in free energy can be properly described by the perturbation of a small number of collective variables - e.g. a bond, an angle and a dihedral angle for a protein. A metadynamics simulation is used to calculate the free energy landscape by inserting a time dependent potential, that knows the history of the collective variables. When all energy minima are sampled, the free energy profile can be reconstructed from the final potential.

Upon using the metadynamics approach, a fundamental concern needs to be kept in mind [200]: the free energy estimation and specifically the error of the estimation is related to the dynamics of the collective variable (CV). If the "diffusion coefficient" of the CV is too small, the free energy will have a large error. More important is the choice of the CVs. If an important CV with a high free-energy barrier but slow degree of freedom is not taken into account, the whole free energy estimation might not be reliable at all.

The description of ionic liquids at electrified interfaces in terms of collective variables has not been done so far. Ideas can be taken from simulations of solid-liquid interfaces of simple model liquids (neutral, non-polar) [205] and phase transitions of mixtures confined in porous materials [194].

Characterizing the phase transition at the interface by two new collective variables, namely the number of ions in the interfacial layer and the nearest-

neighbour-bond-orientational-order parameter, seems reasonable for our specific system. The implementation of both ideas is non-trivial, but can be imagined by modifying the PLUMED packages. Details on the collective variables and the PLUMED package are given below.

A last note should be made on the combination of temperature-replica exchange MD and metadynamics, which is called parallel tempering metadynamics.

Basically the same difficulties as for the standard metadynamics apply here (e.g. implementation of new collective variables). The statistics should be better due to the parallel tempering approach, however this approach also includes the preparation and equilibration of a large number of temperature replicas.

Collective variables As collective variables for the characterization of the interfacial conformations of ionic liquids, we suggest

- the ion number in the interfacial layer;
- the ion distance;
- the bond angular order parameter [226].

Usage of PLUMED Again we want to refer to the free energy tool PLUMED allowing metadynamics simulations with self made collective variables.

PLUMED is a framework that allows several advanced sampling techniques in conjunction with well-known software packages like Gromacs. The tool is based on the definition of a collective variable (CV), that is varied within certain boundaries. Replicas of the simulation setup with the varied CV are done either by direct accessing of the simulation package or by an advanced patching of the simulation software. Those collective variable are for example temperature, bond length or any angle. Usually the reaction path should be known explicitly.

The modification of PLUMED with the CV being the surface charge might be done as suggested in [227]. However extensive testing is required for PLUMED and any self-made extension.

4.7 Conclusion and outlook

Based on the introductory question "Is it possible to use and benefit from advanced sampling techniques while modelling ionic liquids at electrified interfaces?" we draw the following conclusions:

A We do have a frustrated energy landscape with different ion conformations. Therefore the usage of advanced sampling techniques is expected to be beneficial.

B The ion conformations depend on the system temperature T and surface charge density σ. Both variables could be accessed with the REMD approach: either temperature replica exchange or Hamiltonian replica exchange.

   1 For the temperature variation a number of tools have been developed already, however finding a reasonable temperature range, that allows good exchange acceptance ratios and exchange rates is not yet explained for any liquid/solid-interfacial system, nor for ionic liquids in general.

   2 Charge-replica exchange will need considerable programming and testing/benchmarking effort, as it is not yet implemented in any general software. However the PLUMED interface for Gromacs seems a reasonable candidate for implementation.

C The characterization of the structure and structural changes over the whole free energy surface could be done using metadynamics. However, the important collective variable to describe the conformational changes needs still to be developed.

   1 We suggest the ion number in the interfacial layer, the ion distance and the bond angular order parameter [226] as collective variables.

   2 Again the PLUMED interface for Gromacs seems a reasonable candidate for performing the metadynamics simulations as it supports the implementation of new collective variables.

In total, advanced sampling methods might provide new insights in the field of ionic liquids at interfaces. However, what we also understand from our discussion, is the need of a careful and comprehensive study of the systems with classical methods.

Chapter 5

Simulation methodology and justification of the geometry

The following chapter contains a description of the force field parameter and the system geometry, which are in general identical with the simulations performed by Fedorov and Kornyshev [7]. However, we extended the simulation time drastically and also increased the number of surface charges and temperatures under study. High electrostatic force within the ionic liquid and at the electrode surface required the development of a robust and reliable equilibration scheme, which is described below in detail. The large number of simulations made careful calculation of the computational costs necessary and the usage of several supercomputers, which are acknowledged in a separate section. The last sections of the chapter aim to show the reader why we have chosen the specific system geometry and where the simulation setup needs further improvement in case of a subsequent study.

5.1 Force field and system configuration

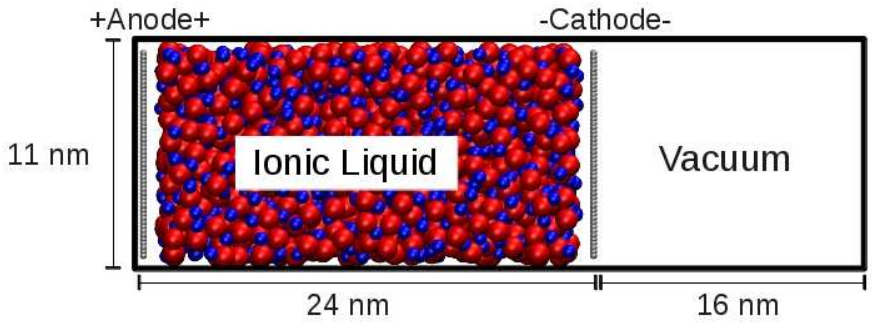

Figure 5.1: Simulation setup shown by a representative snapshot of an initial configuration. The electrodes consist of 2500 Lennard-Jones spheres with a diameter of 0.22 nm that are arranged on a square lattice with 11 nm × 11 nm size in x and y dimension. Anode and cathode have a fixed distance of 24 nm. We added a vacuum slab of length $\Delta z_{\text{vacuum}} = 16\,\text{nm}$ by prolonging the box size in z-direction to 40 nm, thereby following the Berkowitz rule for correct electrostatics in simulations with slab geometry (see text for further information). A model ionic liquid with asymmetric sized ions is confined between the electrodes. The ions are modelled as Lennard-Jones spheres with a short range repulsive potential, every ion is carrying a positive or negative elementary charge.

The nano scale capacitor as shown in Fig. 5.1 is modelled as follows: The electrodes consist of densely packed Lennard-Jones spheres on a square lattice. A model ionic liquid (IL) is confined between the oppositely charged electrodes. All force field parameters are summarized in Table 5.1.

The electrodes consist of 2500 Lennard-Jones spheres with a diameter of 0.22 nm that are arranged on a square lattice with 11 nm × 11 nm size in x and y dimension. Anode and cathode have a fixed distance of 24 nm, therefore the electrode atoms were position restrained with a force constant of $k = 100000\,\text{kJ}/(\text{mol}\cdot\text{nm}^2)$. The electrodes have been charged oppositely with 34 surface charges σ ranging from 0 to 50 μC/cm^2. A surface charge of 1 μC/cm^2 results in a "physical" charge per atom of $3.021 \cdot 10^{-3}$ elementary charges, the effective charge used in the simulation setup is obtained by scaling the "physical" charge by $1/\sqrt{2}$, see Section 3.4.2 for an explanation. The spacing between the surface charges have been chosen to be consistent with the regions of particular interest.

Table 5.1: Force field of the model IL and the electrodes. Ions and counter ions are modelled as Lennard-Jones spheres with a short range repulsive potential $U_{LJ}^{ij} = 4\varepsilon_{LJ}\left(\frac{\sigma_i+\sigma_j}{r}\right)^{12} = 2k_BT\left(\frac{\sigma_i+\sigma_j}{r}\right)^{12}$ with the temperature $T = 450\,\mathrm{K}$ and k_B being the Boltzmann constant. The arithmetic combination rule is used for both σ_{LJ} and ε_{LJ}. To account for polarization effects we scale Coulomb interactions by an effective dielectric constant $\varepsilon^* = 2$, thus multiplying all "physical" charges by $1/\sqrt{2}$. (*) Charge varied according to the surface charge σ under study.

Specie	σ_{LJ} (nm)	ε_{LJ} (kJ/mol)	m (g/mol)	q (e)
Cation	1.00	1.8698	100.8	+0.707
Anion	0.50	1.8698	100.8	-0.707
Wall	0.22	1.8698	120.11	$q(\sigma)$ (*)
Interaction	**σ_{LJ} (nm)**	**ε_{LJ} (kJ/mol)**		
Cation-Anion	0.75	1.8698		
Cation-Wall	0.60	1.8698		
Anion-Wall	0.35	1.8698		

As the important extrema of the differential capacitance naturally occur at small potential drops, which means small surface charges, this region has to be sampled sufficiently. In this study we decided to use the following 34 surface charges given in $\mu C/cm^2$:

0.00	0.25	0.50	0.75	1.00	1.25	1.50
2.00	2.50	3.00	3.50	4.00	4.50	5.00
6.00	7.00	8.00	9.00	10.00	11.00	12.00
14.00	16.00	18.00	20.00	22.00	24.00	26.00
30.00	34.00	38.00	42.00	46.00	50.00	

The ion pair number has been fixed in all simulations to 1050 with a resulting density of approx. 0.36 ionpairs/nm^3. Six different temperatures between 250 K and 500 K have been studied.

5.2 Iterative system preparation

Initial system preparation was performed with the Packmol software [228]. Five independent molecular configurations (replicas) per system setup have been generated.

A square lattice of carbon atoms was chosen to model the electrodes. The distance between the two electrodes is $z_d = 24\,\text{nm}$, resulting in an accessible volume of $2900\,\text{nm}^3$ for the IL. We added a vacuum slab of length Δz_{vacuum} by prolonging the box size in z-direction to 40 nm, thereby following the Berkowitz rule

$$\Delta z_{\text{vacuum}} \geq \max(x, y) \quad \text{and} \quad z_d + \Delta z_{\text{vacuum}} \geq 3 \cdot \max(x, y)$$

to obtain correct electrostatics simulations in slab geometry [229]. The resulting configurations consist of 4600 atoms per simulation box.

For each system several energy minimization steps and short structure equilibration steps with small time step have been performed. The procedure has been proven to be robust in terms of avoiding crashing simulations due to high forces between any kind of particles.

The system preparation consists in detail of the following steps (independent runs for all temperatures, surface charges and replicas):

1. Run Packmol to generate the initial configuration with a given number of ion pairs, the electrodes and a vacuum slab ($z_{\text{vacuum}} = 16\,\text{nm}$ according to the Berkowitz rule).

2. Run Gromacs energy minimization
   (integrator steep, 10000 steps, electrodes neutral)

3. Run Gromacs NVT with a small time step
   (integrator md, $dt = 0.002\,\text{ps}$, $100000\,\text{steps} = 200\,\text{ps}$, electrodes neutral)

4. Run Gromacs energy minimization
   (integrator steep, 10000 steps, electrodes charged)

5. Run Gromacs NVT with a small time step
   (integrator md, $dt = 0.002\,\text{ps}$, $100000\,\text{steps} = 200\,\text{ps}$, electrodes charged)

6. Run Gromacs NVT with a large time step
   (Production run including 10 ns equilibration and 25 ns analysis,
   integrator md, $dt = 0.01\,\text{ps}$, $3500000\,\text{steps} = 35\,\text{ns}$, electrodes charged)

5.3 Simulation parameter

We performed molecular dynamics (MD) simulations with Gromacs 4.5.5 [219].

Periodic boundary conditions were applied in all directions. The cutoff of the Lennard-Jones interactions was taken to be 2.6 nm with shifted potential method to account for the coarse grain model of ions. The long-range Coulomb interactions were handled by the Particle-Mesh Ewald method [230] with a cutoff of 2.9 nm and a grid spacing of 0.112 nm and corrected for slab geometry [229]. The neighbour list for non-bonded interactions was updated every 10th integration step. We used the leap-frog algorithm for integrating Newton's equations of motion with 0.01 ps time step. All simulations were performed at fixed temperature. Velocity rescaling was used with a temperature coupling constant of 2.0 ps [231]. We stored the atomic coordinates of the ions each 5 ps for further analysis.

A note on the temperature coupling To assure constant temperature in the simulation box, we need to choose a thermostat including a coupling constant and define the parts of the system, that should be coupled to the thermostat. The choice of the thermostat is based on clear arguments concerning the robustness, reliability and physical correctness. However, the coupling of the thermostat with the simulation box ("coupling scheme") seems a matter of personal experience. The Gromacs software allows any sub-part of the simulation box to be coupled independently from other parts to the thermostat. As we show in the Appendix A, different coupling schemes do not provide identical results, however the deviations

are of minor importance for our discussion. As there are no strict arguments for or against a specific coupling scheme, we coupled the whole simulation box to the thermostat to assure transferability of the simulations to other software for molecular dynamics simulations.

5.4 A comment on computational costs

The total number of setups summed up to $34 \times 5 \times 6 = 1020$, with a total simulation time for the final production runs of $25.5\,\mu$s with $dt = 0.01\,$ps. The total amount of simulation time for the equilibration summed up to 210 ns with $dt = 0.002\,$ps and $10.2\,\mu$s with $dt = 0.01\,$ps.

The simulations have been carried out on different high performance computing (HPC) facilities, namely

- The British supercomputer HECToR
- The von Neumann-Institut für Computing, FZ Jülich, Juropa
- The Academic and Research Computer Hosting Industry and Enterprise in the West of Scotland, ARCHIE-WeSt
- The computing centre of the Max Planck Institute (Rechenzentrum Garching (RZG) and local computer cluster of the Max Planck Institute for Mathematics in the Science, Leipzig)

Varying with the computational power of each super computing centre, one single simulation took between 24 hours on 32 cores (Juropa) and 90 hours on 24 cores (ARCHIE-WeSt). For the main calculations discussed in this work consumed more than 600'000 core-hours of computational time.

5.5 Influence of the system geometry

Due to the nature of ionic liquids we expect ion correlations up to a few nanometre in all directions. We have to ask ourself the question, how large a simulation box should be constructed, to avoid non-physical interactions of image particles constructed by periodic boundary conditions with their neighbours. Within this section we want to discuss (i) the box dimensions in plane parallel to the electrode surface and (ii) the distance between the electrodes. The first parameter has been already discussed by several authors, whereas for the second parameter we

calculate the ion correlations in a volume in the middle between the electrodes and compare the resulting radial distribution functions with those obtained from bulk simulations.

5.5.1 Ion correlations in plane parallel to the electrode surface are expected to decay within ten times the ion diameter

González-Melchor et al [232] and Merlet et al [120, 121] investigated the liquid-vapour surface tension of model ionic liquids. During their analysis both groups found that the surface tension is drastically depended on the chosen box dimensions in plane parallel to the surface. As suggested by González-Melchor et al and later proven by Merlet et al, the box length in x and y direction should exceed ten times the largest ion diameter under study, to assure a correct simulation of the interfacial properties.

For our model system we used ions with a diameter $d = 1\,\mathrm{nm}$ for cations and $d = 0.5\,\mathrm{nm}$ for anions and prepared a simulation box with

$$x = y = 11\,\mathrm{nm} \quad > \quad 10 \times \max(d_{\mathrm{cation}}, d_{\mathrm{anion}}) = 10\,\mathrm{nm}.$$

Thereby we followed the suggestions made González-Melchor et al [232].

5.5.2 Electrodes are separated by liquid ionic liquid

To understand, whether the bulk properties of the IL in the middle of the slab are affected by the electrodes and whether the distance between the electrodes is sufficiently large, we analysed the ion density and the ion-ion radial distribution functions (RDFs) in the middle of the slab. The middle of the slab is thereby defined as the volume slice with 8 nm distance from both electrodes - the resulting box volume equals $x \times y \times z = 11 \times 11 \times 8\,\mathrm{nm}^3$.

The results of the middle-of-the-slab analysis for the number density is provided in Fig. 5.2(TOP). The main observations are: (i) the density in the middle of the slab decreases with surface charging - the slab is emptying; (ii) the general trend is disturbed at two surface charges: $16.0\,\mu\mathrm{C/cm^2}$ and $38.0\,\mu\mathrm{C/cm^2}$. This effect will be explained later. We note that the density might even increase for both surface charges, which is more pronounced at lower temperatures.

In Fig. 5.2(BOTTOM) the ion correlations in the middle of the slab are presented and compared with the ion correlations in a bulk NVT simulation

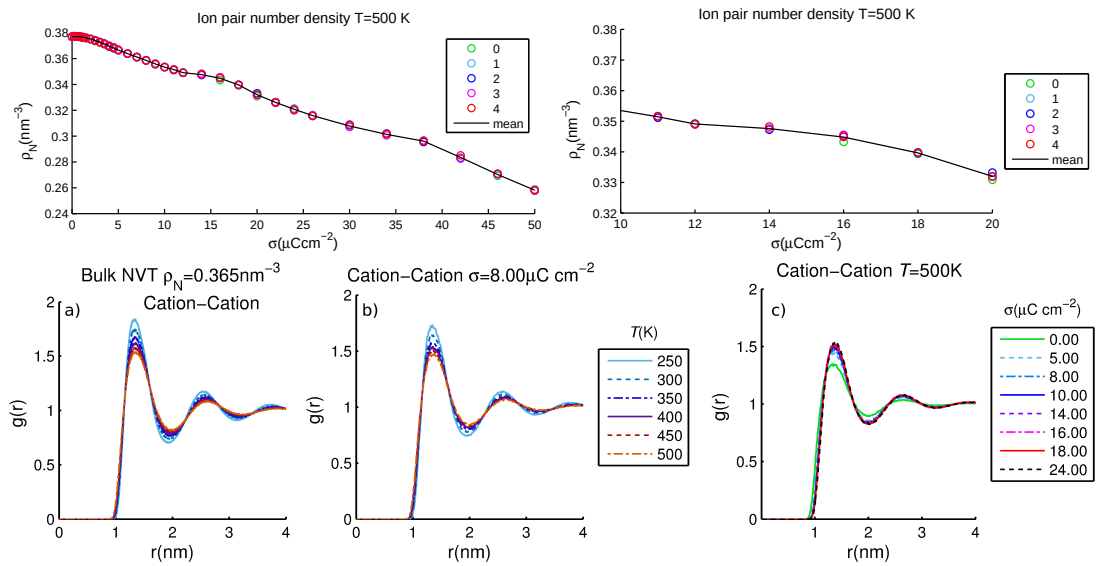

Figure 5.2: **(TOP)** Middle-of-the-slab number density plotted over surface charge density. Number density profiles of all replicas have been calculated independently and the mean number density within a slice of 8 nm length in z-dimension has been evaluated. Results for each replica and surface charge density are shown as open circles. The black line is the resulting mean of all replicas over surface charge. The deviation of the centre of the circles from the black line can be understood as an error estimate. (LEFT) Full surface charge interval ranging from 0.00 to 50.0 μC/cm^2; (RIGHT) Close-up of the left figures with a reduced surface charge interval ranging from 10.0 μC/cm^2 to 20.0 μC/cm^2. **(BOTTOM)** Cation-Cation radial distribution functions (RDFs). (LEFT) Bulk simulations in the NVT-ensemble with ion pair density $\rho_N = 0.365\,\mathrm{nm}^{-3}$ constant for all temperatures. The ion pair density equals the middle-of-the-slab ion pair density in the slab simulations with a surface charge density of $\sigma = 8.0\,\mu\mathrm{C/cm}^2$. (MIDDLE) Middle-of-the-slab radial distribution functions combined for all temperatures under study for $\sigma = 8.0\,\mu\mathrm{C/cm}^2$. (RIGHT) Middle-of-the-slab radial distribution functions combined for several surface charges at $T = 500\,\mathrm{K}$.

with ion pair density $\rho_N = 0.365\,\mathrm{nm}^{-3}$. The bulk simulations with the given ion pair density can be associated with the middle-of-the-slab ion pair density in the slab simulations with a surface charge density of $\sigma = 8.0\,\mu\mathrm{C/cm}^2$.

Most important, the bulk and the slab RDFs show little deviations between each other. Peak and valley position as well as height/depth are equal. Also the temperature dependence appears as expected. We can securely consider the middle-of-the-slab region in our simulations to be in a liquid state similar to a situation in a bulk simulation without electrodes. In Fig. 5.2(BOTTOM-RIGHT) the middle-of-the-slab radial distribution functions combined for several surface charges at $T = 500\,\mathrm{K}$ are shown. Surprisingly, for surface charges larger than

$\sigma = 8.0\,\mu\mathrm{C/cm^2}$ they show very little dependence on the varied surface charge despite the measurable density decrease shown in the (TOP) figure.

To conclude: The number density in the middle of the slab decreases with increasing surface charge as ions are sucked to the electrode surfaces. The ion-ion-RDFs show the same structuring and temperature dependent as expected in a similar bulk simulation, tested for one specific density/surface charge combination. However, within the region of the phase transition the RDFs show little dependence on the surface charge. The bulk phase in the middle-of-the-slab assures that we can analyse structural parameter connected to one electrode independently from the other electrode.

5.6 Conclusion: Are we confident in our setup? What are the drawbacks?

Upon judging and the simulation setup we draw the following conclusions:

+ We assured that the box dimensions in all directions do not lead to non-physical interactions.

+ The choice of the temperature coupling slightly influences the results for very low surface charge densities and the neutral interface, but does not affect the qualitative results nor physical interpretation.

+ The hardware, software and algorithms used for performing simulations and analysis represent a state-of-the-art collection in computational science.

To our best knowledge, we assured the correctness of the chosen combination of simulation method and model setup.

Chapter 6

The differential capacitance: Temperature vs. Voltage

The shape of the differential capacitance over voltage under variation of temperature is the topic of this chapter. A literature review on the conception of the temperature dependence of the differential capacitance precedes a methodological description of the calculation scheme. The resulting differential and integral capacitance are described, followed by a critical discussion of the influence of extrapolation and smoothing algorithms used for the calculation of the differential capacitance.

6.1 Introduction: A missing conception of the temperature dependence of the differential capacitance

The temperature effect on the properties of the electrical double layer (EDL) in ionic liquids is a longstanding question. Since the 60-70s there have been intensive debates on the nature of the temperature dependence of the double layer capacitance in high temperature ionic liquids (e.g. molten alkali halides) within experimental [24] and theoretical & computational communities [25, 26, 27]. However, due to a number of experimental problems related with electrochemical measurements in high temperature molten salts, there was no general agreement in the literature about the true character of this dependence.

The recent wave of interest to electrochemical applications of room temperature ionic liquids (RTILs) provoked a series of new experimental [33, 28, 29, 34, 32, 30, 31] and computational [35, 36, 37] studies on the temperature effects on EDL properties in ionic liquids. Nevertheless, a review of the published results on the temperature dependence of the EDL differential capacitance, C_d, in RTILs shows that this question remains to be controversial.

Indeed, in several experimental studies (Lockett et al [28], 1-alkyl-3-methylimidazolium chlorides at glassy carbon (GC); Silva et al [33], 1-butyl-3-methylimidazolium (BMIM) hexafluorophosphate at Hg, Pt, and GC; Costa et al [34], [BMIM][Tf2N] at Hg) it was shown that the capacitance values increase with increasing temperature. From another side, recently Drüschler et al [31] reported new experimental results on the influence of temperature on the differential capacitance for the extremely pure ionic liquid 1-butyl-1-methylpyrrolidinium tris(pentafluoroethyl)-trifluorophosphate (Py1,4FAP) at an Au(111) electrode. In this work they performed careful analysis of broadband capacitance spectra of the electrode/RTIL interface obtained by combining electrochemical impedance spectroscopy with in situ STM and in situ AFM techniques. Opposite to the references [28, 33, 34] they have shown that the capacitance for fast capacitive process decreases with increasing temperature from 30 to 90 °C. Moreover, these findings correlate with molecular simulations data by Vatamanu et al [36],

who investigated the differential capacitance for N-methyl-N-propylpyrrolidinium bis(trifluoromethane)-sulfonyl imide ([pyr13][TFSI]) near a graphite electrode and also observed negative dependence of C_d from temperature.

We note, that the comparability of carbon materials with metal electrodes has been recently shown by Skinner et al. [233][1].

As the literature analysis shows, see Tab. 6.1 for an overview, currently there is no universal and widely accepted conception of the general dependence of the differential EDL capacitance on temperature and electrode potential. We also note that most of experimental studies on the temperature dependence of the capacitance considered a relatively narrow voltage range, within $\approx$ +/-1 V or even narrower. To get more insights into the problem and investigate capacitance behaviour in RTILs in a wider voltage range we decided to perform simulation and theoretical analysis of the temperature dependence of the capacitance for a model coarse-grained ionic liquid with asymmetric sizes of cations and anions, taking cations twice as large as anions. That generally resembles properties of 'real' ionic liquids. We performed molecular dynamics simulations for this model ionic liquid confined between two "electrodes" and calculated the potential and ion distributions, as well as the differential capacitance of the EDL at each electrode. These were obtained as a function of the electrode potential for different temperatures in the range 250-500 K.

In this work we will make an attempt to answer the following question: What is the temperature dependence of the differential capacitance C_d for our coarse grain model?

Specifically, we used a coarse-grained model of RTIL from a previous study in our group on the EDL behaviour of RTIL at electrified interface [7]. Although we employed the same simulations setup as in Ref. [7] (software, geometry of the electrode, treatment of electrostatic interactions etc.) we increased the overall simulation time for every capacitance profile by an order of magnitude which allowed us to improve the accuracy of the capacitance calculations. That resulted in much smoother capacitance curves as compared to Ref. [7], allowing us to resolve the secondary peaks at the right and left wings of the capacitance curves.

[1] It has been reported earlier that carbon materials (glassy carbon, porous carbon, graphite or graphene) might show metal but also semi metal properties. The T-effect on the EDL capacitance at the semi metal and semiconductor electrode is determined by the T-dependence of the Debye length in the electrode through primarily the variation of the number of charge carriers. However Skinner et al. [233] reported that under reasonable assumptions the electric field decays to zero within the first graphite layer. This finding allows very well to treat graphene as a metal if pore walls are thick enough and ion density is sufficiently high.

Table 6.1: Recent publications on the EDL and ILs including a discussion of the temperature dependence of the differential capacitance over voltage.

First Author & Date	Exp. / Sim.	Ionic Liquid	Electrode	U_{drop} (V)	T (K)	T-dependence [2]
Graves 1970 [24]	Exp.	LiCl/KCl	Pb	-0.3 ... 0.45	725 ... 1075	increasing
Boda 1999 [27]	Sim.	RPM dissolved	Hard wall	reduced units	reduced units	increasing and decreasing with intersection point
Lockett 2008 [28]	Exp.	[EMIm, BMIm, HMIm]Cl	Glassy carbon (GC)	-1.5 ... 1.5	353 ... 413	increasing
Silva 2008 [33]	Exp.	$BMImPF_6$	Hg, Pt, GC	-1.25 ... 1.75	293 ... 348	increasing
Lockett 2010 [29]	Exp.	EMImCl, HMImCl, BMIm[Cl, I, Br, BF_4, PF_6, TFSI]	Au, Hg, Pt, GC	-2.5 ... 2.25	296 ... 373	increasing
Costa 2010 [34]	Exp.	[EMIm, BMIm, HMIm, BMPyr]TFSI	Hg	-2.0 ... 0.1	293 ... 333	increasing
Loth 2010 [35]	Sim.	RPM dissolved	Metal surface	reduced units	reduced units	decreasing at low voltages
Vatamanu 2010 [36]	Sim.	Pyr_{13}TFSI	Graphite	-3.5 ... 3.5	363 ... 453	decreasing
Gnahm 2011 [30]	Exp.	$BMImPF_6$	Au(100)	-1.5 ... 0.8	293 ... 393	independent
Alam 2011 [32]	Exp.	[EMIm, BMIm, OMIm]BF_4	Au(111)	-1.0 ... 1.0	296 ... 348	decreasing for $EMImBF_4$, otherwise increasing
Dou 2011 [37]	Sim.	[MMIm, BMIm, OMIm, C_{12}MIm]PF_6	Graphite	PZC	400 ... 800	? Short range ordering persists
Drüschler 2012 [31]	Exp.	$Py_{1,4}$FAP	Au(111)	-1.14 ... 0.56	273 ... 363	Complicated temperature dependence, for negative potentials decreasing

6.2 Methods: Calculation scheme for the differential capacitance

The analysis of the obtained trajectories of 125 ns total length was performed using Gromacs tools and self-written Matlab functions.

The differential capacitance was obtained while performing the following steps for all trajectories: (i) Calculation of the number density profiles $n(z)$ for cations and anions respectively using a uniform grid with a spacing of 0.015 nm (the average over all replicas is taken into account here); (ii) Calculation of the charge density profile by calculating the sum over the charge scaled number density profiles $\rho_{\text{ion}}(z) = \sum q \cdot n_{\text{Cation}}(z) + \sum -q \cdot n_{\text{Anion}}(z)$ with $q = 1e$; (iii) Integration of the charge density profiles multiplied by z to obtain the potential drop for anode and cathode respectively $U_{\text{drop}} = \int z \cdot \rho_{\text{ion}}(z)\,\mathrm{d}z$; (iv) The resulting surface charge σ vs. potential drop U_{drop} curves are first extended by the expected behaviour at high surface charges (therefore we calculated the least square fit of $a\sqrt{U}+b$ to the asymptotic region); afterwards we smoothed the extended data set using piecewise polynomial curve fitting by weighted least squares; (v) Finally the smoothed curves are differentiated to obtain the differential capacitance $C_d = \mathrm{d}\sigma/\mathrm{d}U_{\text{drop}}$.

A sufficient fitting procedure for the surface charge vs. potential drop dependency is crucial for all upcoming analysis. The non-smoothed data is still too noisy to allow simple differentiating. In the last section of this chapter the fitting procedure is described to obtain a smooth and differentiable surface charge versus potential drop dependency.

6.3 Results: Differential and integral capacitance

6.3.1 Differential capacitance

Figure 6.1 shows the simulation results for the differential capacitance for six different temperatures between 250 K and 500 K. As one can see from the figure, at all temperatures the capacitance curves have an asymmetric shape with a distinctive maximum around +0.5 V (250 K) ... +0.7 V (500 K). The height of the peak *decreases* with increasing the temperature from 13.0 μF/cm^2 for 250 K to 10.3 μF/cm^2 for 500 K that is accompanied by (i) *widening* of the peak; (ii) slight steady *shift* of the peak towards positive potentials. However, the temperature dependence of the capacitance *qualitatively* changes at the voltages higher than +0.8 V where it shows *positive* capacitance dependence from temperature. At

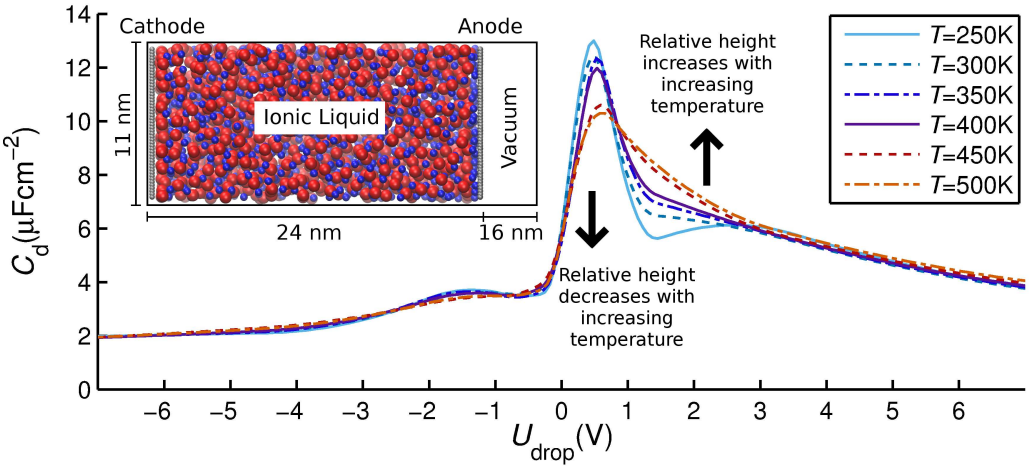

Figure 6.1: Differential capacitance C_d as a function of the potential drop U_{drop} for six different temperatures T ranging from 250 K to 500 K. The differential capacitance curves are the result of molecular dynamics simulations of a model ionic liquid confined between two oppositely charged planes consisting of spheres that are aligned in a square lattice. This model has asymmetry in ion sizes, with cations twice as large as anions. The error bars for the random error of the capacitance calculations (not shown) steadily increase with the voltage from $\pm 0.1\,\mu\text{F/cm}^2$ to $\pm 1.0\,\mu\text{F/cm}^2$ (see Appendix for details). The inset on the left displays a sketch representation of the simulation box showing the geometry of the simulation cell in xy-plane. Cations are shown as red spheres, anions are shown as blue spheres. The size of the particles is rescaled to make them more visible. The small grey spheres represent the electrode atoms. The sketch is illustrative and does not reproduce the proper scale.

high voltage the capacitance curve wings corresponding to different temperatures merge (the difference between the curve is less than the simulation error). We note that this behaviour qualitatively correlates very well with the experimental observations in Ref. [31] for potential-dependent differential capacitance of the fast capacitive process in $[\text{Py}_{1,4}][\text{FAP}]$ at different temperatures.

For low temperatures, the capacitance curves show another maximum around +2.5 V. When performing a careful error analysis of the differential capacitance, it is found that the random error introduced by the quality of the simulation data is reasonable low. The error bars of the capacitance calculations steadily increase with the voltage from $\pm 0.1\,\mu\text{F/cm}^2$ to $\pm 1.0\,\mu\text{F/cm}^2$. However, by assuming a specific asymptotic behaviour to represent the boundary conditions for the fit (see Appendix for further details on the calculation routine), we introduce a systematic error. When varying the assumption, the shape of the differential capacitance changes in the high positive voltage interval. Moreover the minimum

in the 250 K capacitance curve at +1.5 V vanishes as well as the maximum at +2.5 V. However, the general temperature dependency including the intersection interval around +0.8 V are not affected by this systematic error as the error is strongly voltage dependent. The high-voltage anodic 'wings' can be considered as equal as the curves all lie within their error bars. For further details see the Section 6.5 and the Appendix.

All capacitance curves in the cathodic region (see the Appendix Fig. B.8 for a close-up) have additional smaller maxima around -1.4 V with a negative temperature dependence. Below -2.5 V the temperature dependence seems reversed. With regards to the error estimates explained above, we might well interpret the temperature-effect in the whole cathodic part as being neglectable as the curves overlap within their error bars.

6.3.2 Integral capacitance

The integral capacitance C_i reflects the charge stored in an electrode with the unit area upon potential change from potential of zero charge (PZC) to a given potential drop. The integral capacitance is defined as follows [36]

$$C_i = \frac{\sigma}{U_{\text{drop}} - U_{\text{PZC}}},$$

with σ being the surface charge density or surface charge per area, U_{drop} being the potential drop at the electrode and U_{PZC} being the potential of zero charge. The difficulty with calculating the integral capacitance is the precise knowledge of the potential of zero charge. If the potential drop is not well known (e.g. due to random noise), the calculated integral capacitance shows discontinuities and large negative and positive values near the PZC.

Compared with the differential capacitance C_d

$$C_d = \frac{\mathrm{d}\sigma}{\mathrm{d}U_{\text{drop}}},$$

it can be found that the differential capacitance allows an interpretation of the charge storing ability in the double layer as a function of applied voltage and thus is more useful in evaluation of the energy stored by the capacitor than the integral capacitance [36]. However, for completing the physical picture of our model capacitor, a short discussion of the integral capacitance might be useful.

The temperature dependence of the integral capacitance shown in Fig. 6.2 assets an isopiestic point at 1.5-1.6 V. The change in capacitance is much higher at

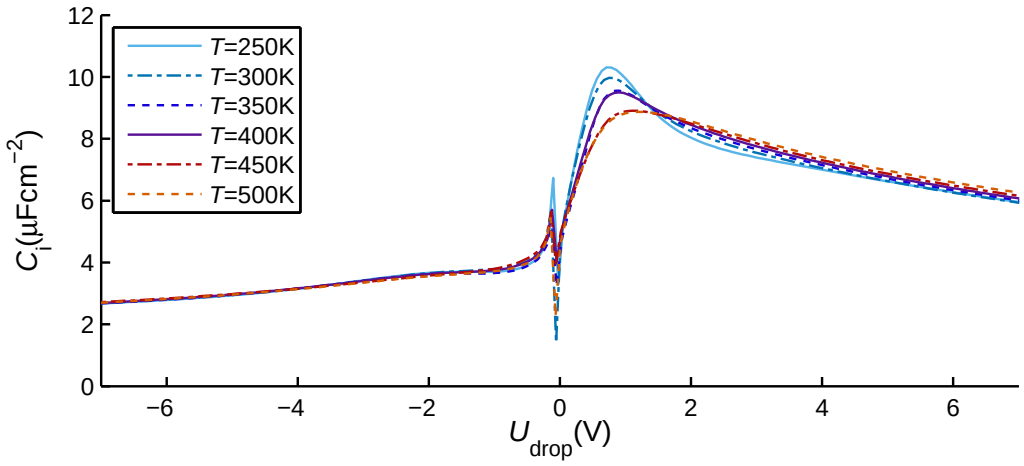

Figure 6.2: Integral capacitance C_i as a function of the potential drop U_{drop} for six different temperatures T ranging from 250 K to 500 K. For a discussion see text.

low temperatures than at high temperatures. At a certain voltage the capacitance does not (much) depend on the temperature.

6.4 Conclusion: The temperature effect on the capacitance depends on the voltage

We are able to draw the following conclusions:

1 Overall, the temperature effect on the EDL capacitance depends on the voltage [3] - at small voltages it decreases with the increase of temperature; then at intermediate voltages the dependence becomes opposite - the EDL capacitance increases with the increase of temperature.

2 At large voltages (while approaching the lattice saturation regime [59], also termed crowding [8]) the EDL capacitance practically does not depend on the temperature.

3 The asymmetry of the ion sizes affects the strength of the temperature dependence, but not its general direction. With large cations and small anions we observe much higher changes of the capacitance with temperature at the anode than at the cathode.

[3] We note, that in the experimental work of Lockett et al [28] and in the simulation work of Vatamanu et al [36] it is also shown that the $C_d(T)$ behaviour in RTILs depends on the voltage.

6.5 Extended methods: Asymptotic extrapolation and influence of the smoothing method for the surface charge vs. potential drop dependency

The error of the differential capacitance needs to be estimated as the combined error of all preparation steps that finally result in the capacitance curve. The steps that can be considered of major importance in this error analysis are the quality of the potential drop data and the assumption made for asymptotic extrapolation. The first error source - the physical noise in the data - will be called random error. The asymptotic extrapolation can be referred to as systematic error as it is introduced by a methodological consideration. In this analysis we assume that the error of the numerical differentiation is small compared with the error of the fit algorithms. Therefore the numerical error is not considered further.

6.5.1 Smoothed potential drop curves and the resulting capacitance curves including error estimations

Within Fig. 6.3 and 6.4 we present the smoothed potential drop curves and the resulting capacitance curves including the confidence interval (CI). The fitting assumption for the asymptotic extrapolation is varied and also the influence of a missing asymptotic extrapolation is shown. The figures will be discussed in detail in the following subsections.

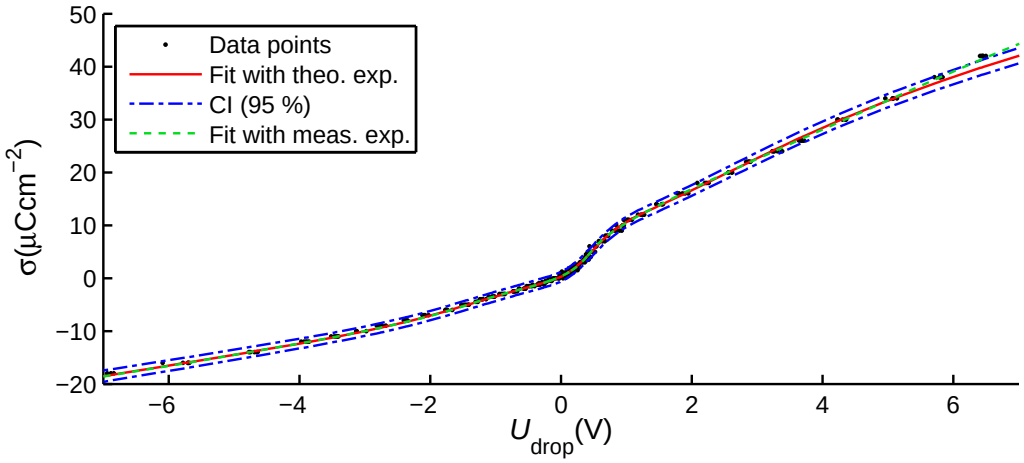

(a) Smoothed surface charge vs. potential drop

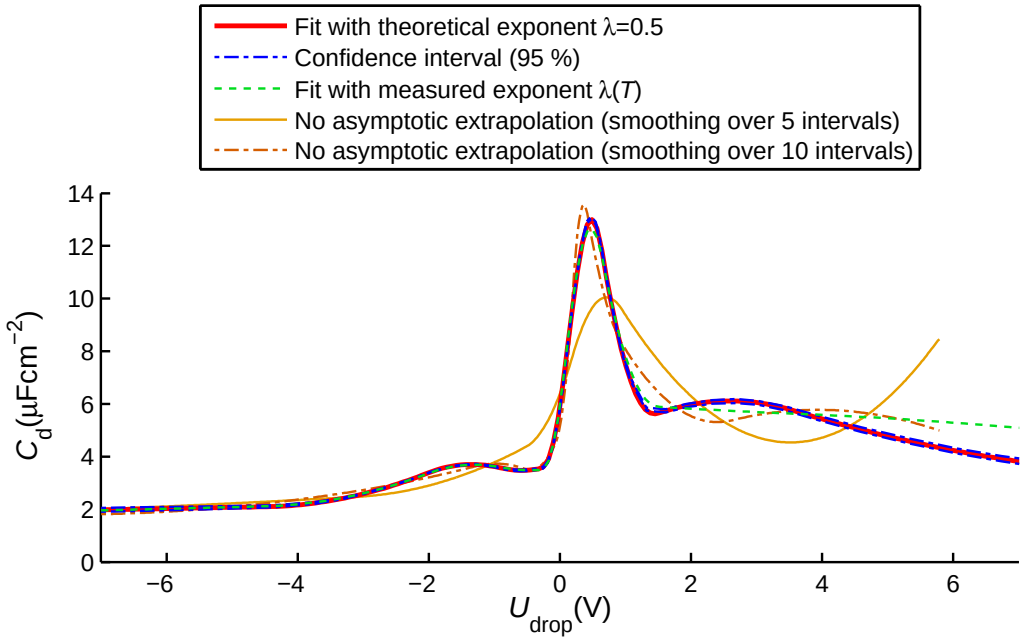

(b) Differential capacitance

Figure 6.3: Error estimation of the smoothed potential drop and the resulting capacitance curves at 250 K. (a) Smoothed surface charge vs. potential drop. (b) Differential capacitance. The blue dashed curve represents the random error introduced by the quality of the potential drop estimation from MD simulations. The green dashed curve represents a fitting assumption for the asymptotic extrapolation of the surface charge vs. potential drop data. The assumption was made that the asymptotes follow a $|U_{\mathrm{drop}}|^{0.5}$ dependency. The blue graph is calculated by assuming an asymptotic behaviour of $|U_{\mathrm{drop}}|^{\lambda(T)}$, with $\lambda(250\,\mathrm{K}) = 0.6689$ based on the fitted cathodic asymptotic behaviour. The orange and the vermilion curves are obtained by differentiating the smoothed raw data without asymptotic extrapolation. Smoothing is performed by piecewise polynomial fitting with either five or ten intervals.

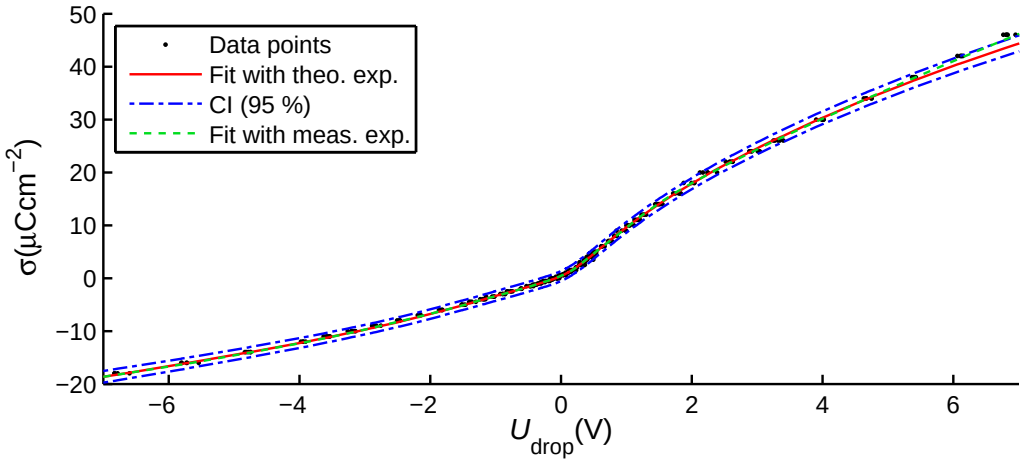

(a) Smoothed surface charge vs. potential drop

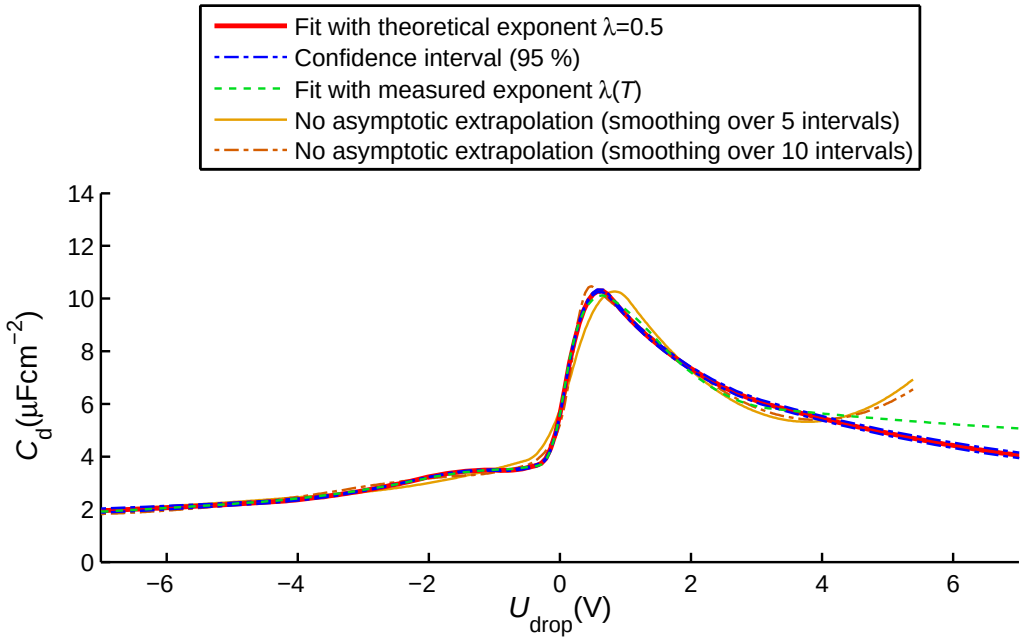

(b) Differential capacitance

Figure 6.4: Error estimation of the smoothed potential drop and the resulting capacitance curves at 500 K. (a) Smoothed surface charge vs. potential drop. (b) Differential capacitance. The blue dashed curve represents the random error introduced by the quality of the potential drop estimation from MD simulations. The green dashed curve represents a fitting assumption for the asymptotic extrapolation of the surface charge vs. potential drop data. The assumption was made that the asymptotes follow a $|U_{\mathrm{drop}}|^{0.5}$ dependency. The blue graph is calculated by assuming an asymptotic behaviour of $|U_{\mathrm{drop}}|^{\lambda(T)}$, with $\lambda(500\,\mathrm{K}) = 0.8109$ based on the fitted cathodic asymptotic behaviour. The orange and the vermilion curves are obtained by differentiating the smoothed raw data without asymptotic extrapolation. Smoothing is performed by piecewise polynomial fitting with either five or ten intervals.

6.5.2 Error analysis of the surface charge vs. potential drop dependency

For a sufficient analysis of the random error of the fit we will consider the confidence interval $P_{\bar{Y}}$ and the prediction interval P_Y with a confidence level of 95 %. Both measured quantities $X = U_{\text{drop}}$ and $Y = \sigma$ may have an error, therefore we have to include both errors in our calculations. The prediction and the confidence interval are calculated as follows:

$$P_{\bar{Y}} = t \cdot s \cdot \sqrt{\frac{1}{N} + \frac{(x - \bar{x})^2}{S_{xx}}},$$

$$P_Y = t \cdot s \cdot \sqrt{1 + \frac{1}{N} + \frac{(x - \bar{x})^2}{S_{xx}}}.$$

The residual (error) mean square s can be calculated from

$$s = \sqrt{\frac{1}{N-2}\left(S_{yy} - \frac{S_{xy}^2}{S_{xx}}\right)},$$

where S_{xy} corresponds to the sample covariance

$$S_{xy} = \sum_{i=1}^{N} x_i y_i - \frac{1}{N}\left(\sum_{i=1}^{N} x_i\right)\left(\sum_{i=1}^{N} y_i\right)$$

and S_{xx} being the sample corrected sum of squares (calculation of S_{yy} is analogue)

$$S_{xx} = \sum_{i=1}^{N} x_i^2 - \frac{1}{N}\left(\sum_{i=1}^{N} x_i\right)^2 = \sum_{i=1}^{N} (x_i - \bar{x})^2 .$$

The critical value or t-score is calculated as follows

$$t = \frac{\bar{x} - \hat{\mu}}{s_N/\sqrt{N}}.$$

We have an estimate for the sample mean $\bar{x}$ (our fit) and we know the standard deviation s_N as well as the sample size N. But what is unknown to us is the hypothetical mean $\hat{\mu}$. Due to the fact that we do not know $\hat{\mu}$, we have to make an assumption here: We assume that the distribution of our data points is symmetric and bell-shaped, which is also referred to as t-distribution. The confidence level is transformed into the cumulative or critical probability p^* and together with

the number of degrees of freedom $df = N - 1$ the t-score can be calculated or taken from tables.

In our case we assume that 34 surface charges and five replicas for each surface charge result in 340 independent measurements. Every surface charge counts twice as the potential drop can be calculated at the positively and at the negatively charged electrode. The confidence level is set to 95 %.

$$\alpha = 1 - \frac{\text{confidence level}}{100\,\%} = 1 - \frac{95\,\%}{100\,\%} = 0.05,$$

$$p^* = 1 - \frac{\alpha}{2} = 0.975,$$

$$df = N - 1 = 339.$$

With the specific input given above ($\alpha = 0.05$, $p^* = 0.975$, $df = 339$), the t-score equals $t = 1.967$. The final confidence interval and prediction interval are shown in figure B.9 for all temperatures. Table B.3 allows a numeric comparison of the error of all fits.

6.5.3 Influence of the fitting procedure for the surface charge vs. potential drop dependency

The method of choice for fitting the raw data is piecewise polynomial curve fitting by weighted least squares. In detail the data set is split into a specific amount of single data sets and every data set is fitted to a single polynomial curve. The advantage of this method compared to fitting the whole data set to a fractional polynomial curve is the possibility to account for structuring within the data set that is limited to a small interval. No unrealistic over smoothing of the curve is introduced.

When using any spline fitting method it is important to construct the right boundary conditions as splines (e.g. polynomials) with infinite size are fitted to a finite interval. The result of not considering periodic boundaries for the fitting is shown in Fig. 6.3 and 6.4 as the solid orange ("No asymptotic extrapolation (smoothing over 5 intervals)") and the dot-dashed vermilion line ("No asymptotic extrapolation (smoothing over 10 intervals)"). The capacitance curves are artificially exaggerated at high positive voltages and the peak height and position might not be reproduced properly. The comment about the number of intervals refers to the fitting procedure, in which the data points are divided into a number of intervals, and every interval is fitted separately by a polynomial curve. A higher number of intervals reduces the artificial curvature for low temperatures,

but does not have an influence in the high temperature case.

In this work we applied suitable boundary conditions by extending the data set by its asymptotics. A detailed description is given in Fig. 6.5. The asymptotics of $\sigma(U_{\mathrm{drop}})$ have been fitted to the theoretically described $\sqrt{|U_{\mathrm{drop}}|}$ dependency [59]. We will discuss the influence of the exponent below. Data points at very high potentials have been overwritten by the asymptotic fit to smooth the boundary. On the positive and on the negative x-axis an interval of the same size as the original data set was added and filled with 20 data points of the asymptotic fit. The initial data set of 68 data points increased to 102.

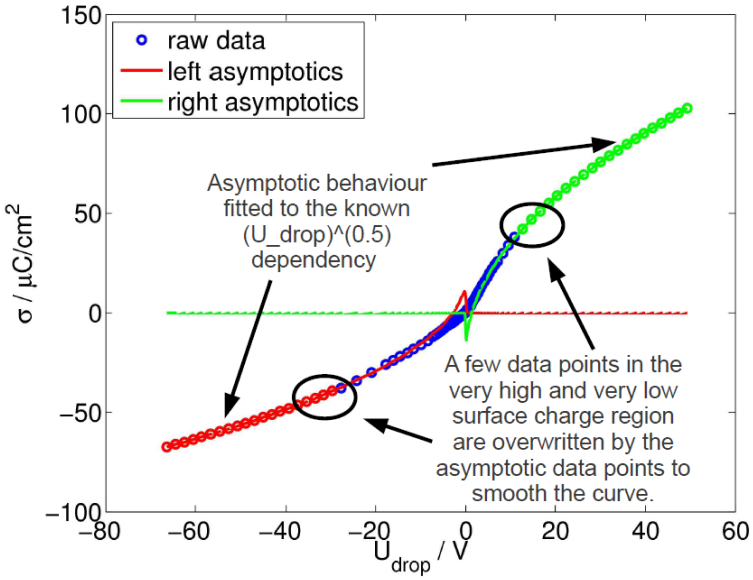

Figure 6.5: To account for suitable boundary conditions the asymptotics of $\sigma(U_{\mathrm{drop}})$ have been fitted to the known $\sqrt{|U_{\mathrm{drop}}|}$ dependency. Data points at very high potentials have been overwritten by the asymptotic fit to smooth the boundary. On the positive and on the negative x-axis an interval of the same size as the original data set was added and filled with 20 data points of the asymptotic fit. The initial data set of 68 data points increased to 102.

With the asymptotic data set piecewise polynomial curve fitting by weighted least squares has been performed. The potential of zero charge was excluded from the analysis, therefore the data set of $102-2=100$ data points was divided into 17 pieces. For every piece the robust spline fitting was performed. For the physical analysis only the original data set being a direct result from MD simulations was taken into account.

6.5.4 Results: Error analysis of the differential capacitance curve

Random error: Noise of the data We assume that our data set $f(x)$ is approximated by a fit function $g(x)$ with a *random error* $e(x)$, which we consider being the 95 % confidence interval of the surface charge σ vs. potential drop U_{drop} curves. To obtain the random error of the first derivative of $f(x)$, the error of the fit function is differentiated $e'(x) = \frac{\mathrm{d}e}{\mathrm{d}x} = e(f'(x))$.

Differentiating the confidence interval results in an error of 0.4 % for the maximum equal to $C = 0.05\,\mu\mathrm{C/cm^2}$. At the boundaries ($U_{\mathrm{drop}} = \pm 7.0\,\mathrm{V}$) we estimate an error of 4.7 % equal to $C = 0.09\,\mu\mathrm{C/cm^2}$ at the negative axis (cathodic part) and an error of 2.0 % equal to $C = 0.1\,\mu\mathrm{C/cm^2}$ at the positive axis (anodic part). The absolute errors are equal for all temperatures. The errors are visualized in Fig. 6.3 and 6.4 as blue dashed curves.

Systematic error: Asymptotic extrapolation The estimation of the *systematic error* introduced by the fitting assumption for the asymptotic wings is more complicated. We already showed the importance of boundary conditions for the smoothing fit. However we have to discuss the influence of the applied asymptotic extrapolation.

The systematic error is introduced by the asymptotic extrapolation of the surface charge vs. potential drop data. The assumption was made that the asymptotes follow a $|U_{\mathrm{drop}}|^{0.5}$ dependency as it has been predicted by Kornyshev [59] by using fundamental principles as the charge conservation law. When fitting the fractional exponent only for the right - cathodic - wing of the surface charge vs. potential drop curve, the exponent shows a reliable dependency between $|U_{\mathrm{drop}}|^{0.66}$ for 250 K and $|U_{\mathrm{drop}}|^{0.81}$ for 500 K. Similar values have been reported earlier by Vatamanu et al [36]. For the left - anodic - wing the exponent cannot be determined as lattice saturation is not reached at 7.5 V.

When changing the assumption from a fractional power law with exponent 0.5 to 0.8, the shape of the differential capacitance changes in the high positive voltage interval, see the green dashed curve in Fig. 6.3 and 6.4. Moreover the minimum in the 250 K capacitance curve at 1.5 V vanishes. However, the shape of the main peak does not change for all temperatures under study. Thereby we conclude, that the discussed temperature dependency is not affected by this choice of the asymptotic exponent

Chapter 7

Heating the electric double-layer: Melting of ion structures

In the last chapter we discussed the temperature dependence of the differential capacitance. Molecular dynamics simulations allow a detailed atomistic view, in our case especially on the electric double-layer structure. Thus a natural question arises: Can we extract the origin of the temperature dependence of the differential capacitance?

7.1 Introduction: The differential capacitor as a series of layer capacitors

According to the Stern model, the differential capacitance C_d results from the connection of two separate capacitors defined by the Helmholtz layer capacitance C_H and by the diffuse layer capacitance C_D

$$\frac{1}{C_d} = \frac{1}{C_H} + \frac{1}{C_D},$$

both capacitors are thought to act in series [18].

Upon charging an electrode, the ionic liquid close to the electrode surface is forced to change its structure. The application of a potential drop can be understood as the *perturbation* of the system, whereas the structural changes in the ionic liquid can be called a *response*.

$$C_d = \frac{\mathrm{d}\sigma}{\mathrm{d}U_{\mathrm{drop}}} = \frac{\text{Response}}{\text{Perturbation}}.$$

Similar to the concept of structural changes of the whole electric double-layer, we discuss the structural change in a single interfacial ionic layer upon applying a potential drop. The structural change in a single interfacial ionic layer is thereby defined as:

$$\chi_{\mathrm{ion}} = \frac{\text{Response}}{\text{Perturbation}} = \frac{\mathrm{d}(\text{Structural change in ion layer})}{\mathrm{d}U_{\mathrm{drop}}}.$$

Upon combining the perturbation-response-concept with the layer capacitance supposed by Stern, we suggest a representation of the differential capacitance as follows:

$$\frac{1}{C_d} \sim \frac{1}{\chi_{\text{counter-ion}}} + \frac{1}{\chi_{\text{co-ion}}} + \dots.$$

We consider the structural response of the first two interfacial ion layers and compare the resulting differential response function with the differential capacitance. Thereby we have a direct access to the connection between ion structuring and differential capacitance. We may understand, how the interfacial layers contribute to the total differential capacitance of the electric double-layer and if information of the ion structuring are lost during the calculation and smoothing of the potential drop.

7.2 Methods: Calculation and analysis of the number density profiles

The analysis of the obtained trajectories was performed using Gromacs tools and self-written Matlab functions.

The number density profiles are calculated using the Gromacs tool `g_density`, while applying a slicing of the simulation box along the z-dimension - normal to the electrode surfaces - in slices of 0.015 nm thickness. The five replicas modelled for every surface charge are averaged and the resulting number density profile split into cathodic and anodic part, resulting in 816 curves to proceed for further analysis.

Furthermore we define the cumulative number $cn(z)$ as the total number of ions in the slab $[z_0; z]$ where z_0 corresponds to the position of the electrode. As a reference curve we define the potential of zero charge (PZC) curve, and thus analyse the cumulative number difference $cn_{U_{\mathrm{drop}}}(z) - cn_{\mathrm{PZC}}(z)$ for different voltages.

All analysis steps have been incorporated in the NaRIBaS scripting framework, see Appendix C.

7.3 Results: Melting of the double-layer changes the ion layer response on charging the electrode

7.3.1 Snapshots and the cumulative number curves reveal melting of ion layers

Differences in the structural response of the model ionic liquid upon changing the temperature are shown in Fig. 7.1. Snapshots and the cumulative number curves are both feasible to understand that a "melting" process takes place. Within the volume between the anion layers the cations show a broad distribution for small surface charges. At intermediate surface charges and low temperature a stiff cation layer is formed with a well defined distance from the electrode. Upon increasing the temperature, the cation layer is "melted" as shown by the broadening of the cation distribution and the smoothed slope of the cumulative number curves.

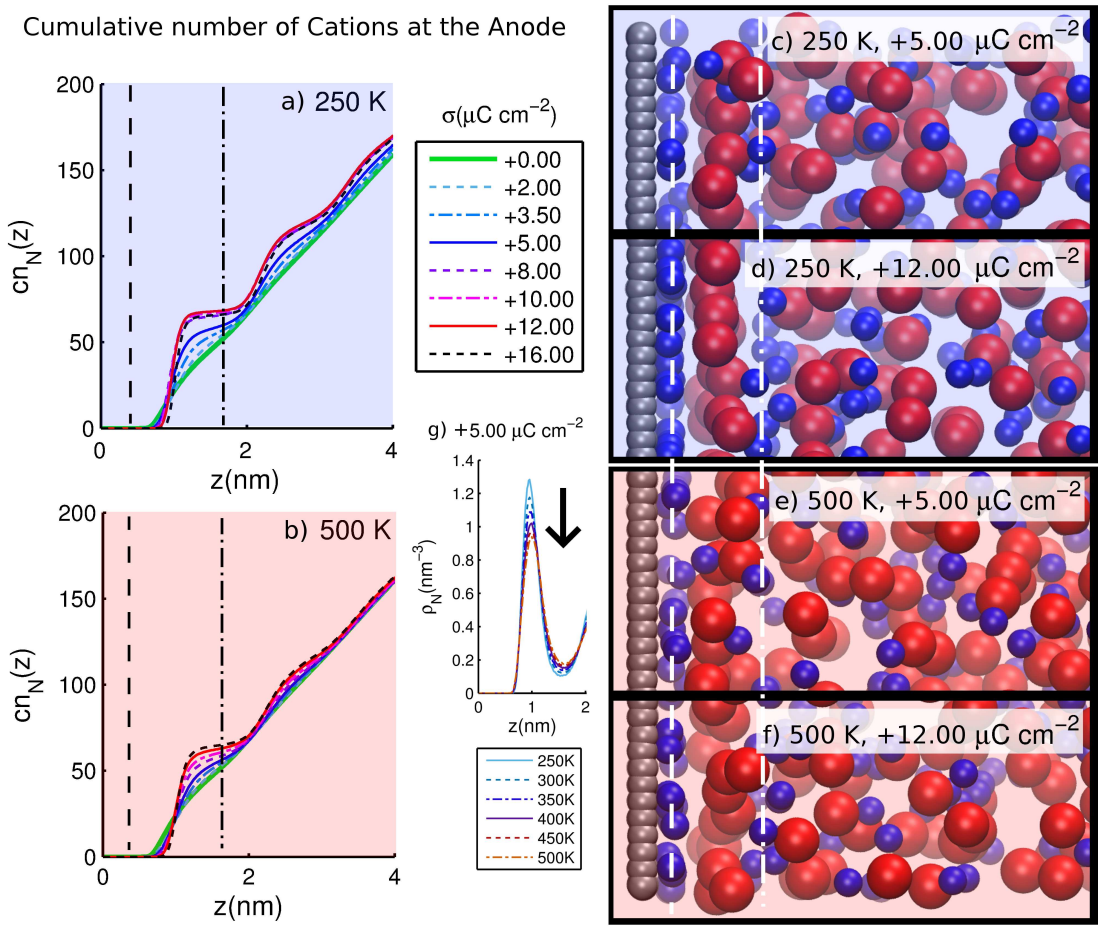

Figure 7.1: (LEFT) Simulated cumulative number curves of cations at the positively charged electrode (anode) for different surface charges between $0.0\,\mu C/cm^2$ and $+16.0\,\mu C/cm^2$ at two temperatures: (a) 250 K and (b) 500 K. The dashed and dot dashed lines indicate the positions of anion layers. (RIGHT) Simulation snapshots of the interfacial ion configurations at (c) 250 K and $+5.0\,\mu C/cm^2$, (d) 250 K and $+12.0\,\mu C/cm^2$, (e) 500 K and $+5.0\,\mu C/cm^2$ and (f) 500 K and $+12.0\,\mu C/cm^2$. White dashed and dot dashed lines indicate again the anion layer positions. (g) Number density profile of cations at the anode for $+5.0\,\mu C/cm^2$ comparing different temperatures. Within the volume between the anion layers the cations show a broad distribution for small surface charges. At intermediate surface charges and low temperature a stiff cation layer is formed with a well defined distance from the electrode. Upon increasing the temperature, the cation layer is "melted" as shown by the broadening of the cation distribution and the smoothed slope of the cumulative number curves.

7.3.2 The ion layer response on electrode charging

To explain the voltage dependent temperature effect of the differential capacitance, we compare the simulated cumulative numbers. The cumulative number $cn(z)$ is defined as the total number of ions in the slab $[z_0; z]$ where z_0 corresponds to the position of the electrode. As a reference curve we define the potential of zero charge (PZC) curve, and thus analyse the cumulative number difference $cn_{U_{\mathrm{drop}}}(z) - cn_{\mathrm{PZC}}(z)$ for different voltages. Figure 7.2(a)-(c) illustrate the cumulative number difference of cations at the positively charged electrode (anode) for voltages between +0.2 V and +1.8 V. Three different temperatures are considered: 250 K, 300 K and 500 K.

The initial minimum in the cumulative number difference curves can be attributed to the repulsion of cations by the positively charged anode. The number of cations in the layer close to the electrode decreases until no cations are left, which explains that the negative peak at the highest voltage appears equal for all temperatures. Moreover the peak width corresponds roughly to the size of the anions, that fill the very first layer close to the electrode surface. Interestingly, the steric repulsion of cations by anions is not very sensitive to temperature in contrast to the filling and emptying of other layers discussed below.

Surprisingly, the total number of cations *increases* while the anode gets charged, which is in contrast to the behaviour of anions at the cathode. The unexpected observation is discussed in detail in Chapter 8.3.

The maxima of the cumulative number differences correspond to the layering of cations in the EDL. In Fig. 7.2(d)-(e) we show the height of the first positive peak of the cumulative number difference over potential drop for all temperatures between 250 K and 500 K. The peak height corresponds to the varying amount of cations and anions in the EDL as a response on the increased surface charge. It is normalized by the number of cations/anions in the EDL at the neutral electrode. The comparison of the peak height at the same potential but different temperatures reveals the so called "melting" effect - the number of ions in the EDL decreases with increasing temperature. Several authors already referred to this process, e.g. Lockett et al [29] by stating: while increasing the temperature "ion association is thermally disrupted and the outer layer of the EDL thins".

However, we observe an effect, that has been to our best knowledge not yet reported: a stagnation of the cationic layer formation at low temperatures. The first cation layer at the anode reaches a 'metastable' state - a layer configuration that does not change while increasing the surface charge. While temperature increases, the formation of the 'metastable' state is delayed. At 250 K the 'metastable' state

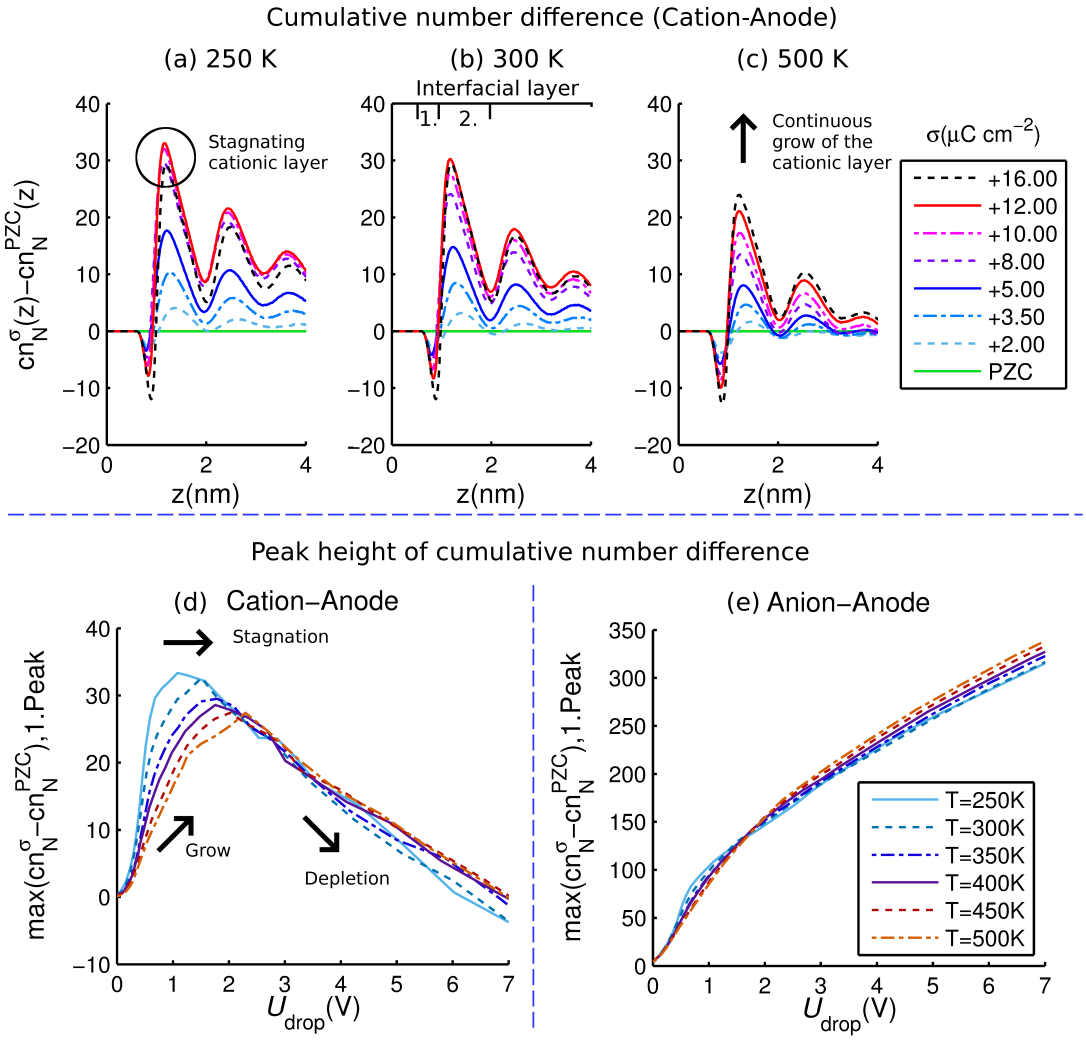

Figure 7.2: (TOP) Simulated cumulative number differences of cations - with PZC curve being the reference curve - at the positively charged electrode (anode) for different surface charge densities between $+2.0\,\mu C/cm^2$ (+0.2 V) and $+16.0\,\mu C/cm^2$ (+1.8 V). From left to right three different temperatures are considered: (a) 250 K, (b) 300 K and (c) 500 K. The total number of cations increases while the anode gets charged. The first minimum of the cumulative number difference can be explained through an increase of the electrostatic repulsion between electrode and ions. The comparison of the peak height at the same potential but different temperatures reveals the so called "melting" effect - the number of cations in the EDL decreases with increasing temperature. However at low temperatures we find a stagnation in the layer formation process, whereas at high temperatures the EDL grows continuously with increasing voltage. (BOTTOM) Height of the first peak of the cumulative number difference over potential drop for (d) cations at the anode and (e) anions at the anode for all temperatures between 250 K and 500 K. The peak height corresponds to the varying amount of ions in the EDL as a response on the increased surface charge with respect to the EDL at the neutral electrode.

is formed at +0.8 V; at 300 K the cation layer does not change from +1.0 V on; at 500 K there is no stagnation in the layer growing visible at all up to +1.7 V. Thus at high temperatures there is a continuous filling of the second - cationic - layer with cations corresponding to the continuous grow of the EDL.

We see no indication that reduced structuring of the EDL at high temperatures is combined with a widening of the EDL, which can be associated with the strong ion-ion interaction. At a specific voltage, a well structured - 'textbook like' or 'lattice like' - EDL is temperature independent formed. However, the pathway for the EDL formation differs drastically between the temperatures, as it is continuous for high temperatures and fast / abrupt for low temperatures.

7.3.3 Understanding the ion structure response as a differential response function

Similar to the concept of structural changes of the whole electric double-layer, we discuss the structural change in a single interfacial ionic layer upon applying a potential drop. The structural change in a single interfacial ionic layer is thereby defined as the change in the amount of ions in the specified layer using the peak height of cumulative number differences $\max(cn_N^{\sigma} - cn_N^{PZC})$:

$$\chi_{\text{ion}} = \frac{\mathrm{d}(\max(cn_N^{\sigma} - cn_N^{PZC}))}{\mathrm{d}U_{\text{drop}}} = \frac{\text{Response}}{\text{Perturbation}}.$$

In Fig. 7.3 we present the differential height of the first peak of the cumulative number difference (differential response function χ_{ion}) over potential drop compared with the differential capacitance.

The peak position and shape of the differential response function for anions and cations in the interfacial layer is similar to the differential capacitance. The temperature dependence is qualitatively the same including the intersection point.

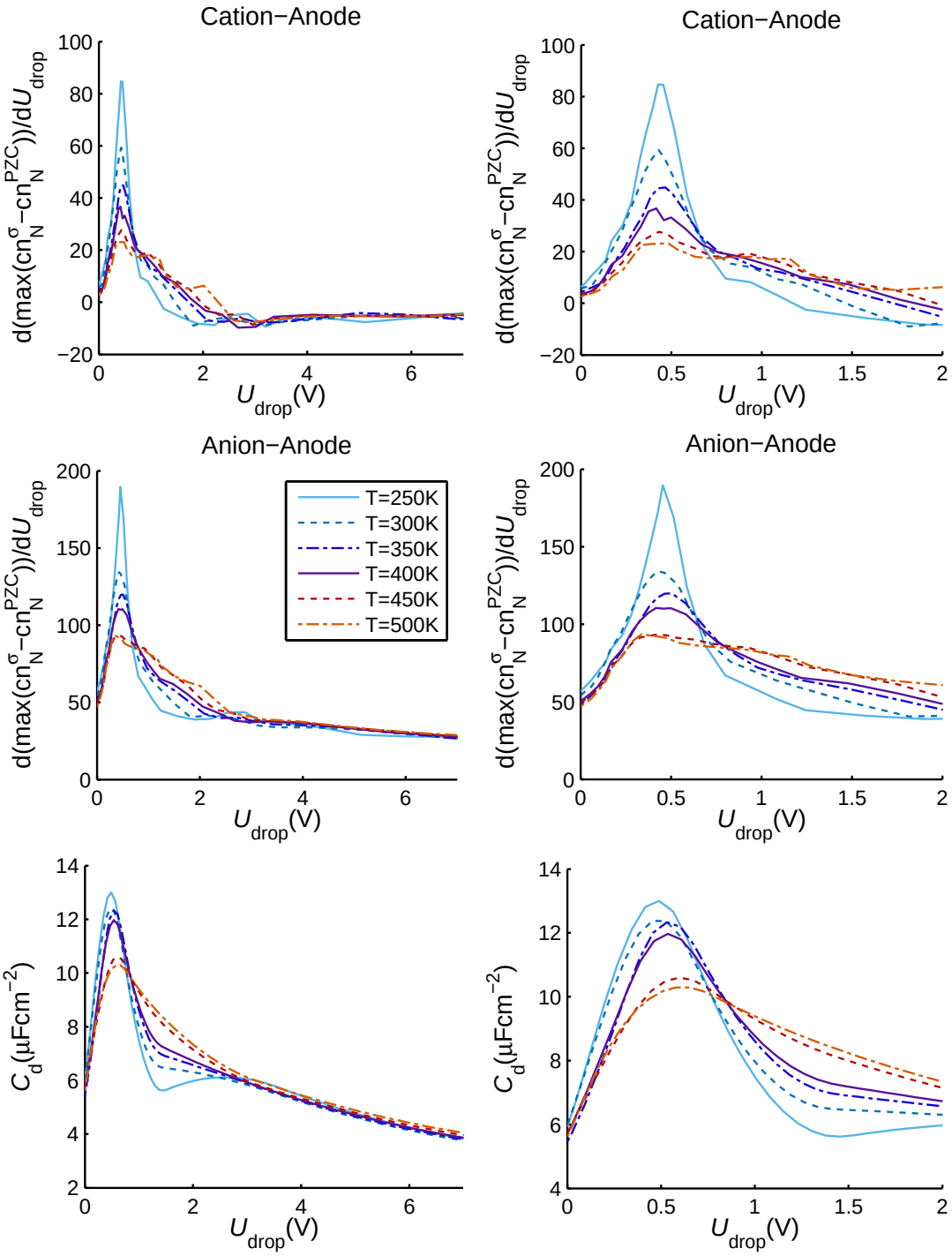

Figure 7.3: Differential height of the first peak of the cumulative number difference (differential response function) over potential drop for (TOP) *cations* and (MIDDLE) *anions* at the *anode* for all temperatures between 250 K and 500 K. The differential response function corresponds to the structural response of ions in the EDL as a response on the increased surface charge. Thus the differential response function can be directly compared with the differential capacitance (BOTTOM). (LEFT) Potential drop between 0 V and +7 V; (RIGHT) Close-up with a potential drop between 0 V and +2 V.

7.4 Conclusions: The differential capacitance as a structural response function influenced by a temperature induced melting

In the beginning of this chapter we raised the question, if we can extract a physical origin of the temperature dependence of the differential capacitance. Upon studying number density profiles and the related cumulative numbers of ions over distance from the electrode surface, we found a melting process to take place as the temperature of the system is increased. Stiff electric double-layer structures are 'melted' when the temperature is raised due to the increase of temperature fluctuations and associated depletion of ion concentration in the interfacial layers at the electrode.

The shape and temperature dependence of the differential capacitance can be directly associated with the structural response of the ions in the first two interfacial layers at the electrode. The differential response shows at low temperatures a steep incline until 0.5 V to be continued by a sharp decrease. In contrast the differential response at high temperatures appears as a flattened curve with steady increase and decrease. The overall response of the ions is continuous at high temperatures, and abrupt at low temperatures. The strong ion response at low surface charge density and the weak or negligible response at higher surface charge densities causes the sharp increase and decrease of the differential capacitance.

The difference in the *structural ion response* at different temperatures induced by *melting* causes the voltage dependent increase or decrease of the differential capacitance with temperature.

Chapter 8

Alternated layering, charge compensation and co-ionic enrichment

Key-features of the electric double layer are alternating layering of counter-ions and co-ions and charge overcompensation [6, 7, 8, 9, 10, 11]. Both basic conceptions will be studied in detail within the following chapter.

8.1 Number density profiles reveal multiple ion layers

The basic method for the analysis of the number density profiles was explained earlier, see Section 7.2. Figure 8.1 and 8.3 show cathodic and anodic number density profiles for both ion species in comparison at the neutral electrode and at surface charge densities of $\sigma = 2.00\,\mu\mathrm{C/cm^2}$ and $\sigma = 5.00\,\mu\mathrm{C/cm^2}$. More number density profiles are shown in the Appendix.

8.1.1 Layering at the neutral interface is driven by Entropy and Coulombic attraction between ions

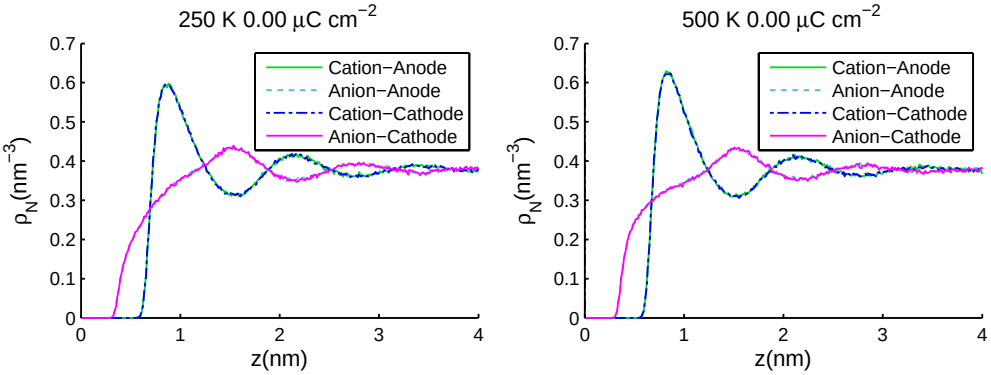

Figure 8.1: Number density profiles for the neutral electrode surface at (LEFT) $T = 250\,\mathrm{K}$ and (RIGHT) $T = 500\,\mathrm{K}$. The centre of mass of the electrode atoms are situated on the xy-plane with $z = 0$. The number density profiles at the anode and cathode are identical as both electrodes are neutral.

First, we want to study the ion layering at the neutral electrode interface. We explained earlier, that the ion model under study is considered to consist of indifferently adsorbing ions, as no attractive forces at all are modelled, except for the Coulombic attraction of oppositely charged species. A naive view on a neutral electrode would first raise the picture of bulk like ionic liquid close to the electrode surface. However, this is not the case as it is shown in Fig. 8.1: even at a neutral interface we obtain definite ion layering as shown by alternating peaks and valleys in the number density profiles of anions and cations. The length of the ion-correlations in the direction normal to the electrode surface appears to be 3.5 nm to 4.0 nm depending on the temperature. As expected, the layering disappears earlier at higher temperatures due to the enhanced kinetic energy of the ions.

Closest to the electrode surface is a small number of anions, followed by a layer of cations at approx. 0.9 nm. At 1.5 nm distance from the electrode, the number density profile of cations shows a local minimum, whereas the anion profile exhibits a local maximum. Further minima and maxima are visible.

What is the origin of the layering at a neutral interface as no attractive potential is modelled between the electrode and the ions? Upon studying the ion layering at different temperatures, see Fig. 8.2, we can see that with increasing temperature the height of the number density profile increases for both, anions and cations, that are closest to the electrode.

First we have to keep in mind, that particles with spherical geometry attached to a flat surface provide a considerable empty volume close to the surface. Driven by Entropy [234, 235, 236, 237] the number of small sized anions moves close to the electrode surface, thereby filling the gabs or holes that are formed between the larger cations. Second, co-ions attract counter-ions due to Coulombic attraction. If there is an excess of anions at the surface, they will attract cations to build up a layer close to the electrode. Furthermore, the new formed layer of cations might attract another layer of anions [237], continuing until the correlations are diminished.

8.1.2 Layering at the charged interface is driven by Coulombic attraction

After discussing layering at the neutral interface, we have to consider electrode charging. Figure 8.3 shows the ionic layering at small surface charge densities of $\sigma = \pm 2.0\,\mu\mathrm{C/cm^2}$ and $\sigma = \pm 5.0\,\mu\mathrm{C/cm^2}$. In both cases an excess of counter-ions is visible close to the surface. The counter-ion excess is followed by several distinguishable co-ion / counter-ion layers indicated by several maxima and minima in the density profile. Upon electrode charge increase, the first peak of all number density profiles narrows and becomes higher. This is explained by the enhanced interaction between the electrode surface and the first interfacial ionic layer.

8.2 Charge density profile and cumulative charge reveal overcharging

The number density profiles $\rho_N(z)$ of cations and anions provide a separated view of their response on the electrode surface charge. Another way to analyse the solvent response on electrode charging is the discussion of charge density

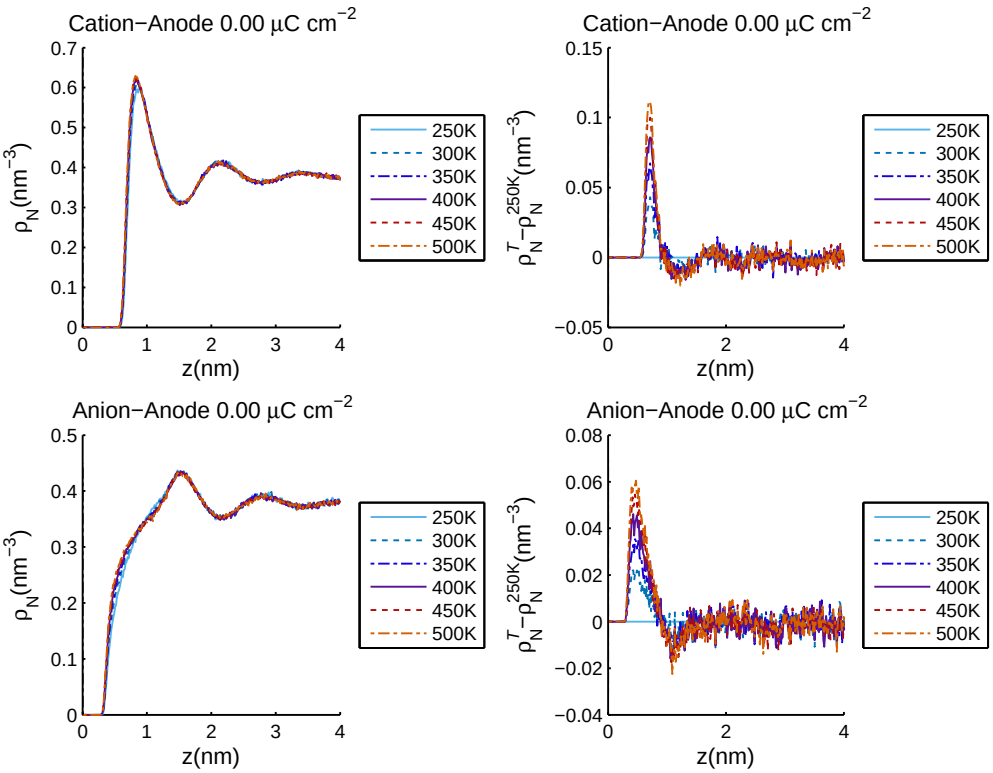

Figure 8.2: Number density profiles for the neutral electrode surface, comparison of different temperatures. The centre of mass of the electrode atoms are situated on the xy-plane with $z = 0$. (LEFT) Number density profile, (RIGHT) Difference between all number density profiles and the profile at lowest temperature 250 K. (TOP) Cations, (BOTTOM) Anions.

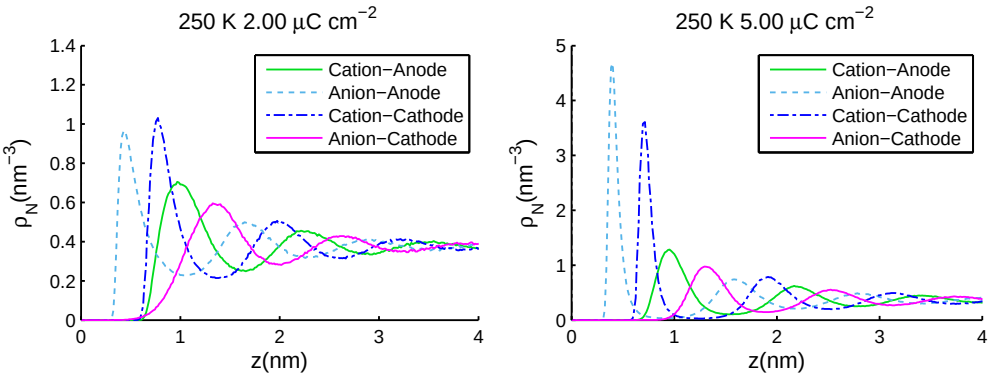

Figure 8.3: Number density profiles for different surface charges at $T = 250\,\mathrm{K}$. The centre of mass of the electrode atoms are situated on the xy-plane with $z = 0$. (LEFT) Surface charge $\sigma = \pm 2.0\,\mu\mathrm{C/cm^2}$, (RIGHT) Surface charge $\sigma = \pm 5.0\,\mu\mathrm{C/cm^2}$.

profiles $\rho_Q(z)$. Those profiles are obtained by summing up all number density profiles multiplied by the charge q_{ion} of the ionic specie

$$\rho_Q(z) = \rho_N^{\text{Cation}}(z) \cdot q_N^{\text{Cation}} + \rho_N^{\text{Anion}}(z) \cdot q_N^{\text{Anion}}.$$

The resulting charge density profiles for the model under study are shown in Fig. 8.4. For the neutral electrode and all surface charges we observe charge waves as expected for the model.

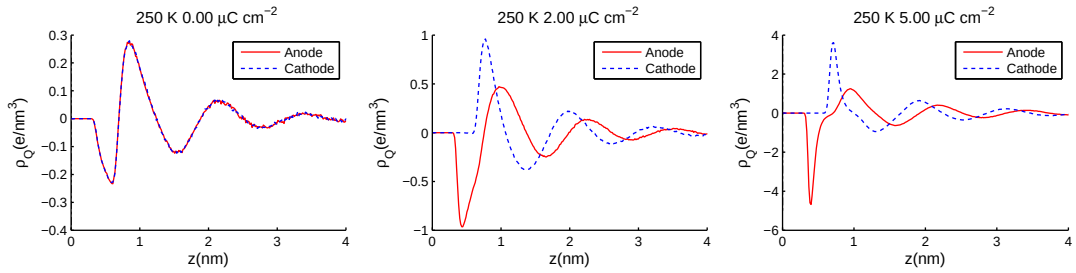

Figure 8.4: Charge density profiles for different surface charges at $T = 250\,\text{K}$. The centre of mass of the electrode atoms are situated on the xy-plane with $z = 0$. (LEFT) Surface charge $\sigma = 0.0\,\mu\text{C/cm}^2$ corresponding to the PZC, (MIDDLE) Surface charge $\sigma = \pm 2.0\,\mu\text{C/cm}^2$, (RIGHT) Surface charge $\sigma = \pm 5.0\,\mu\text{C/cm}^2$.

As we have discussed the origin of the charge waves in the section about number density profiles above, we now consider another concept known for ionic liquids at electrified interfaces, namely "overcharging" [59, 8]. Against physical intuition, it can be observed, that the excess counter-ions at the electrode surface over-compensates the electrode charge. We refer to Fig. 8.5 and 8.6 for a visualization of the effect as it can be observed in our model system. Given in both figures is the cumulative charge $cn_Q(z) = \int_0^z \rho_N(z')\mathrm{d}z'$ for different surface charge densities normalized by the number of elementary charges on the electrode $q_{\text{electrode}}$.

It is clearly visible that at low surface charges the number of counter-ions in the first interfacial layer reaches nearly two times the number of elementary charges on the electrode. With increased temperature, the number of ions in the given interfacial layers is reduced. A similar reduction is observable upon increase of the electrode charge. Surprisingly, at the cathode, the normalized cumulative charges moves to a plateau upon reaching a surface charge density of $\sigma = -16.0\,\mu\text{C/cm}^2$. The plateau value equals one, which means simple charge compensation. No charge waves indicate a bulk phase close to the first interfacial layer. These observations can be explained via a structural transition at the interface, which is discussed in detail in Chapter 9.

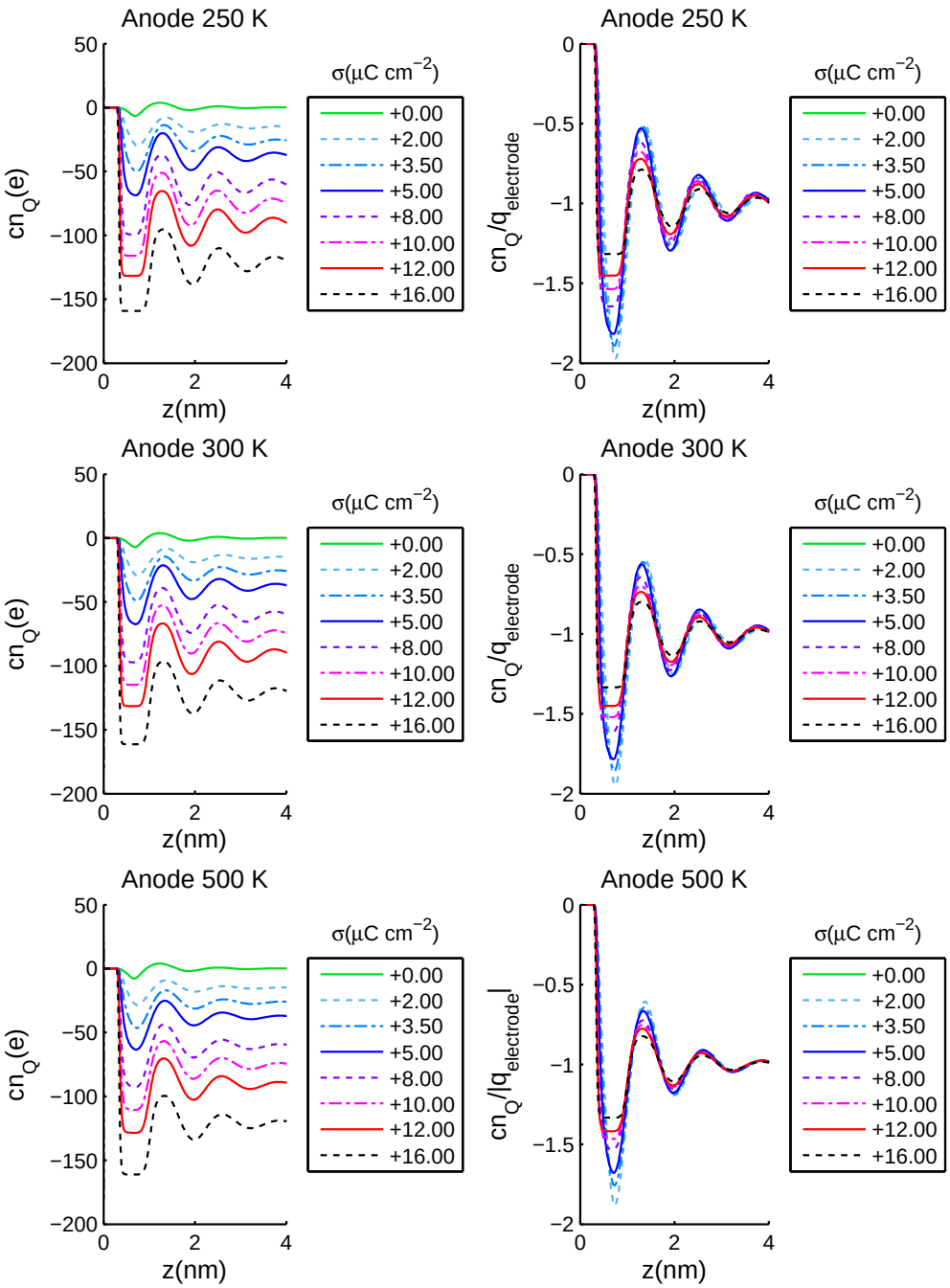

Figure 8.5: Cumulative charge at the anode for different surface charges. The centre of mass of the electrode atoms are situated on the xy-plane with $z = 0$. (TOP) $T = 250\,\mathrm{K}$, (MIDDLE) $T = 300\,\mathrm{K}$, (BOTTOM) $T = 500\,\mathrm{K}$. (LEFT) Cumulative charge for different surface charges, (RIGHT) Cumulative charge normalized by the number of elementary charges on the electrode. The charge normalization is identical to the concept of dividing the local charge density in the solution side of the electric double layer by the absolute surface charge density of the electrode.

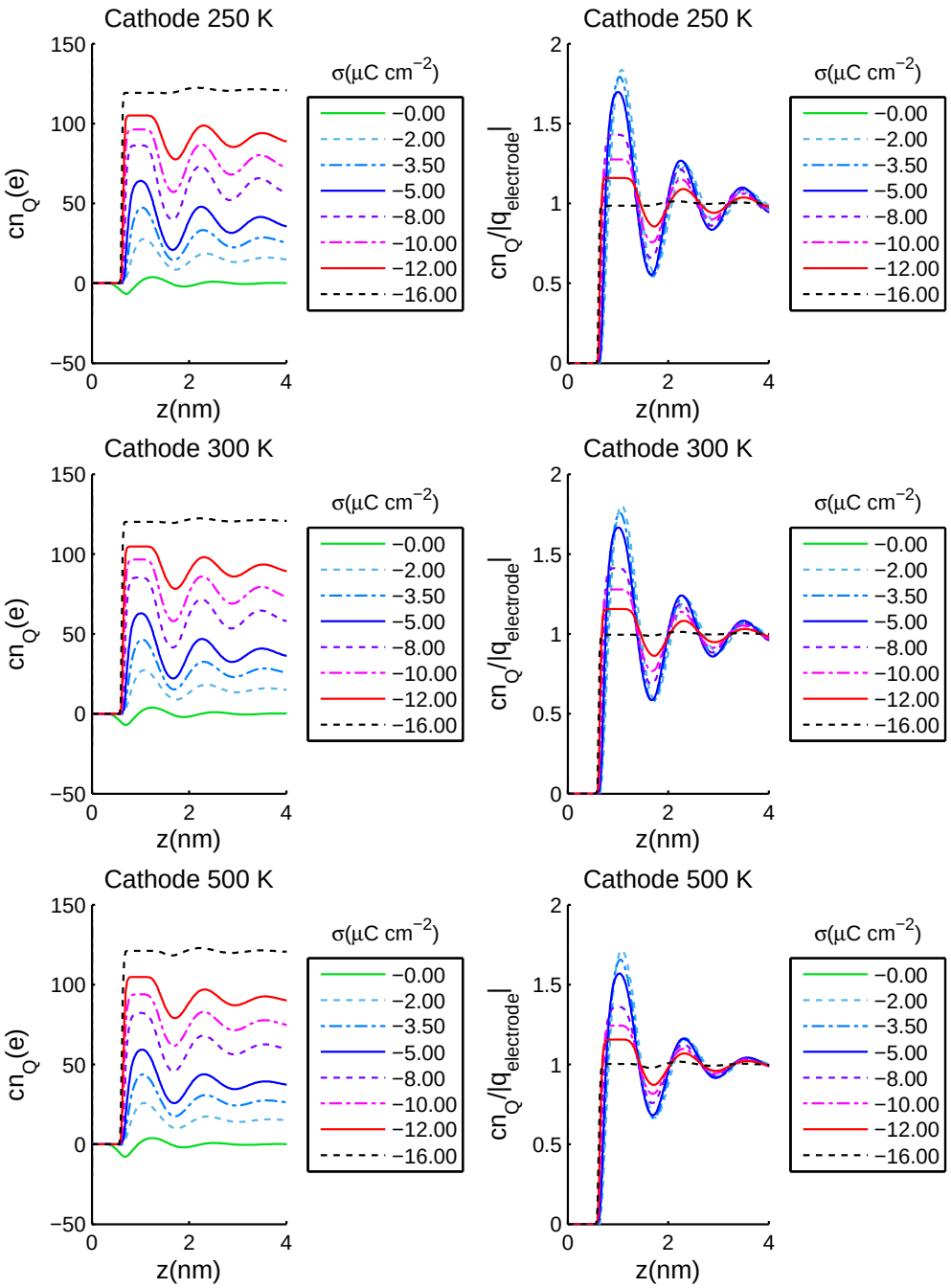

Figure 8.6: Cumulative charge at the cathode for different surface charges. The centre of mass of the electrode atoms are situated on the xy-plane with $z = 0$. (TOP) $T = 250\,\mathrm{K}$, (MIDDLE) $T = 300\,\mathrm{K}$, (BOTTOM) $T = 500\,\mathrm{K}$. (LEFT) Cumulative charge for different surface charges, (RIGHT) Cumulative charge normalized by the number of elementary charges on the electrode. The charge normalization is identical to the concept of dividing the local charge density in the solution side of the electric double layer by the absolute surface charge density of the electrode.

8.3 Ion-number within an interfacial volume: a co-ionic enrichment at the anode

In the following section we discuss the number of ions that can be found within a given distance from the electrode surface. Upon analysing the evolution of ion number over surface charge (or potential drop) within well defined volumes, we want to obtain a deeper understanding of the formation and appearance of the electric double layer. Surprisingly, we found a co-ionic enrichment at the anode, which we present and discuss in detail below.

8.3.1 Methods: Calculating the number of ions near the electrodes using a geometrical approach

The number of cations and anions within a specific distance - called cutoff z_{cutoff} - from the electrodes is calculated and normalized by the mean number of ions N_0 that would be found in an equivalent bulk volume. The cutoff can be chosen arbitrarily, however it might be useful to make some considerations concerning the basic geometry of the system under study.

Table 5.1 summarizes geometric properties of the system under study. For cutoff definitions both the geometric radii as well as the Lennard-Jones parameter σ_{LJ} might be of interest. Figure 8.7 presents a basic picture of the ionic liquid structure near anode and cathode including the suggestion of interesting distances between the ion layers. Based on the schematic representation, we consider alternating ion layers to build up within $\sigma_{LJ}^{\text{Ion-Wall}} + i \cdot \sigma_{LJ}^{\text{Cation-Anion}}$ with $i \in \mathbb{N}$, where $\sigma_{LJ}^{\text{Ion-Wall}} = \sigma_{LJ}^{\text{Cation-Wall}}$ for the cathode and $\sigma_{LJ}^{\text{Ion-Wall}} = \sigma_{LJ}^{\text{Anion-Wall}}$ for the anode. We expect an increase of counter-ion number and a decrease of the co-ion number in the closest volume defined by $z_{\text{cutoff}} = \sigma_{LJ}^{\text{Ion-Wall}} + \sigma_{LJ}^{\text{Cation-Anion}}$.

The normalization factor N_0 is the result of the bulk density ρ_{Bulk} multiplied by the accessible volume $V = A \cdot \Delta z$, with A being the surface of the electrodes. The definition of the accessible volume is the result of a simple geometrical consideration: The volume between the centre-of-mass of the wall atoms and the centre-of-mass of the ions will not contribute to the accessible volume because of the steric repulsion between wall and ionic liquid. The mean number of ions in the volume close to the electrode is finally calculated as follows:

$$N_0 = \rho_{\text{bulk}} \cdot A \cdot \Delta z = \rho_{\text{bulk}} \cdot A \cdot (z_{\text{cutoff}} - \sigma_{LJ}^{\text{ion-wall}}).$$

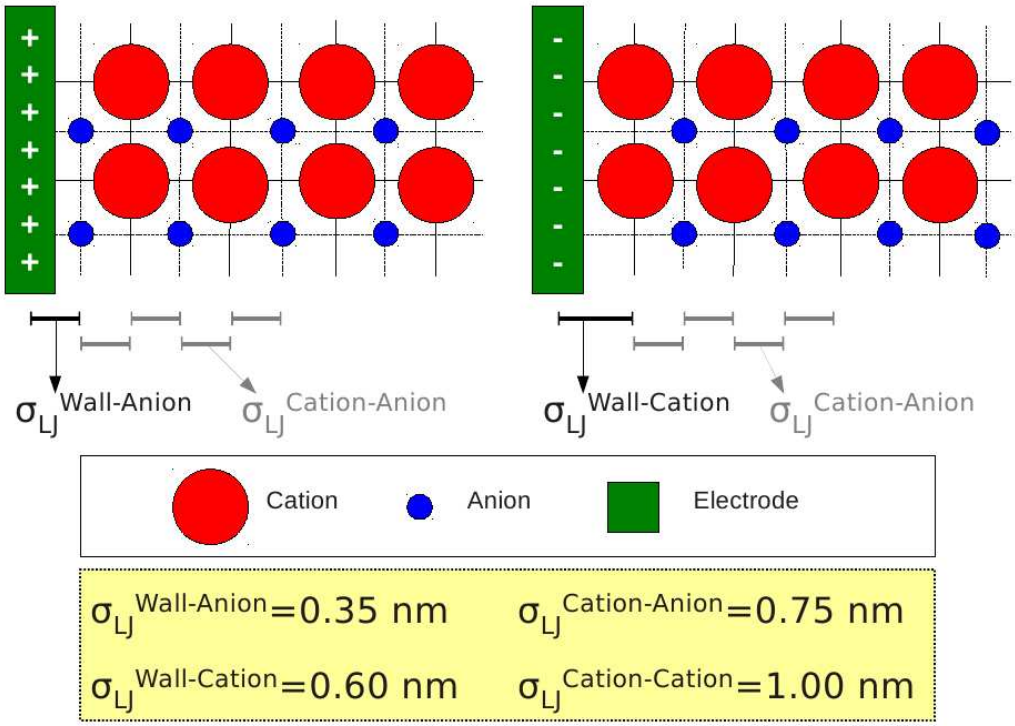

Figure 8.7: Definition of the cutoff for ion number analysis based on the geometric size of ions and electrode atoms.

8.3.2 Results: A co-ionic enrichment at the anode

Within Fig. 8.8 we present the normalized ion numbers comparable to the ion density over potential drop. The figure shows anion and cation number within the interfacial volume with surface $A = A_{\text{electrode}}$ and a length in z-direction normal to the electrode surface of $z_{\text{cutoff}} = 1.0\,\text{nm}$. Within the given cutoff we expect

- At the cathode (negative voltages) a repulsion of anions and an attraction of cations with increasing potential;
- At the anode (positive voltages) a repulsion of cations and an attraction of anions with increasing potential.

Moreover the cutoff is chosen to be smaller than $\sigma_{LJ}^{\text{Anion-Wall}} + \sigma_{LJ}^{\text{Anion-Cation}} = 1.1\,\text{nm}$. Therefore we include two more expectation:

- The number of anions in the cathodic interfacial volume should decrease to zero at intermediate voltages, where cations are likely to fill the interfacial layer.
- The number of cations in the anodic interfacial volume should decrease to zero at intermediate voltages, where anions are likely to fill the interfacial

layer.

The expectations are based on the Coulombic attraction of counter-ions by the electrode, the Coulombic repulsion of co-ions by the electrode and the steric repulsion of co-ions at the electrode surface by the excess of counter-ions.

The cathodic part of Fig. 8.8 meets our expectations, as the number of anions shows a rapid decrease to zero at intermediate charges, whereas the the number of cations increases steadily upon electrode charging. However, the picture looks completely different at the anode. Between +0.1 V and +1.5 V the number of cations increases. The maximum ion density reaches 2.4 times the normal ion number N_0 at $T = 250\,\mathrm{K}$ and exceeds 1.5 times the normal ion number N_0 at $T = 500\,\mathrm{K}$. The ion number decreases after reaching its maximum, but does not reach zero before +7.0 V are applied.

The physical concepts discussed above – (i) Coulombic electrode-ion interaction and (ii) steric repulsion of particles – need to be extended by a third concept: (iii) the Coulombic attraction or co-ions and counter-ions. The co-ionic enrichment at the anode we see in Fig. 8.8 is caused by the attraction of cations by the anion layer that is formed close to the electrode surface. The ion-counter-ion-correlation seems to exceed drastically the steric repulsion and the Coulombic electrode-repulsion. Thereby cations are able to approach a seemingly unfavourable configuration.

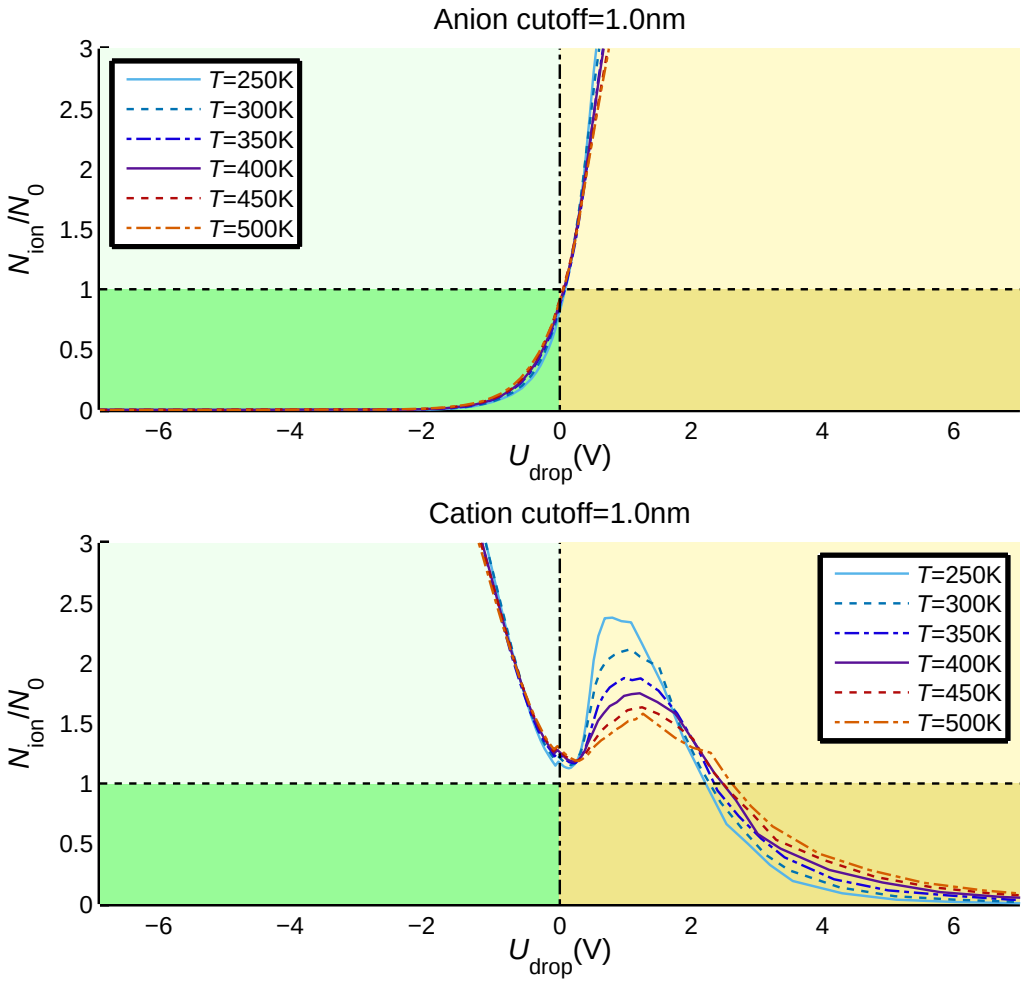

Figure 8.8: Anion and cation number in the interfacial volume with $z_{\text{cutoff}} = 1.0\,\text{nm}$. For a definition of the cutoff, see Section 8.3.1. The cutoff is chosen to be smaller than $\sigma_{LJ}^{\text{Anion-Wall}} + \sigma_{LJ}^{\text{Anion-Cation}} = 1.1\,\text{nm}$. Within the given volume defined by the cutoff $z_{\text{cutoff}} = 1.0\,\text{nm}$ we expect: (i) At the cathode (negative voltages) a repulsion of anions and an attraction of cations with increasing potential; (ii) At the anode (positive voltages) a repulsion of cations and an attraction of anions with increasing potential; (iii) The number of cations in the anodic interfacial volume is expected to decrease to zero at intermediate voltages.

8.4 Conclusion

Within this chapter we have discussed basic features of the electric double layer of ionic liquids, namely alternating layering of counter-ions and co-ions and charge overcompensation.

We have observed a layering of ions even at the neutral electrode driven by the Entropy and ion/counter-ion correlation, but also the classical alternating layering at charged surfaces. We have seen that the electrode charge is overcompensated by the first interfacial ion layer and we observed a co-ionic enrichment at the anode caused by Coulombic ion/counter-ion attraction.

Upon discussing charge overcompensation or charge screening, we have been surprised by the charge density profile at the cathode, which shows at a specific surface charge density charge compensation by a single cationic layer and a liquid like ionic liquid close to the interfacial ion layer. These observations can be explained by a structural transition at the interface, which is discussed in detail in the following Chapter 9.

Chapter 9

Structural transition at the interfacial

Using molecular dynamics (MD) simulations of a model coarse grain ionic liquid (IL) we provide insights into the structural organization of ionic liquids at the electrified interface under various temperatures. In the first section of this chapter we will summarize briefly experimental and simulation results obtained for structuring of Coulombic fluids - liquid metals, molten salts and room temperature ionic liquids - at interfaces followed by a discussion of two-dimensional structural transitions including theoretical considerations and recent simulation results. We introduce the methodology we used for our analysis. The "Results" section contains a documentation of the structural transition and a characterization of the interfacial structure of the ions.

The results presented in the following chapter are submitted for publication (the manuscript is currently under review) in Electrochimica Acta (Ref. [238]).

9.1 Introduction

For a decade leading scientists in the field consider room temperature ionic liquids (RTILs) as highly important for the electrochemical technology [18, 19, 20]. The high charge density of ions in RTILs changes the nature of common phenomena at electrified interfaces. New perspectives in galvanic deposition, etching, corrosion science, electrocatalysis and other branches of applied electrochemistry are revealed.

One of the fascinating interfacial phenomena is potential-induced 2D-ordering-disordering of the ionic layer nearest to the surface.

Within the range of "real" Coulombic fluids - fluids with properties in two and three dimensions dominated by Coulomb or Coulombic interactions - three types of substances need to be considered, namely liquid metals, molten salts and room temperature ionic liquids composed of organic cations and organic/inorganic anions. Experimental findings for the structuring of these substances at interfaces will be summarized by providing insight in the works of Frank Endres and co-workers [19, 22, 239, 39, 240, 31, 42] and in the works of Werner Freyland and his group [241, 38, 21, 2].

Among the molecular dynamics simulation, the restricted primitive model (RPM) and its variations (e.g. asymmetric sized primitive model - ASPM) have been quite popular [226, 242, 175, 243], followed by hard and soft spheres modelled using the Lennard Jones potential and coarse grain models of ionic species in colloidal suspensions and ionic liquids [244, 5]. The simulation of a molten salt at an electrified was performed by Tazi et al [245].

9.1.1 Experimental results on structuring of solvated ions and ionic liquids at electrified surfaces

Weakly solvated ions, such as SO_4^{2-}, Cl^-, Br^-, I^-, are known to form ordered adlayers at the interface between electrode and aqueous electrolyte [246]. The formation of such adlayers is originated in the partial stripping of the solvation shell and direct adhesion to the electrode surface [247]. An absence of solvent molecules in RTILs implies that the factors determining the ordering in aqueous electrolytes must be different from those in ionic liquids [59, 80, 248]. However, Pan and co-workers [38] observed similar ordering in the ionic liquid 1-butyl-3-methylimidazolium hexafluorophosphate ([BMIm][PF_6]) at the Au(111) surface. The PF_6^- anions form Moire-like structures.

Adlayers are observable using Scanning Tunneling Microscopy (STM) due to the structures' specific rigidity. We emphasize STM among other experimental techniques (such as atomic force microscopy [249], X-ray based spectroscopy techniques [250, 251, 252, 253, 131] and others [128]) due to the ability to visualize extremely small segments of the interface. Therefore the method is capable of providing molecular evidence of ordering at the surface [1].

As has been reported by Aal et al [39] and Drüschler et al [31], the Au(111) surface reconstructs upon charging within some RTILs. The reconstruction appears as the formation of a herring bone super structure, that is not yet explained.

Within their documentation of the temperature dependence of the differential capacitance, Drüschler et al [31] found processes on several time scales controlling the structuring and electrode surface reconstruction. Thereby the authors conclude, that slow processes are caused "by temperature-independent activation barriers, most likely barriers for the reconstruction of the electrode surface and/or barriers for the reorientation of strongly bound ions in the innermost layer."

Waldmann et al [40] resolved STM images of pyrrolidinium cations at the Au(111) surface on a molecular level. Ordered molecular structure were found only at low temperatures (210 K). At room temperature the mobility of the ions appeared to be too high to preserve the same structure, instead making STM images blur [41, 42, 43].

Formation of distinctive ion layers in RTILs, alternating in the direction perpendicular to the surface (so-called charge waves) has been confirmed in a number of experimental studies starting from high-energy X-ray reflectivity [254] to sur-

[1] We note, that also results obtained by atomic force microscopy and X-ray based spectroscopy indicate the formation of cationic layer of negative surface charges [250, 251, 253] and existence of ordered mixed ionic layer at the neutral surface [252, 131, 128].

face force apparatus study [16]. Observation of such alternating ion layers in the modelled electrical double layer (EDL) were made for a simple coarse grain model of an RTIL [79] as well as in case of more sophisticated simulation studies applying all-atom polarisable force field [36, 170]. Polarisation effect was accounted also in a MD simulation of molten salt LiCl near Al(100) surface [245] and was found to induce a potential-driven ordering transition for the very first LiCl layer at the interface.

Results for surface freezing/crystallization of metal-molten salt solutions and fluid metals on vapour and solid interfaces have been reviewed by Freyland [21]. Surface freezing was found to coincide with the formation of a 2D fluid-hexatic phase transition. For CCl_4 and aniline in activated carbon fibers similar structures have been observed [255].

9.1.2 Theoretical results on two-dimensional melting/freezing: formation of a hexatic structure

In her review article dated from 1988 Strandburg summarized state-of-the-art theory and simulation results of two-dimensional freezing and melting [226]. In combination with two-dimensional freezing and melting a 2D-hexatic structure is described by the Klosterlitz-Thouless-Halperin-Nelson-Young (KTHNY) theory [226] and has been shown in computer simulations of the restricted primitive model (RPM) and its variations [226, 242, 256, 175, 257, 243], coarse grain models of ionic species in colloidal suspensions and ionic liquids [244, 5].

The transition between fluid and solid phase is intermitted by a so-called *hexatic phase*. The specific structure, that forms before a solid two-dimensional structure melts, is characterized as nearest-neighbour-bond-orientational-ordered fluid. The term describes the specific property of the hexatic phase: (i) short-range positional correlations like a liquid and (ii) long range bond-orientational correlations similar to a solid structure. The hexatic phase is well described by the Klosterlitz-Thouless-Halperin-Nelson-Young (KTHNY) theory from 1979. For a deeper discussion of the hexatic phase, structural defects and theoretical analysis we refer to the Strandburgs review [226].

Boda and co-workers simulated series of computational experiments of charged dipolar hard spheres [242] showing strong layering structure of the liquid at solid interfaces, and even at higher charges, charge inversion in the second layer were found. The structuring of ionic liquids at electrified surfaces obtained via the simulation of the restricted primitive model (RPM) was discussed by Resyko-Zygmunt et al [177] and compared with a modified density functional theory

(DFT) showing reasonable agreements with simulation results. Tazi et al [245] simulated the molten salt LiCl on an Al(100) surface. The authors found a potential-driven ordering transition of a LiCl interfacial layer to occur under certain conditions.

Grandner and Klapp investigated the surface-charge-induced freezing of colloidal suspensions [244, 5], thereby finding that crystalline, hexagonal- and square-ordered phases can be constructed within a colloidal suspension upon charging electrodes. Layering transitions and first-order, in-plane freezing and melting transitions including re-entrant behaviour has been reported by the group.

The possible coexistence of a liquid and a solid phase in a formamide droplet under an applied electric field has been shown recently by Luedtke et al [258]. Using molecular dynamics simulations, the authors found the transition of formamide from a spherical droplet to a crystalline structure under applying an electric field greater than 0.5 V/nm. The effect is called "electro-crystallization". By particular spatial reordering into a lattice, the formamide molecules optimized the interactions between the positive and negative ends of the dipoles of neighbouring molecules.

Considering that interfacial layers are already speculated to play an important role in interfacial processes [239] we continue the studies of [79, 7, 81, 80, 259] on structural phenomena in ionic liquids.

9.2 Methods

The simulation setup was chosen similar to our former work [7], but extended by the simulation of six different temperatures (compared to one temperature) and 34 surface charges (compared to 24 surface charges) and five replicas (compared to one single simulation per setup), thereby massively increasing the amount of processable data. The total number of setups summed up to $34 \times 5 \times 6 = 1020$, with a total simulation time for the production runs of 25.5 μs with $dt = 0.01$ ps. The total amount of simulation time for the equilibration summed up to 210 ns with $dt = 0.002$ ps and 10.2 μs with $dt = 0.01$ ps.

In the following two paragraphs, the simulation methodology is described and the subsequent analysis of the trajectories.

Calculation and analysis of the number density profiles The number density profiles are calculated using the Gromacs tool `g_density`, while applying a slicing of the simulation box along the z-dimension - normal to the electrode

surfaces - in slices of 0.015 nm thickness. The five replicas modelled for every surface charge are averaged and the resulting number density profile split into cathodic and anodic part, resulting in 816 curves to proceed for further analysis. All analysis have been incorporated in the NaRIBaS scripting framework, see Appendix C.

To compare structural properties of the number density profiles for different surface charges and temperatures, a signal processing routine written in Matlab by Tom O'Haver was used [260] The routine involves two steps to obtain peak or valley position, height and full width of half maximum (FWHM): (i) Finding the peak position: the profile is differentiated, the first derivative of the profile is smoothed, downward-going zero-crossings are determined; (ii) Characterizing the peak: estimate the position, height, and width of each peak by least-squares curve-fitting of a segment of the original non-smoothed profile in the vicinity of the zero-crossing. The routine has been carefully applied to account for the structural features of the number density profiles, e.g. mixtures of extremely narrow peaks and steep broad valleys.

9.3 Results

We analysed the number density profiles of both ion species close to the electrode surface. Thereby we found at a surface charge density of $\sigma = -16.0\,\mu\mathrm{C/cm^2}$, that the electric double layer with several ion layers on the solvation side is drastically re-ordered. Instead of alternating ion layers we observe only one counter-ion layer close to the electrode. The counter-ions in the interfacial layer are well structured and the remaining ions behave bulk like showing no correlation to the interfacial layers.

The following characterization of the phase transition and the interfacial structure is driven by a number of questions:

1. How do the number density profiles evolve near the transition points?

2. How does the interfacial structure of counter-ions look like?

3. What is the role of the ion size? We see the phase transition for cations at the cathode - do we also see the phase transition for the smaller anions at the anode?

9.3.1 Definition of a surface charge compensation parameter

For the ordering of ions in the first layer close to the electrode surface we draw a picture of a densely packed ion monolayer. The ion size determines the maximum number of ions that can be packed in a single monolayer. The smaller the ions, the more ions can fit into the first interfacial layer. According to this conception, we introduce a *surface charge compensation* parameter, named κ, as the ratio between the electrode surface charge density σ and the theoretical maximum counter-ion charge density in a closely packed ion monolayer $\theta_{\max}$:

$$\kappa = \left| \frac{\sigma}{\theta_{\max}} \right| \tag{9.1}$$

As an estimation for the $\theta_{\max}$ we use an assumption of a cubic lattice structure for the ion monolayer. Accordingly, we define the $\theta_{\max}$ to be equal to the ion charge q_{ion} divided by the squared counter-ion diameter d_{ion}^2:

$$\kappa = d_{\text{ion}}^2 \cdot |\sigma / q_{\text{ion}}| \,.$$

Several simulated surface charges σ are expressed as compensation parameter κ for cations and anions in Tab. 9.1.

Table 9.1: Surface charge compensation parameter $\kappa = \alpha \cdot d_{\text{ion}}^2 \cdot |\sigma / q_{\text{ion}}|$, with σ being the electrode surface charge density, d_{ion} being the diameter of the ion and $q_{\text{ion}} = \pm 1 \cdot e = \pm 1.602 \cdot 10^{-19}\,\text{C}$ being the charge on the cation or anion, respectively. The correction parameter α takes into account details of the dense packing of ions and is set to one. Surface charges under study are ranging from 0.00 to $\pm 50.0\,\mu\text{C/cm}^2$.

$\sigma\,(\mu\text{C/cm}^2)$	κ (Anode) $d_{\text{anion}} = 0.5\,\text{nm}$	$\sigma\,(\mu\text{C/cm}^2)$	κ (Cathode) $d_{\text{cation}} = 1.0\,\text{nm}$
+0.25	0.0039	-0.25	0.0156
+1.00	0.0156	-1.00	0.0624
+5.00	0.0780	-5.00	0.312
+16.0	0.250	-16.0	1.00
+24.0	0.375	-24.0	1.50
+34.0	0.530	-34.0	2.12
+50.0	0.780	-50.0	3.12

Note that introducing the κ parameter was inspired by Kornyshev's work [59]. Kornyshev introduced a parameter (γ) describing the ratio between the total number of ions and the total number of sites available for the ions. The difference is that κ may exceed values of one as it compares the surface charge density with a theoretical local ion concentration – the surface charge density may likely exceed the ion density in a monolayer.

While the anionic charge compensation parameter does not exceed 0.8, the charge compensation parameter for the cations at the cathode becomes 1.0 at $-16.0\,\mu\mathrm{C/cm^2}$ and 2.0 at $-32.0\,\mu\mathrm{C/cm^2}$. We will see below that these integer points are of special interest and will be called *transition points*.

9.3.2 The number density profile evolution near the transition point

In Fig. 9.1 we present the number density profile for anions at the cathode between $\kappa = 0.75$ ($\sigma = -12.0\,\mu\mathrm{C/cm^2}$) and $\kappa = 1.12$ ($\sigma = -18.0\,\mu\mathrm{C/cm^2}$). The profiles show a clear transition: (A) the first peak decreases in size; (B) the first peak vanishes while the profile shifts to larger z values becoming flat; (C) the first peak arise again at a position shifted by approximately 0.85 nm compared to the density profile at $\kappa = 0.75$.

The right part of Fig. 9.1 shows number density profiles for cations and anions at the cathode for the surface charge density of $\sigma = -20.0\,\mu\mathrm{C/cm^2}$ equal to a compensation parameter $\kappa = 1.25$. As it is indicated in the figure, the solution side of the EDL consists of alternating cation and anion layers, that build up further from the rigid counter-ion monolayer.

In conclusion from Fig. 9.1 we can state, that at $\kappa = 1.0$ ($\sigma = -16.0\,\mu\mathrm{C/cm^2}$) the interfacial layer close to the electrode is filled by the counter-ions to its maximum packing capacity. At the same point the cations and anions in the remaining volume behave similar to the liquid phase in the middle of the simulation box without further layering.

The weak alternating layering at the transition point might be considered similar to the point of vanishing potential drop at very low positive surface charge densities. Therefore we compare the number density profiles as they change while charging from $\sigma = 0.00\,\mu\mathrm{C/cm^2}$ to $-8.0\,\mu\mathrm{C/cm^2}$ ($\kappa = 0.0$ to 0.5) and from $\sigma = -16.0\,\mu\mathrm{C/cm^2}$ – the transition point – to $-24.0\,\mu\mathrm{C/cm^2}$ ($\kappa = 1.0$ to 1.5). The result is shown in Fig. 9.2. Similar for both charging processes, we observe: the peak height of the first peak increases from $0.45\,\mathrm{nm^{-3}}$ to $0.9\,\mathrm{nm^{-3}}$; the overall structure of the profile gets sharper, the peaks become better distinguishable. On

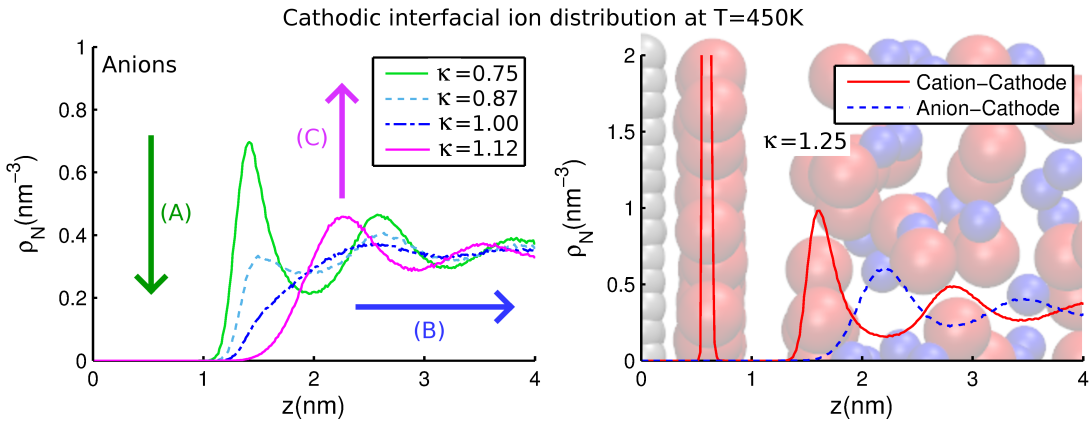

Figure 9.1: (LEFT) Number density profile for the anions at the cathode at $T = 450\,\mathrm{K}$. Four different local compensation parameter κ are shown: $\kappa = 0.75$, 0.87, 1.00 and 1.12 (equal to $\sigma = -12.0\,\mu\mathrm{C/cm^2}$, $-14.0\,\mu\mathrm{C/cm^2}$, $-16.0\,\mu\mathrm{C/cm^2}$ and $-18.0\,\mu\mathrm{C/cm^2}$). The profiles show a clear transition: (A) the first peak decreases in size; (B) the first peak vanishes completely, the profile shifts to larger z values, the profile becomes flat; (C) the first peak builds up again but is shifted by approx. 0.85 nm compared to the density profile at $\kappa = 0.75$. (RIGHT) Number density profile for cations and anions at the cathode at the local compensation parameter of $\kappa = 1.25$ ($\sigma = -20.0\,\mu\mathrm{C/cm^2}$) and the temperature $T = 450\,\mathrm{K}$. The red solid curve represents the cation-cathode profile with two subsequent peaks. Between those two peaks no anion-cathode profile peak (blue dashed curve) shows up, clearly indicating the formation of two cationic layers close to the electrode – both filled purely with cations – followed *afterwards* by a third layer filled with anions. The number density profile is underlaid with a simulation snapshot showing electrode atoms as gray, cations as red and anions as blue balls.

comparing the position of the first peaks at $-8.0\,\mu\mathrm{C/cm^2}$ and $-24.0\,\mu\mathrm{C/cm^2}$ a shift of approx. 0.85 nm becomes apparent. The shifting peak position or layer position can be explained through the size of the cations, that fill the space between electrode and the ionic liquid.

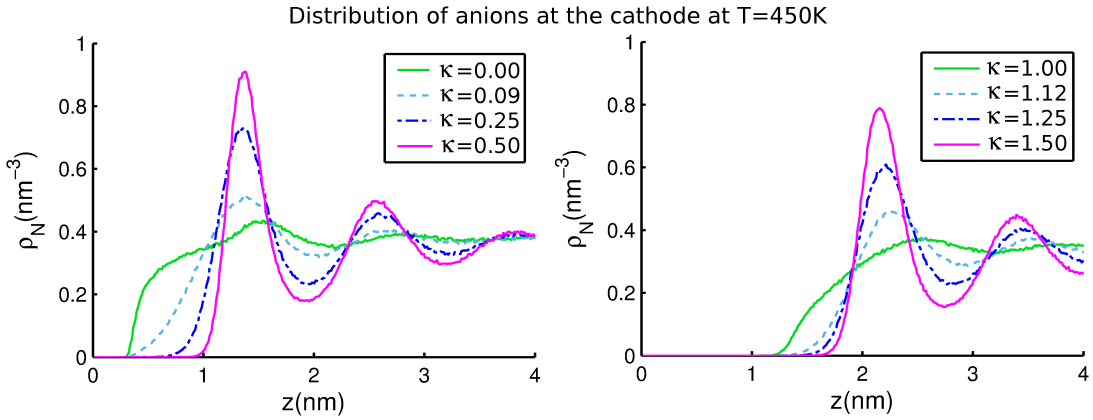

Figure 9.2: (LEFT) Number density profile for the anions at the cathode at $T = 450\,\mathrm{K}$ and four different surface charge compensation parameters κ between 0.0 and 0.5 ($\sigma = 0.00\,\mu\mathrm{C/cm^2}$, $-1.5\,\mu\mathrm{C/cm^2}$, $-4.0\,\mu\mathrm{C/cm^2}$ and $-8.0\,\mu\mathrm{C/cm^2}$). The peak height of the first peak increases from $0.45\,\mathrm{nm^{-3}}$ to $0.9\,\mathrm{nm^{-3}}$. The overall structure of the profile gets sharper, the peaks become better distinguishable. (RIGHT) Number density profile for the anions at the cathode at $T = 450\,\mathrm{K}$ and four different surface charge compensation parameters κ between 1.0 and 1.5 ($\sigma = -16.0\,\mu\mathrm{C/cm^2}$, $-18.0\,\mu\mathrm{C/cm^2}$, $-20.0\,\mu\mathrm{C/cm^2}$ and $-24.0\,\mu\mathrm{C/cm^2}$). The peak height of the first peak increases similar to the profile evolution shown in the (LEFT) figure. Compared to the (LEFT) figure, the peaks are shifted by approx. $0.85\,\mathrm{nm}$.

The number density profiles are characterized by their specific maxima (peaks) and minima (valleys). To quantify the number density profile evolution over κ, we estimated the following properties of the profiles for all surface charge densities under study:

- *Full width at half maximum* ($\mathrm{FWHM}^{1.\mathrm{max}}$, Fig. 9.3-TOP): The width of the first peak of the number density profile is estimated at the position on the half peak height. This quantity can be understood as the width of the ionic layer. An increase with temperature indicates a widening of the EDL with increasing temperature.

- *Position of the first minimum* ($z^{1.\mathrm{min}}$, Fig. 9.3-MIDDLE): The position of the first minimum of the number density profiles is measured. Our previous results indicate a sharp step in the evolution of this quantity over κ as the position of the co-ionic layer is shifted by the counter-ion layer.

- *Height of the first minimum* ($\rho^{1.\mathrm{min}}$, Fig. 9.3-BOTTOM): The height of the first minimum of the number density profiles is measured. The lower the height of the first minimum, the less diffuse is the ion layer.

The resulting peak evolution over surface charge density for anions at the cathode is shown in Fig. 9.3. On analysing the evolution of the position of the first valley, a second transition point at $\kappa = 2.38$ ($\sigma = -38.0\,\mu\mathrm{C/cm^2}$) becomes visible. We notice, that the position is shifted from the expected 2.0 to 2.38 due to the compression of the ordered layer under the hight electrostatic field from the electrode (the ions are modelled as *soft* charged Lennard–Jones spheres).

The valley position is nearly constant at $z^{1.\mathrm{min}} = 2.0\,\mathrm{nm}$ at low κ values (Fig. 9.3-TOP). At the transition points $\kappa = 1.0$ and $\kappa = 2.38$, the valley position shifts first by approximately 1.25 nm. Initially, the whole co-ion layer is shifted by more than the diameter of a counter-ion. However, at higher surface charge density, the ion layers are squeezed in z-direction as indicated by the decreased distance $z^{1.\mathrm{min}} = 2.75\,\mathrm{nm}$ of the ion layer from the electrode surface.

The height of the minimum $\rho^{1.\mathrm{min}}$ decreases first upon electrode charging indicating a less diffuse appearance of the ion layer as expected for higher surface charge density (Fig. 9.3-MIDDLE). Before reaching the transition points, the height of the minima increases. At the transition point the cycle of decreasing and increasing starts over again.

At the neutral interface and at the transition points $\kappa = 1.0$ and $\kappa = 2.38$, the first maximum (peak) of the number density profile is flat and wide. Thus the full

width at half maximum of the first peak has a large value. With increased surface charge density the peak is narrowing accounting for definite layering within the solution part of the EDL – the full width at half maximum of the first peak decreases. This structural evolution of the number density profile is shown in Fig. 9.3-BOTTOM. The shapes of the FWHM-curve in the interval between the transition points look similar, thereby reflecting the similarity of the structural transition at both transition points.

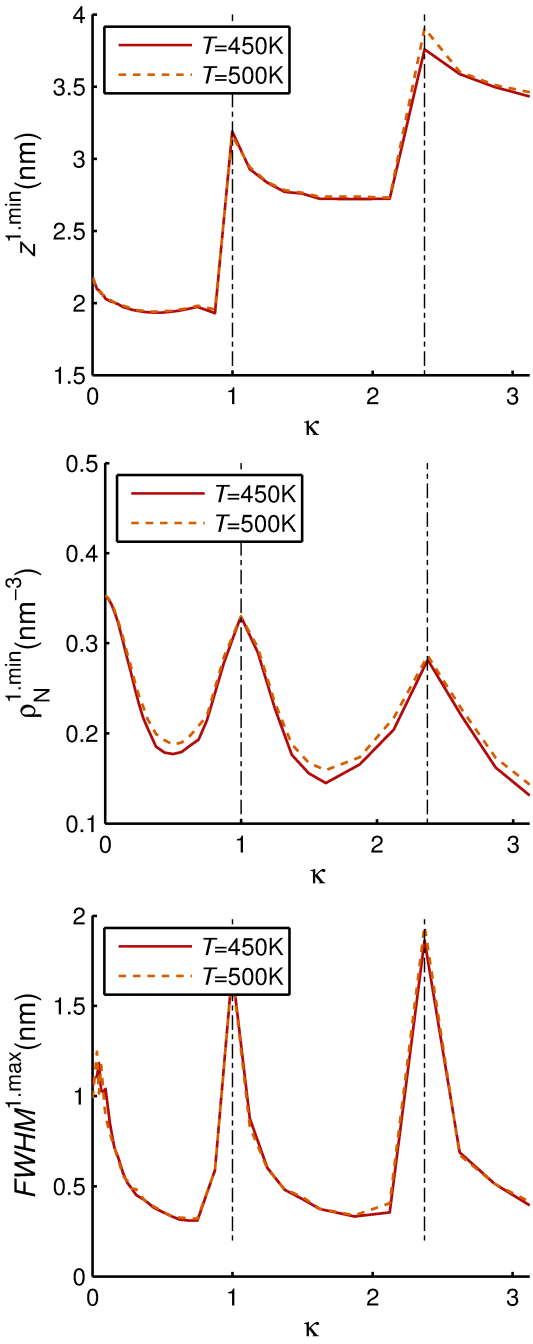

Figure 9.3: Evolution of the first peak of the number density profile of anions at the cathode. The peak is defined by the position and height of the global maximum of the number density profile (see 9.1). As z is increased, a minimum follows the global maximum in the number density profile. This local minimum is called *valley*. (TOP) Position of the first valley. (MIDDLE) Height of the first valley. (BOTTOM) Full width at half maximum (FWHM) of the first peak of the profile.

9.3.3 Charge waves vanish at the transition point

To analyse the solvent response on electrode charging we discuss charge density profiles $\rho_Q(z)$ and the connected cumulative charge $cn_Q(z) = \int_0^z \rho_N(z')\mathrm{d}z'$. Charge density profiles are obtained by summing up all number density profiles multiplied by the charge q_{ion} of the ionic specie

$$\rho_Q(z) = \rho_N^{\text{Cation}}(z) \cdot q_N^{\text{Cation}} + \rho_N^{\text{Anion}}(z) \cdot q_N^{\text{Anion}}.$$

Against physical intuition, it can be observed, that the excess counter-ions at the electrode surface over-compensates the electrode charge, as is seen in Fig. 9.4 for low surface charges.

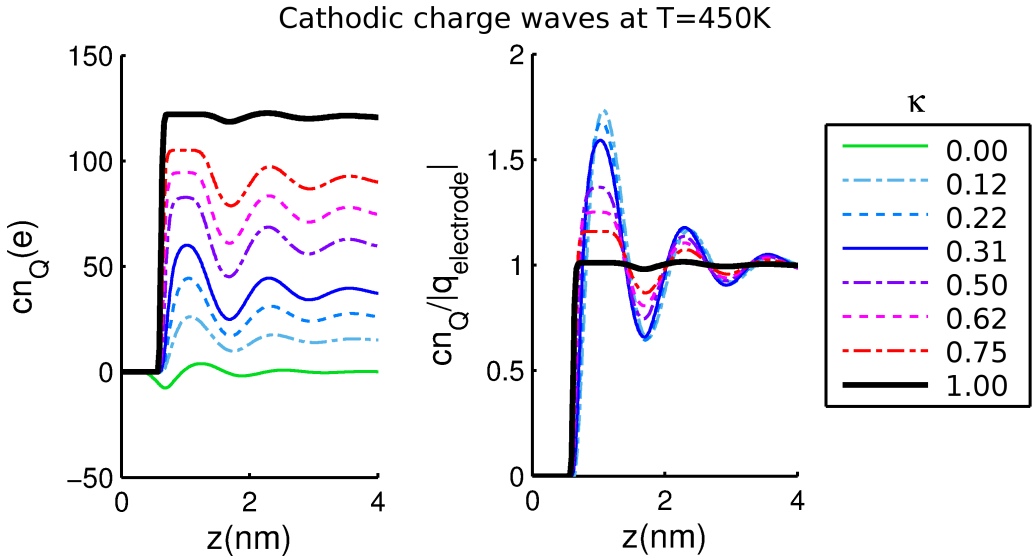

Figure 9.4: Cumulative charge $cn_Q(z) = \int_0^z \rho_N(z')\mathrm{d}z'$ at the Cathode for different surface charges at $T = 450\,\mathrm{K}$. The centre of mass of the electrode atoms are situated on the xy-plane with $z = 0$. (LEFT) Cumulative charge for different surface charges, (RIGHT) Cumulative charge normalized by the number of elementary charges on the electrode. The charge normalization is identical to the concept of dividing the local charge density in the solution side of the electric double layer by the absolute surface charge density of the electrode.

As can be seen from the figure (Fig. 9.4-LEFT) the cumulative charge shows reveals significant oscillations between $0 < \kappa < 1.0$, which correspond to multilayer structure.

The normalized charge density profiles for the cathode are shown in Fig. 9.4-RIGHT. At lower charge densities ($\kappa < 1.0$) the profiles oscillate due to to so-called overscreening effect [79, 80, 8]. These oscillations manifest that the number of counter-ions in the first interfacial layer overcompensates the surface

charge at the electrode. However, at $\kappa = 1.0$ the normalized cumulative charge density profile becomes a step-wise curve with a flat plateau. At this value of κ the $\rho_Q(z)/q_{\text{electrode}} = 1.0$ that shows complete compensation of the electrode charge by the first monolayer of the counter-ions. The absence of the charge waves indicates a non-ordered liquid phase coexist close to the first interfacial monolayer.

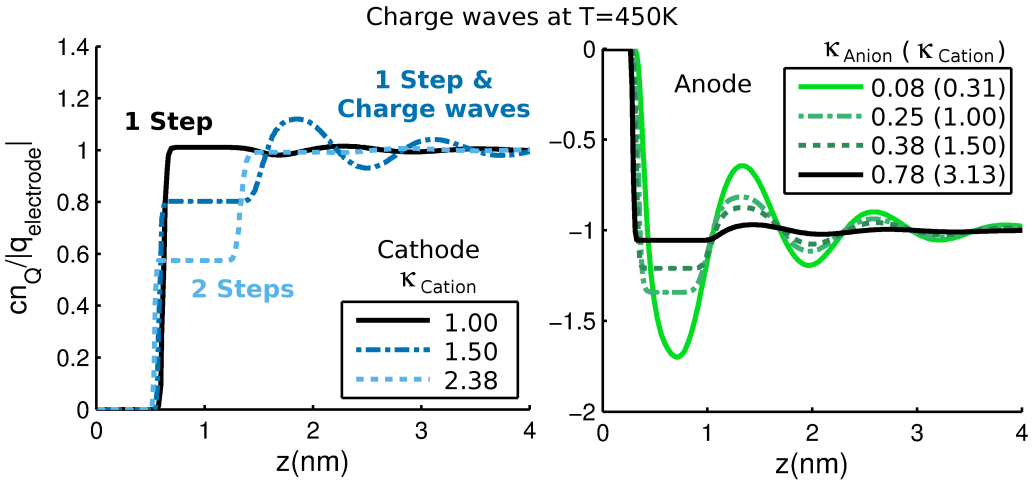

Figure 9.5: Cumulative charge $cn_Q(z) = \int_0^z \rho_N(z')\mathrm{d}z'$ normalised by the number of elementary charges on the electrode for different surface charges at $T = 450\,\mathrm{K}$. (LEFT) Cathodic cumulative charge for local compensation parameter $\kappa_{\text{Cation}} \geq 1.00$, (RIGHT) Anodic cumulative charge for local compensation parameter $\kappa_{\text{Anion}} \leq 0.78$.

Upon increasing the surface charge density and thus reaching local compensation parameters $\kappa > 1.00$, charge waves are formed again. On top of a cationic monolayer, alternating cation and anion layers form. At $\kappa = 2.38$ we observe a second structural transition with a two-step cumulative charge density profile, see Fig. 9.5-LEFT. As presented in Fig. 9.5-RIGHT, the cumulative charge density profile of the Anode shows a similar flattening upon increasing.

9.3.4 2D ion structuring at the transition point: Formation of hexatic layers and herring-bone structures

Snapshots of the counter-ion structure at different surface charges are shown in Fig. 9.6 ($-10.0\,\mu C/cm^2$, $-14.0\,\mu C/cm^2$ and $-18.0\,\mu C/cm^2$ ($\kappa = 0.62$ to 1.12)) and Fig. 9.7 ($-38.0\,\mu C/cm^2$, $\kappa = 2.37$). The transition from a layered solution-side-EDL to a co-existence of counter-ion layer and liquid IL becomes clearly understandable as the formation of a nearest-neighbour-bond-orientational-ordered fluid phase close to the electrode, also called hexatic phase or Moiré-like structure. From theoretical investigation and simulations it is known, that the hexatic phase is an intermediate structure within the transition between solids and liquids if a surface is apparent in the solution [226].

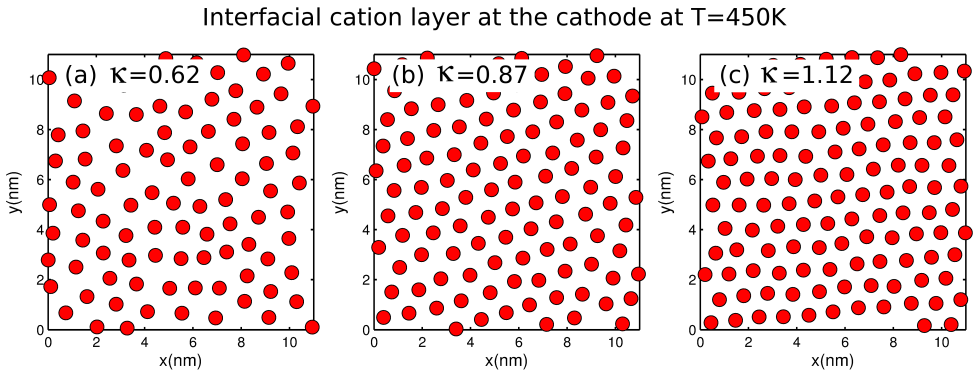

Figure 9.6: Snapshots of the interfacial cation layer at the cathode at 450 K for three different surface charge compensation parameters (a) $\kappa = 0.62$, (b) $\kappa = 0.87$ and (c) $\kappa = 1.12$, showing the transition from a multilayered EDL to a hexatic monolayer.

We note, that the temperature effect on the structuring is overall very week, but increases in the region of the transition point.

Figure 9.8 shows number density profiles for electrode-co-ions at different surface charge densities. For the cathodic part, we show the profiles that are approaching towards the point of structural transition. Apparently, the same decrease of the peak height that appears at the cathode upon scanning different surface charge densities, is visible for cations at the anode if the highest surface charges under study are visualized. Also the interfacial structure of cations at the cathode near the transition point and of anions at the anode at the highest surface charge under study, are similar on slightly different length scales.

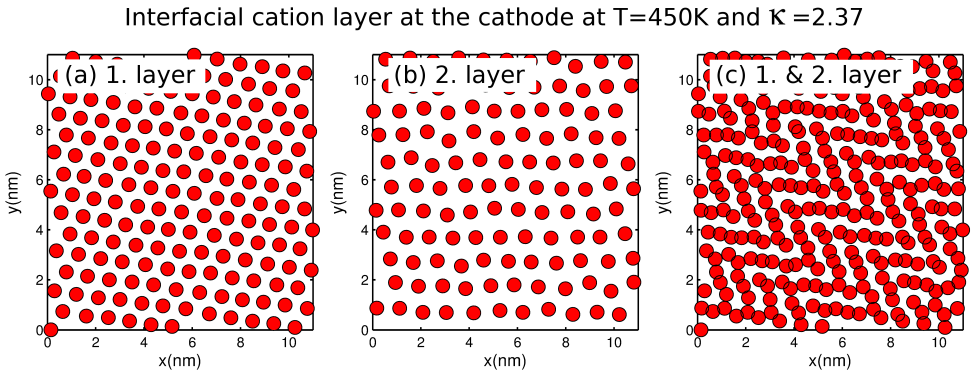

Figure 9.7: Snapshots of the first two interfacial cation layers at the cathode at 450 K at a local compensation parameter of $\kappa = 2.37$ showing the point of structural transition to a hexatic structure within the second interfacial layer and thereby the construction of a herring bone structure. (LEFT) First interfacial layer, (MIDDLE) second interfacial layer and (RIGHT) first and second interfacial layer merged.

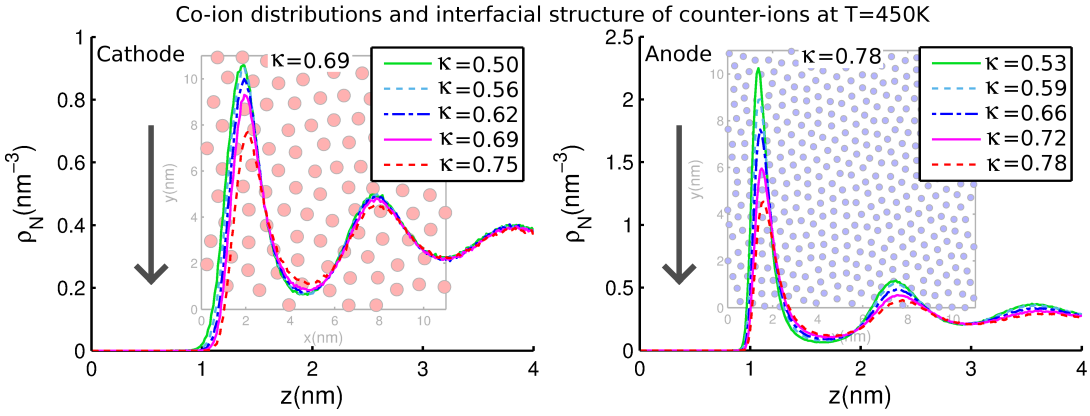

Figure 9.8: Number density profiles for electrode-co-ion at 450 K. (LEFT) Anion-cathode profile. The peak height decreases while increasing the surface charge short before the transition point is reached. (RIGHT) Cation-anode profile. Considering the highest surface charges studied in this work, a decrease of the peak height is visible for the anions at the cathode near the transition point similar to the cathodic behaviour. (INSETS) Snapshots for the interfacial layers of counter-ions are shown, indicating similar structures for both cations at the cathode short before the transition point and anions at the anode. The length scales differs due to the asymmetry in size of both ion species.

9.3.5 An effect of general nature: Structural transition under parameter variation

A plausible expansion of the system presented in this work would be the size symmetric system with $d^{\text{Cation}}/d^{\text{Anions}} = 1.0$. A visualisation of the structural transition in the symmetric system is presented in Fig. 9.9 and 9.10. We have chosen a simulation setup with 590 ion pairs with $d^{\text{Cation}} = d^{\text{Anions}} = 1.0\,\text{nm}$ confined between the electrodes with a distance of 24 nm. Moreover, the anode is modelled to be sterically thicker than the cathode. The structural transition from a multilayered EDL to a hexatic ordered monolayer is identical compared with the asymmetric system, including the same compensation parameter $\kappa = 1$. At increased surface charge density, the herring-bone structure as superposition of two hexatic monolayers is visible. The results to not depend on the electrode thickness.

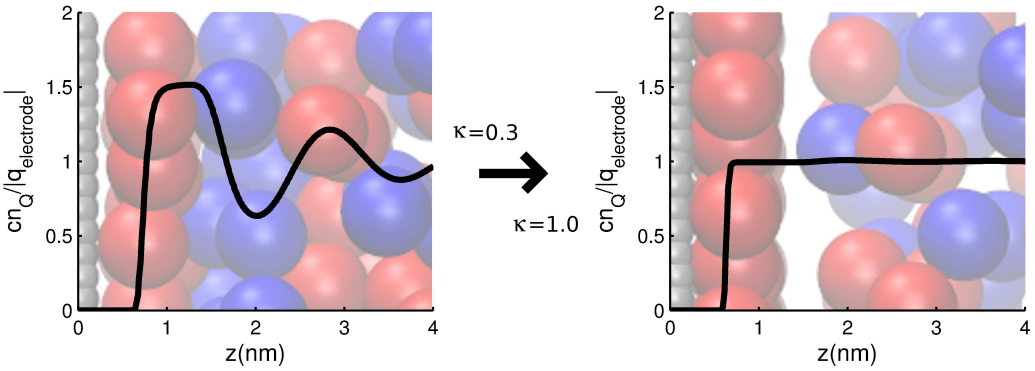

Figure 9.9: Cumulative charge $cn_Q(z) = \int_0^z \rho_N(z')\mathrm{d}z'$ normalized by the number of elementary charges on the electrode $q_{\text{electrode}}$. (LEFT) At lower charge densities ($\kappa < 1.0$) the profile oscillates due to the so-called overscreening effect [79, 80, 8]. These oscillations manifest that the number of counter-ions in the first interfacial layer overcompensates the surface charge at the electrode. (RIGHT) At $\kappa = 1.0$ the normalized cumulative charge density profile becomes a step-wise curve with a flat plateau, that shows complete compensation of the electrode charge by the first monolayer of the counter-ions. The absence of the charge waves indicates a non-ordered liquid phase coexist close to the first interfacial monolayer.

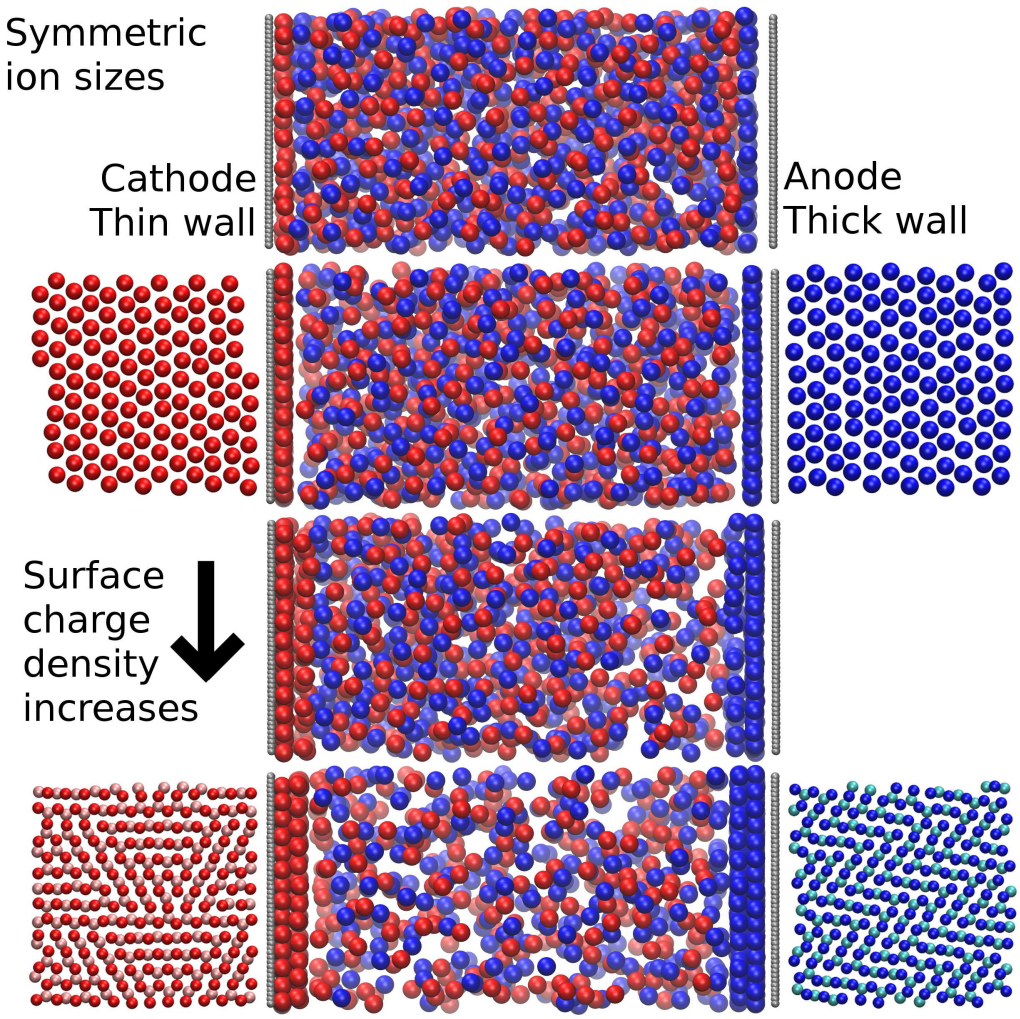

Figure 9.10: Snapshots of the simulated size symmetric system with thin cathode and thick anode. From top to bottom four different surface charge densities are presented: $\sigma = 5.00\,\mu\mathrm{C/cm^2}$, $\sigma = 16.00\,\mu\mathrm{C/cm^2}$,$\sigma = 24.00\,\mu\mathrm{C/cm^2}$ and $\sigma = 42.00\,\mu\mathrm{C/cm^2}$. Thereby $\sigma = 16.00\,\mu\mathrm{C/cm^2}$ corresponds to the compensation parameter $\kappa = 1.0$. Independent from the electrode thickness, the structural transition to a hexatic ordered monolayer is apparent. At the highest surface charge density under study, the first and second interfacial layer form a herringbone structure.

9.4 Conclusion: A hexatic ordered monolayer compensates the electrode charge and separates electrode and non-structured ionic liquid

Within this chapter we have been able to draw the following conclusions:

1. For the most studied charge densities the EDL has a multilayered structure with multiple alternating layers of the electrode counter-ions and co-ions at the electrode interface. At certain charge densities the alternating multilayer structure of the EDL undergoes a structural transition to an ordered hexatic monolayer of densely packed electrode counter-ions. At this point the dense ordered monolayer of counter-ions close to the electrode surface coexists with apparently non-structured ionic liquid further in the z-direction from the electrode.

2. The points of the structural transitions are largely determined by the balance between the surface/counter-ion attraction and the ion-ion steric repulsion. The multilayer to monolayer transition effect is directly correlated with the surface charge density, counter-ion diameter and counter-ion charge; thereby indicating:

    a. Total charge compensation of the electrode charge by the interfacial monolayer of counter-ions at the transition point, i.e. over-screening and alternating layers are almost absent;

    b. Geometric ordering of interfacial counter-ions in a form of a dense hexatic structure (so-called Moiré-like structure).

By comparing our results with recently published experimental and theoretical results on the interfacial structuring of ILs, electrode reconstruction and two-dimensional phase transitions at interfaces, we found:

1. The presented results are in general agreement with the findings of Freyland and co-workers [38, 21] who reported an ordered structure of PF_6^- anions adsorbed on an electrode surface to coexist with uncompressed structures.

2. The observed herring-bone structures at high surface charge densities, that form as a superposition of two hexatic monolayers, are similar to the structures visualized via STM at the interface between gold electrode and RTILs [39, 31].

We note that the effect of vanishing charge waves and formation of a hexatic monolayer is found to be of general nature, as it can be reproduced in simulations with a size symmetric ion model. Moreover it seems to be independent from the electrode structure as a variation of the electrode thickness does not influence the structural transition.

Chapter 10

Conclusions and further work

Provoked by the recent wave of interest in room temperature ionic liquids and a wide number of open questions concerning their physical behaviour, we simulated a simple Coulombic fluid composed of asymmetric sized repulsive Lennard-Jones spheres. Most important, we aimed to understand the electric double layer structure of the ionic liquid under the influence of temperature changes. By performing extensive molecular dynamics simulations of the ionic liquid confined between oppositely charged electrodes, we (i) identified the differential capacitance as a structural response function influenced by a temperature induced melting and (ii) revealed a hexatic ordered ion layer that compensates the electrode charge under certain conditions. The results will be summarized in this chapter followed by a list of possible extensions of the work.

10.1 Conclusions

(A) Our model reproduces main mechanisms of the general behaviour of ionic liquids at electrified interfaces. In the beginning of this work we described the model ionic liquid and system setup. To clarify possible drawbacks of the chosen simulation parameter, we reviewed the ionic force field and analysed the influence of the system geometry. We note, that the hardware, software and algorithms used for performing simulations and analysis represent a state-of-the-art collection in computational science.

We want to study the origin of experimentally reported effects of ionic liquids at electrified interfaces on a fundamental level by only including steric effects and Coulombic interaction in our model. These constraints lead to the choice of an extremely simplified force field model for the ionic liquid and electrodes.

As we are interested in the qualitative comparison of simulation results with real experiments made with room temperature ionic liquids, we have chosen ion sizes that are comparable to the size of real room temperature ionic liquids [90]. We integrated polarization effects by charge scaling, comparable with the introduction of an effective dielectric constant [169]. The method is considered as "the poor man's way" of introducing polarisability [168], however Fedorov and Kornyshev [7] used the model successfully. We have to keep in mind, that our model is coarse-grained similar to [120, 121]. We do not include quantum effects and charge transfer, neither for the ionic liquid nor for the electrodes in contrast to [245, 36, 170, 171]. Moreover, the electrode atoms are purely repulsive [180]. Reviewing literature on similar models [178, 179], namely the restricted primitive model with asymmetric sized ions, we considered the possibility of a phase coexistence of liquid and vapour phase.

We assured that the box dimensions in all directions do not lead to non-physical interactions [232]. The choice of the temperature coupling slightly influences the results for very low surface charge densities and the neutral interface, but does not affect the qualitative results nor physical interpretation.

Naturally, any chosen model contains drawbacks that should be discussed and possibly eliminated in upcoming studies. However, we are confident, that the structural analysis of the ion distribution at the electrode surfaces is physically meaningful.

(B) The temperature effect on the differential capacitance depends on the voltage. Our simulation results provide insight in the differential capacitance evolution with temperature from a molecular level. Thereby we find that the temperature effect of the differential capacitance depends on the voltage. The differential capacitance ...

- ... decreases with the increase of temperature at small voltages, ...
- ... increase with the increase of temperature at intermediate voltages, ...
- ... does not depend on the temperature at large voltages.

We reviewed published results on the temperature dependence of the differential capacitance in room temperature ionic liquids. Despite the large interest in the topic, yet no satisfactory conclusion has been found. Recently it has been suggested by Drüschler et al [31], that single-frequency measurements of the differential capacitance under various temperatures are artificial as they do not pay attention to temperature-dependent relaxation processes.

We found the reason for the varying temperature dependency in a temperature induced melting of the electric double layer.

(C) The differential capacitance is a structural response function influenced by a temperature induced melting. Upon studying number density profiles and the related cumulative numbers of ions over distance from the electrode surface, we found a "melting process" to take place as the temperature of the system is increased. At low temperatures a stiff electric double layer structure is formed. Due to temperature fluctuations and the associated depletion of ion concentration in the interfacial layers at the electrodes the double layer structure is changed - a process we call "melting".

The shape and temperature dependence of the differential capacitance can be directly associated with the structural response of the ions in the first two interfacial layers at the electrode. The differential response shows at low temperatures a steep incline to be continued by a sharp decrease. In contrast the differential response at high temperatures appears as a flattened curve with steady increase and decrease. The overall response of the ions is continuous at high temperatures, and abrupt at low temperatures. The strong ion response at low surface charge density and the weak or negligible response at higher surface charge densities causes the sharp increase and decrease of the differential capacitance.

The difference in the *structural ion response* at different temperatures induced by *melting* causes the voltage dependent increase or decrease of the differential capacitance with temperature.

(D) Ion/counter-ion interactions are an important element for the electric double layer structuring. Basic features of the electric double layer of ionic liquids are alternating layering of counter-ions and co-ions and overcompensation of the electrode charge. We observe a layering of ions even at the neutral electrode driven by entropic effects and Coulombic attraction between ions similar to [234, 235, 236, 237], but also the classical alternating layering at charged surfaces [6, 7, 8, 9, 10, 11]. Charge waves are caused by the alternating layering of ions, showing that the electrode charge is over-compensated.

The importance and strength of ion/counter-ion interactions becomes apparent by the observation of a co-ionic enrichment at the anode. Caused by Coulombic ion/counter-ion attraction, an excess of co-ions near electrode takes place although the electrode is highly charged.

Under certain conditions, an ion structure close to the electrode surface results in an elimination of charge waves. This observation is explained by a hexatic ordered ion layer.

(E) A multilayered structure undergoes a structural transition to a hexatic ordered monolayer. The electric double layer at the electrode interface contains multiple alternating layers of counter-ions and co-ions. At transition points, we found the formation of a hexatic ordered layer (also called Moiré-structure) of counter-ions close to the electrode surface. The point of structural transition is directly correlated with the ratio between applied surface charge, counter-ion diameter and counter-ion charge. Thereby a total charge compensation by the ionic monolayer takes place resulting in the absence of alternating layers in the subsequent ionic liquid.

The results are in agreement with findings of Freyland and co-workers [38, 21], reporting a structure of PF_6 anions adsorbed on an electrode surface. Moreover, we found the formation of herring-bone structures at higher surface charge densities, that form as the superposition of two hexatic layers. Similar structures have been observed upon surface reconstruction of a charged gold electrode within RTILs [39, 31].

10.2 Further work

We answered a number of questions in the given work, however, there can be no stagnation of ideas in science.

Open questions provoked by the presented results are: How does the observed structural transition depends on ion asymmetry $\sigma^{+}_{LJ}/\sigma^{-}_{LJ} = d^{\text{Cation}}/d^{\text{Anions}}$? Does the electrode structure and possible defects affect the structural transition? How does the ion molecular structure and molecular charge density distribution affect the structural transition?

Further possibilities to develop the project are presented below.

Application of temperature replica exchange MD and metadynamics for enhanced sampling of the phase space. A crucial question for a wide range of applications of interfacial chemistry of ionic liquids is the influence of impurities on the electric double layer structure. Room temperature ionic liquids are known to contain water and alkali halides, that might have a considerable influence on the interfacial structuring. However, the amount of impurities is considered to be small, which makes modelling of impure ionic liquids comparable to "real" ionic liquids challenging. Especially when the three-dimensional volume of interest is reduced to two-dimensional structures, the inclusion of impurities becomes modelling of rare events.

Advanced sampling methods like temperature replica exchange MD and metadynamics are useful to sample the phase space of systems that have a frustrated energy landscape. Ionic liquids at electrified interfaces do have a frustrated energy landscape with different ion conformations. Therefore the usage of advanced sampling techniques is expected to be beneficial.

As ion conformations depend on the systems temperature T and surface charge density σ, we consider the temperature replica exchange or Hamiltonian replica exchange as one possibility to enhance the sampling. For the temperature variation a number of tools has been developed already, however finding a reasonable temperature range, that allows good exchange acceptance ratios and exchange rates is not yet explored for any liquid/solid-interfacial system, nor ionic liquids in general. Charge-replica exchange will need considerable programming and testing/benchmarking effort, as it is not implemented yet in any general software.

The characterization of the structure and structural changes over the whole free energy surface could also be done using metadynamics. However the important collective variable to describe the conformational changes need still to be developed. We suggest the ion number in the interfacial layer (in two interfa-

cial layers in case of herring bone), the ion distance and the bond angular order parameter [226] as collective variables.

The electric double layer and differential capacitance under thermal expansion of the ionic liquid. State-of-the-art devices for experimental measuring of the differential capacitance are open container filled with the dielectric / ionic liquid and electrodes pushed manually inside. Thus the ionic liquid is not confined to a specific volume, but allowed to expand or to shrink upon temperature variation. We performed additional molecular dynamics simulations of ions at interfaces similar to the systems discussed in this work but under thermal expansion: The volume between the electrodes is adjusted to allow thermal expansion of the ionic liquid. Preliminary results suggest that the differential capacitance increases slightly if the ionic liquid is allowed to expand while heated.

The influence of electrode properties on the electric double layer structure and differential capacitance We measured the differential capacitance for two setups that appeared equal on the first glance but have a very small difference: the electrode atoms appear sterically thicker for the ions in the second system. The change in differential capacitance is drastic, the maximum is decreased by 70 % from 13 μF/cm^2 to 4 μF/cm^2. Moreover the curves show no (or very few) temperature dependence in the thick wall system. To expand the analysis we can use or easily extend simulations with further changes of the wall properties: square lattice to hexagonal lattice, repulsive wall atom potential to attractive wall atom potential.

The observation of Nano-bubbles and Nano-pancakes Ten years ago there have been cavities reported in ionic liquids modelled by the restricted primitive model (RPM) [261]. The phenomena of small cavities or voids in ionic liquids has attracted new interest recently due to some experimental results indicating that the void formation is not only connected with theoretical models but does occur in real ionic liquids. Vincent Craig reported in 2010: Very small bubbles at surfaces - the nanobubble puzzle [262]. Currently Seddon, Lohse, Ducker and Craig published a mini review on the classification of voids [263]. Void structures in bulk ionic liquids and near interfaces are called in their work 'bulk nanobubbles', 'surface nanobubbles' and 'micropancakes'.

We have to report that all of these structures are apparent at different surface charges in the system under study, see Fig. 10.1. An explanation for the occurrence of cavities in the ionic liquid could be found in the phase diagram: as we

suggested earlier, it might be possible that the liquid under study is close to the co-existence line - thereby being either in the liquid state or in a liquid/vapour co-existence depending on the actual temperature and density.

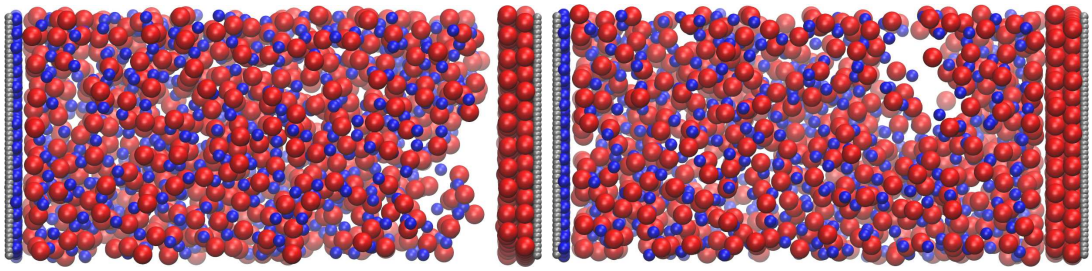

Figure 10.1: Simulation snapshots of void structures in bulk ionic liquid and near interfaces as observed at 300 K and 38-42 μC/cm^2. (LEFT) A flat void structure on the surface separating the electrode and two cation layers from the bulk liquid reminds on a 'nano-pancake' [263]; (RIGHT) a void in the middle of the simulation box is called 'nano-bubble' [263].

A straight forward way of measuring the size, position and life time of the voids would be the overlaying of a three dimensional grid over the whole simulation box and counting of empty grid-boxes in every frame. However, the technical implementation seems elaborate. For estimating the void size we might refer to algorithms applied in the Ising model [264] for counting cluster sizes.

Final words

The current work provides new insights into the structuring of ionic liquids at electrified interfaces. Still, we are far from understanding every phenomena, we can observe. Fundamental research on ionic liquids is an obligatory requirement for applications of this lucrative material class.

Bibliography

[1] Y. Levin. Electrostatic correlations: from plasma to biology. *Reports on Progress in Physics*, 65(11):1577–1632, November 2002.

[2] W. Freyland. *Coulombic fluids: bulk and interfaces*. Springer series in solid-state sciences; 168. Springer, Berlin, Heidelberg, 2011.

[3] T. Scopigno, G. Ruocco, and F. Sette. Microscopic dynamics in liquid metals: The experimental point of view. *Reviews of Modern Physics*, 77(3):881–933, July 2005.

[4] M. S. Loth, B. Skinner, and B. I. Shklovskii. Non-mean-field theory of anomalously large double layer capacitance. *Physical Review E*, 82(1):016107, July 2010.

[5] S. H. L. Klapp, S. Grandner, Y. Zeng, and R. von Klitzing. Charged silica suspensions as model materials for liquids in confined geometries. *Soft Matter*, 6(10):2330–2336, 2010.

[6] A. A. Kornyshev, S. Leikin, and G. Sutmann. "overscreening" in a polar liquid as a result of coupling between polarization and density fluctuations. *Electrochimica Acta*, 42(5):849–865, 1997.

[7] M. V. Fedorov and A. A. Kornyshev. Ionic liquid near a charged wall: Structure and capacitance of electrical double layer. *Journal of Physical Chemistry B*, 112(38):11868–11872, 2008.

[8] M. Z. Bazant, B. D. Storey, and A. A. Kornyshev. Double Layer in Ionic Liquids: Overscreening versus Crowding. *Physical Review Letters*, 106(4):046102, Jan 2011.

[9] G. A. Feng, R. Qiao, J. S. Huang, S. Dai, B. G. Sumpter, and V. Meunier. The importance of ion size and electrode curvature on electrical double layers in ionic liquids. *Physical Chemistry Chemical Physics*, 13(3):1152–1161, 2011.

[10] V. Demery, D. S. Dean, T. C. Hammant, R. R. Horgan, and R. Podgornik. Overscreening in a 1D lattice Coulomb gas model of ionic liquids. *Europhysics Letters*, 97(2):28004, January 2012.

[11] H. Zhou, M. Rouha, G. Feng, S. S. Lee, H. Docherty, P. Fenter, P. T. Cummings, P. F. Fulvio, S. Dai, J. McDonough, V. Presser, and Y. Gogotsi. Nanoscale Perturbations of Room Temperature Ionic Liquid Structure at Charged and Uncharged Interfaces. *ACS Nano*, 6(11):9818–9827, 2012.

[12] J. P. Hansen and I. R. McDonald. Statistical Mechanics Of Dense Ionized Matter. 4. Density And Charge Fluctuations In A Simple Molten-Salt. *Physical Review A*, 11(6):2111–2123, 1975.

[13] J.-P. Hansen and I. R. McDonald. *Theory of Simple Liquids, 3rd ed.* Academic Press, London, 1991.

[14] M. N. Tamashiro, Y. Levin, and M. C. Barbosa. The one-component plasma: a conceptual approach. *Physica A*, 268(1-2):24–49, June 1999.

[15] T. E. Angelini, H. Liang, W. Wriggers, and G. C. L. Wong. Like-charge attraction between polyelectrolytes induced by counterion charge density waves. *Proceedings of the National Academy of Sciences of the United States of America*, 100(15):8634–8637, July 2003.

[16] S. Perkin. Ionic liquids in confined geometries. *Physical Chemistry Chemical Physics*, 14(15):5052–5062, 2012.

[17] M. Gaune-Escard and K. R. Seddon, editors. *Molten Salts and Ionic Liquids: Never the Twain?* John Wiley and Sons, August 2009.

[18] A. Bard and L. R. Faulkner. *Electrochemical Methods. Fundamentals and Applications.* John Wiley & Sons, 2001.

[19] F. Endres. Ionic liquids: Solvents for the electrodeposition of metals and semiconductors. *Chemphyschem*, 3(2):144–154, February 2002.

[20] A. A. Kornyshev, E. Spohr, and M. A. Vorotyntsev. Electrochemical Interfaces: At the Border line. In A. Bard et al., editor, *Encyclopedia of Electrochemistry*, volume 1, pages 33–132. Wiley-VCH, New York, 2002.

[21] W. Freyland. Interfacial phase transitions in conducting fluids. *Physical Chemistry Chemical Physics*, 10(7):923–936, 2008.

[22] M. Armand, F. Endres, D. R. MacFarlane, H. Ohno, and B. Scrosati. Ionic-liquid materials for the electrochemical challenges of the future. *Nature Materials*, 8(8):621–629, August 2009.

[23] H. T. Liu, Y. Liu, and J. H. Li. Ionic liquids in surface electrochemistry. *Physical Chemistry Chemical Physics*, 12(8):1685–1697, 2010.

[24] A. D. Graves and D. Inman. The Electrical Double Layer In Molten Salts. Part 2. The Double-Layer Capacitance. *Journal of Electroanalytical Chemistry*, 25(3):357–372, 1970.

[25] W. Schmickler and D. Henderson. New Models for the Structure of the Electrochemical Interface. *Progress in Surface Science*, 22(4):323–420, 1986.

[26] J. R. Henderson and Z. A. Sabeur. Liquid-State Integral-Equations At High-Density - On The Mathematical Origin Of Infinite-Range Oscillatory Solutions. *Journal of Chemical Physics*, 97(9):6750–6758, November 1992.

[27] D. Boda, D. Henderson, K. Y. Chan, and D. T. Wasan. Low temperature anomalies in the properties of the electrochemical interface. *Chemical Physics Letters*, 308(5-6):473–478, July 1999.

[28] V. Lockett, R. Sedev, J. Ralston, M. Horne, and T. Rodopoulos. Differential Capacitance of the Electrical Double Layer in Imidazolium-Based Ionic Liquids: Influence of Potential, Cation Size, and Temperature. *Journal of Physical Chemistry C*, 112(19):7486–7495, 2008.

[29] V. Lockett, M. Horne, R. Sedev, T. Rodopoulos, and J. Ralston. Differential capacitance of the double layer at the electrode/ionic liquids interface. *Physical Chemistry Chemical Physics*, 12(39):12499–12512, 2010.

[30] M. Gnahm, C. Müller, R. Répánszki, T. Pajkossy, and D. M. Kolb. The interface between Au(100) and 1-butyl-3-methyl-imidazolium-hexafluorophosphate. *Physical Chemistry Chemical Physics*, 13(24):11627–11633, 2011.

[31] M. Drüschler, N. Borisenko, J. Wallauer, C. Winter, B. Huber, F. Endres, and B. Roling. New insights into the interface between a single-crystalline metal electrode and an extremely pure ionic liquid: slow interfacial processes and the influence of temperature on interfacial dynamics. *Physical Chemistry Chemical Physics*, 14(15):5090–5099, 2012.

[32] M. T. Alam, J. Masud, M. M. Islam, T. Okajima, and T. Ohsaka. Differential Capacitance at Au(111) in 1-Alkyl-3-methylimidazolium Tetrafluoroborate Based Room-Temperature Ionic Liquids. *Journal of Physical Chemistry C*, 115(40):19797–19804, October 2011.

[33] F. Silva, C. Gomes, M. Figueiredo, R. Costa, A. Martins, and C. M. Pereira. The electrical double layer at the [BMIM][PF6] ionic liquid/electrode interface - Effect of temperature on the differential capacitance, journal = Journal of Electroanalytical Chemistry. 622(2):153–160, October 2008.

[34] R. Costa, C. M. Pereira, and F. Silva. Double layer in room temperature ionic liquids: influence of temperature and ionic size on the differential capacitance and electrocapillary curves. *Physical Chemistry Chemical Physics*, 12(36):11125–11132, 2010.

[35] M. S. Loth, B. Skinner, and B. I. Shklovskii. Anomalously large capacitance of an ionic liquid described by the restricted primitive model. *Physical Review E*, 82(5):056102, November 2010.

[36] J. Vatamanu, O. Borodin, and G. D. Smith. Molecular Insights into the Potential and Temperature Dependences of the Differential Capacitance of a Room-Temperature Ionic Liquid at Graphite Electrodes. *Journal of the American Chemical Society*, 132(42):14825–14833, October 2010.

[37] Q. Dou, M. L. Sha, H. Y. Fu, and G. Z. Wu. Molecular dynamics simulation of the interfacial structure of [C(n)mim][PF6] adsorbed on a graphite surface: effects of temperature and alkyl chain length. *Journal of Physics-condensed Matter*, 23(17):175001, May 2011.

[38] G. B. Pan and W. Freyland. 2D phase transition of PF6 adlayers at the electrified ionic liquid/Au(111) interface. *Chemical Physics Letters*, 427(1-3):96–100, August 2006.

[39] A. A. Aal, R. Al-Salman, M. Al-Zoubi, N. Borissenko, F. Endres, O. Hofft, A. Prowald, and S. Z. El Abedin. Interfacial electrochemistry and electrodeposition from some ionic liquids: In situ scanning tunneling microscopy, plasma electrochemistry, selenium and macroporous materials. *Electrochimica Acta*, 56(28):10295–10305, December 2011.

[40] T. Waldmann, H. H. Huang, H. E. Hoster, O. Hofft, F. Endres, and R. J. Behm. Imaging an Ionic Liquid Adlayer by Scanning Tunneling Microscopy

at the Solid vertical bar Vacuum Interface. *Chemphyschem*, 12(14):2565–2567, October 2011.

[41] T. Carstens, R. Hayes, S. Z. El Abedin, B. Corr, G. B. Webber, N. Borisenko, R. Atkin, and F. Endres. In situ STM, AFM and DTS study of the interface 1-hexyl-3-methylimidazolium tris(pentafluoroethyl)trifluorophosphate/Au(111). *Electrochimica Acta*, 2012.

[42] N. Borisenko, S. Z. El Abedin, and F. Endres. An in Situ STM and DTS Study of the Extremely Pure [EMIM]FAP/Au(111) Interface. *Chemphyschem*, 13(7):1736–1742, May 2012.

[43] R. Atkin, S. Z. El Abedin, R. Hayes, L. H. S. Gasparotto, N. Borisenko, and F. Endres. AFM and STM Studies on the Surface Interaction of [BMP]TFSA and [EMIm]TFSA Ionic Liquids with Au(111). *Journal of Physical Chemistry C*, 113(30):13266–13272, July 2009.

[44] G. C. Schatz. Using theory and computation to model nanoscale properties. *Proceedings of the National Academy of Sciences of the United States of America*, 104(17):6885–6892, April 2007.

[45] S. Yan, S. J. Lee, S. Kang, and J. Y. Lee. Computational approaches in molecular recognition, self-assembly, electron transport, and surface chemistry. *Supramolecular Chemistry*, 19(4-5):229–241, 2007.

[46] M. P. Allen and D. J. Tildesley. *Computer Simulation of Liquids*. Oxford University Press; Clarendon Press, 1989.

[47] D. Frenkel and B. Smit. *Understanding molecular simulation*. Academic Press, 2002.

[48] M. J. Embrechts, B. Szymanski, and K. Sternickel. Introduction to Scientific Data Mining: Direct Kernel Methods & Applications. In S. J. Ovaska, editor, *Computationally Intelligent Hybrid Systems: The Fusion of Soft Computing and Hard Computing*. Wiley New York, 2005.

[49] D. Kumar and D. Bhardwaj. Rise of Data Mining: Current and Future Application Areas. *International Journal of Computer Science Issues*, 8(5):256–260, 2011.

[50] M. Sletholt, H. P. Langtangen, J. E. Hannay, and D. Pfahl. Making Modern Scientific Software Development Explicitly Agile. Technical report, Workshop on Changing Dynamics of Scientific Collaboration at HICSS 2011, 2011.

[51] M. T. Sletholt, J. E. Hannay, D. Pfahl, and H. P. Langtangen. What Do We Know about Scientific Software Development's Agile Practices? *Computing in Science Engineering*, 14(2):24–37, 2012.

[52] J. Pitt-Francis, M. O. Bernabeu, J. Cooper, A. Garny, L. Momtahan, J. Osborne, P. Pathmanathan, B. Rodriguez, J. P. Whiteley, and D. J. Gavaghan. Chaste: using agile programming techniques to develop computational biology software. *Philosophical Transactions of the Royal Society A-mathematical Physical and Engineering Sciences*, 366(1878):3111–3136, September 2008.

[53] J. J. Bikerman. Electrokinetic equations and surface conductance. A survey of the diffuse double layer theory of colloidal solutions. *Transactions of the Faraday Society*, 35:154–160, 1940.

[54] J. W. Halley, B. Johnson, D. Price, and M. Schwalm. Quantum-theory of the Double-layer - A Model of the Electrode-electrolyte Interface. *Physical Review B*, 31(12):7695–7709, 1985.

[55] R. Parsons. Electrical Double-Layer - Recent Experimental And Theoretical Developments. *Chemical Reviews*, 90(5):813–826, July 1990.

[56] P. Attard. Electrolytes and the Electric Double Layer. *Advances in Chemical Physics*, 92:1–159, 1996.

[57] L. M. Varela, M. Garcia, and V. Mosquera. Exact mean-field theory of ionic solutions: non-Debye screening. *Physics Reports*, 382:1–111, April 2003.

[58] D. di Caprio, Z. Borkowska, and J. Stafiej. Simple extension of the Gouy-Chapman theory including hard sphere effects. Diffuse layer contribution to the differential capacity curves for the electrode vertical bar electrolyte interface. *Journal of Electroanalytical Chemistry*, 540:17–23, January 2003.

[59] A. A. Kornyshev. Double-Layer in Ionic Liquids: Paradigm Change? *Journal of Physical Chemistry B*, 111(20):5545–5557, 2007.

[60] S. Baldelli. Surface structure at the ionic liquid-electrified metal interface. *Accounts of Chemical Research*, 41(3):421–431, March 2008.

[61] W. R. Fawcett, P. J. Ryan, and T. G. Smagala. Properties of the Diffuse Double Layer at High Electrolyte Concentrations. *Journal of Physical Chemistry B*, 113(43):14310–14314, October 2009.

[62] B. B. Damaskin and O. A. Petrii. Historical development of theories of the electrochemical double layer. *Journal of Solid State Electrochemistry*, 15(7-8):1317–1334, July 2011.

[63] A. V. Delgado, E. Gonzalez-Caballero, R. J. Hunter, L. K. Koopal, and J. Lyklema. Measurement and interpretation of electrokinetic phenomena - (IUPAC technical report). *Pure and Applied Chemistry*, 77(10):1753–1805, October 2005.

[64] K. Izutsu. *Electrochemistry in Nonaqueous Solutions*. Wiley-VCH, October 2009.

[65] W. Schmickler and E. Santos. *Interfacial Electrochemistry*. Springer, New York, 2 edition, 2010.

[66] Zoltan Nagy. Electrochemical Science and Technology Information Resource (ESTIR). http://electrochem.cwru.edu/estir/history.htm, April 2013.

[67] H. Helmholtz. Über einige Gesetze der Vertheilung elektrischer Ströme in körperlichen Leitern, mit Anwendung auf die thierischen elektrischen Versuche. *Annalen der Physik und Chemie*, 89:211–233, 353–377, 1853.

[68] H. Helmholtz. Über elektrische Grenzschichten. *Annalen der Physik und Chemie*, 7:337–382, 1879.

[69] L. G. Gouy. Sur la constitution de la charge électrique à la surface d'un électrolyte. *Comptes rendus hebdomadaires des séances de l'Académie des sciences*, 149:654–657, 1909.

[70] L. G. Gouy. Sur la constitution de la charge électrique à la surface d'un électrolyte. *Journal de Physique Théorique et Appliquée*, 9:457–468, 1910.

[71] D. L. Chapman. A Contribution to the Theory of Electrocapillarity. *The London, Edinburgh, and Dublin Philosophical Magazine and Journal of Science*, 25:475–481, 1913.

[72] P. J. W. Debye and E. A. A. J. Hückel. Zur Theorie der Elektrolyte. I. Gefrierpunktserniedrigung und verwandte Erscheinungen. *Physikalische Zeitschrift*, 24:185–206, 1923.

[73] O. Stern. Zur Theorie der elektrolytischen Doppelschicht (The theory of the electrolytic double-layer). *Zeitschrift für Elektrochemie und Angewandte Physikalische Chemie*, 30:508–516, 1924.

[74] S. Kondrat and A. Kornyshev. Superionic state in double-layer capacitors with nanoporous electrodes. *Journal of Physics-condensed Matter*, 23(2):022201, January 2011.

[75] M. M. Islam, M. T. Alam, and T. Ohsaka. Electrical Double-Layer Structure in Ionic Liquids: A Corroboration of the Theoretical Model by Experimental Results. *Journal of Physical Chemistry C*, 112(42):16568–16574, October 2008.

[76] M. M. Islam, M. T. Alam, T. Okajima, and T. Ohsaka. Electrical Double Layer Structure in Ionic Liquids: An Understanding of the Unusual Capacitance-Potential Curve at a Nonmetallic Electrode. *Journal of Physical Chemistry C*, 113(9):3386–3389, 2009.

[77] W. R. Fawcett and P. J. Ryan. An improved version of the Kornyshev-Eigen-Wicke model for the diffuse double layer in concentrated electrolytes. *Physical Chemistry Chemical Physics*, 12(33):9816–9821, 2010.

[78] M. V. Fedorov and A. A. Kornyshev. Unravelling the solvent response to neutral and charged solutes. *Molecular Physics*, 105(1):1–16, January 2007.

[79] Maxim V. Fedorov and Alexei A. Kornyshev. Towards understanding the structure and capacitance of electrical double layer in ionic liquids. *Electrochimica Acta*, 53(23):6835–6740, 2008.

[80] N. Georgi, A. A. Kornyshev, and M. V. Fedorov. The anatomy of the double layer and capacitance in ionic liquids with anisotropic ions: Electrostriction vs. lattice saturation. *Journal of Electroanalytical Chemistry*, 649(1-2):261–267, 2010.

[81] M. V Fedorov, N. Georgi, and A. A. Kornyshev. Double layer in ionic liquids: The nature of the camel shape of capacitance. *Electrochemistry Communications*, 12(2):296–299, 2010.

[82] S. Kondrat, N. Georgi, M. V. Fedorov, and A. A. Kornyshev. A superionic state in nano-porous double-layer capacitors: insights from Monte Carlo simulations. *Physical Chemistry Chemical Physics*, 13:11359–11366, 2011.

[83] W. F. van Gunsteren and H. J. C. Berendsen. Computer-simulation of Molecular-dynamics - Methodology, Applications, and Perspectives In Chemistry. *Angewandte Chemie-international Edition in English*, 29(9):992–1023, September 1990.

[84] J. F. Fernandez, J. Neumann, and J. Thoming. Regeneration, Recovery and Removal of Ionic Liquids. *Current Organic Chemistry*, 15(12):1992–2014, June 2011.

[85] M. C. Kroon, W. Buijs, C. J. Peters, and G. J. Witkamp. Decomposition of ionic liquids in electrochemical processing. *Green Chemistry*, 8(3):241–245, March 2006.

[86] J. T. Ye, S. Inoue, K. Kobayashi, Y. Kasahara, H. T. Yuan, H. Shimotani, and Y. Iwasa. Liquid-gated interface superconductivity on an atomically flat film. *Nature Materials*, 9(2):125–128, February 2010.

[87] M. J. Earle and K. R. Seddon. Ionic liquids. Green solvents for the future. *Pure and Applied Chemistry*, 72(7):1391–1398, July 2000.

[88] H. Mizuuchi, V. Jaitely, S. Murdan, and A. T. Florence. Room temperature ionic liquids and their mixtures: Potential pharmaceutical solvents. *European Journal of Pharmaceutical Sciences*, 33(4-5):326–331, April 2008.

[89] N. V. Plechkova and K. R. Seddon. Applications of ionic liquids in the chemical industry. *Chemical Society Reviews*, 37(1):123–150, 2008.

[90] A. J. L. Costa, M. R. C. Soromenho, K. Shimizu, I. M. Marrucho, J. M. S. S. Esperanca, J. N. C. Lopes, and L. P. N. Rebelo. Density, Thermal Expansion and Viscosity of Cholinium-Derived Ionic Liquids. *Chemphyschem*, 13(7):1902–1909, May 2012.

[91] S. J. Zhang, N. Sun, X. Z. He, X. M. Lu, and X. P. Zhang. Physical properties of ionic liquids: Database and evaluation. *Journal of Physical and Chemical Reference Data*, 35(4):1475–1517, December 2006.

[92] S. Zhang, X. Lu, Q. Zhou, X. Li, X. Zhang, and S. Li. *Ionic liquids physicochemical properties*. Elsevier, Amsterdam, 2009.

[93] H. Tokuda, K. Hayamizu, K. Ishii, M. Abu Bin Hasan Susan, and M. Watanabe. Physicochemical properties and structures of room temperature ionic liquids. 1. Variation of anionic species. *Journal of Physical Chemistry B*, 108(42):16593–16600, October 2004.

[94] H. Tokuda, K. Hayamizu, K. Ishii, M. A. B. H. Susan, and M. Watanabe. Physicochemical properties and structures of room temperature ionic liquids. 2. Variation of alkyl chain length in imidazolium cation. *Journal of Physical Chemistry B*, 109(13):6103–6110, April 2005.

[95] H. Tokuda, K. Ishii, M. A. B. H. Susan, S. Tsuzuki, K. Hayamizu, and M. Watanabe. Physicochemical properties and structures of room-temperature ionic liquids. 3. Variation of cationic structures. *Journal of Physical Chemistry B*, 110(6):2833–2839, February 2006.

[96] The molecular volumes and radii as well as the solvent-accessible surface and the different enthalpies calculated with COSMO-RS. http://portal.uni-freiburg.de/molchem/research/ionicliq/physical-data/physical-data-ils6.

[97] S. Bulut, P. Eiden, W. Beichel, J. M. Slattery, T. F. Beyersdorff, T. J. S. Schubert, and I. Krossing. Temperature Dependence of the Viscosity and Conductivity of Mildly Functionalized and Non-Functionalized [Tf2N](-) Ionic Liquids. *Chemphyschem*, 12(12):2296–2310, August 2011.

[98] Temperature-dependent viscosities and conductivities. http://portal.uni-freiburg.de/molchem/research/ionicliq/physical-data/physical-data-ils3.

[99] Kamlet-taft solvent parameters, alpha (hydrogen bond donor), beta (hydrogen bond acceptor), and pi* (polarizability). http://www.stenutz.eu/chem/solv26.php.

[100] M. N. Kobrak. The relationship between solvent polarity and molar volume in room-temperature ionic liquids. *Green Chemistry*, 10(1):80–86, 2008.

[101] P. G. Jessop, D. A. Jessop, D. B. Fu, and L. Phan. Solvatochromic parameters for solvents of interest in green chemistry. *Green Chemistry*, 14(5):1245–1259, 2012.

[102] N. V. Shvedene, S. V. Borovskaya, V. V. Sviridov, E. R. Ismailova, and I. V. Pletnev. Measuring the solubilities of ionic liquids in water using ion-selective electrodes. *Analytical and Bioanalytical Chemistry*, 381(2):427–430, January 2005.

[103] M. Tariq, M. G. Freire, B. Saramago, J. A. P. Coutinho, J. N. C. Lopes, and L. P. N. Rebelo. Surface tension of ionic liquids and ionic liquid solutions. *Chemical Society Reviews*, 41(2):829–868, 2012.

[104] F. Endres, D. MacFarlane, and A. Abbott, editors. *Electrodeposition from ionic liquids*. Wiley-VCH, 2008.

[105] S. T. Handy. Room temperature ionic liquids: Different classes and physical properties. *Current Organic Chemistry*, 9(10):959–988, July 2005.

[106] L. E. Barrosse-Antle, A. M. Bond, R. G. Compton, A. M. O'Mahony, E. I. Rogers, and D. S. Silvester. Voltammetry in Room Temperature Ionic Liquids: Comparisons and Contrasts with Conventional Electrochemical Solvents. *Chemistry-an Asian Journal*, 5(2):202–230, 2010.

[107] S. Jayaraman and E. J. Maginn. Computing the melting point and thermodynamic stability of the orthorhombic and monoclinic crystalline polymorphs of the ionic liquid 1-n-butyl-3-methylimidazolium chloride. *Journal of Chemical Physics*, 127(21):214504, December 2007.

[108] Y-H. Tian, G. S. Goff, W. H. Runde, and E. R. Batista. Exploring Electrochemical Windows of Room-Temperature Ionic Liquids: A Computational Study. *Journal of Physical Chemistry B*, 116(39):11943–11952, October 2012.

[109] E. J. Maginn. Atomistic simulation of the thermodynamic and transport properties of ionic liquids. *Accounts of Chemical Research*, 40(11):1200–1207, November 2007.

[110] H. Weingaertner. Understanding ionic liquids at the molecular level: Facts, problems, and controversies. *Angewandte Chemie-international Edition*, 47(4):654–670, 2008.

[111] D. A. Turton, J. Hunger, A. Stoppa, G. Hefter, A. Thoman, M. Walther, R. Buchner, and K. Wynne. Dynamics of Imidazolium Ionic Liquids from a Combined Dielectric Relaxation and Optical Kerr Effect Study: Evidence for Mesoscopic Aggregation. *Journal of the American Chemical Society*, 131(31):11140–11146, August 2009.

[112] S. Tsuzuki, H. Tokuda, K. Hayamizu, and M. Watanabe. Magnitude and directionality of interaction in ion pairs of ionic liquids: Relationship with

ionic conductivity. *Journal of Physical Chemistry B*, 109(34):16474–16481, September 2005.

[113] S. Tsuzuki, W. Shinoda, H. Saito, M. Mikami, H. Tokuda, and M. Watanabe. Molecular Dynamics Simulations of Ionic Liquids: Cation and Anion Dependence of Self-Diffusion Coefficients of Ions. *Journal of Physical Chemistry B*, 113(31):10641–10649, August 2009.

[114] M. H. Kowsari, S. Alavi, M. Ashrafizaadeh, and B. Najafi. Molecular dynamics simulation of imidazolium-based ionic liquids. I. Dynamics and diffusion coefficient. *Journal of Chemical Physics*, 129(22):224508, December 2008.

[115] Q. S. Liu, P. F. Yan, M. Yang, Z. C. Tan, C. P. Li, and U. Welz-Biermann. Dynamic Viscosity and Conductivity of Ionic Liquids [C(n)py][NTf2] (n=2, 4, 5). *Acta Physico-chimica Sinica*, 27(12):2762–2766, December 2011.

[116] L. M. N. B. F. Santos, J. N. C. Lopes, J. A. P. Coutinho, J. M. S. S. Esperanca, L. R. Gomes, I. M. Marrucho, and L. P. N. Rebelo. Ionic liquids: First direct determination of their cohesive energy. *Journal of the American Chemical Society*, 129(2):284–285, January 2007.

[117] C. Schroder, T. Sonnleitner, R. Buchner, and O. Steinhauser. The influence of polarizability on the dielectric spectrum of the ionic liquid 1-ethyl-3-methylimidazolium triflate. *Physical Chemistry Chemical Physics*, 13(26):12240–12248, 2011.

[118] P. Wasserscheid and T. Welton, editors. *Ionic Liquids in Synthesis*. Wiley-VCH, 2003.

[119] A. S. Pensado, M. F. C. Gomes, J. N. C. Lopes, P. Malfreyt, and A. A. H. Padua. Effect of alkyl chain length and hydroxyl group functionalization on the surface properties of imidazolium ionic liquids. *Physical Chemistry Chemical Physics*, 2011.

[120] C. Merlet, M. Salanne, B. Rotenberg, and P. A. Madden. Imidazolium Ionic Liquid Interfaces with Vapor and Graphite: Interfacial Tension and Capacitance from Coarse-Grained Molecular Simulations. *Journal of Physical Chemistry C*, 115(33):16613–16618, August 2011.

[121] C. Merlet, M. Salanne, and B. Rotenberg. New Coarse-Grained Models of Imidazolium Ionic Liquids for Bulk and Interfacial Molecular Simulations. *Journal of Physical Chemistry C*, 116(14):7687–7693, April 2012.

[122] J. P. Vivek and I. J. Burgess. Quaternary Ammonium Bromide Surfactant Adsorption on Low-Index Surfaces of Gold. 2. Au(100) and the Role of Crystallographic-Dependent Adsorption in the Formation of Anisotropic Nanoparticles. *Langmuir*, 28(11):5040–5047, March 2012.

[123] H. Kurig, M. Vestli, A. Janes, and E. Lust. Electrical Double Layer Capacitors Based on Two 1-Ethyl-3-Methylimidazolium Ionic Liquids with Different Anions. *Electrochemical and Solid State Letters*, 14(8):A120–A122, 2011.

[124] B. Roling, M. Drüschler, and B. Huber. Slow and fast capacitive process taking place at the ionic liquid/electrode interface. *Faraday Discussions*, 154:303–311, 2012.

[125] R. Atkin, N. Borisenko, M. Drüschler, S. Z. El Abedin, F. Endres, R. Hayes, B. Huber, and B. Roling. An in situ STM/AFM and impedance spectroscopy study of the extremely pure 1-butyl-1-methylpyrrolidinium tris(pentafluoroethyl) trifluorophosphate/Au(111) interface: potential dependent solvation layers and the herringbone reconstruction. *Physical Chemistry Chemical Physics*, 13(15):6849–6857, 2011.

[126] C. Y. Penalber and S. Baldelli. Observation of Charge Inversion of an Ionic Liquid at the Solid Salt-Liquid Interface by Sum Frequency Generation Spectroscopy. *Journal of Physical Chemistry Letters*, 3(7):844–847, April 2012.

[127] S. Baldelli. Interfacial Structure of Room-Temperature Ionic Liquids at the Solid-Liquid Interface as Probed by Sum Frequency Generation Spectroscopy. *The Journal of Physical Chemistry Letters*, 4(0):244–252, 2013.

[128] R. Foulston, S. Gangopadhyay, C. Chiutu, P. Moriarty, and R. G. Jones. Mono- and multi-layer adsorption of an ionic liquid on Au(110). *Physical Chemistry Chemical Physics*, 14(17):6054–6066, 2012.

[129] S. Chen, K. Kobayashi, R. Kitaura, Y. Miyata, and H. Shinohara. Direct HRTEM Observation of Ultrathin Freestanding Ionic Liquid Film on Carbon Nanotube Grid. *Acs Nano*, 5(6):4902–4908, June 2011.

[130] V. Lockett, R. Sedev, C. Bassell, and J. Ralston. Angle-resolved X-ray photoelectron spectroscopy of the surface of imidazolium ionic liquids. *Physical Chemistry Chemical Physics*, 10(9):1330–1335, 2008.

[131] T. Cremer, M. Stark, A. Deyko, H. P. Steinruck, and F. Maier. Liquid/-Solid Interface of Ultrathin Ionic Liquid Films: [C(1)C(1)lm][Tf2N] and [C(8)C(1)Im][Tf2N] on Au(111). *Langmuir*, 27(7):3662–3671, April 2011.

[132] O. Russina, B. Fazio, C. Schmidt, and A. Triolo. Structural organization and phase behaviour of 1-butyl-3-methylimidazolium hexafluorophosphate: an high pressure raman spectroscopy study. *Physical Chemistry Chemical Physics*, 13(25):12067–12074, 2011.

[133] S. A. Kislenko, R. H. Amirov, and I. S. Samoylov. Influence of temperature on the structure and dynamics of the [BMIM][PF6] ionic liquid/graphite interface. *Physical Chemistry Chemical Physics*, 12(37):11245–11250, 2010.

[134] G. Feng, J. S. Huang, B. G. Sumpter, V. Meunier, and R. Qiao. A "counter-charge layer in generalized solvents" framework for electrical double layers in neat and hybrid ionic liquid electrolytes. *Physical Chemistry Chemical Physics*, 13(32):14723–14734, 2011.

[135] M. V. Fedorov and R. M. Lynden-Bell. Probing the neutral graphene-ionic liquid interface: insights from molecular dynamics simulations. *Physical Chemistry Chemical Physics*, 14(8):2552–2556, 2012.

[136] J. Vatamanu, O. Borodin, D. Bedrov, and G. D. Smith. Molecular Dynamics Simulation Study of the Interfacial Structure and Differential Capacitance of Alkylimidazolium Bis(trifluoromethanesulfonyl)imide [C(n)mim][TFSI] Ionic Liquids at Graphite Electrodes. *Journal of Physical Chemistry C*, 116(14):7940–7951, April 2012.

[137] G. Feng, D. E. Jiang, and P. T. Cummings. Curvature Effect on the Capacitance of Electric Double Layers at Ionic Liquid/Onion-Like Carbon Interfaces. *Journal of Chemical Theory and Computation*, 8(3):1058–1063, March 2012.

[138] J. K. McDonough, A. I. Frolov, V. Presser, J. J. Niu, C. H. Miller, T. Ubieto, M. V. Fedorov, and Y. Gogotsi. Influence of the structure of carbon onions on their electrochemical performance in supercapacitor electrodes. *Carbon*, 50(9):3298–3309, August 2012.

[139] C. Merlet, B. Rotenberg, P. A. Madden, P. L. Taberna, P. Simon, Y. Gogotsi, and M. Salanne. On the molecular origin of supercapacitance in nanoporous carbon electrodes. *Nature Materials*, 11(4):306–310, April 2012.

[140] A. C. F. Mendonca, P. Malfreyt, and A. A. H. Padua. Interactions and Ordering of Ionic Liquids at a Metal Surface. *Journal of Chemical Theory and Computation*, 8(9):3348–3355, September 2012.

[141] M. L. Sha, D. X. Niu, Q. Dou, G. Z. Wu, H. P. Fang, and J. Hu. Reversible tuning of the hydrophobic-hydrophilic transition of hydrophobic ionic liquids by means of an electric field. *Soft Matter*, 7(9):4228–4233, 2011.

[142] S. Li, J. L. Banuelos, J. Guo, L. Anovitz, G. Rother, R. W. Shaw, P. C. Hillesheim, S. Dai, G. A. Baker, and P. T. Cummings. Alkyl Chain Length and Temperature Effects on Structural Properties of Pyrrolidinium-Based Ionic Liquids: A Combined Atomistic Simulation and Small-Angle X-ray Scattering Study. *Journal of Physical Chemistry Letters*, 3(1):125–130, January 2012.

[143] R. K. Kalluri, M. M. Biener, M. E. Suss, M. D. Merrill, M. Stadermann, J. G. Santiago, T. F. Baumann, J. Biener, and A. Striolo. Unraveling the potential and pore-size dependent capacitance of slit-shaped graphitic carbon pores in aqueous electrolytes. *Physical Chemistry Chemical Physics*, 15(7):2309–2320, February 2013.

[144] C. Aliaga, C. S. Santos, and S. Baldelli. Surface chemistry of room-temperature ionic liquids. *Physical Chemistry Chemical Physics*, 9(28):3683–3700, 2007.

[145] B. L. Bhargava, S. Balasubramanian, and M. L. Klein. Modelling room temperature ionic liquids. *Chemical Communications*, (29):3339–3351, 2008.

[146] P. A. Hunt. The simulation of imidazolium-based ionic liquids. *Molecular Simulation*, 32(1):1–10, January 2006.

[147] R. M. Lynden-Bell, M. G. Del Popolo, T. G. A. Youngs, J. Kohanoff, C. G. Hanke, J. B. Harper, and C. C. Pinilla. Simulations of ionic liquids, solutions, and surfaces. *Accounts of Chemical Research*, 40:1138–1145, 2007.

[148] E. J. Maginn. Molecular simulation of ionic liquids: current status and future opportunities. *Journal of Physics-Condensed Matter*, 21(37):373101, September 2009.

[149] F. Dommert, K. Wendler, R. Berger, L. Delle Site, and C. Holm. Force Fields for Studying the Structure and Dynamics of Ionic Liquids: A Critical Review of Recent Developments. *Chemphyschem*, 13(7):1625–1637, May 2012.

[150] J. N. C. Lopes, J. Deschamps, and A. A. H. Pádua. Modeling ionic liquids using a systematic all-atom force field. *Journal of Physical Chemistry B*, 108(6):2038–2047, February 2004.

[151] S. M. Urahata and M. C. C. Ribeiro. Structure of ionic liquids of 1-alkyl-3-methylimidazolium cations: A systematic computer simulation study. *Journal of Chemical Physics*, 120(4):1855–1863, January 2004.

[152] J. N. C. Lopes and A. A. H. Padua. Molecular force field for ionic liquids III: Imidazolium, pyridinium, and phosphonium cations; Chloride, bromide, and dicyanamide anions. *Journal of Physical Chemistry B*, 110(39):19586–19592, October 2006.

[153] T. Koddermann, D. Paschek, and R. Ludwig. Molecular dynamic simulations of ionic liquids: A reliable description of structure, thermodynamics and dynamics. *Chemphyschem*, 8(17):2464–2470, December 2007.

[154] W. Zhao, H. Eslami, W. L. Cavalcanti, and F. Muller-Plathe. A refined all-atom model for the ionic liquid 1-n-butyl 3-methylimidazolium bis(trifluoromethylsulfonyl)imide [bmim][Tf2N]. *Zeitschrift für Physikalische Chemie-international Journal of Research In Physical Chemistry & Chemical Physics*, 221(11-12):1647–1662, 2007.

[155] S. V. Sambasivarao and O. Acevedo. Development of OPLS-AA Force Field Parameters for 68 Unique Ionic Liquids. *Journal of Chemical Theory and Computation*, 5(4):1038–1050, April 2009.

[156] K. Shimizu, D. Almantariotis, M. F. C. Gomes, A. A. H. Padua, and J. N. C. Lopes. Molecular Force Field for Ionic Liquids V: Hydroxyethylimidazolium, Dimethoxy-2-Methylimidazolium, and Fluoroalkylimidazolium Cations and Bis(Fluorosulfonyl)Amide, Perfluoroalkanesulfonylamide, and Fluoroalkylfluorophosphate Anions. *Journal of Physical Chemistry B*, 114(10):3592–3600, March 2010.

[157] N. M. Micaelo, A. M. Baptista, and C. M. Soares. Parametrization of 1-butyl-3-methylimidazolium hexafluorophosphate/nitrate ionic liquid for the GROMOS force field. *Journal of Physical Chemistry B*, 110(29):14444–14451, July 2006.

[158] Z. P. Liu, X. P. Wu, and W. C. Wang. A novel united-atom force field for imidazolium-based ionic liquids. *Physical Chemistry Chemical Physics*, 8(9):1096–1104, 2006.

[159] Z. P. Liu, T. Chen, A. Bell, and B. Smit. Improved United-Atom Force Field for 1-Alkyl-3-methylimidazolium Chloride. *Journal of Physical Chemistry B*, 114(13):4572–4582, April 2010.

[160] X. J. Zhong, Z. P. Liu, and D. P. Cao. Improved Classical United-Atom Force Field for Imidazolium-Based Ionic Liquids: Tetrafluoroborate, Hexafluorophosphate, Methylsulfate, Trifluoromethylsulfonate, Acetate, Trifluoroacetate, and Bis(trifluoromethylsulfonyl)amide. *Journal of Physical Chemistry B*, 115(33):10027–10040, August 2011.

[161] Y. Wang, W. Jiang, T. Yan, and G. A. Voth. Understanding ionic liquids through atomistic and coarse-grained molecular dynamics simulations. *Accounts of Chemical Research*, 40(11):1193–1199, November 2007.

[162] M. Masia. Ab initio based polarizable force field parametrization. *Journal of Chemical Physics*, 128(18):184107, May 2008.

[163] O. Borodin. Polarizable Force Field Development and Molecular Dynamics Simulations of Ionic Liquids. *Journal of Physical Chemistry B*, 113(33):11463–11478, August 2009.

[164] D. Bedrov, O. Borodin, Z. Li, and G. D. Smith. Influence of Polarization on Structural, Thermodynamic, and Dynamic Properties of Ionic Liquids Obtained from Molecular Dynamics Simulations. *Journal of Physical Chemistry B*, 114(15):4984–4997, April 2010.

[165] T. Y. Yan, Y. T. Wang, and C. Knox. On the Structure of Ionic Liquids: Comparisons between Electronically Polarizable and Nonpolarizable Models I. *Journal of Physical Chemistry B*, 114(20):6905–6921, May 2010.

[166] J. B. Hooper, O. N. Starovoytov, O. Borodin, D. Bedrov, and G. D. Smith. Molecular dynamics simulation studies of the influence of imidazolium

structure on the properties of imidazolium/azide ionic liquids. *Journal of Chemical Physics*, 136(19):194506, May 2012.

[167] K. Fumino, T. Peppel, M. Geppert-Rybczynska, D. H. Zaitsau, J. K. Lehmann, S. P. Verevkin, M. Kockerling, and R. Ludwig. The influence of hydrogen bonding on the physical properties of ionic liquids. *Physical Chemistry Chemical Physics*, 13(31):14064–14075, 2011.

[168] C. Schroder. Comparing reduced partial charge models with polarizable simulations of ionic liquids. *Physical Chemistry Chemical Physics*, 14(9):3089–3102, 2012.

[169] I. V. Leontyev and A. A. Stuchebrukhov. Electronic continuum model for molecular dynamics simulations. *Journal of Chemical Physics*, 130(8):085102, February 2009.

[170] J. Vatamanu, O. Borodin, and G. D. Smith. Molecular Simulations of the Electric Double Layer Structure, Differential Capacitance, and Charging Kinetics for N-Methyl-N-propylpyrrolidinium Bis(fluorosulfonyl)imide at Graphite Electrodes. *Journal of Physical Chemistry B*, 115(12):3073–3084, March 2011.

[171] C. Merlet, C. Péan, B. Rotenberg, P. A. Madden, P. Simon, and M. Salanne. Simulating Supercapacitors: Can We Model Electrodes As Constant Charge Surfaces? *The Journal of Physical Chemistry Letters*, 4:264–268, January 2013.

[172] C. Vega, E. Sanz, J. L. F. Abascal, and E. G. Noya. Determination of phase diagrams via computer simulation: methodology and applications to water, electrolytes and proteins. *Journal of Physics-Condensed Matter*, 20(15):153101, April 2008.

[173] N. Rai and E. J. Maginn. Vapor-Liquid Coexistence and Critical Behavior of Ionic Liquids via Molecular Simulations. *Journal of Physical Chemistry Letters*, 2(12):1439–1443, June 2011.

[174] G. C. Ganzenmüller and P. J. Camp. Phase behaviour and dynamics in primitive models of molecular ionic liquids. *Condensed Matter Physics*, 14(3):33602, 2011.

[175] A. P. Hynninen and A. Z. Panagiotopoulos. Simulations of phase transitions and free energies for ionic systems. *Molecular Physics*, 106(16-18):2039–2051, 2008.

[176] A. Ciach and O. Patsahan. Field-theoretic description of ionic crystallization in the restricted primitive model. *Physical Review E*, 74(2):021508, August 2006.

[177] J. Reszko-Zygmunt, S. Sokolowski, D. Henderson, and D. Boda. Temperature dependence of the double layer capacitance for the restricted primitive model of an electrolyte solution from a density functional approach. *Journal of Chemical Physics*, 122(8):084504, February 2005.

[178] Q. L. Yan and J. J. de Pablo. Phase equilibria and clustering in size-asymmetric primitive model electrolytes. *Journal of Chemical Physics*, 114(4):1727–1731, January 2001.

[179] A. Z. Panagiotopoulos and M. E. Fisher. Phase transitions in 2 : 1 and 3 : 1 hard-core model electrolytes. *Physical Review Letters*, 88(4):045701, January 2002.

[180] M. Trulsson, J. Algotsson, J. Forsman, and C. E. Woodward. Differential Capacitance of Room Temperature Ionic Liquids: The Role of Dispersion Forces. *Journal of Physical Chemistry Letters*, 1(8):1191–1195, April 2010.

[181] Y. Sugita and Y. Okamoto. Replica-exchange molecular dynamics method for protein folding. *Chemical Physics Letters*, 314(1-2):141–151, November 1999.

[182] D. J. Earl and M. W. Deem. Parallel tempering: Theory, applications, and new perspectives. *Physical Chemistry Chemical Physics*, 7(23):3910–3916, 2005.

[183] W. Janke, editor. *Rugged Free Energy Landscapes: Common Computational Approaches to Spin Glasses, Structural Glasses and Biological Macromolecules*, volume 736 of *Lecture Notes in Physics*. Springer, 2008.

[184] M. Christen and W. F. Van Gunsteren. On searching in, sampling of, and dynamically moving through conformational space of biomolecular systems: A review. *Journal of Computational Chemistry*, 29(2):157–166, January 2008.

[185] M. S. Shell. Advanced sampling. www.engr.ucsb.edu/ shell/che210d/Advanced_sampling.pdf, May 2012. Lecture notes on advanced sampling techniques. Course CHE210D: Principles of modern molecular simulation methods.

[186] C. Chipot and A. Pohorille, editors. *Free Energy Calculations - Theory and Applications in Chemistry and Biology*, volume 86 of *Springer Series in Chemical Physics*. Springer, Berlin, Heidelberg, 2007.

[187] E. Marinari and G. Parisi. Simulated Tempering - A New Monte-Carlo Scheme. *Europhysics Letters*, 19(6):451–458, July 1992.

[188] A. Mitsutake and Y. Okamoto. From multidimensional replica-exchange method to multidimensional multicanonical algorithm and simulated tempering. *Physical Review E*, 79(4):047701, April 2009.

[189] R. H. Swendsen and J. S. Wang. Replica Monte-Carlo Simulation of Spinglasses. *Physical Review Letters*, 57(21):2607–2609, November 1986.

[190] E. Gallicchio, M. Andrec, A. K. Felts, and R. M. Levy. Temperature weighted histogram analysis method, replica exchange, and transition paths. *Journal of Physical Chemistry B*, 109(14):6722–6731, April 2005.

[191] X. Periole and A. E. Mark. Convergence and sampling efficiency in replica exchange simulations of peptide folding in explicit solvent. *Journal of Chemical Physics*, 126(1):014903, January 2007.

[192] N. V. Buchete and G. Hummer. Peptide folding kinetics from replica exchange molecular dynamics. *Physical Review E*, 77(3):030902, March 2008.

[193] S. Kumar, J. M. Rosenberg, D. Bouzida, R. H. Swendsen, and P. A. Kollman. THE weighted histogram analysis method for free-energy calculations on biomolecules. I. The method. *Journal of Computational Chemistry*, 13(8):1011–1021, 1992.

[194] B. Coasne, J. Czwartos, M. Sliwinska-Bartkowiak, and K. E. Gubbins. Freezing of mixtures confined in silica nanopores: Experiment and molecular simulation. *Journal of Chemical Physics*, 133(8):084701, August 2010.

[195] M. Chen, M. A. Cuendet, and M. E. Tuckerman. Heating and flooding: A unified approach for rapid generation of free energy surfaces. *Journal of Chemical Physics*, 137(2):024102, July 2012.

[196] W. Zhang, C. Wu, and Y. Duan. Convergence of replica exchange molecular dynamics. *Journal of Chemical Physics*, 123(15):154105, October 2005.

[197] B. Cooke and S. C. Schmidler. Preserving the Boltzmann ensemble in replica-exchange molecular dynamics. *Journal of Chemical Physics*, 129(16):164112, October 2008.

[198] I. Vyalov. *Molecular dynamics simulation of dissolution of cellulose in supercritical fluids and mixtures of cosolvents/supercritical fluids*. PhD thesis, University of Lille, 2011.

[199] A. Barducci, M. Bonomi, and M. Parrinello. Metadynamics. *Wiley Interdisciplinary Reviews-computational Molecular Science*, 1(5):826–843, September 2011.

[200] G. Bussi, F. L. Gervasio, A. Laio, and M. Parrinello. Free-energy landscape for beta hairpin folding from combined parallel tempering and metadynamics. *Journal of the American Chemical Society*, 128(41):13435–13441, October 2006.

[201] S. Piana and A. Laio. A bias-exchange approach to protein folding. *Journal of Physical Chemistry B*, 111(17):4553–4559, May 2007.

[202] C. Camilloni, D. Provasi, G. Tiana, and R. A. Broglia. Exploring the protein G helix free-energy surface by solute tempering metadynamics. *Proteins-structure Function and Bioinformatics*, 71(4):1647–1654, June 2008.

[203] M. Bonomi and M. Parrinello. Enhanced Sampling in the Well-Tempered Ensemble. *Physical Review Letters*, 104(19):190601, May 2010.

[204] J. Smiatek and A. Heuer. Calculation of Free Energy Landscapes: A Histogram Reweighted Metadynamics Approach. *Journal of Computational Chemistry*, 32(10):2084–2096, July 2011.

[205] S. Angioletti-Uberti, M. Ceriotti, P. D. Lee, and M. W. Finnis. Solid-liquid interface free energy through metadynamics simulations. *Physical Review B*, 81(12):125416, March 2010.

[206] S. Orlandini, S. Meloni, and G. Ciccotti. Combining Rare Events Techniques: Phase Change in Si Nanoparticles. *Journal of Statistical Physics*, 145(4):812–830, November 2011.

[207] A. Giacomello, S. Meloni, M. Chinappi, and C. M. Casciola. Cassie-Baxter and Wenzel States on a Nanostructured Surface: Phase Diagram, Metastabilities, and Transition Mechanism by Atomistic Free Energy Calculations. *Langmuir*, 28(29):10764–10772, July 2012.

[208] E. S. Savoy and F. A. Escobedo. Simulation Study of Free-Energy Barriers in the Wetting Transition of an Oily Fluid on a Rough Surface with Reentrant Geometry. *Langmuir*, 28(46):16080–16090, 2012.

[209] D. Hamelberg, J. Mongan, and J. A. McCammon. Accelerated molecular dynamics: A promising and efficient simulation method for biomolecules. *Journal of Chemical Physics*, 120(24):11919–11929, June 2004.

[210] A. F. Voter. Hyperdynamics: Accelerated molecular dynamics of infrequent events. *Physical Review Letters*, 78(20):3908–3911, May 1997.

[211] A. F. Voter. A method for accelerating the molecular dynamics simulation of infrequent events. *Journal of Chemical Physics*, 106(11):4665–4677, March 1997.

[212] A. Laio and M. Parrinello. Escaping free-energy minima. *Proceedings of the National Academy of Sciences of the United States of America*, 99(20):12562–12566, October 2002.

[213] C. Jarzynski. Nonequilibrium equality for free energy differences. *Physical Review Letters*, 78(14):2690–2693, April 1997.

[214] S. Park, F. Khalili-Araghi, E. Tajkhorshid, and K. Schulten. Free energy calculation from steered molecular dynamics simulations using jarzynski's equality. *Journal of Chemical Physics*, 119(6):3559–3566, August 2003.

[215] T. Bastug and S. Kuyucak. Application of jarzynski's equality in simple versus complex systems. *Chemical Physics Letters*, 436(4-6):383–387, March 2007.

[216] G. M. Torrie and J. P. Valleau. Non-physical Sampling Distributions In Monte-carlo Free-energy Estimation - Umbrella Sampling. *Journal of Computational Physics*, 23(2):187–199, 1977.

[217] B. Roux. The Calculation of the Potential of Mean Force Using Computer-simulations. *Computer Physics Communications*, 91(1-3):275–282, September 1995.

[218] D. Wu and D. A. Kofke. Phase-space overlap measures. II. Design and implementation of staging methods for free-energy calculations. *Journal of Chemical Physics*, 123(8):084109, August 2005.

[219] B. Hess, C. Kutzner, D. van der Spoel, and E. Lindahl. GROMACS 4: Algorithms for highly efficient, load-balanced, and scalable molecular simulation. *Journal of Chemical Theory and Computation*, 4(3):435–447, March 2008.

[220] K. Hukushima and K. Nemoto. Exchange Monte Carlo method and application to spin glass simulations. *Journal of the Physical Society of Japan*, 65(6):1604–1608, June 1996.

[221] Unknown. Replica-Exchange Molecular Dynamics. Implementation in Gromacs. http://www.gromacs.org/Documentation/How-tos/REMD, December 2012.

[222] Daniel Weinstock. Replica Exchange Molecular Dynamics. http://biomaps.rutgers.edu/lecture_7_2_11_2010.pdf, February 2010. Simulations in Computational Biophysics in Spring 2010.

[223] Jianhan Chen. Replica Exchange Sampling. https://mmtsb.org/workshops/mmtsb-ctbp_workshop_2009/Lecture_pdf/replica-exchange.pdf, August 2009. MMTSB/CTBP Workshop in August 4-9, 2009, Kansas State University.

[224] B. W. Zhang, D. Jasnow, and D. M. Zuckerman. Transition-event durations in one-dimensional activated processes. *Journal of Chemical Physics*, 126(7):074504, February 2007.

[225] Y. G. Mu. Dissociation aided and side chain sampling enhanced Hamiltonian replica exchange. *Journal of Chemical Physics*, 130(16):164107, April 2009.

[226] K. J. Strandburg. Two-dimensional Melting. *Reviews of Modern Physics*, 60(1):161–207, January 1988.

[227] Unknown. Modifying PLUMED package - adding your own CV. https://sites.google.com/site/scienceuprising/code-packages/modifying-plumed-package, December 2012.

[228] L. Martínez, R. Andrade, E. G. Birgin, and J. M. Martínez. PACKMOL: A Package for Building Initial Configurations for Molecular Dynamics Simulations. *Journal of Computational Chemistry*, 30(13):2157–2164, October 2009.

[229] I.C. Yeh and M.L. Berkowitz. Ewald summation for systems with slab geometry. *Journal of Chemical Physics*, 111:3155–3162, 1999.

[230] U. Essmann, L. Perera, M. L. Berkowitz, T. Darden, H. Lee, and L. G. Pedersen. A Smooth Particle Mesh Ewald Method. *Journal of Chemical Physics*, 103(19):8577–8593, November 1995.

[231] G. Bussi, D. Donadio, and M. Parrinello. Canonical sampling through velocity rescaling. *The Journal of Chemical Physics*, 126(1):014101, January 2007.

[232] M. Gonzalez-Melchor, F. Bresme, and J. Alejandre. Molecular dynamics simulations of the surface tension of ionic liquids. *Journal of Chemical Physics*, 122(10):104710, March 2005.

[233] B. Skinner, T. Chen, M. S. Loth, and B. I. Shklovskii. Theory of volumetric capacitance of an electric double layer supercapacitor. *Physical Review E*, 83(5):056102, 2011.

[234] W. H. Briscoe and P. Attard. Counterion-only electrical double layer: A constrained entropy approach. *Journal of Chemical Physics*, 117(11):5452–5464, September 2002.

[235] G. I. Guerrero-Garcia, E. Gonzalez-Tovar, and M. O. de la Cruz. Effects of the ionic size-asymmetry around a charged nanoparticle: unequal charge neutralization and electrostatic screening. *Soft Matter*, 6(9):2056–2065, 2010.

[236] Z. Y. Wang and Y. Q. Ma. Computational evidence of two driving mechanisms for overcharging in an electric double layer near the point of zero charge. *Physical Review E*, 85(6):062501, June 2012.

[237] Z. Y. Wang, Y. P. Xie, Q. Liang, Z. W. Ma, and J. W. Wei. Looking deeper into the structure of mixed electric double layers near the point of zero charge. *Journal of Chemical Physics*, 137(17):174707, November 2012.

[238] K. Kirchner, T. Kirchner, V. Ivaništšev, and M. V. Fedorov. Electrical double layer in ionic liquids: structural transitions from multilayer to monolayer structure at the interface. *Electrochimica Acta*, April 2013. Preprint version.

[239] F. Endres, O. Hofft, N. Borisenko, L. H. Gasparotto, A. Prowald, R. Al-Salman, T. Carstens, R. Atkin, A. Bund, and S. Z. El Abedin. Do solvation layers of ionic liquids influence electrochemical reactions? *Physical Chemistry Chemical Physics*, 12(8):1724–1732, 2010.

[240] F. Endres. Ionic Liquids for Electrochemical Deposition: Prospects and Challenges. *Chemie Ingenieur Technik*, 83(9):1485–1492, September 2011.

[241] V. Halka, R. Tsekov, and W. Freyland. Interfacial phase transitions in imidazolium-based ionic liquids. *Journal of Physics-Condensed Matter*, 17(45):S3325–S3331, November 2005.

[242] D. Boda, K. Y. Chan, and D. Henderson. Monte carlo simulation of an ion-dipole mixture as a model of an electrical double layer. *Journal of Chemical Physics*, 109(17):7362–7371, November 1998.

[243] W. Schröer. A Short History of Phase Transitions in Ionic Fluids. *Contributions to Plasma Physics*, 52(1):78–88, January 2012.

[244] S. Grandner and S. H. L. Klapp. Surface-charge-induced freezing of colloidal suspensions. *Epl*, 90(6):68004, June 2010.

[245] S. Tazi, M. Salanne, C. Simon, P. Tury, M. Pounds, and P. A. Madden. Potential-Induced Ordering Transition of the Adsorbed Layer at the Ionic Liquid/Electrified Metal Interface. *Journal of Physical Chemistry B*, 114(25):8453–8459, July 2010.

[246] T. Wandlowski. Phase transitions in two-dimensional adlayers at electrode surfaces: Thermodynamics, kinetics and structural aspects. In *Encyclopedia of Electrochemistry, Volume 1, Thermodynamics and Electrified Interfaces*, volume 1, pages 383–467. Wiley-VCH, 2002.

[247] O. M. Magnussen. Ordered anion adlayers on metal electrode surfaces. *Chemical Reviews*, 102(3):679–725, March 2002.

[248] A. I. Frolov, E. L. Ratkova, D. S. Palmer, and M. V. Fedorov. Hydration Thermodynamics using the Reference Interaction Site Model: Speed or Accuracy? *The Journal of Physical Chemistry B*, 115(19):6011–6022, 2011.

[249] R. Hayes, N. Borisenko, M. K. Tam, P. C. Howlett, F. Endres, and R. Atkin. Double Layer Structure of Ionic Liquids at the Au(111) Electrode Interface: An Atomic Force Microscopy Investigation. *Journal of Physical Chemistry C*, 115(14):6855–6863, April 2011.

[250] W. Y. Zhou, W. J. Ma, Z. Q. Niu, L. Song, and S. S. Xie. Freestanding single-walled carbon nanotube bundle networks: Fabrication, properties and composites. *Chinese Science Bulletin*, 57(2-3):205–224, January 2012.

[251] Y. Lauw, M. D. Horne, T. Rodopoulos, V. Lockett, B. Akgun, W. A. Hamilton, and A. R. J. Nelson. Structure of [C(4)mpyr][NTf2] Room-Temperature Ionic Liquid at Charged Gold Interfaces. *Langmuir*, 28(19):7374–7381, May 2012.

[252] L. Tamam, B. M. Ocko, H. Reichert, and M. Deutsch. Checkerboard Self-Patterning of an Ionic Liquid Film on Mercury. *Physical Review Letters*, 106(19):197801, May 2011.

[253] K. Tamura, S. Miyaguchi, K. Sakaue, Y. Nishihata, and J. Mizuki. Direct observation of Au(111) electrode surface structure in bis(trifluoromethylsulfonyl)amide-based ionic liquids using surface X-ray scattering. *Electrochemistry Communications*, 13(5):411–413, May 2011.

[254] M. Mezger, H. Schroder, H. Reichert, S. Schramm, J. S. Okasinski, S. Schoder, V. Honkimaki, M. Deutsch, B. M. Ocko, J. Ralston, M. Rohwerder, M. Stratmann, and H. Dosch. Molecular layering of fluorinated ionic liquids at a charged sapphire (0001) surface. *Science*, 322(5900):424–428, October 2008.

[255] R. Radhakrishnan, K. E. Gubbins, and M. Sliwinska-Bartkowiak. Existence of a hexatic phase in porous media. *Physical Review Letters*, 89(7):076101, August 2002.

[256] M. Marzec, B. Kuchta, and L. Firlej. Adsorption and phase transitions in adsorbed systems: structural properties of CCl4 layers adsorbed on a graphite surface. *Journal of Molecular Modeling*, 13(4):537–542, April 2007.

[257] N. Gribova, A. Arnold, T. Schilling, and C. Holm. How close to two dimensions does a Lennard-Jones system need to be to produce a hexatic phase? *Journal of Chemical Physics*, 135(5):054514, August 2011.

[258] W. D. Luedtke, J. P. Gao, and U. Landman. Dielectric Nanodroplets: Structure, Stability, Thermodynamics, Shape Transitions and Electrocrystallization in Applied Electric Fields. *Journal of Physical Chemistry C*, 115(42):20343–20358, October 2011.

[259] R. M. Lynden-Bell, A. I. Frolov, and M. V. Fedorov. Electrode screening by ionic liquids. *Physical Chemistry Chemical Physics*, 2012.

[260] T. O'Haver. Peak Finding and Measurement. http://terpconnect.umd.edu/˜toh/spectrum/PeakFindingandMeasurement.htm, October 2012.

[261] F. Bresme and J. Alejandre. Cavities in ionic liquids. *Journal of Chemical Physics*, 118(9):4134–4139, March 2003.

[262] V. S. J. Craig. Very small bubbles at surfaces-the nanobubble puzzle. *Soft Matter*, 7(1):40–48, 2011.

[263] J. R. T. Seddon, D. Lohse, W. A. Ducker, and V. S. J. Craig. A Deliberation on Nanobubbles at Surfaces and in Bulk. *Chemphyschem*, 13(8):2179–2187, June 2012.

[264] J. P. Sethna. *Statistical Mechanics: Entropy, Order Parameters and Complexity*. Oxford Master Series in Physics. Oxford University Press, 2006.

[265] H. C. Andersen. Molecular-dynamics Simulations At Constant Pressure and-or Temperature. *Journal of Chemical Physics*, 72(4):2384–2393, 1980.

[266] S. Nose. A Molecular-dynamics Method For Simulations In the Canonical Ensemble. *Molecular Physics*, 52(2):255–268, 1984.

[267] W. G. Hoover. Canonical Dynamics: Equilibrium Phase-Space Distributions. *Physical Review A*, 31(3):1695–1697, 1985.

[268] H. J. C. Berendsen, J. P. M. Postma, W. F. van Gunsteren, A. Dinola, and J. R. Haak. Molecular dynamics with coupling to an external bath. *Journal of Chemical Physics*, 81(8):3684–3690, 1984.

[269] P. Hünenberger. Thermostat algorithms for molecular dynamics simulations. In C. Holm and K. Kremer, editors, *Advanced Computer Simulation*, volume 173 of *Advances in Polymer Science*, pages 105–147. Springer Berlin Heidelberg, 2005.

[270] B. Hess, H. Bekker, H. J. C. Berendsen, and J. G. E. M. Fraaije. LINCS: A linear constraint solver for molecular simulations. *Journal of Computational Chemistry*, 18(12):1463–1472, September 1997.

Appendix A

Influence of the temperature coupling

A.1 Molecular dynamics simulations at constant temperature require a thermostat with a coupling constant and a coupling scheme

Molecular dynamics simulations in the canonical ensemble require a simulation setup with constant number of particles N, constant volume V and constant temperature T. In the early days of molecular dynamics simulations, several

thermostats have been developed to assure the equilibration of the system at a desired temperature [47]. Among them are approaches from Andersen [265], Nosé and Hoover [266, 267] and Berendsen [268] - all of them contain advances and drawbacks [269]. Recently, a method for velocity rescaling was proposed by Bussi et al [231] and proved robust and capable of providing correct results.

Despite the pure choice of a specific thermostat, its application on the system requires careful thoughts and probably tests on stability and equilibration. Whereas the coupling constant is usually provided in the methodology part of reviewed articles, it is seldom described which parts of the system are coupled to the thermostat. In Fig. A.1 we present sketches of possible coupling schemes.

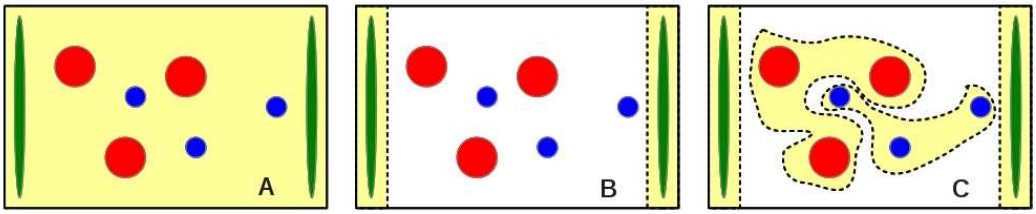

Figure A.1: Possible coupling schemes for the thermostat. The simulation box is defined through a black solid line, green ellipsoids refer to the electrodes, cations and anions are shown as large red and small blue spheres. In system A the whole box including electrodes and ions are coupled to the thermostat, as indicated by the yellow background colour. In system B the thermostat is only allowed to act on the electrodes (separately). System C shows the implementation of separate temperature coupling to the four sub-systems anode, cathode, anions and cations.

Whereas the attachment of the thermostat to the whole simulation box seems straightforward, it might influence heterogeneous systems - like (solid) electrodes and liquids - in an artificial way. Method B as shown in the Fig. A.1 is physically reasonable as the dielectric in a capacitor is usually surrounded by the electrode material and thus will be heated or cooled through the electrodes. However in molecular systems with a large distance between the electrodes, the influence of the thermostat might not be strong enough to assure a constant temperature in the liquid between the electrodes. Thus, scheme C with temperature coupling to both, electrodes and liquid, might be reasonable in specific cases.

In the following sections we present and discuss results of the temperature coupling schemes A and B. Note, that scheme C was applied by Fedorov and Kornyshev [7] for the same system.

A.2 Temperature coupling schemes under discussion: Whole system vs. only electrodes

We performed molecular dynamics (MD) simulations with Gromacs 4.5.5 [219]. All simulations were performed at fixed temperature. Velocity rescaling was used with a temperature coupling constant of 2.0 ps [231]. Further simulation parameter are described in Chapter 5.

A.2.1 Temperature coupling to the whole system: Artificially increasing restraining potential with negligible influence on the ion structuring

To discuss the equilibration behaviour of our specific system, we plotted the time evolution of the total energy and the resulting energy distributions of the system for all 1020 simulations. Details are given in Fig. A.2 and A.3.

The total energy E_{total}[1] is identical to the *internal energy* U and represents the sum of the *kinetic energy* E_{kin} and the *potential energy* E_{pot} of the whole system. The potential energy includes Coulombic contributions, Van-der-Waals contributions and finally, in our case, the restraining potential that is used to keep the electrode atoms at their positions.

Figure A.2 shows the time evolution of the total energy for several simulations at 450 K. Apparently the total energy does not reach a plateau for the lower surface charges in the first 10 ns as we expected from lower temperature simulations. Indeed, comparing the energy distributions of all temperatures for one specific surface charge, see Fig. A.3, we find smooth bell shaped curves for low temperatures for the same time interval, that shift to noisy skewed curves as the temperature is increased.

Upon analysing the energy terms that contribute to the total energy, we found that the restraining potential increases with time. All other potentials show a small drift of less than 3 %. The increase occurs for all surface charges and temperatures, indicating that it is connected with the electrode force field rather than the system geometry. The reason for seeing the effect only at high temperatures and low surface charges is the varying amplitude and sign of all other contributions to the total energy, resulting in a larger percentage of the restraining potential.

[1] The term total energy is used in the Gromacs analysis tool g_energy and accumulates all accessible energy terms.

We assume, that the increasing restraining potential is caused by a displacement of the electrode atoms, that increases slightly over time. A short estimation of the mean atom displacement results in $dz_{\text{electrode atom}} = 0.003\,\text{nm} = 0.03\,\text{Å}$. Apparently such a small displacement is not visible in most representations of the atomic structuring. However due to the large restraining potential constant $k = 100000\,\text{kJ}/(\text{mol} \cdot \text{nm}^2)$ and the large atom mass $m = 120.11\,\text{u}$, already a small displacement results in a large operating potential. Moreover the time step for the coarse grain model is chosen to be $dt = 0.01\,\text{ps}$. The high restraining potential for the electrode atoms combined with the large time step for the MD integrator result in an artificial escalation.

Despite the unfavourable parameter combination, does it have an influence on structural results we want to discuss in more detail in this work? Fortunately we can state that within the given simulation time of 35 ns the influence on the escalating restraining potential is negligible. The proof is presented in Fig. A.4, where the time evolution of four sample number density profiles is discussed. The number density profiles show within their fluctuations few deviations from the mean number density obtained as a sum of all profiles.

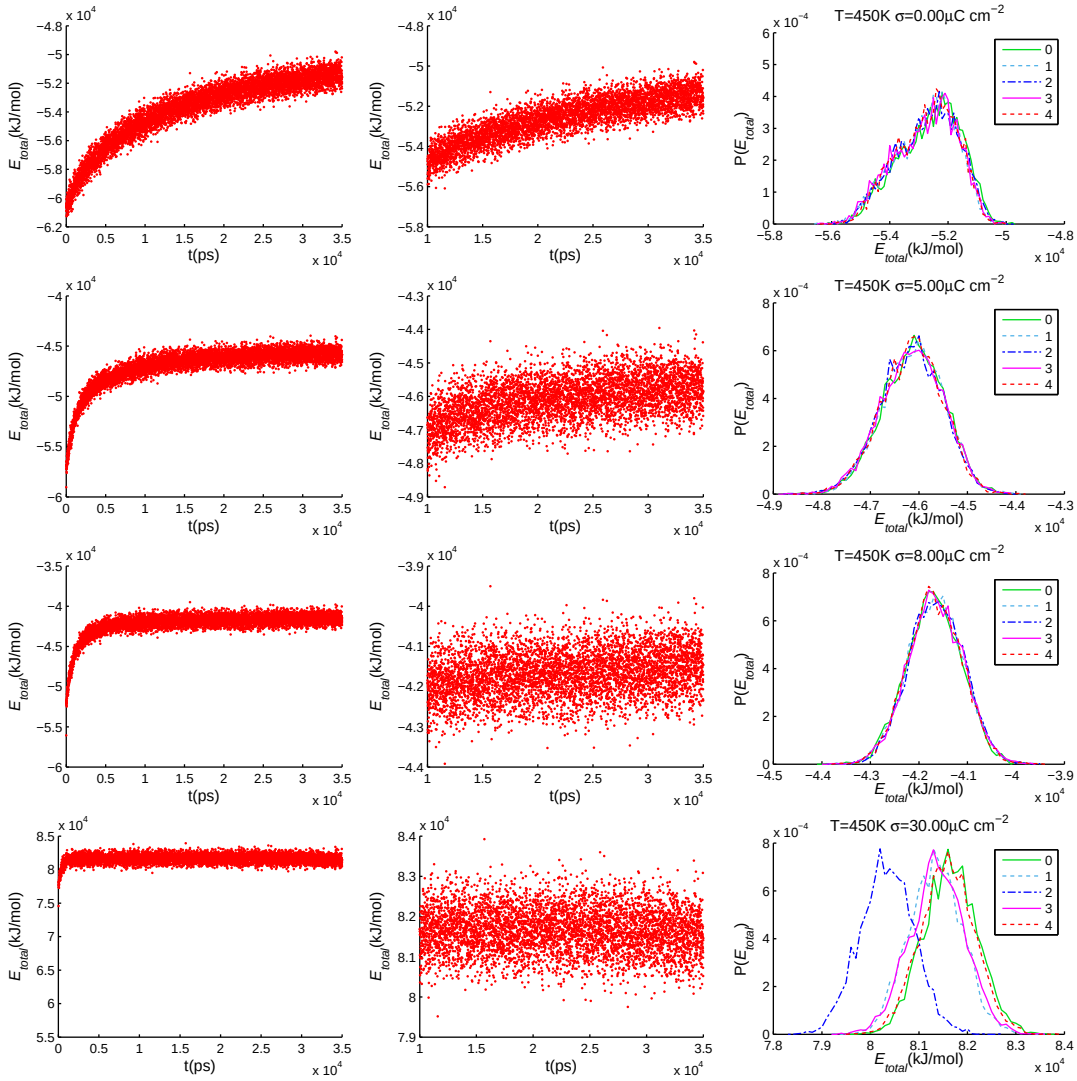

Figure A.2: Time evolution of the total energy and resulting energy distribution. (LEFT) Total energy plotted over time for the whole simulation time starting from 0 ns to 35 ns. Only one replica is shown. (MIDDLE) Close up of the left figure showing only the time interval 10 ns to 35 ns. Only one replica is shown. This interval is used for all (earlier and future) analysis steps. (RIGHT) Energy distribution of the time interval 10 ns to 35 ns for five replicas. From TOP to BOTTOM four different surface charges are shown: $\sigma = 0.00\,\mu\mathrm{C/cm^2}$, $\sigma = 5.00\,\mu\mathrm{C/cm^2}$, $\sigma = 8.00\,\mu\mathrm{C/cm^2}$ and $\sigma = 30.00\,\mu\mathrm{C/cm^2}$. All simulations shown here have been performed at 450 K.

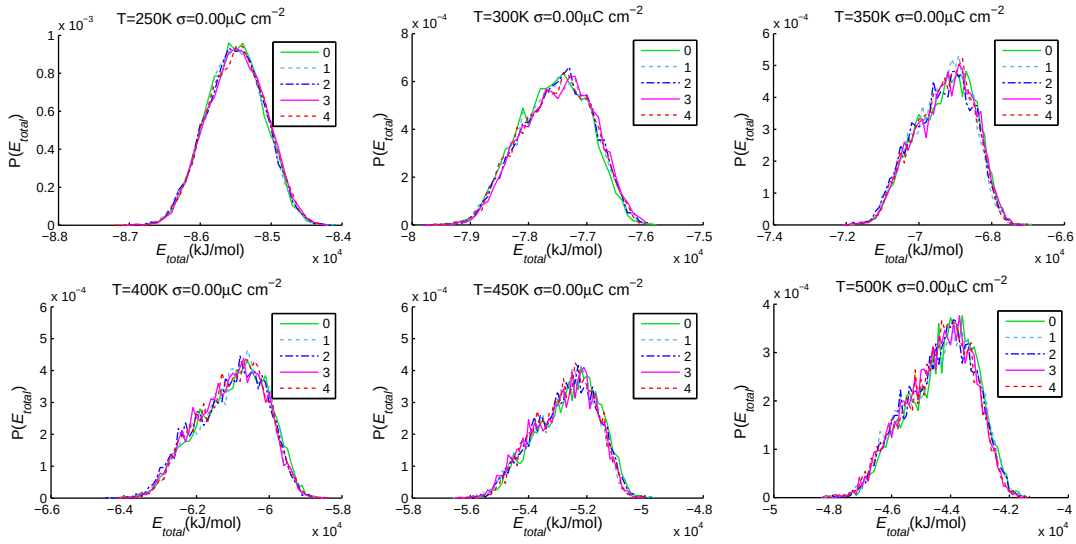

Figure A.3: Distribution of the total energy for all simulations at the surface charge density of $\sigma = 0.00\,\mu\mathrm{C/cm^2}$. From left to right and top to bottom, six different temperatures are shown: 250 K, 300 K, 350 K, 400 K, 450 K and 500 K. Every sub-figure contains the five replicas 0-4 that have been simulated.

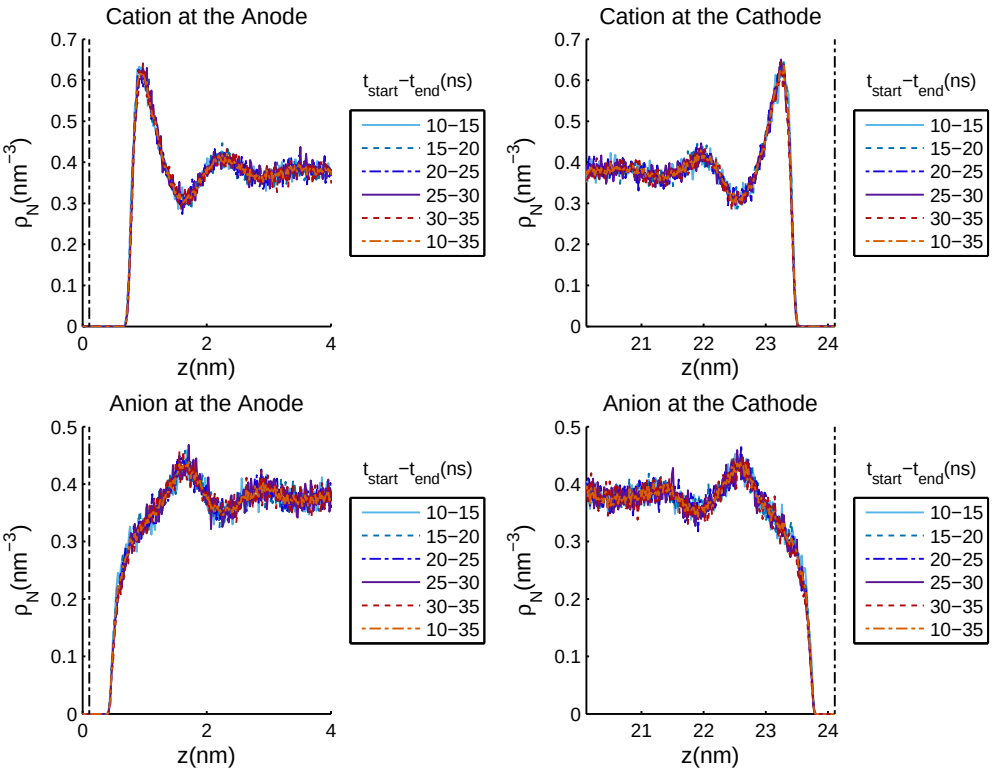

Figure A.4: Number density profile evolution with time for five different time intervals of 5 ns length each. The simulation has been carried out at $T = 450\,\mathrm{K}$ and $\sigma = 0.00\,\mu\mathrm{C/cm^2}$. The number density profiles within their fluctuations show few deviations from the mean number density obtained as a sum of all profiles (vermilion line). (LEFT) Anode; (RIGHT) Cathode. (TOP) Cations; (BOTTOM) Anions.

A.2.2 Solution: Temperature coupling only to the electrodes

The unfavourable parameter combination can be compensated by the application of a different temperature coupling scheme. Simulations, where only electrodes are coupled to the thermostat are compared with the simulations, where the whole box is coupled to the thermostat. Figure A.5 A.6, A.7, A.8 and Tab. A.1 provide insights in the differences between the coupling schemes.

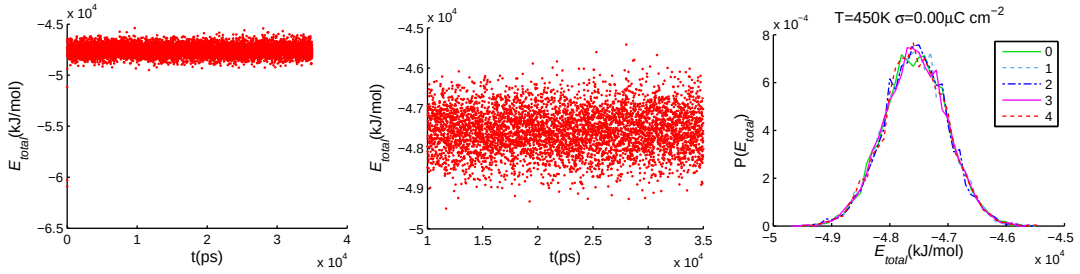

Figure A.5: Time evolution of the total energy and resulting energy distribution. (LEFT) Total energy plotted over time for the whole simulation time starting from 0 ns to 35 ns. Only one replica is shown. (MIDDLE) Close up of the left figure showing only the time interval 10 ns to 35 ns. Only one replica is shown. (RIGHT) Energy distribution of the time interval 10 ns to 35 ns for five replicas. All simulations shown here have been performed at 450 K and 0.00 μC/cm^2.

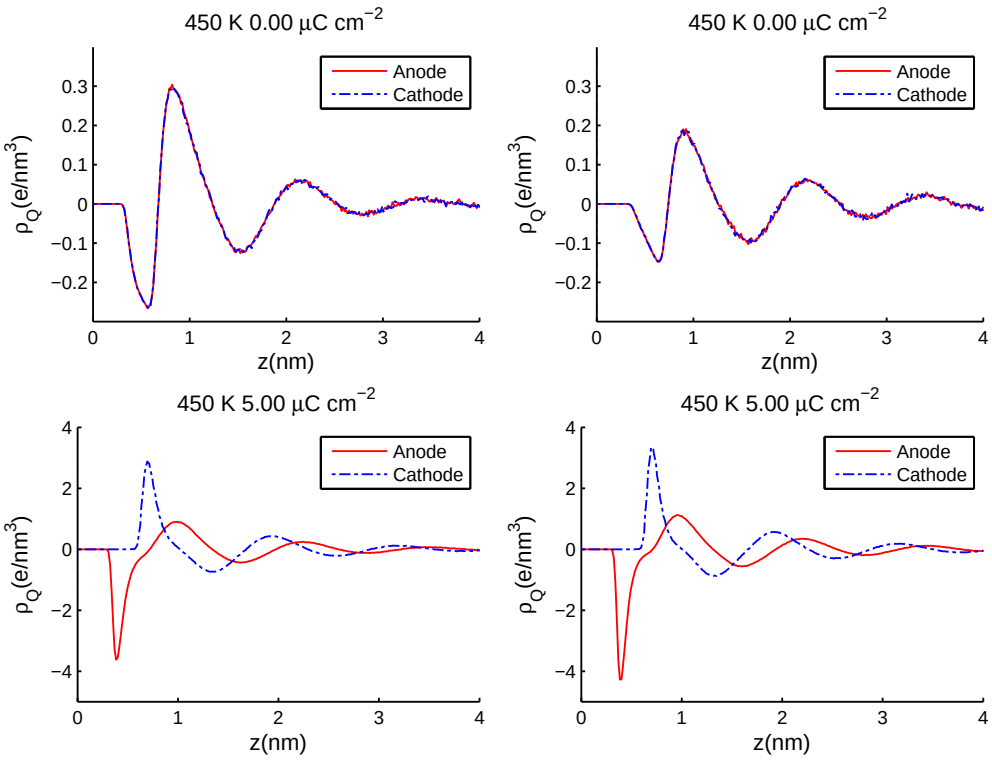

Figure A.6: Comparison of charge density profiles ρ_Q from different temperature coupling schemes. (LEFT) Temperature coupling applied on the whole simulation box, (RIGHT) Temperature coupling applied on the electrodes. (TOP) Neutral electrode $\sigma = 0.00\,\mu\text{C/cm}^2$; (BOTTOM) Surface charge density $\sigma = \pm 5.00\,\mu\text{C/cm}^2$. All simulations shown here have been performed at 450 K.

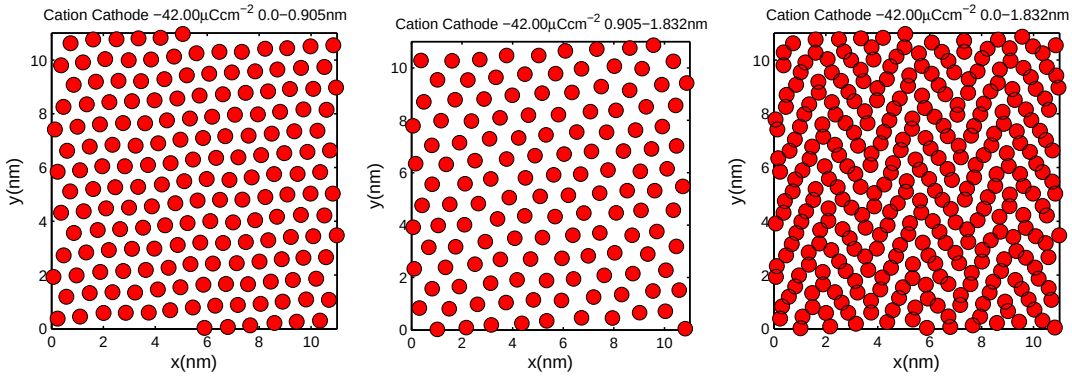

Figure A.7: Snapshots of the first two interfacial cation layers at the cathode at 450 K at a local compensation parameter of $\kappa = 2.62$ showing the construction of a herring bone structure. (LEFT) First interfacial layer, (MIDDLE) second interfacial layer and (RIGHT) first and second interfacial layer merged. Compare with Fig. 9.7 obtained by temperature coupling of the whole simulation box.

Table A.1: Comparison of potential drops for different temperature coupling schemes. Scheme A refers to temperature coupling applied on the whole simulation box, in scheme B only electrodes are coupled to the thermostat. Deviations are larger are lower surface charge densities σ, however the calculated potential drops fall still within the confidence interval and thus do not affect the resulting capacitance curves.

σ (μC/cm^2)	U_{drop} (V)	
	Scheme A	Scheme B
-42.0	-21.77	-21.77
-24.0	-9.845	-9.895
-16.0	-5.453	-5.560
-5.0	-1.419	-1.395
0.0	-0.09365	-0.07205
0.0	-0.07832	0.001447
5.0	0.4954	0.4469
16.0	1.687	1.679
24.0	3.005	3.076
42.0	6.139	6.129

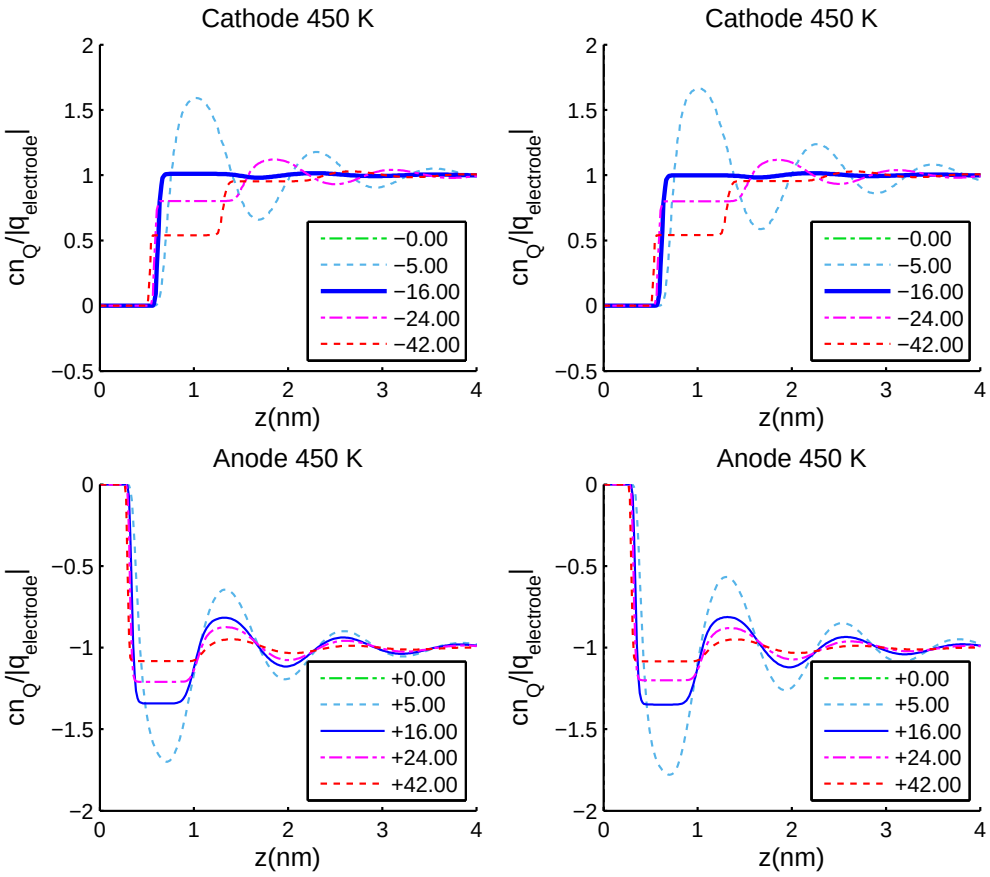

Figure A.8: Cumulative charge $cn_Q(z) = \int_0^z \rho_N(z')\mathrm{d}z'$ normalized by the number of elementary charges on the electrode $q_{\mathrm{electrode}}$. (LEFT) Temperature coupling applied on the whole simulation box, (RIGHT) Temperature coupling applied on the electrodes. (TOP) Cathode; (BOTTOM) Anode. Small deviations between the coupling schemes are only apparent at small surface charge densities. Especially the transition point at $\sigma = -16\,\mu\mathrm{C/cm}^2$ (blue thick curve) is not affected.

A.3 Conclusion and outlook

A.3.1 The coupling scheme might influence the system but does not affect qualitative results

Upon coupling the whole simulation box to a temperature bath, an unfavourable simulation parameter combination leads to an artificial escalation of the electrode restraining potential. Within our observation time, the influence of the increasing potential is negligible. A variation of the coupling scheme for the thermostat solves the increasing potential issue. However, the application of different coupling schemes might not be possible within every simulation software. Our results for different coupling schemes show the comparability of qualitative results, although quantitative results vary slightly under certain conditions. Thus, the final choice of the coupling scheme should depend on availability, stability and reliability.

A.3.2 Possible improvements of the simulation setup without changing the coupling scheme

The influence of the restraining potential does not seem to influence our current simulations, however the increasing restraining potential might destabilize the simulations in some cases. We suggest the following possibilities for improving the simulation setup without changing the temperature coupling scheme:

1. Decrease of the time step – Probably the simplest idea, but results in a considerable increase of computational costs;

2. Variation of the restraining potential constant and atom mass;

3. Using the LINCS algorithm [270] for position restraining instead of a harmonic restraining potential;

4. Modelling the electrode as one molecule – Currently one electrode is modelled as a combination of 2500 single atoms. The Lennard-Jones potential between wall atoms is set to zero, yet the Coulombic interaction is not excluded as it would be possible upon combining all electrode atoms into one single molecule. If the electrode is modelled as one molecule, one could investigate the influence of restraining only parts of the molecule to further reduce the influence of the restraining potential.

Appendix B

Extended simulation data

B.1 Energy distributions

To discuss the equilibration behaviour of our specific system, we plotted the time evolution of the total energy and the resulting energy distributions of the system for all 1020 simulations. The energy distributions for surface charge density of $\sigma = 0.00\,\mu\text{C/cm}^2$, $\sigma = 5.00\,\mu\text{C/cm}^2$, $\sigma = 16.00\,\mu\text{C/cm}^2$, $\sigma = 24.00\,\mu\text{C/cm}^2$, $\sigma = 26.00\,\mu\text{C/cm}^2$ and $\sigma = 30.00\,\mu\text{C/cm}^2$ are shown in Fig. B.1 to B.6.

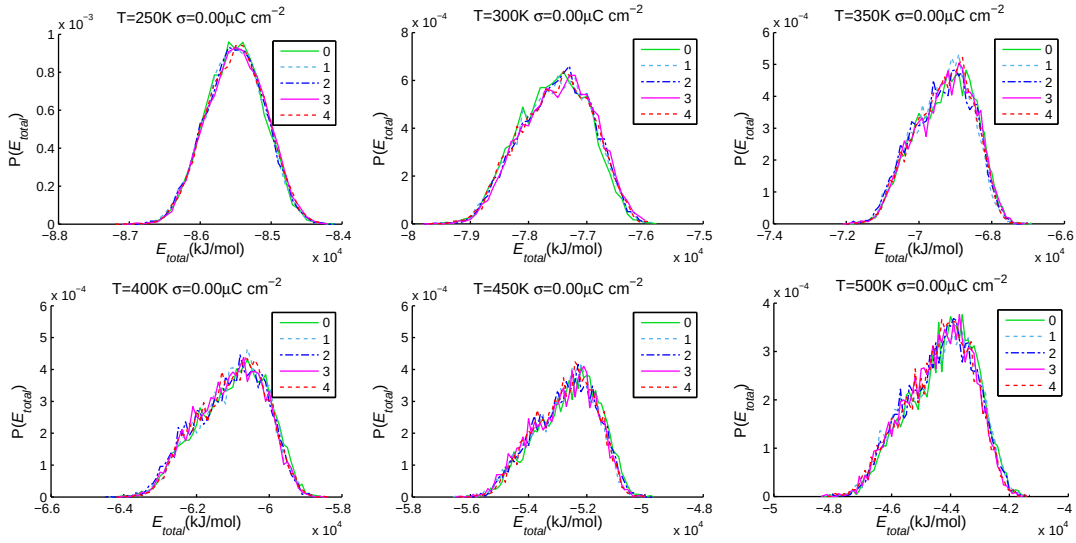

Figure B.1: Distribution of the total energy for all simulations at the surface charge density of $\sigma = 0.00\,\mu\mathrm{C/cm^2}$. From left to right and top to bottom, six different temperatures are shown: 250 K, 300 K, 350 K, 400 K, 450 K and 500 K. Every sub-figure contains the five replicas 0-4 that have been simulated.

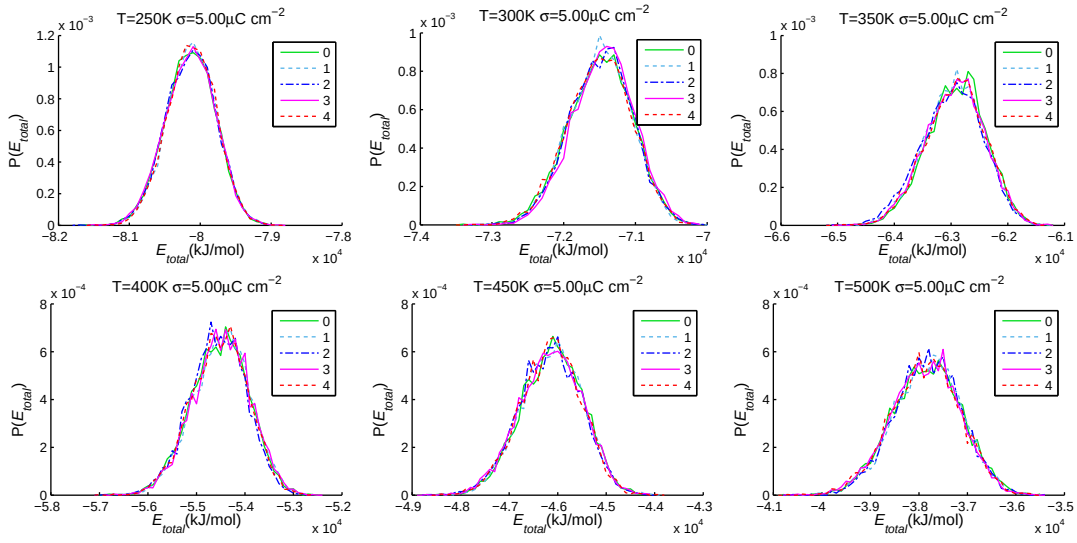

Figure B.2: Distribution of the total energy for all simulations at the surface charge density of $\sigma = 5.00\,\mu\mathrm{C/cm^2}$. From left to right and top to bottom, six different temperatures are shown: 250 K, 300 K, 350 K, 400 K, 450 K and 500 K. Every sub-figure contains the five replicas 0-4 that have been simulated.

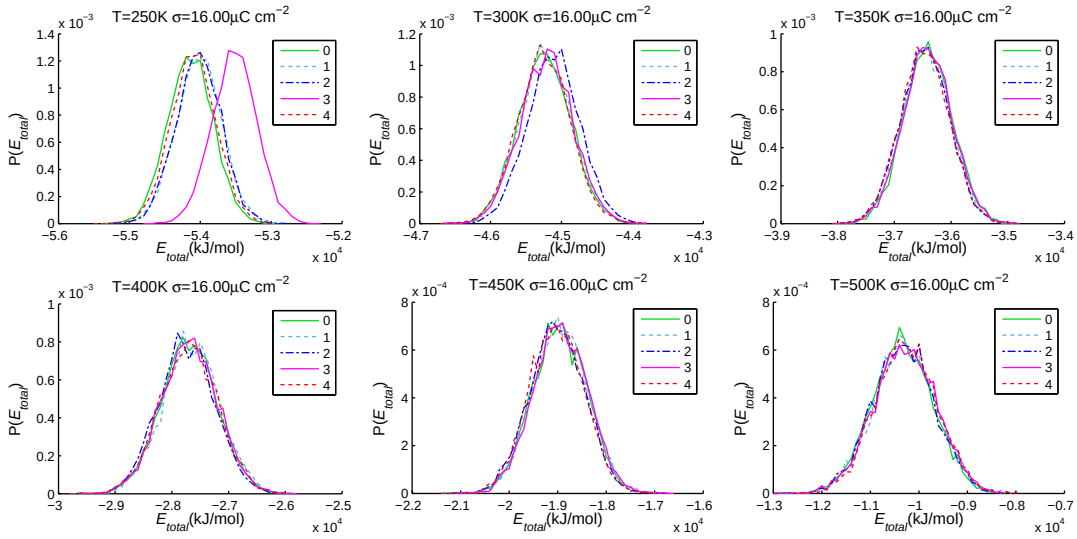

Figure B.3: Distribution of the total energy for all simulations at the surface charge density of $\sigma = 16.00\,\mu\mathrm{C/cm^2}$. From left to right and top to bottom, six different temperatures are shown: 250 K, 300 K, 350 K, 400 K, 450 K and 500 K. Every sub-figure contains the five replicas 0-4 that have been simulated.

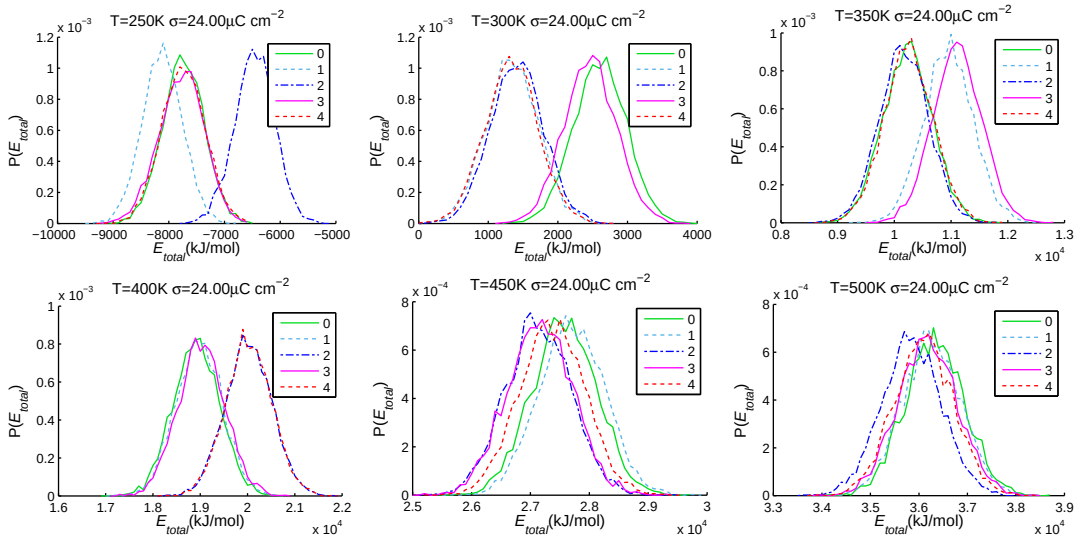

Figure B.4: Distribution of the total energy for all simulations at the surface charge density of $\sigma = 24.00\,\mu\mathrm{C/cm^2}$. From left to right and top to bottom, six different temperatures are shown: 250 K, 300 K, 350 K, 400 K, 450 K and 500 K. Every sub-figure contains the five replicas 0-4 that have been simulated.

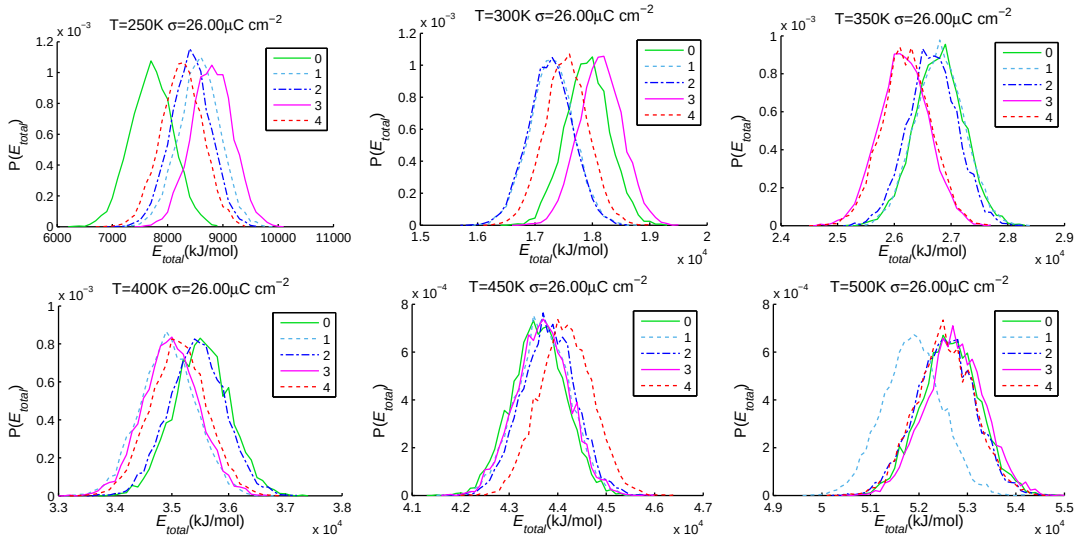

Figure B.5: Distribution of the total energy for all simulations at the surface charge density of $\sigma = 26.00\,\mu\mathrm{C/cm^2}$. From left to right and top to bottom, six different temperatures are shown: 250 K, 300 K, 350 K, 400 K, 450 K and 500 K. Every sub-figure contains the five replicas 0-4 that have been simulated.

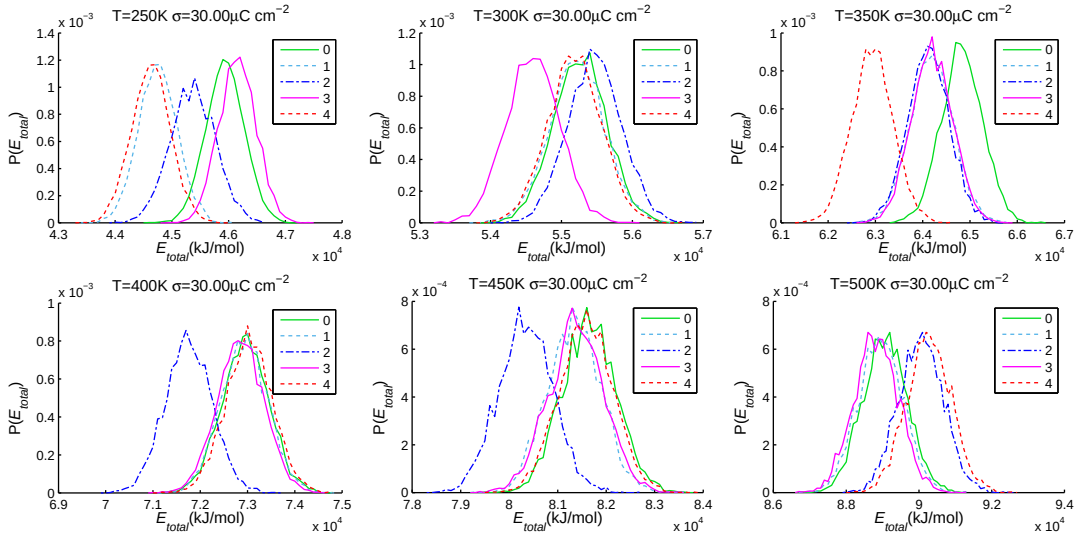

Figure B.6: Distribution of the total energy for all simulations at the surface charge density of $\sigma = 30.00\,\mu\mathrm{C/cm^2}$. From left to right and top to bottom, six different temperatures are shown: 250 K, 300 K, 350 K, 400 K, 450 K and 500 K. Every sub-figure contains the five replicas 0-4 that have been simulated.

B.2 Differential capacitance - close-ups and supplementary material

B.2.1 Tabulated potential drop for all temperatures under study

Table B.1: The potential drop in V for all temperatures under study. The potential drop is obtained from the smoothing spline fit.

$\sigma\,(\mu\mathrm{C/cm^2})$	$T = 250\,\mathrm{K}$	$T = 300\,\mathrm{K}$	$T = 350\,\mathrm{K}$	$T = 400\,\mathrm{K}$	$T = 450\,\mathrm{K}$	$T = 500\,\mathrm{K}$
-50.0	-29.23	-29.44	-29.39	-29.64	-29.86	-29.52
-24.0	-9.881	-9.95	-10.01	-10	-9.937	-9.976
-16.0	-5.714	-5.678	-5.69	-5.652	-5.609	-5.654
-12.0	-3.846	-3.837	-3.844	-3.83	-3.852	-3.872
-10.0	-3.001	-3.023	-3.036	-3.039	-3.095	-3.101
-8.0	-2.265	-2.302	-2.325	-2.335	-2.402	-2.402
-5.0	-1.419	-1.414	-1.45	-1.437	-1.455	-1.467
-3.5	-1.027	-1.006	-1.041	-1.019	-1.012	-1.029
-2.0	-0.5791	-0.5746	-0.6019	-0.5881	-0.5867	-0.5967
-1.0	-0.2922	-0.3023	-0.3193	-0.3163	-0.3253	-0.3265
0.0	-0.06667	-0.0764	-0.08003	-0.08491	-0.09565	-0.08895
1.0	0.1008	0.09613	0.1058	0.09618	0.08936	0.09973
2.0	0.2283	0.2209	0.2408	0.2287	0.2258	0.2342
3.5	0.3625	0.3542	0.3858	0.3743	0.383	0.3865
5.0	0.4555	0.4646	0.5054	0.4991	0.5293	0.5333
8.0	0.6829	0.7171	0.7596	0.7616	0.8233	0.8344
10.0	0.9362	0.949	0.9779	0.9765	1.031	1.044
12.0	1.244	1.22	1.229	1.219	1.253	1.265
16.0	1.897	1.815	1.788	1.76	1.749	1.75
24.0	3.197	3.128	3.065	3.011	2.952	2.91
50.0	9.234	9.291	9.088	8.913	8.676	8.457

B.2.2 Potential of zero charge (PZC)

The potential of zero charge (PZC) is tabulated in Tab. B.2. The potential is slightly negative indicating a preferential adsorption of anions at the electrodes. This is expected due to the asymmetry of the ion sizes. With increasing temperature the PZC decreases further. Indeed the increased temperature should result in an increase of the entropy of the anions which is considered as the driving process of the ion adsorption at the uncharged repulsive electrode. The potential decrease is visible for all temperatures, but the strength of the effect lies within the error bars - and thus might not be overestimated.

Table B.2: The potential of zero charge (PZC) for all temperatures under study. The experimental values for both electrodes (left and right uncharged sheet) are labelled as 'electrode 1' and 'electrode 2'. In the 'fit' column the PZC is obtained from the smoothing spline fit. The deviation of the spline fit from the experimental values provides an estimate for the error or reliability of the results. The maximum error is approximately $\pm 0.025\,\mathrm{V}$.

T (K)	PZC (V)		
	electrode 1	electrode 2	fit
250	-0.0937	-0.0456	-0.0667
300	-0.0869	-0.0703	-0.0764
350	-0.1232	-0.0524	-0.0800
400	-0.0958	-0.0795	-0.0849
450	-0.0912	-0.0898	-0.0957
500	-0.1009	-0.0837	-0.0890

B.2.3 Smoothed surface charge vs. potential drop and resulting differential and integral capacitance

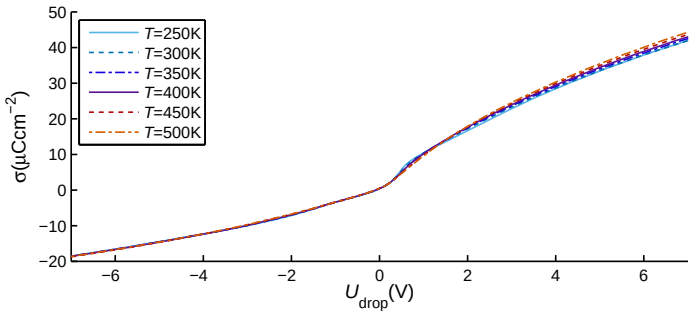

(a) Smoothed surface charge vs. potential drop

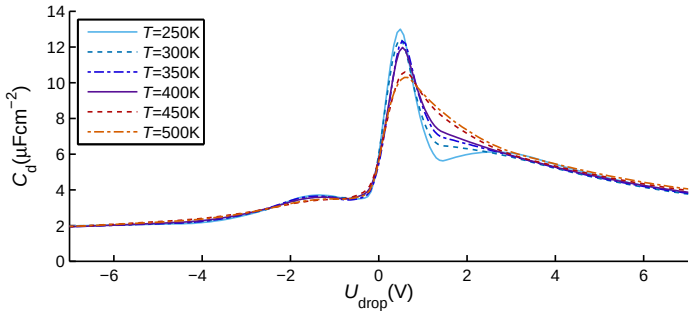

(b) Differential capacitance

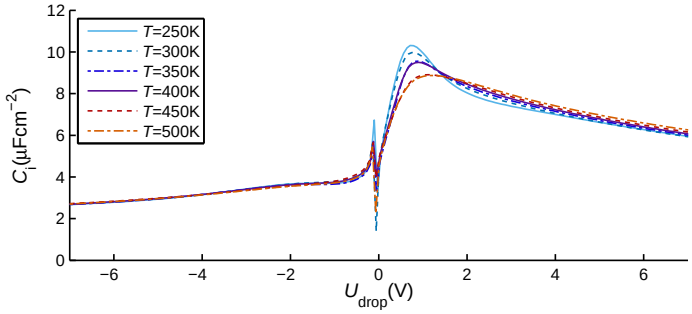

(c) Integral capacitance

Figure B.7: The smoothed potential drop and the resulting capacitance curves. (a) Smoothed surface charge vs. potential drop. (b) Differential capacitance as the result of differentiating the smoothed surface charge vs. potential drop curves. (c) Integral capacitance calculated by dividing the surface charge through the smoothed potential drop; the PZC is subtracted from the smoothed potential drop before the division.

B.2.4 Differential capacitance - cathodic part

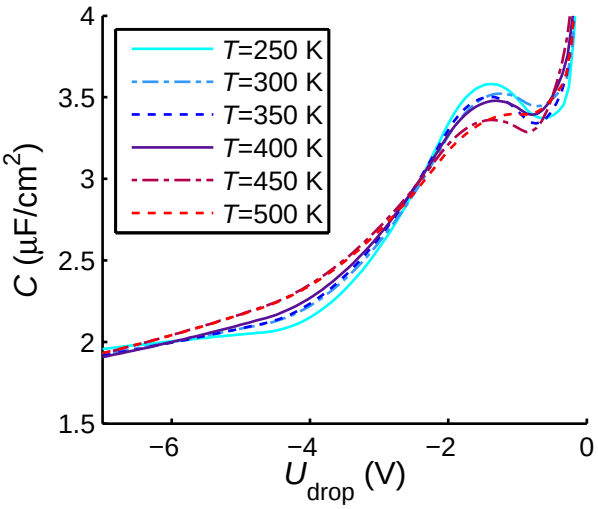

Figure B.8: Differential capacitance C_d as a function of the potential drop U_{drop} for six different temperatures T ranging from 250 K to 500 K; only the cathodic part is shown. The same change in temperature dependence as in the anodic part is visible. However, the size of the effect is much smaller.

B.2.5 Error estimation of the differential capacitance: asymptotic extrapolation and smoothing of the surface charge vs. potential drop dependency

Table B.3: Error analysis of the spline fit of the surface charge vs. potential drop dependency. Sample corrected sum of squares S_{xx}, S_{yy} and S_{xy} are given here together with the residual (error) mean square s. The total number of samples equals 340. Obviously the error of the surface charge vs. potential drop fit s increases with increasing temperature. However the effect can be considered as small as the percental difference between 250 K and 500 K is 2.2 %. We conclude that the observed temperature dependency in the differential capacitance is not a matter of insufficient smooth data.

$T\,(\mathrm{K})$	$S_{xx}\,(10^4\,\mathrm{V}^2)$	$S_{yy}\,(10^5\,\mu\mathrm{C}^2/\mathrm{cm}^4)$	$S_{xy}\,(10^4\,\mathrm{V}\mu\mathrm{C}/\mathrm{cm}^2)$	$s\,(\mu\mathrm{C}/\mathrm{cm}^2)$
250	1.6386	1.3485	4.2776	8.2826
300	1.6334	1.3485	4.2668	8.3205
350	1.6239	1.3485	4.2508	8.3529
400	1.6228	1.3485	4.2430	8.4125
450	1.6195	1.3485	4.2331	8.4630
500	1.6092	1.3485	4.2183	8.4758

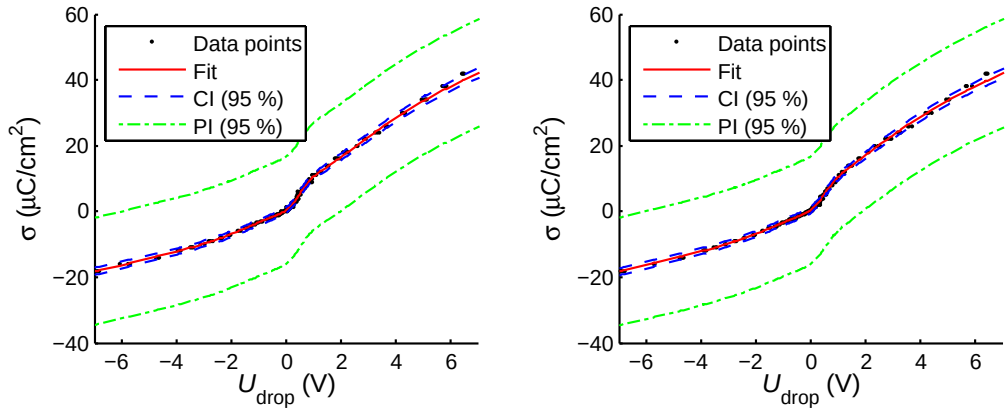

(a) 250 K

(b) 300 K

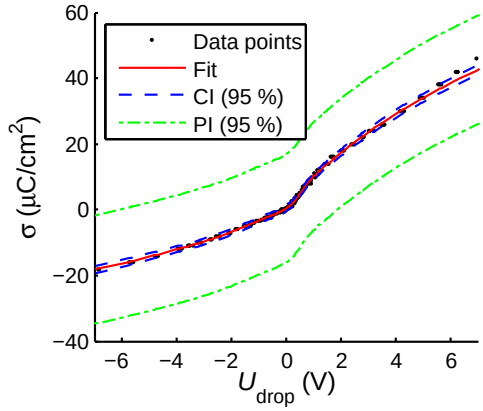

(c) 350 K

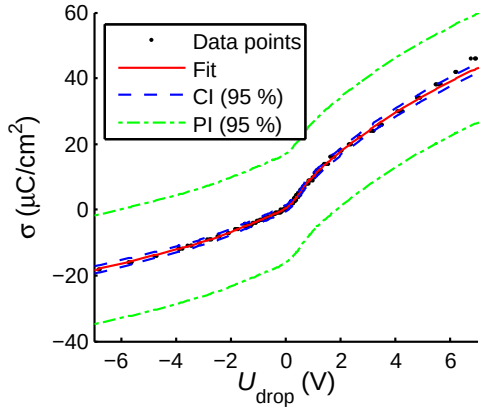

(d) 400 K

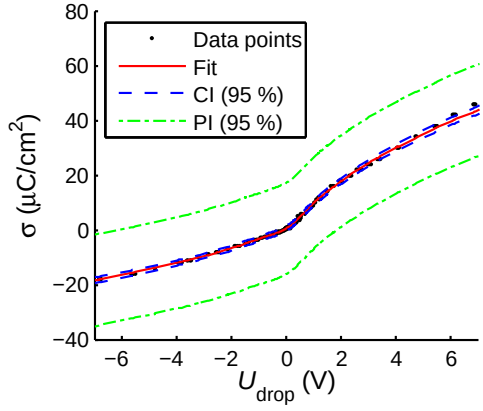

(e) 450 K

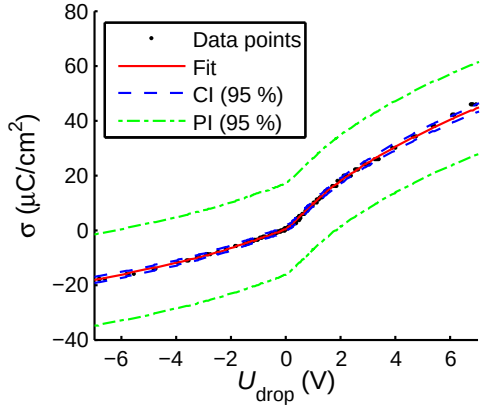

(f) 500 K

Figure B.9: Error analysis of the spline fit of the surface charge vs. potential drop dependency. Five replicas taken into account. The confidence level equals 95 % and the total number of samples 340. Confidence interval (CI) and prediction interval (PI) are calculated.

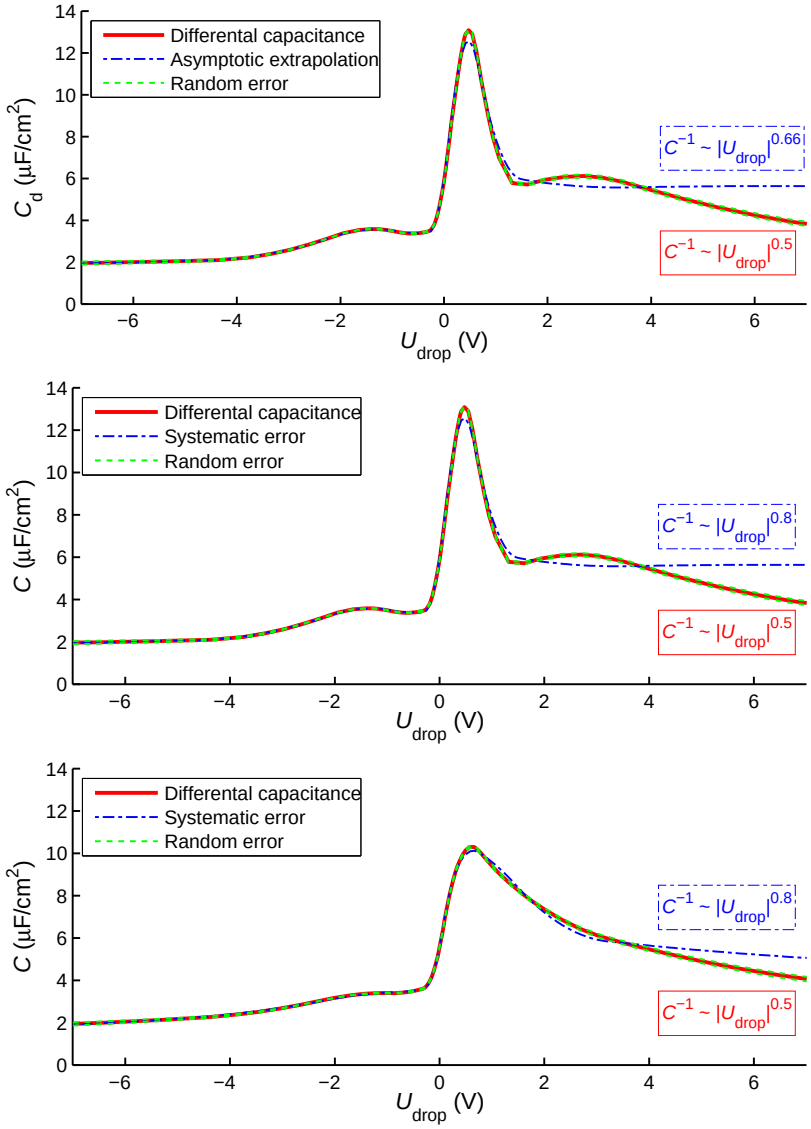

Figure B.10: Differential capacitance at (Top,Middle) 250 K and (Bottom) 500 K including error estimation. The blue dashed curve represent the systematic error introduced by the asymptotic extrapolation of the surface charge vs. potential drop data. The assumption was made that the asymptotes follow a $|U_{\mathrm{drop}}|^{0.5}$ dependency. The blue graph is calculated by assuming an asymptotic behaviour of $|U_{\mathrm{drop}}|^{\lambda(T)}$, with $\lambda(250\,\mathrm{K}) = 0.66$ and $\lambda(500\,\mathrm{K}) = 0.8$. For further discussion of the errors see text. The green dashed curve represents the random error introduced by the quality of the potential drop estimation from MD simulations. This error can be reduced by increasing the number of configurations that are sampled (e.g. by increasing the simulation time or the number of replicas). The random error is calculated by differentiating the upper and lower confidence interval (CI) of the surface charge vs. potential drop dependency. The resulting errors between 0.4 % and 4.7 % equal a maximum error of $C = 0.1\,\mu\mathrm{C/cm^2}$.

B.2.6 Asymptotic extrapolation and the resulting capacitance

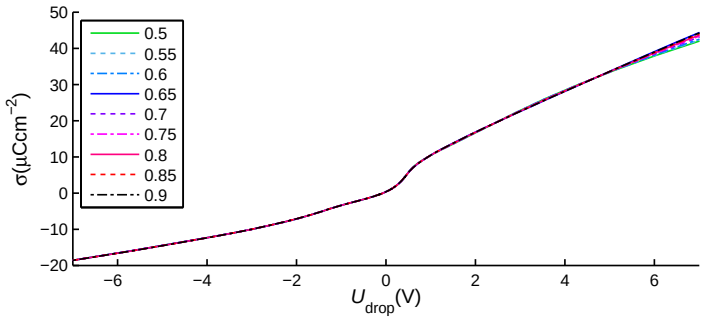

(a) Smoothed surface charge vs. potential drop

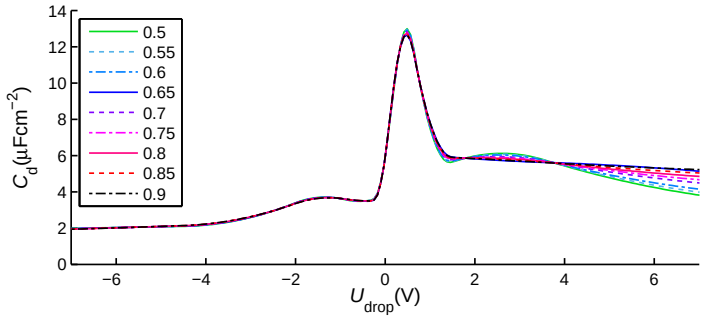

(b) Differential capacitance

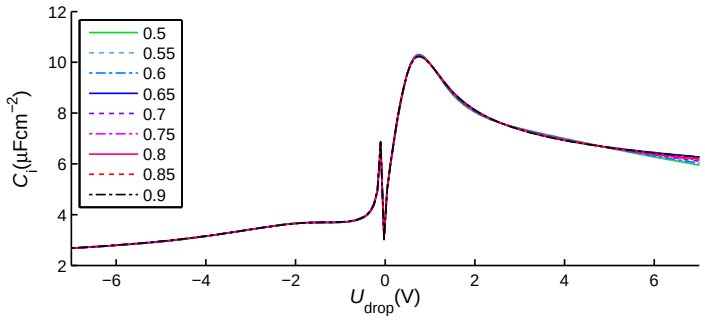

(c) Integral capacitance

Figure B.11: The smoothed potential drop and the resulting capacitance curves at 250 K and different asymptotic extrapolations $|U_{\mathrm{drop}}|^{\lambda}$. The exponent for the asymptotic extrapolation λ varies between 0.5 (theoretical value) and 0.9. (a) Smoothed surface charge vs. potential drop. (b) Differential capacitance as the result of differentiating the smoothed surface charge vs. potential drop curves. (c) Integral capacitance calculated by dividing the surface charge through the smoothed potential drop; the PZC is subtracted from the smoothed potential drop before the division.

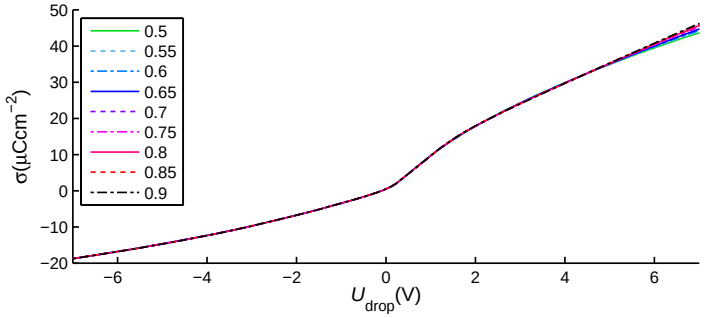

(a) Smoothed surface charge vs. potential drop

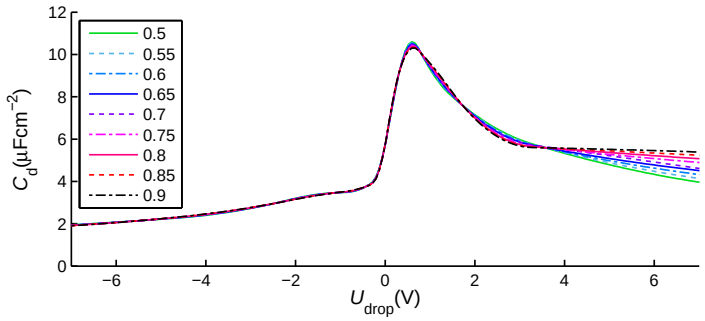

(b) Differential capacitance

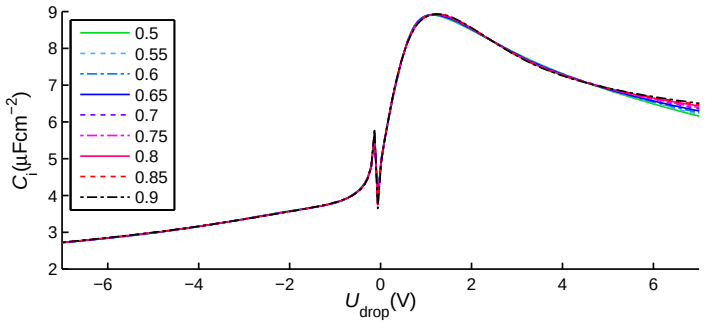

(c) Integral capacitance

Figure B.12: The smoothed potential drop and the resulting capacitance curves at 450 K and different asymptotic extrapolations $|U_{\mathrm{drop}}|^{\lambda}$. The exponent for the asymptotic extrapolation λ varies between 0.5 (theoretical value) and 0.9. (a) Smoothed surface charge vs. potential drop. (b) Differential capacitance as the result of differentiating the smoothed surface charge vs. potential drop curves. (c) Integral capacitance calculated by dividing the surface charge through the smoothed potential drop; the PZC is subtracted from the smoothed potential drop before the division.

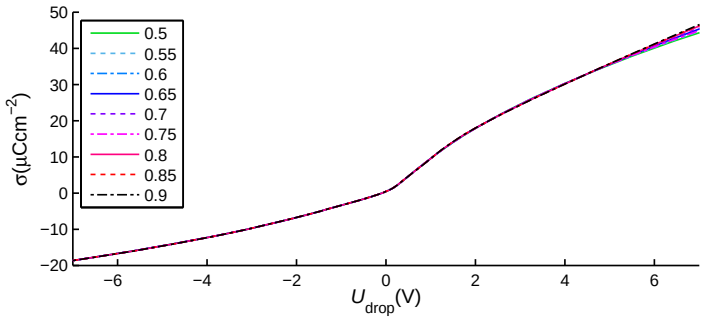

(a) Smoothed surface charge vs. potential drop

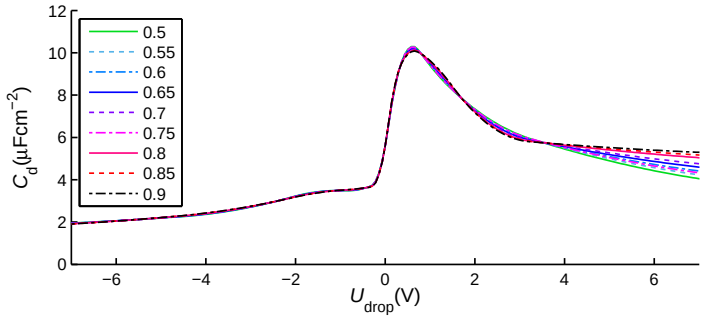

(b) Differential capacitance

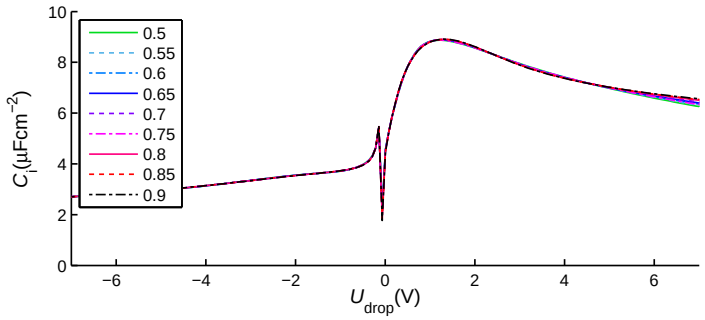

(c) Integral capacitance

Figure B.13: The smoothed potential drop and the resulting capacitance curves at 500 K and different asymptotic extrapolations $|U_{\mathrm{drop}}|^{\lambda}$. The exponent for the asymptotic extrapolation λ varies between 0.5 (theoretical value) and 0.9. (a) Smoothed surface charge vs. potential drop. (b) Differential capacitance as the result of differentiating the smoothed surface charge vs. potential drop curves. (c) Integral capacitance calculated by dividing the surface charge through the smoothed potential drop; the PZC is subtracted from the smoothed potential drop before the division.

B.3 Number density profiles and cumulative number, charge density profiles and cumulative charge

B.3.1 Number density profiles and charge density profiles in comparison

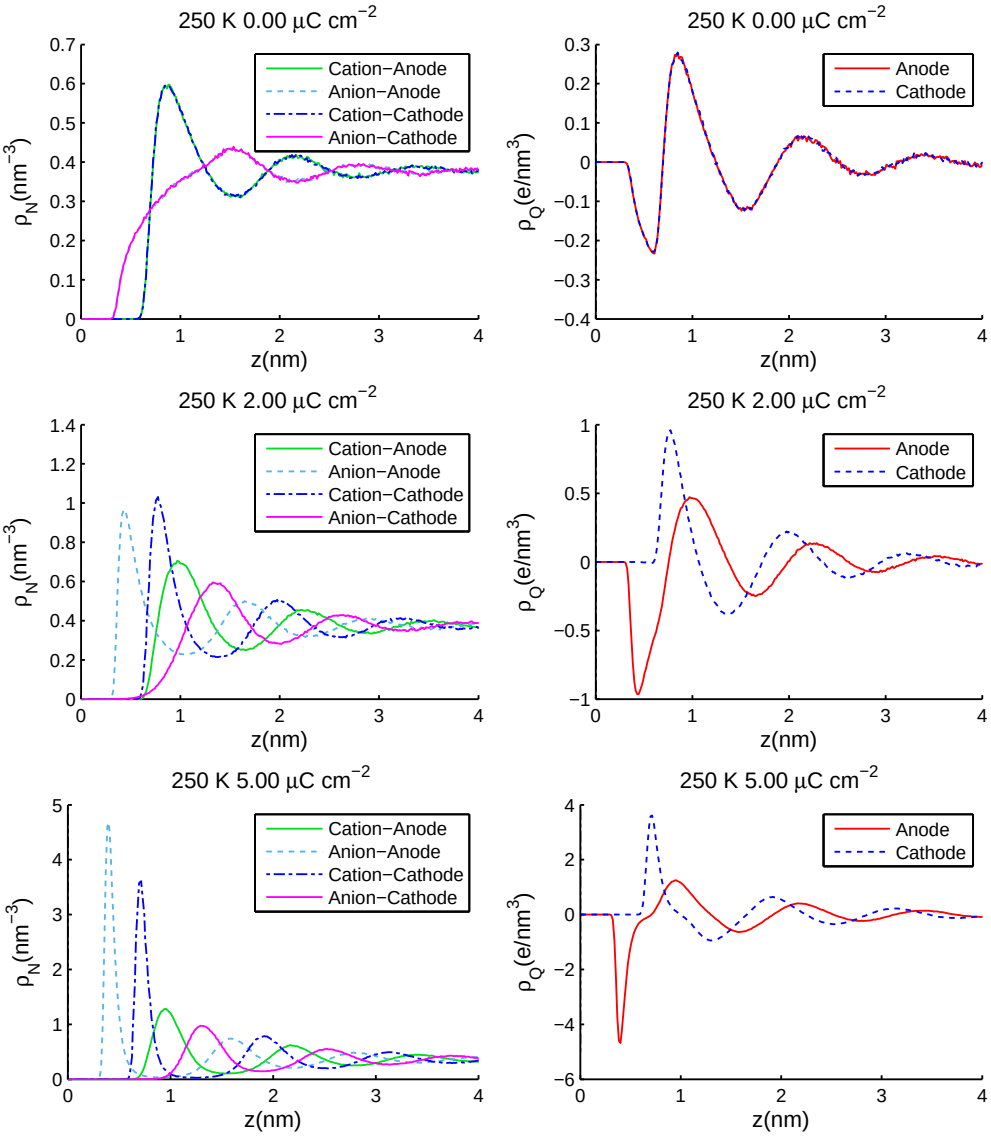

Figure B.14: Number density and charge density profiles for different surface charges at $T = 250\,\mathrm{K}$. The centre of mass of the electrode atoms are situated on the xy-plane with $z = 0$. (LEFT) Number density profile, (RIGHT) Charge density profile. (TOP) Surface charge $\sigma = 0.0\,\mu\mathrm{C/cm^2}$ corresponding to the PZC, (MIDDLE) Surface charge $\sigma = 2.0\,\mu\mathrm{C/cm^2}$ corresponding to $U_{\mathrm{drop}} = +0.23\,\mathrm{V}$, (BOTTOM) Surface charge $\sigma = 5.0\,\mu\mathrm{C/cm^2}$ corresponding to $U_{\mathrm{drop}} = +0.46\,\mathrm{V}$.

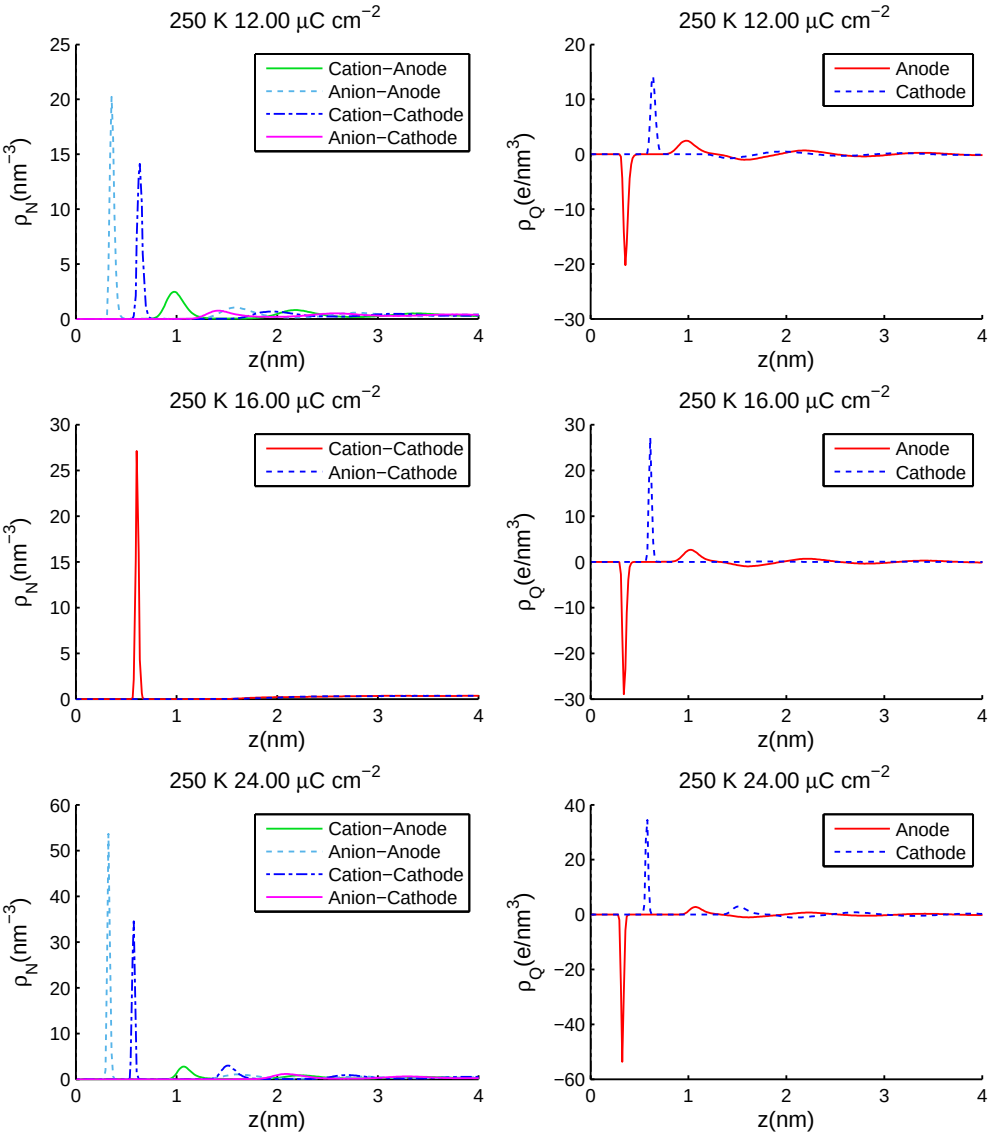

Figure B.15: Number density and charge density profiles for different surface charges at $T = 250\,\mathrm{K}$. The centre of mass of the electrode atoms are situated on the xy-plane with $z = 0$. (LEFT) Number density profile, (RIGHT) Charge density profile. (TOP) Surface charge $\sigma = 12.0\,\mu\mathrm{C/cm^2}$ corresponding to $U_{\mathrm{drop}} = +1.24\,\mathrm{V}$, (MIDDLE) Surface charge $\sigma = 16.0\,\mu\mathrm{C/cm^2}$ corresponding to $U_{\mathrm{drop}} = +1.90\,\mathrm{V}$, (BOTTOM) Surface charge $\sigma = 24.0\,\mu\mathrm{C/cm^2}$ corresponding to $U_{\mathrm{drop}} = +3.20\,\mathrm{V}$.

B.3.2 Number density profiles and cumulative number

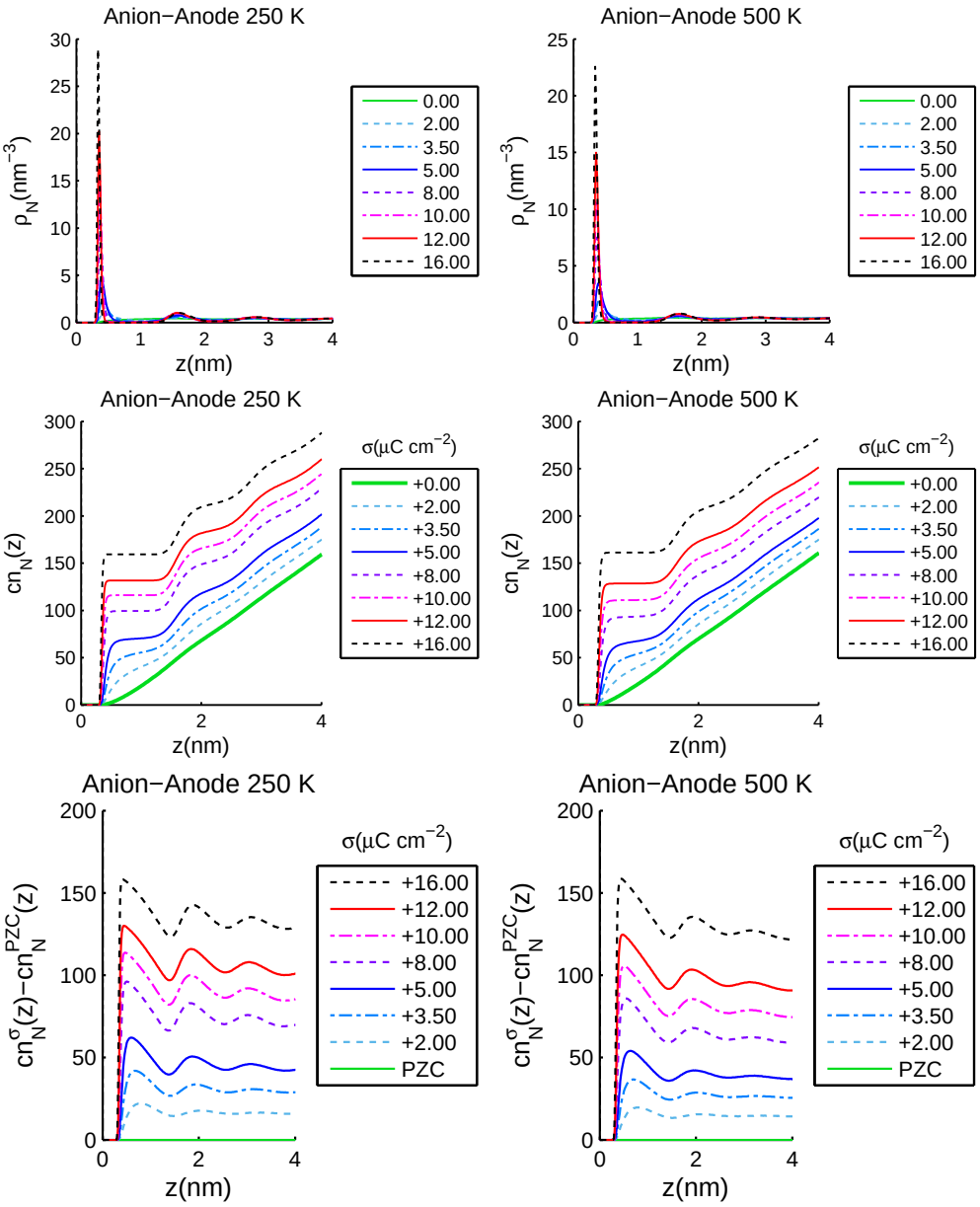

Figure B.16: Number density of Anions at the Anode for different surface charges σ in μC/cm^2. The centre of mass of the electrode atoms are situated on the xy-plane with $z = 0$. (LEFT) $T = 250\,\mathrm{K}$, (RIGHT) $T = 500\,\mathrm{K}$. (TOP) Number density profile, (MIDDLE) Cumulative number density profile, (BOTTOM) Cumulative number differences with PZC being the reference curve.

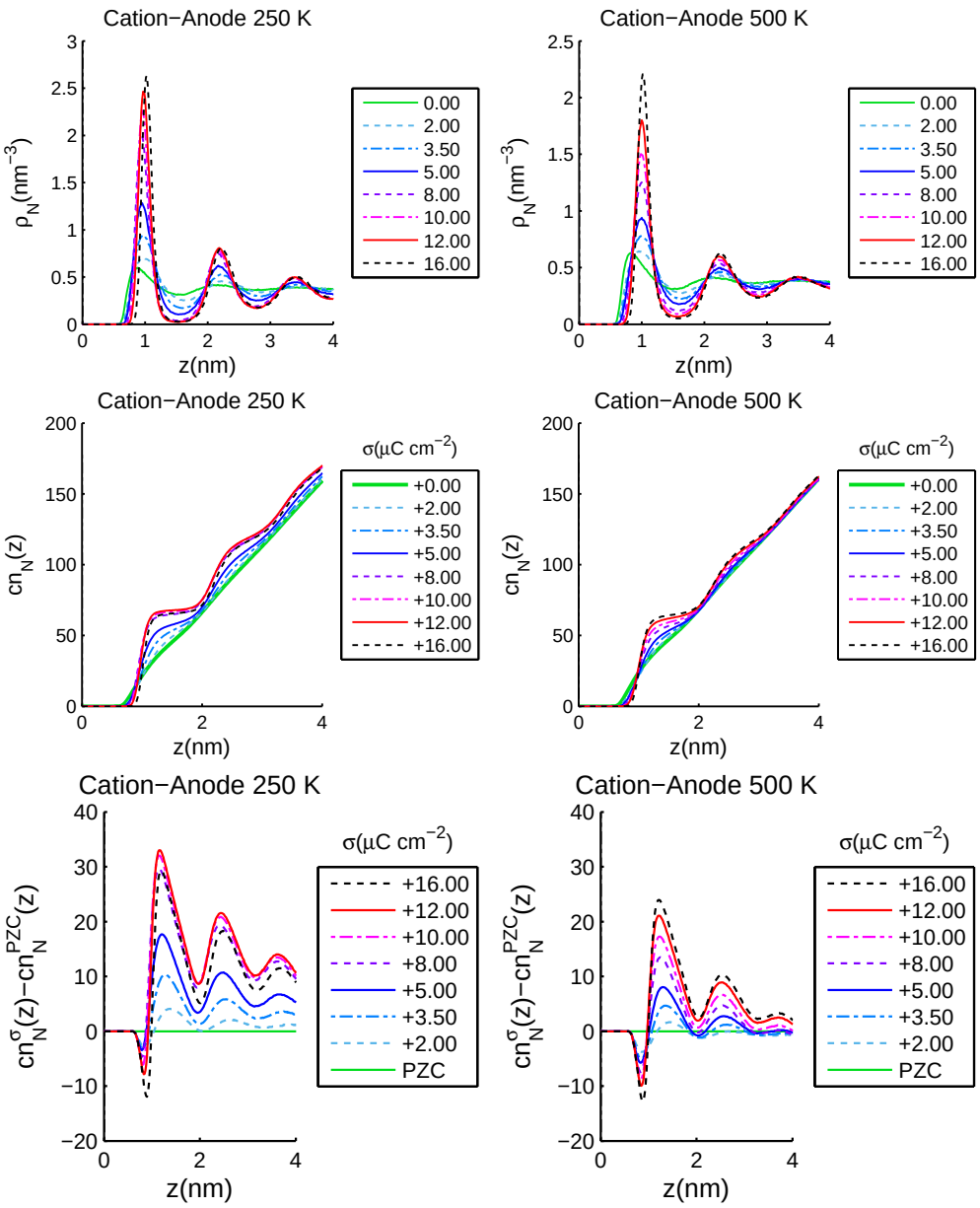

Figure B.17: Number density of Cations at the Anode for different surface charges. The centre of mass of the electrode atoms are situated on the xy-plane with $z = 0$. (LEFT) $T = 250\,\mathrm{K}$, (RIGHT) $T = 500\,\mathrm{K}$. (TOP) Number density profile, (MIDDLE) Cumulative number density profile, (BOTTOM) Cumulative number differences with PZC being the reference curve.

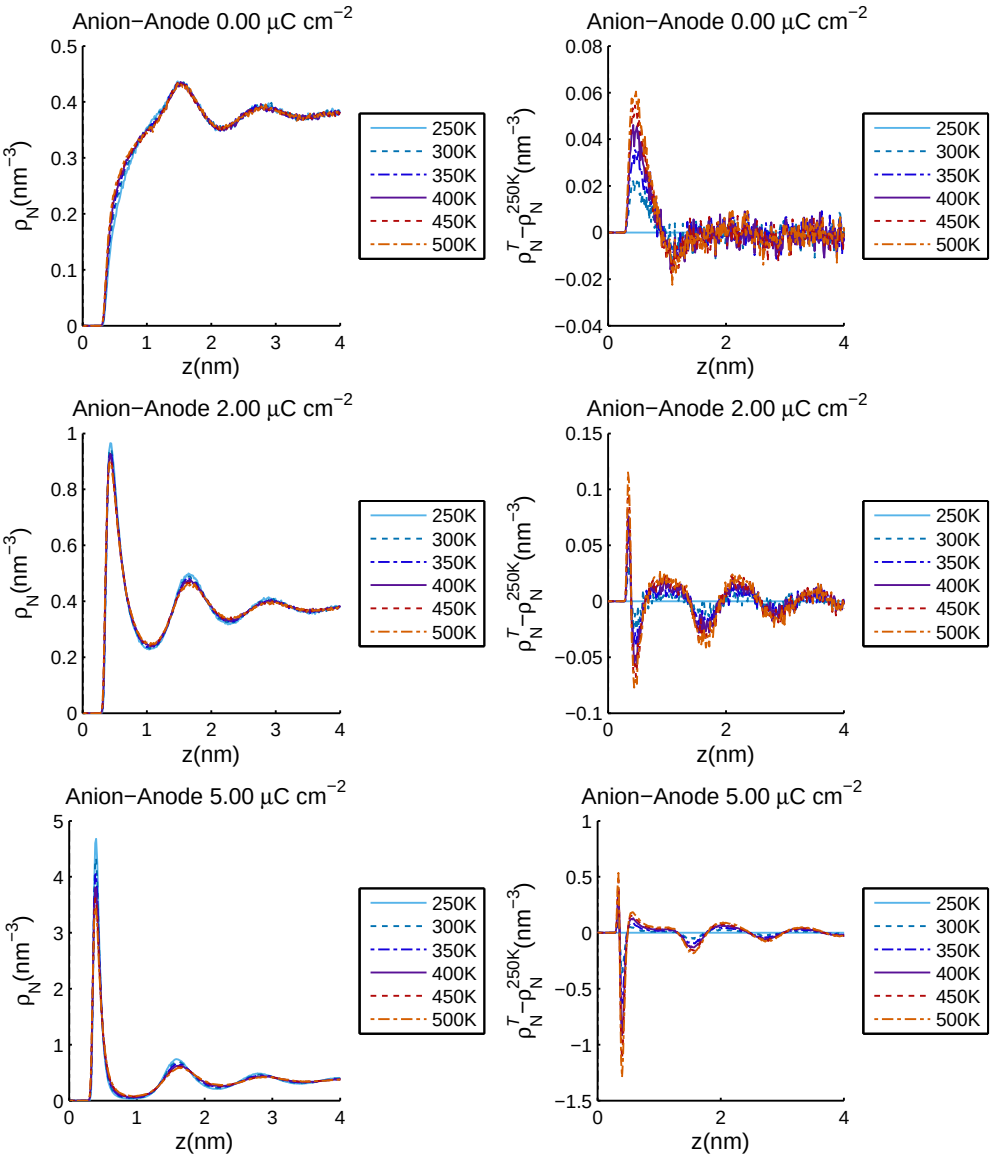

Figure B.18: Number density of Anions at the Anode for different temperatures. The centre of mass of the electrode atoms are situated on the xy-plane with $z = 0$. (LEFT) Number density profile, (RIGHT) Number density profile difference with the 250 K curve being the reference curve. (TOP) Surface charge $\sigma = 0.0\,\mu\mathrm{C/cm^2}$, (MIDDLE) Surface charge $\sigma = 2.0\,\mu\mathrm{C/cm^2}$, (BOTTOM) Surface charge $\sigma = 5.0\,\mu\mathrm{C/cm^2}$.

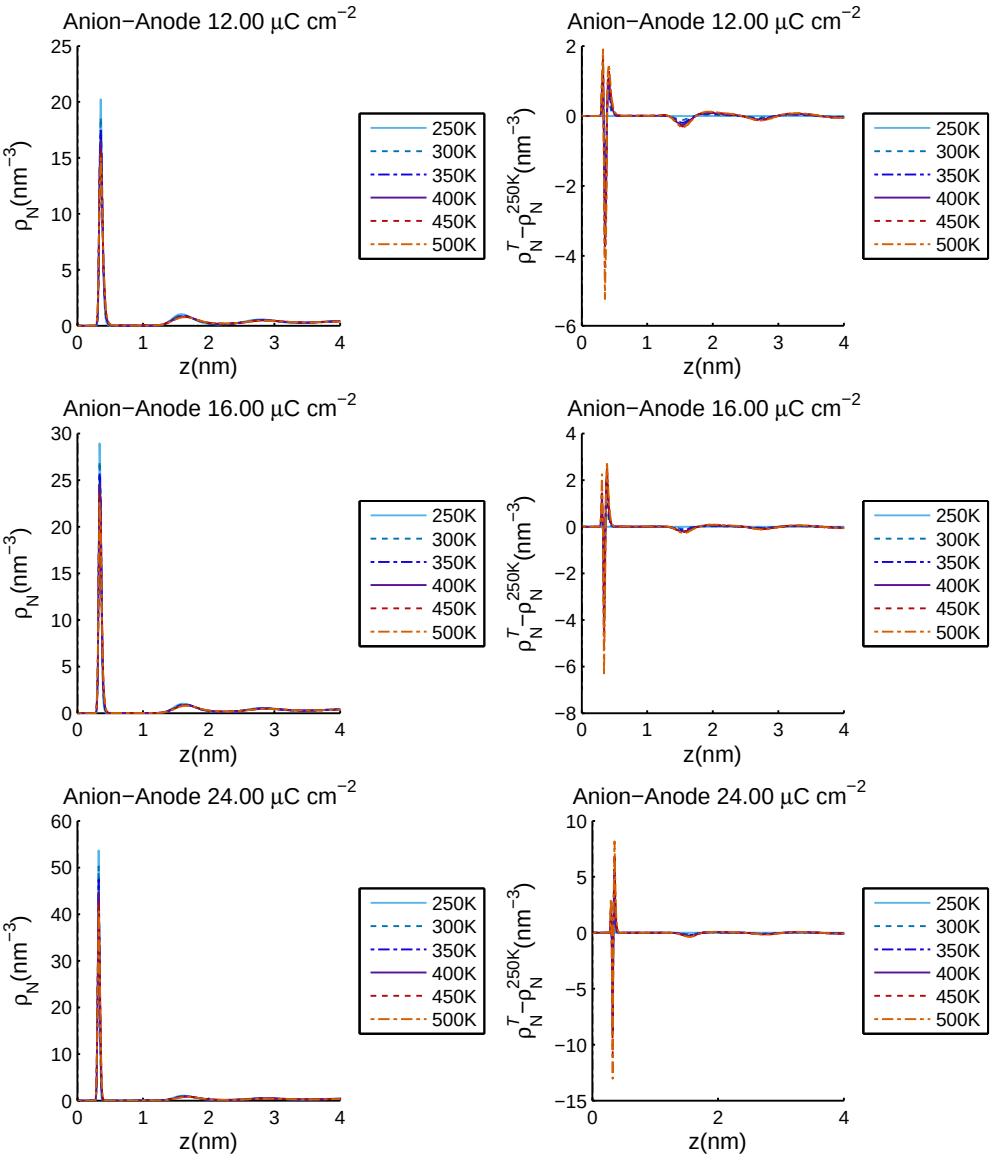

Figure B.19: Number density of Anions at the Anode for different temperatures. The centre of mass of the electrode atoms are situated on the xy-plane with $z = 0$. (LEFT) Number density profile, (RIGHT) Number density profile difference with the 250 K curve being the reference curve. (TOP) Surface charge $\sigma = 12.0\,\mu\text{C/cm}^2$, (MIDDLE) Surface charge $\sigma = 16.0\,\mu\text{C/cm}^2$, (BOTTOM) Surface charge $\sigma = 24.0\,\mu\text{C/cm}^2$.

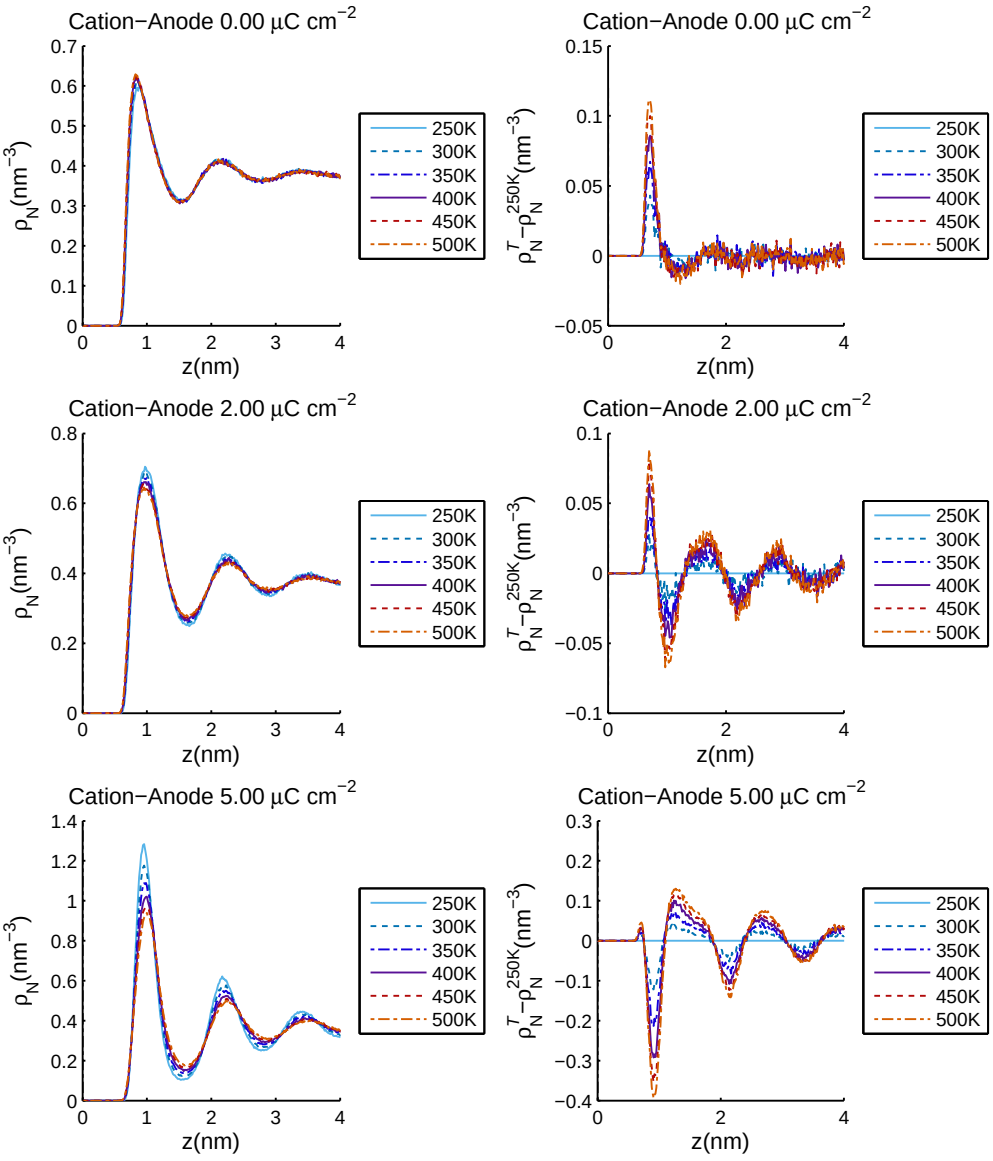

Figure B.20: Number density of Cations at the Anode for different temperatures. The centre of mass of the electrode atoms are situated on the xy-plane with $z = 0$. (LEFT) Number density profile, (RIGHT) Number density profile difference with the 250 K curve being the reference curve. (TOP) Surface charge $\sigma = 0.0\,\mu\mathrm{C/cm^2}$, (MIDDLE) Surface charge $\sigma = 2.0\,\mu\mathrm{C/cm^2}$, (BOTTOM) Surface charge $\sigma = 5.0\,\mu\mathrm{C/cm^2}$.

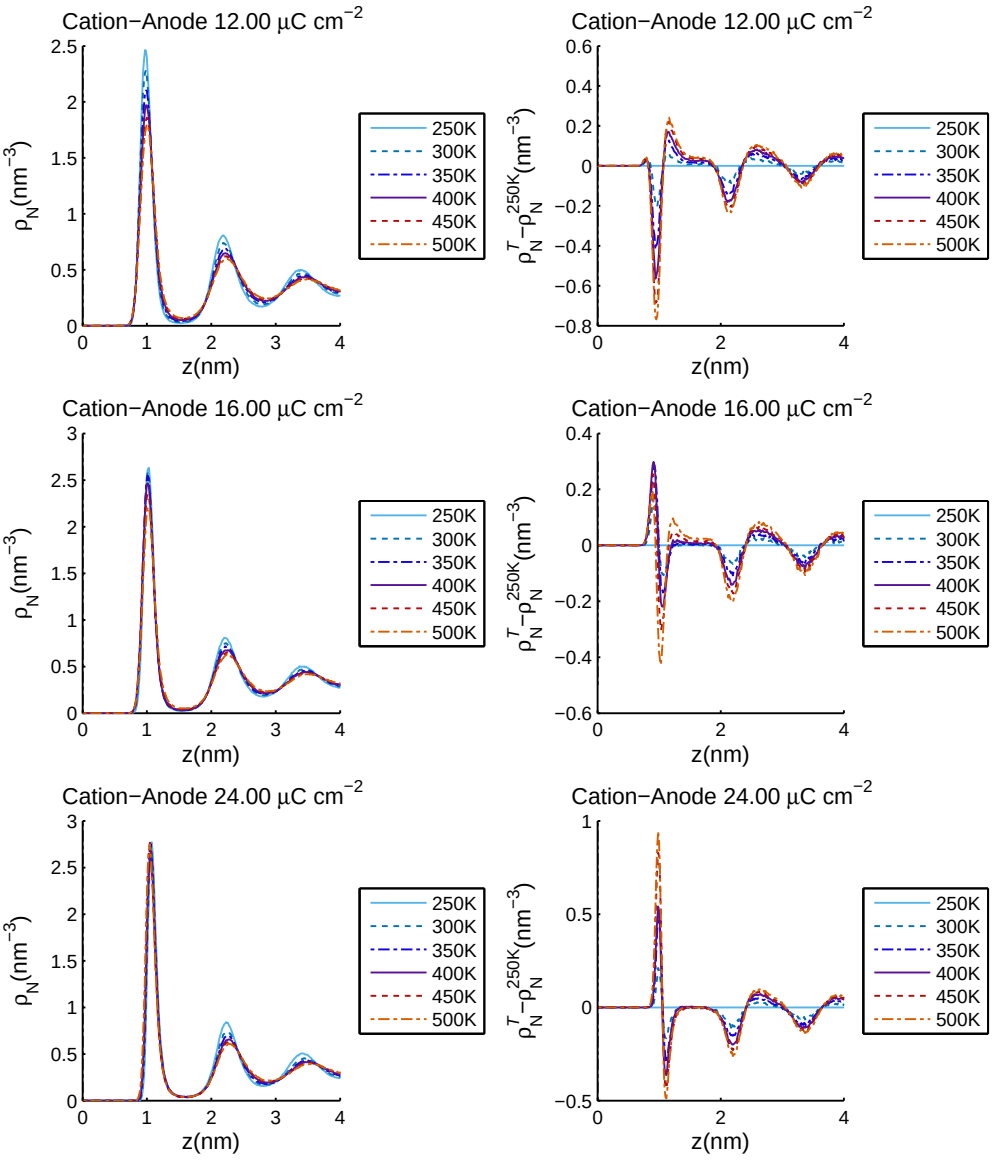

Figure B.21: Number density of Cations at the Anode for different temperatures. The centre of mass of the electrode atoms are situated on the xy-plane with $z = 0$. (LEFT) Number density profile, (RIGHT) Number density profile difference with the 250 K curve being the reference curve. (TOP) Surface charge $\sigma = 12.0\,\mu\text{C/cm}^2$, (MIDDLE) Surface charge $\sigma = 16.0\,\mu\text{C/cm}^2$, (BOTTOM) Surface charge $\sigma = 24.0\,\mu\text{C/cm}^2$.

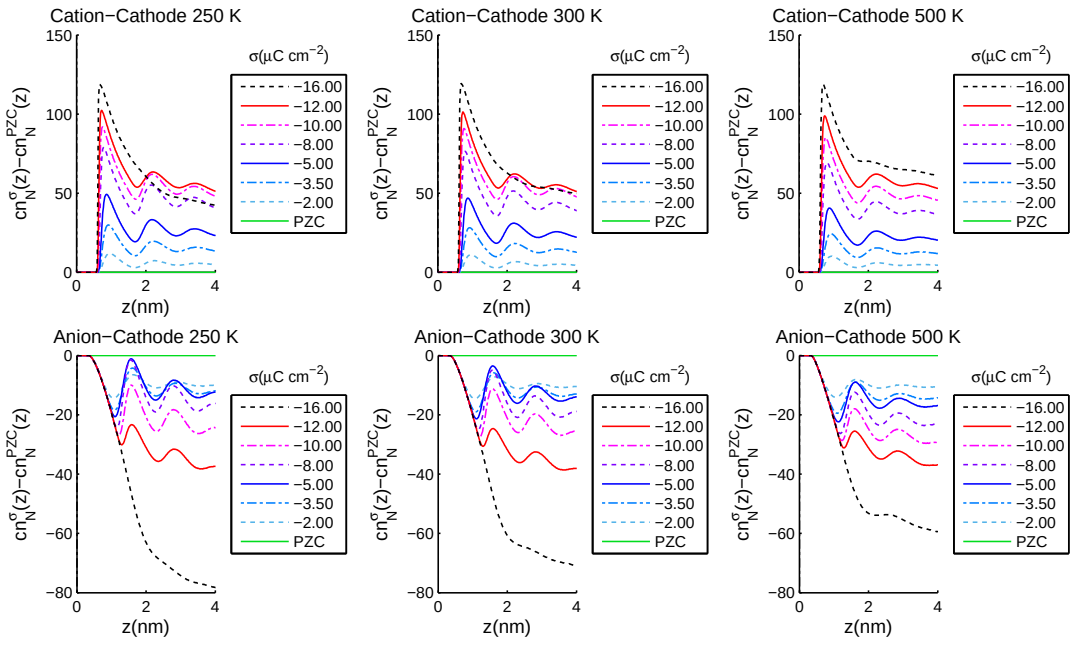

Figure B.22: Cumulative number differences of (TOP) cations and (BOTTOM) anions - with PZC curve being the reference curve - at the negatively charged electrode (cathode) for different surface charges between $-2.00\,\mu\mathrm{C/cm^2}$ and $-16.00\,\mu\mathrm{C/cm^2}$. From left to right three different temperatures are considered: (a) 250 K, (b) 300 K and (c) 500 K.

B.3.3 Charge density profile and cumulative charge

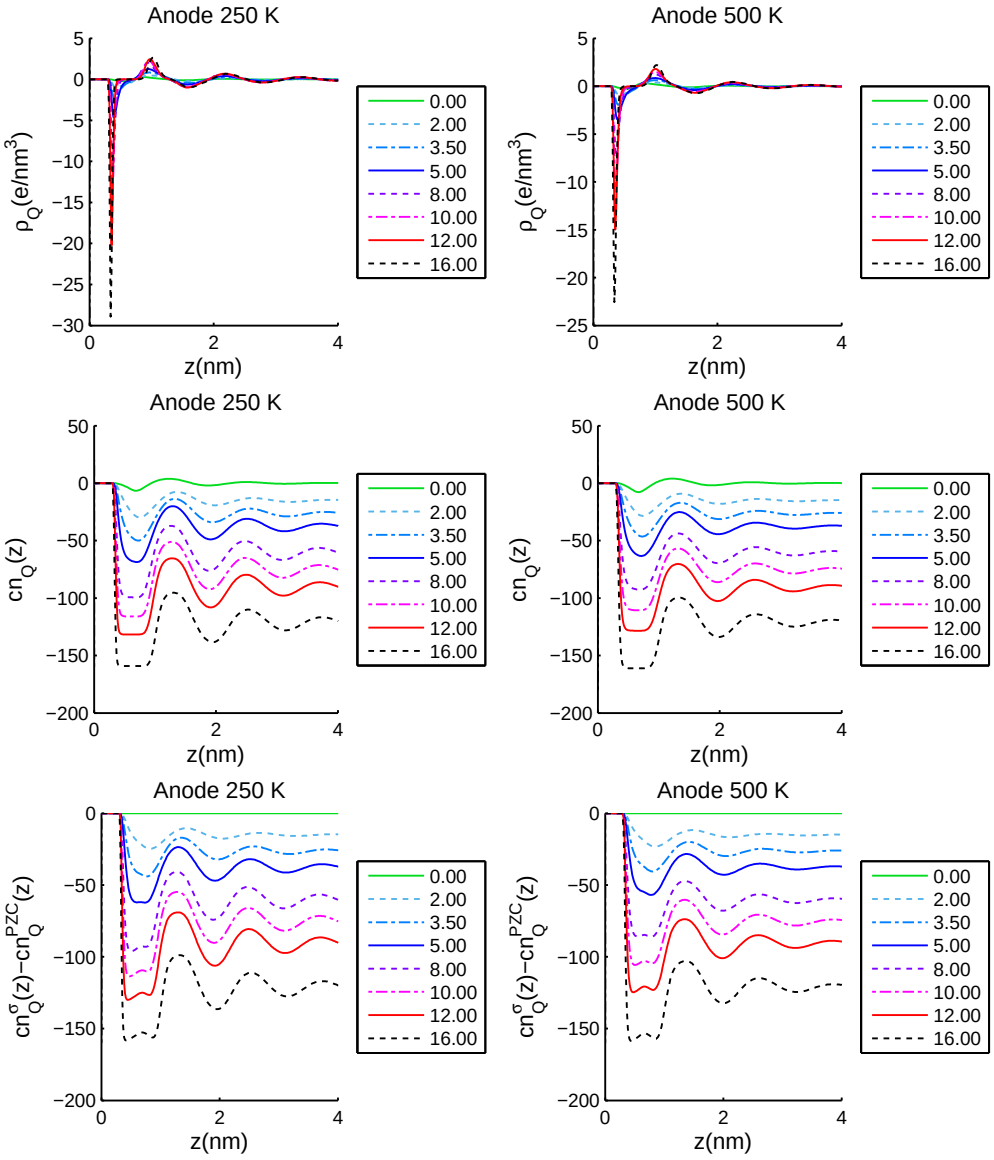

Figure B.23: Charge density at the Anode for different surface charges. The centre of mass of the electrode atoms are situated on the xy-plane with $z = 0$. (LEFT) $T = 250\,\mathrm{K}$, (RIGHT) $T = 500\,\mathrm{K}$. (TOP) Charge density profile, (MIDDLE) Cumulative charge density profile, (BOTTOM) Cumulative charge differences with PZC being the reference curve.

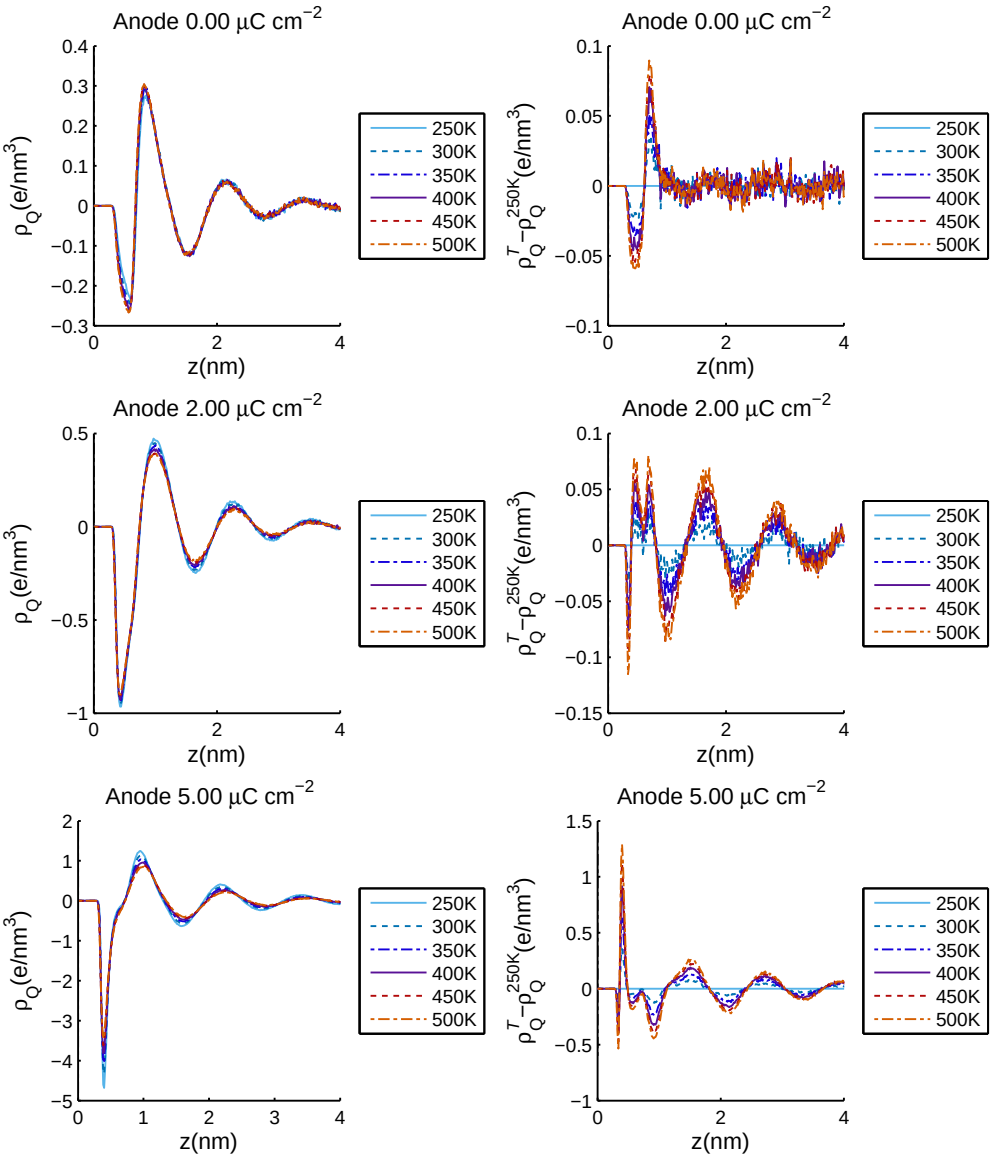

Figure B.24: Charge density at the Anode for different temperatures. The centre of mass of the electrode atoms are situated on the xy-plane with $z = 0$. (LEFT) Charge density profile, (RIGHT) Charge density profile difference with the 250 K curve being the reference curve. (TOP) Surface charge $\sigma = 0.0\,\mu\text{C/cm}^2$, (MIDDLE) Surface charge $\sigma = 2.0\,\mu\text{C/cm}^2$, (BOTTOM) Surface charge $\sigma = 5.0\,\mu\text{C/cm}^2$.

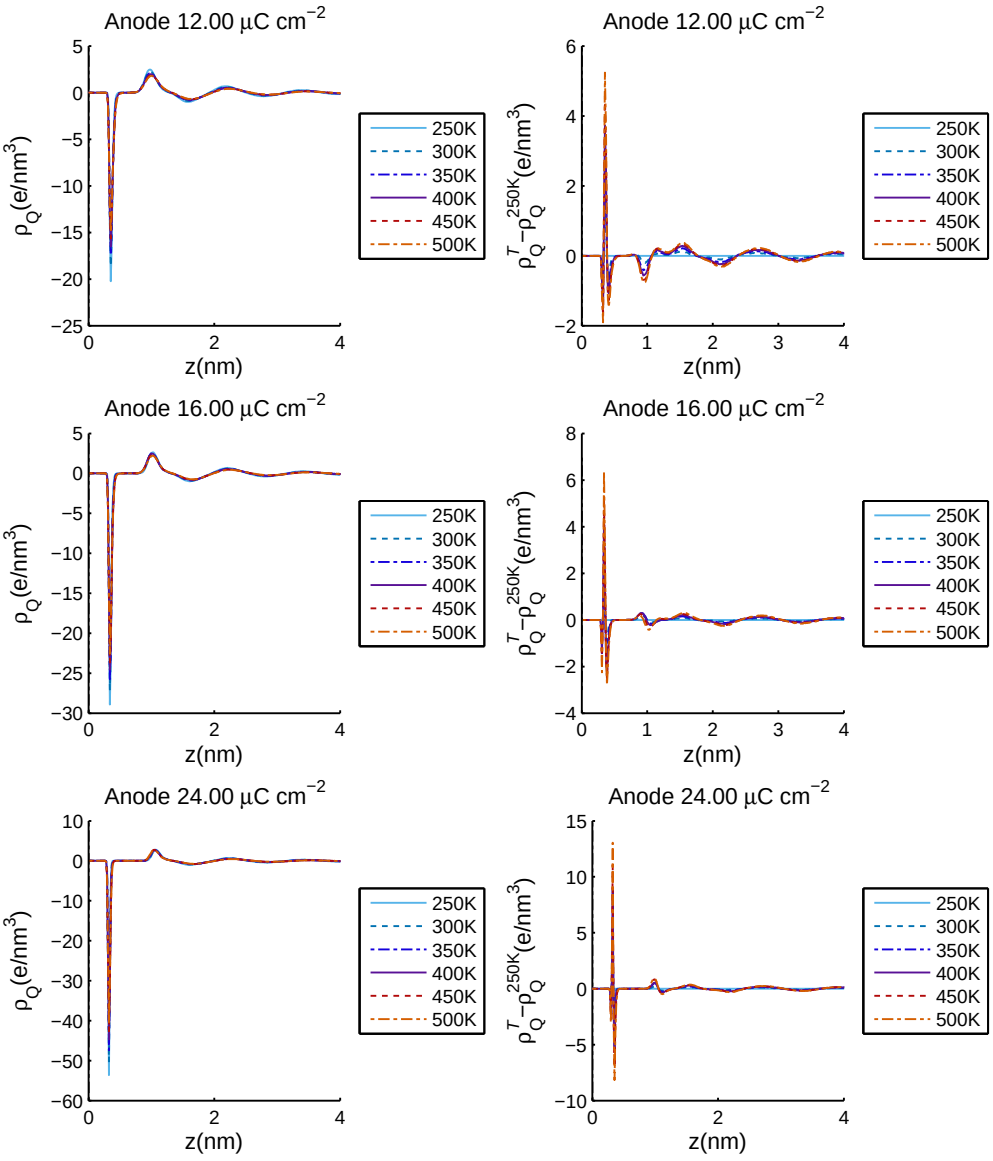

Figure B.25: Charge density at the Anode for different temperatures. The centre of mass of the electrode atoms are situated on the xy-plane with $z = 0$. (LEFT) Charge density profile, (RIGHT) Charge density profile difference with the 250 K curve being the reference curve. (TOP) Surface charge $\sigma = 12.0\,\mu\text{C/cm}^2$, (MIDDLE) Surface charge $\sigma = 16.0\,\mu\text{C/cm}^2$, (BOTTOM) Surface charge $\sigma = 24.0\,\mu\text{C/cm}^2$.

B.3.4 Cumulative number differences with reference to the potential of zero charge

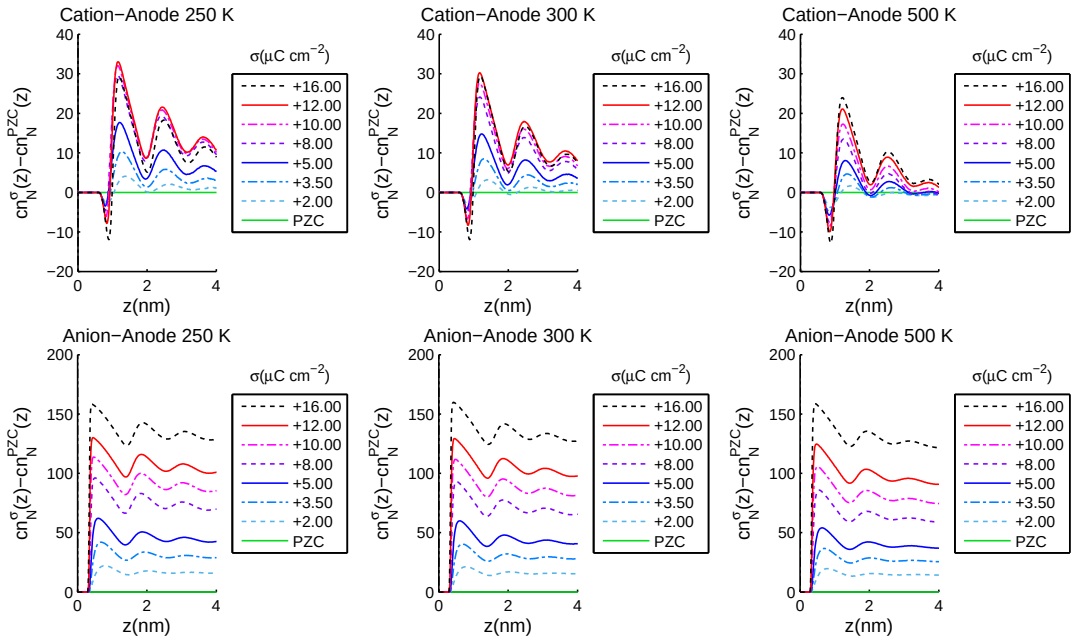

Figure B.26: Cumulative number differences of (TOP) cations and (BOTTOM) anions - with PZC curve being the reference curve - at the positively charged electrode (anode) for different surface charges between $+2.00\,\mu C/cm^2$ and $+16.00\,\mu C/cm^2$. From left to right three different temperatures are considered: (a) 250 K, (b) 300 K and (c) 500 K.

B.3.5 Peak height of cumulative number differences

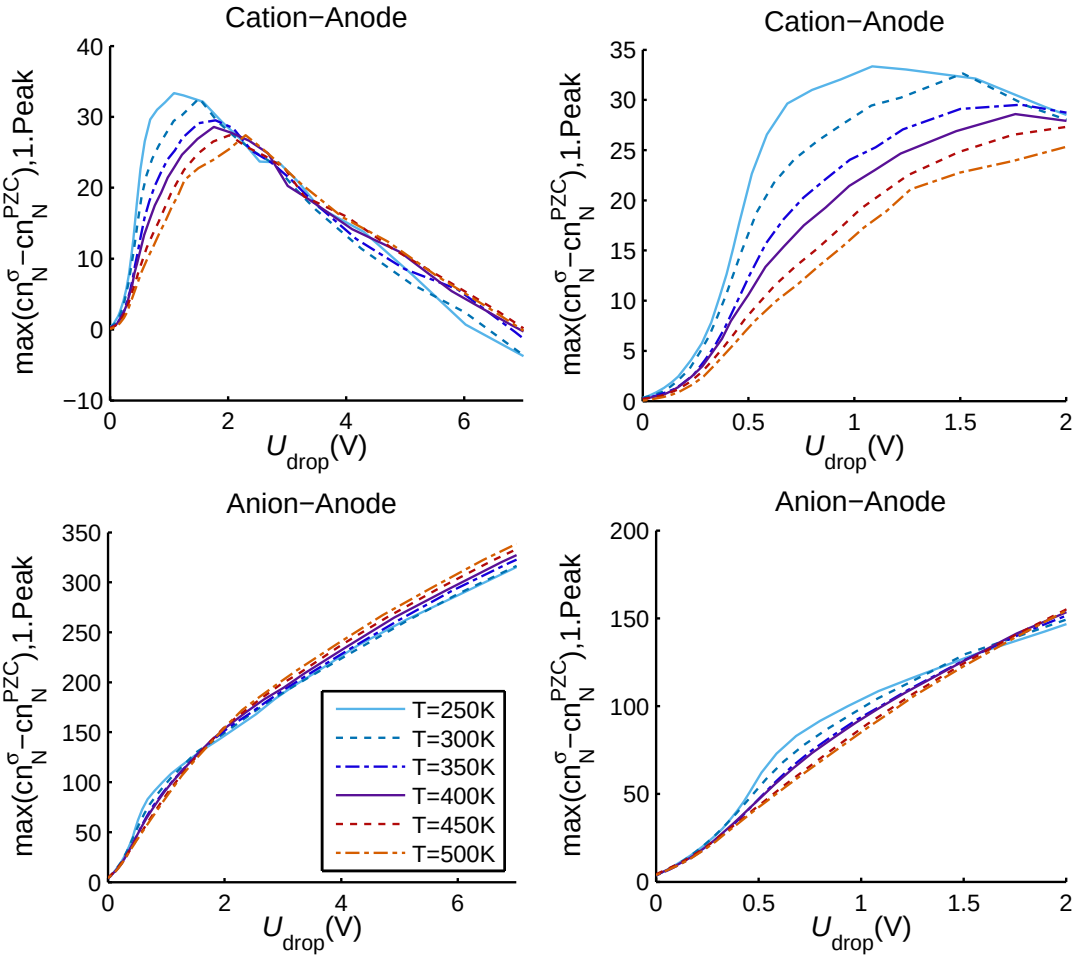

Figure B.27: Height of the first peak of the cumulative number difference over potential drop for (TOP) *cations* and (BOTTOM) *anions* at the *anode* for all temperatures between 250 K and 500 K. The peak height corresponds to the varying amount of ions in the EDL as a response on the increased surface charge with respect to the EDL at the neutral electrode. (LEFT) Potential drop between 0 V and +7 V; (RIGHT) Close-up with a potential drop between 0 V and +2 V.

B.3.6 Ion-number within an interfacial volume - first approach

Table B.4 provides an overview over the considered cutoffs and their physical relevance. We were not able to carefully explain the choice of every cutoff mentioned in this table. This was the reason to move further to a second approach including a more systematic choice of cutoffs. However, there are still interesting results visible within this first approach, which is the reason to keep it in the discussion.

Table B.4: Cutoffs considered for the interpretation of the ion number near a charged wall and their physical relevance.

z_{cutoff} (nm)	Origin	Comment
0.5	$1 \cdot d_{\text{anion}}$	
1.0	$2 \cdot d_{\text{anion}}$ or $1 \cdot d_{\text{cation}}$	
1.11	$1 \cdot d_{\text{cation}} + r_{\text{wall}}$	
1.25		
1.61	$1.5\,\text{nm} + r_{\text{wall}}$	Size of the first cation layer in the EDL at the PZC, decreases with increasing surface charge to 1.25 nm.
2.00	$2 \cdot d_{\text{cation}}$	
2.11	$2 \cdot d_{\text{cation}} + r_{\text{wall}}$	
3.0	$r_{\text{Coulomb}} + r_{\text{wall}}$	Cutoff used for electrostatic interactions in the MD simulations, extended by the wall radius.

The ion number curves over potential drop for both ion species are shown in Fig. B.28 and Fig. B.29. As mentioned earlier, the physical interpretation of this data should be based on well defined cutoffs, which is not the case here. However we would like to point to the curves with cutoff 1.0 nm, 1.11 nm and 1.25 nm shown in the first and second row of Fig. B.28 and Fig. B.29. All cutoffs are relatively close together, the same is represented in the resulting ion number over potential drop curves, as the change in the curve structure is monotone and the main features between +0.5 V and +3 V are visible for all cutoffs. I conclude, that small variations of the cutoff by few tenth of nm will not change the physical result. This is an important result as we have to ensure that the precise cutoff choice will not have a drastic influence on the results.

B.3.7 Ion-number within an interfacial volume - second approach

The following systematic approach for the cutoff choice differs from the first approach in terms of cutoff definitions. Within the first method, all cutoffs are

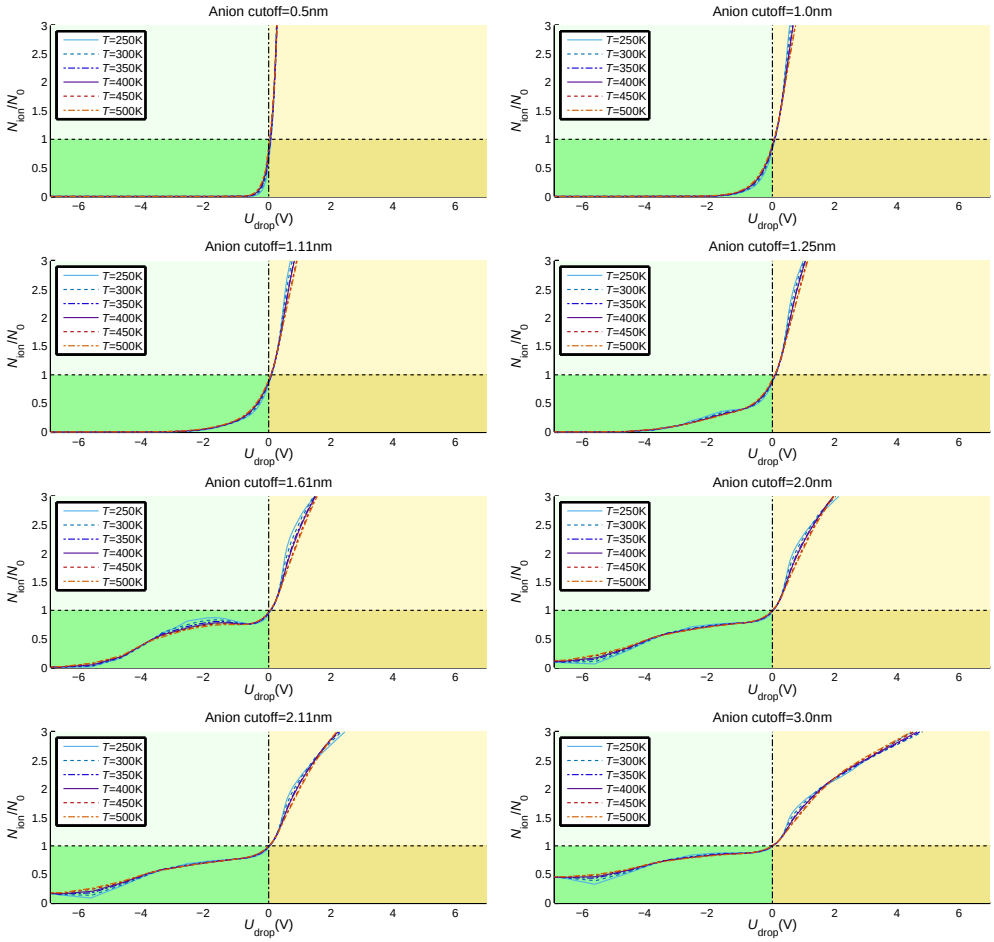

Figure B.28: Anion number at given distance from the electrode. Choice of cutoff based on the geometric size of ions and electrode atoms. The cutoffs follow no specific rule, choice for cutoffs are given in Table B.4.

based on elementary geometric considerations concerning the particle diameter. Now, we shift this basic estimation to the advanced consideration of mixing rules applied to these simulations. Table B.5 provides an overview over the considered cutoffs and their physical relevance.

Table B.5: Cutoffs considered for the interpretation of the ion number near a charged wall and their physical relevance.

z_{cutoff} (nm)	Origin	Comment	Expectation
0.35	$\sigma_{LJ}^{\text{Anion-Wall}}$	Number of ions in the first geometric layer close to the wall.	Only anions are expected in this volume.
1.10	$\sigma_{LJ}^{\text{Anion-Wall}} + \sigma_{LJ}^{\text{Anion-Cation}}$	Number of ions in the first and second geometric layer close to the wall.	At the Anode we expect the first interfacial layer being filled with Anions and the second interfacial layer being filled with Cations. At the Cathode we expect Cation filling (attraction) and Anion depletion (repulsion).
1.85	$\sigma_{LJ}^{\text{Anion-Wall}} + 2 \cdot \sigma_{LJ}^{\text{Anion-Cation}}$		
2.60	$\sigma_{LJ}^{\text{Anion-Wall}} + 3 \cdot \sigma_{LJ}^{\text{Anion-Cation}}$		
3.35	$\sigma_{LJ}^{\text{Anion-Wall}} + 4 \cdot \sigma_{LJ}^{\text{Anion-Cation}}$		
0.60	$\sigma_{LJ}^{\text{Cation-Wall}}$		
1.35	$\sigma_{LJ}^{\text{Cation-Wall}} + \sigma_{LJ}^{\text{Anion-Cation}}$		
2.10	$\sigma_{LJ}^{\text{Cation-Wall}} + 2 \cdot \sigma_{LJ}^{\text{Anion-Cation}}$		
2.85	$\sigma_{LJ}^{\text{Cation-Wall}} + 3 \cdot \sigma_{LJ}^{\text{Anion-Cation}}$		
3.60	$\sigma_{LJ}^{\text{Cation-Wall}} + 4 \cdot \sigma_{LJ}^{\text{Anion-Cation}}$		
0.60	$\sigma_{LJ}^{\text{Cation-Wall}}$		First interfacial layer at the Cathode filled with Cations.
1.60	$\sigma_{LJ}^{\text{Cation-Wall}} + \sigma_{LJ}^{\text{Cation-Cation}}$	Purely of interest at the Cathode as there might be the formation of a saturated Cation layer visible with a second interfacial layer filled again by Cations instead of Anions.	Second interfacial layer at the Cathode filled with Cations.
2.60	$\sigma_{LJ}^{\text{Cation-Wall}} + 2 \cdot \sigma_{LJ}^{\text{Cation-Cation}}$	Purely of interest at the Cathode as there might be the formation of a saturated Cation layer visible with a third interfacial layer filled again by Cations instead of Anions.	Third interfacial layer at the Cathode filled with Cations.

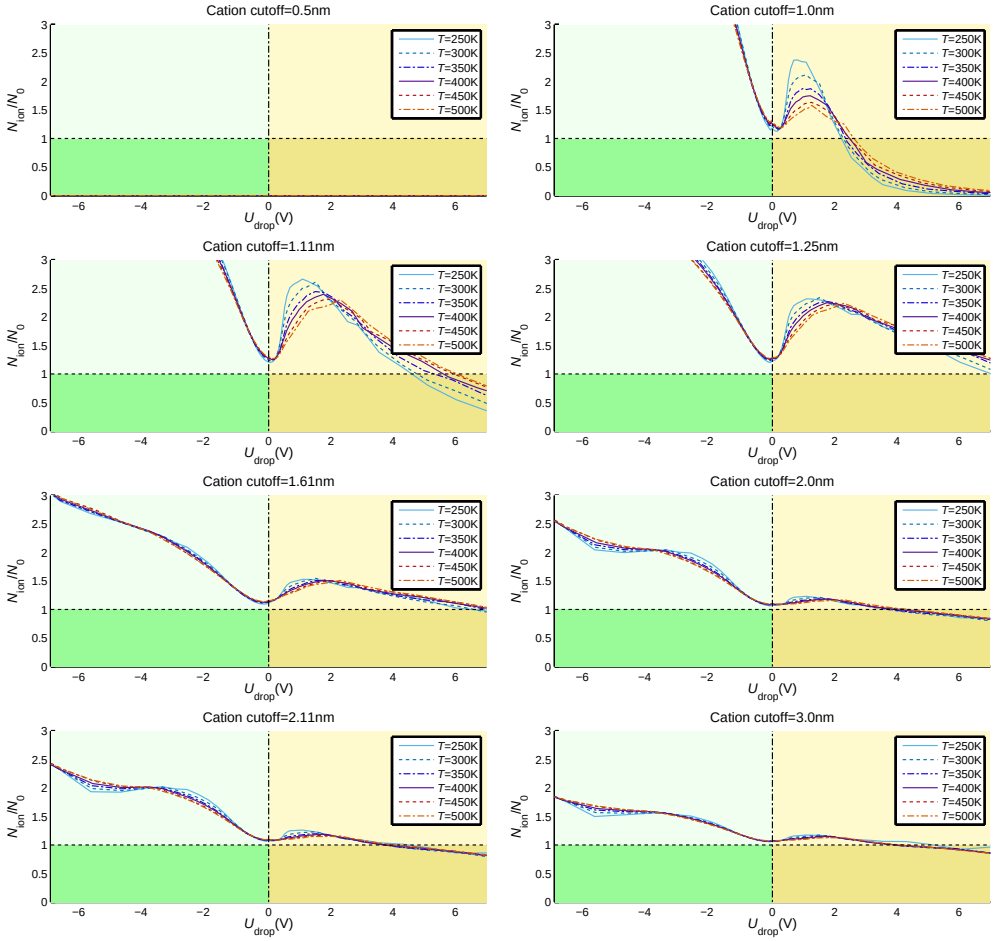

Figure B.29: Cation number at given distance from the electrode. Choice of cutoff based on the geometric size of ions and electrode atoms. The cutoffs follow no specific rule, choice for cutoffs are given in Table B.4.

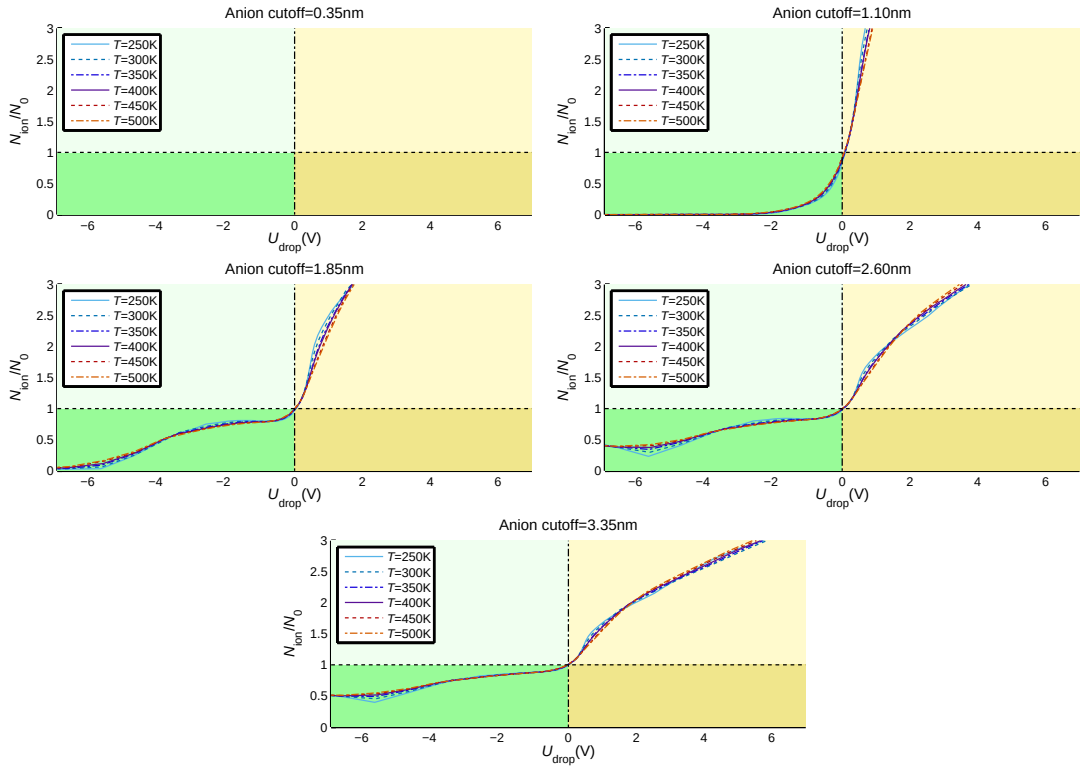

Figure B.30: Anion number at given distance from the electrode. Choice of cutoff based on the interaction parameter between wall-ion and ion-counterion. The cutoffs follow the rule $\sigma_{LJ}^{\text{Anion-Wall}} + i \cdot \sigma_{LJ}^{\text{Anion-Cation}}$ with i varying between 0 and 4.

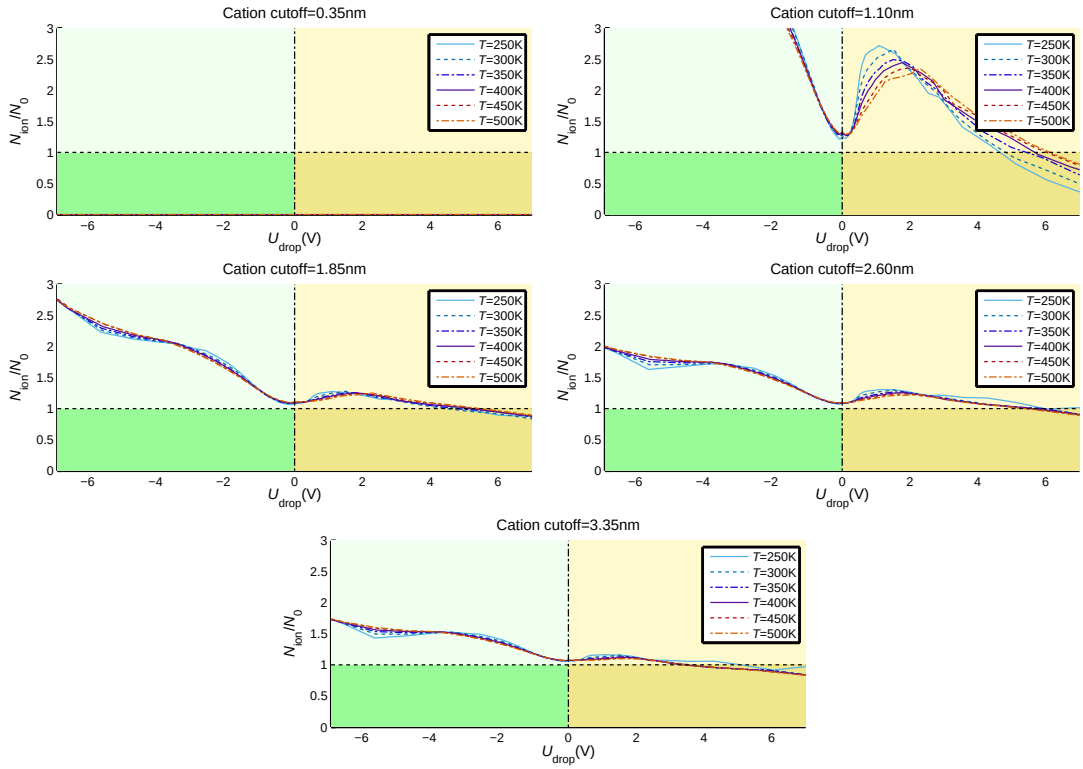

Figure B.31: Cation number at given distance from the electrode. Choice of cutoff based on the interaction parameter between wall-ion and ion-counterion. The cutoffs follow the rule $\sigma_{LJ}^{\text{Anion-Wall}} + i \cdot \sigma_{LJ}^{\text{Anion-Cation}}$ with i varying between 0 and 4.

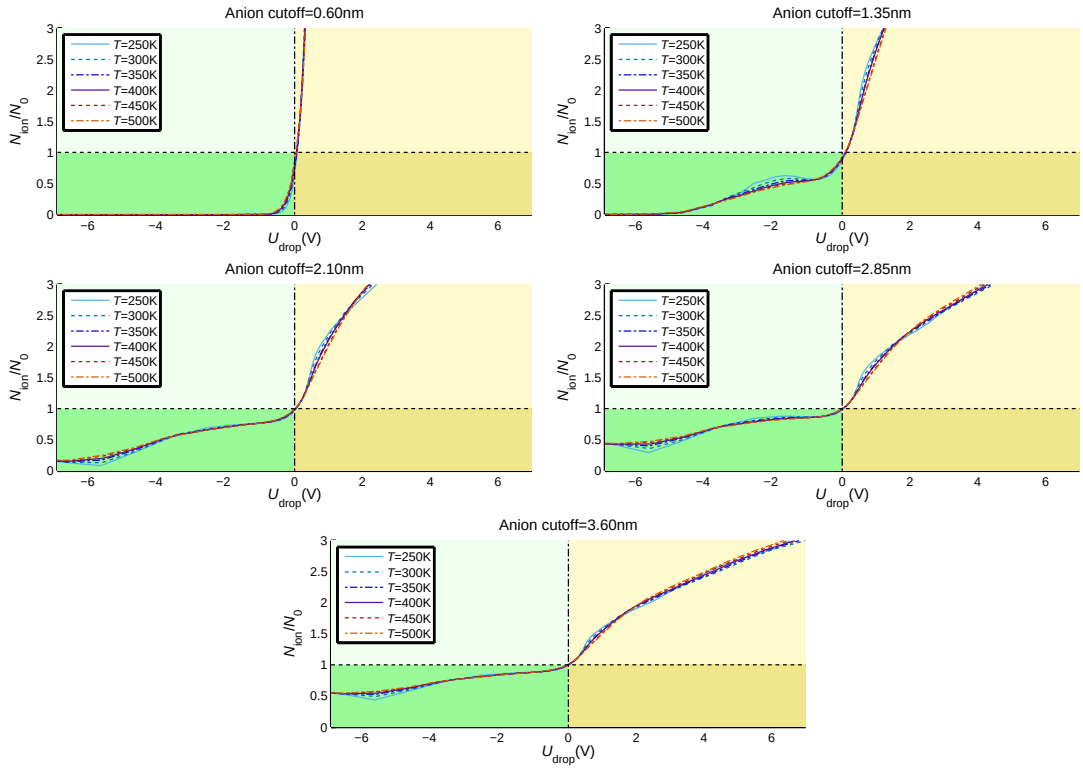

Figure B.32: Anion number at given distance from the electrode. Choice of cutoff based on the interaction parameter between wall-ion and ion-counterion. The cutoffs follow the rule $\sigma_{LJ}^{\text{Cation-Wall}} + i \cdot \sigma_{LJ}^{\text{Anion-Cation}}$ with i varying between 0 and 4.

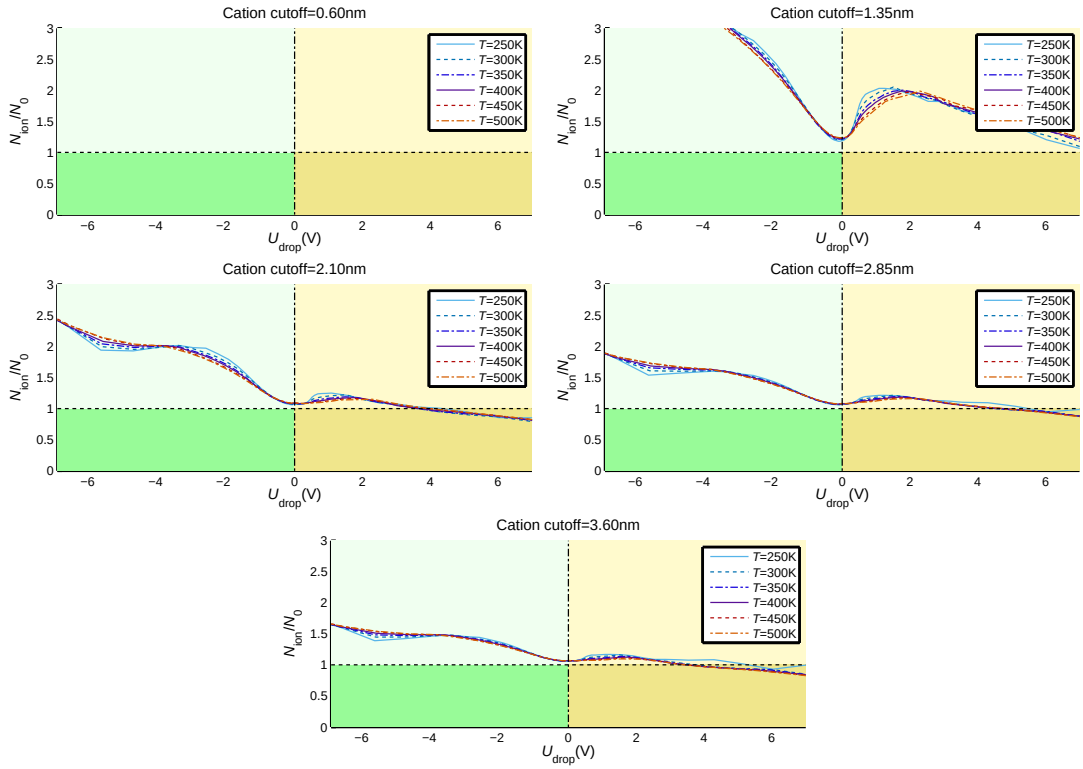

Figure B.33: Cation number at given distance from the electrode. Choice of cutoff based on the interaction parameter between wall-ion and ion-counterion. The cutoffs follow the rule $\sigma_{LJ}^{\text{Cation-Wall}} + i \cdot \sigma_{LJ}^{\text{Anion-Cation}}$ with i varying between 0 and 4.

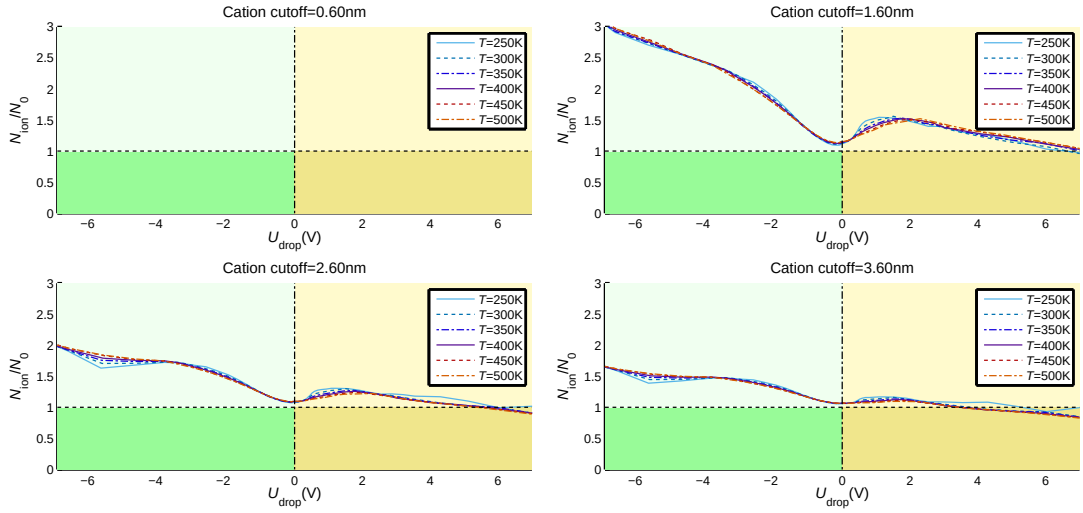

Figure B.34: Cation number at given distance from the electrode. Choice of cutoff based on the interaction parameter between wall-ion and ion-counterion. The cutoffs follow the rule $\sigma_{LJ}^{\text{Cation-Wall}} + i \cdot \sigma_{LJ}^{\text{Cation-Cation}}$ with i varying between 0 and 3. Purely of interest at the Cathode as there might be the formation of a saturated Cation layer visible with a second or third interfacial layer filled again by Cations instead of Anions. Other analysis has shown that this effect happens at lower voltages than -7 V. I will probably replot the figures - however there will be only scientific interest in the outcome as voltages are much to high for any application.

B.4 Structural transition at the interface: comparison of all temperatures

B.4.1 Evolution of the first peak of the number density profile of anions at the cathode

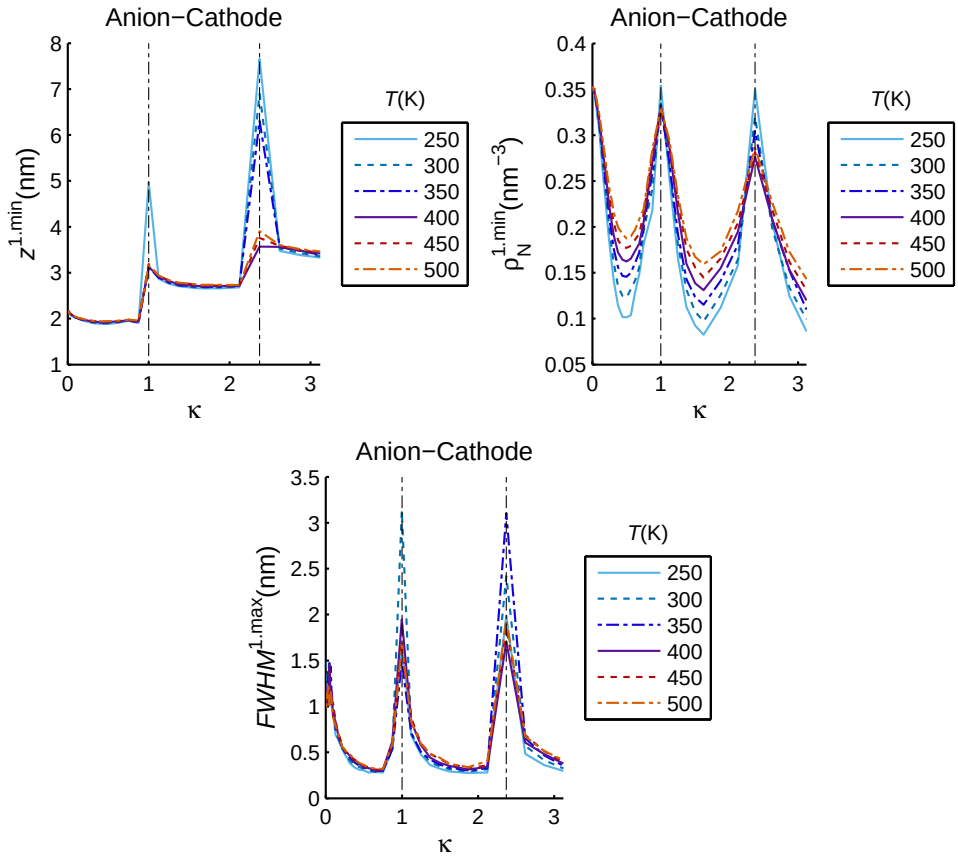

Figure B.35: Evolution of the first peak of the number density profile of anions at the cathode. The peak is defined by the position and height of the global maximum of the number density profile. As z is increased, a minimum follows the global maximum in the number density profile. This local minimum is called valley. (TOP-LEFT) Position of the first valley (minimum). (TOP-RIGHT) Height of the first valley (minimum). (BOTTOM) Full width of half maximum (FWHM) of the first maximum of the profile.

B.4.2 Cumulative charge at the Cathode and normalization

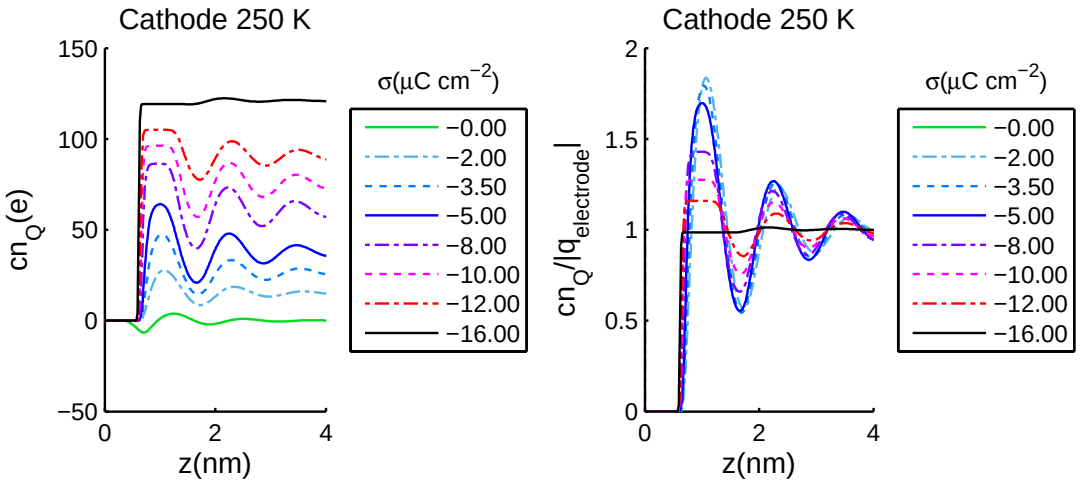

Figure B.36: Cumulative charge $cn_Q(z) = \int_0^z \rho_N(z')\mathrm{d}z'$ at the Cathode for different surface charges at $T = 250\,\mathrm{K}$. The centre of mass of the electrode atoms are situated on the xy-plane with $z = 0$. (LEFT) Cumulative charge for different surface charges, (RIGHT) Cumulative charge normalized by the number of elementary charges on the electrode. The charge normalization is identical to the concept of dividing the local charge density in the solution side of the electric double layer by the absolute surface charge density of the electrode.

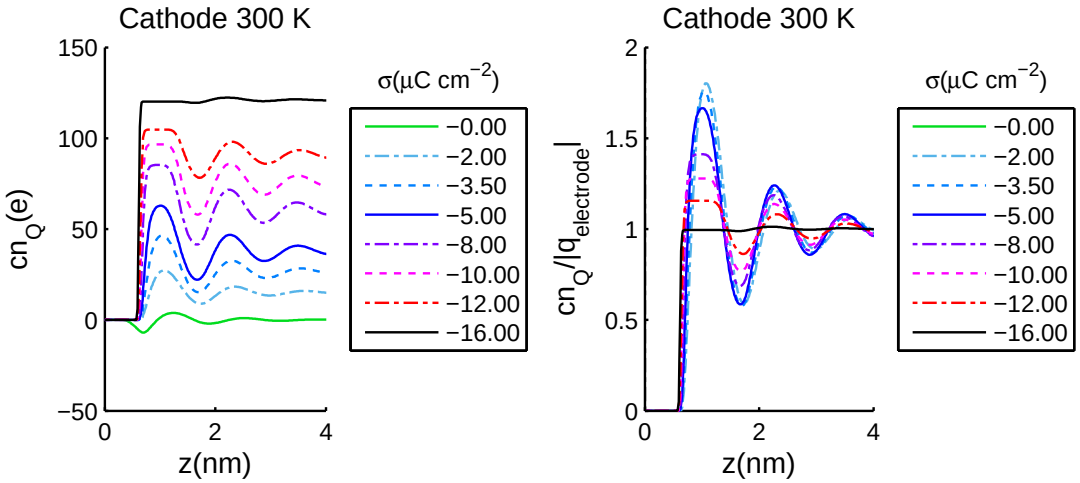

Figure B.37: Cumulative charge $cn_Q(z) = \int_0^z \rho_N(z')\mathrm{d}z'$ at the Cathode for different surface charges at $T = 300\,\mathrm{K}$. The centre of mass of the electrode atoms are situated on the xy-plane with $z = 0$. (LEFT) Cumulative charge for different surface charges, (RIGHT) Cumulative charge normalized by the number of elementary charges on the electrode. The charge normalization is identical to the concept of dividing the local charge density in the solution side of the electric double layer by the absolute surface charge density of the electrode.

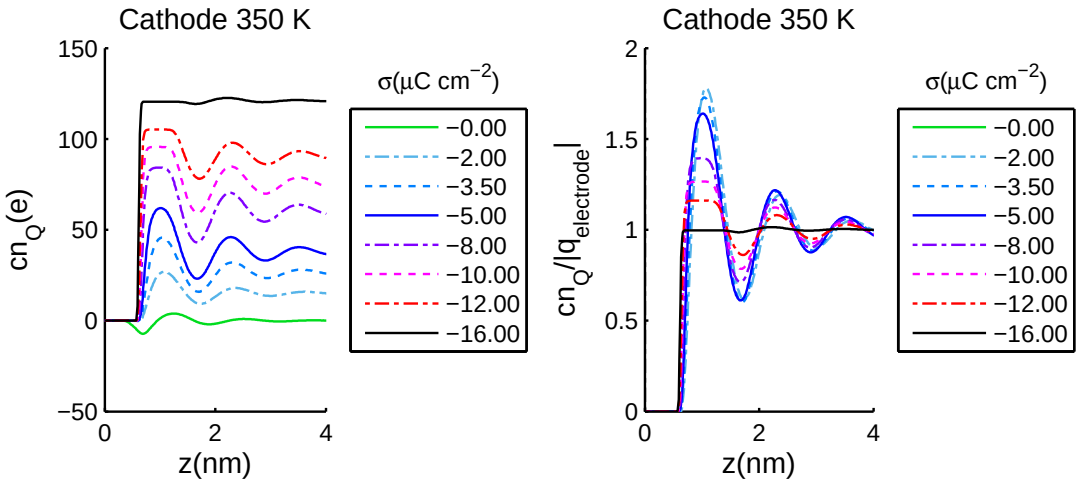

Figure B.38: Cumulative charge $cn_Q(z) = \int_0^z \rho_N(z')\mathrm{d}z'$ at the Cathode for different surface charges at $T = 350\,\mathrm{K}$. The centre of mass of the electrode atoms are situated on the xy-plane with $z = 0$. (LEFT) Cumulative charge for different surface charges, (RIGHT) Cumulative charge normalized by the number of elementary charges on the electrode. The charge normalization is identical to the concept of dividing the local charge density in the solution side of the electric double layer by the absolute surface charge density of the electrode.

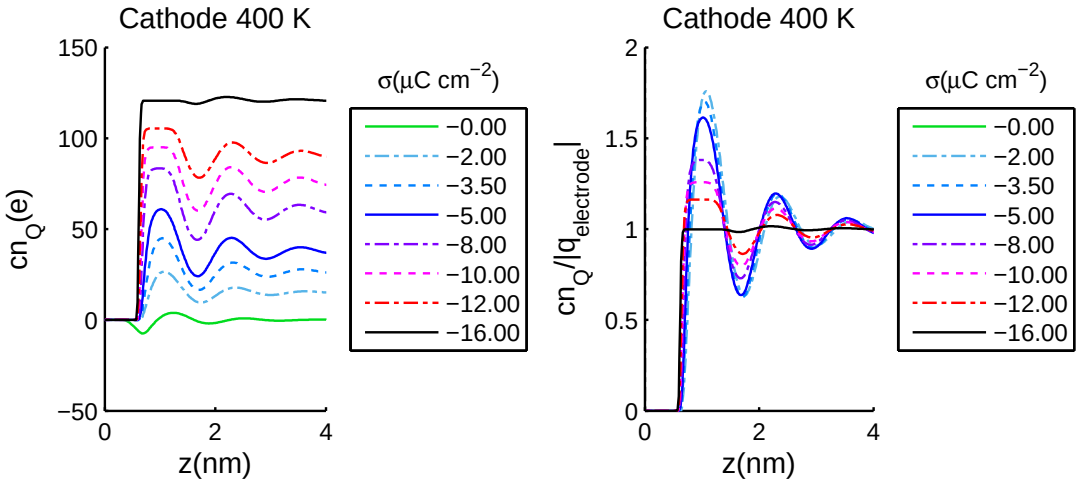

Figure B.39: Cumulative charge $cn_Q(z) = \int_0^z \rho_N(z')\mathrm{d}z'$ at the Cathode for different surface charges at $T = 400\,\mathrm{K}$. The centre of mass of the electrode atoms are situated on the xy-plane with $z = 0$. (LEFT) Cumulative charge for different surface charges, (RIGHT) Cumulative charge normalized by the number of elementary charges on the electrode. The charge normalization is identical to the concept of dividing the local charge density in the solution side of the electric double layer by the absolute surface charge density of the electrode.

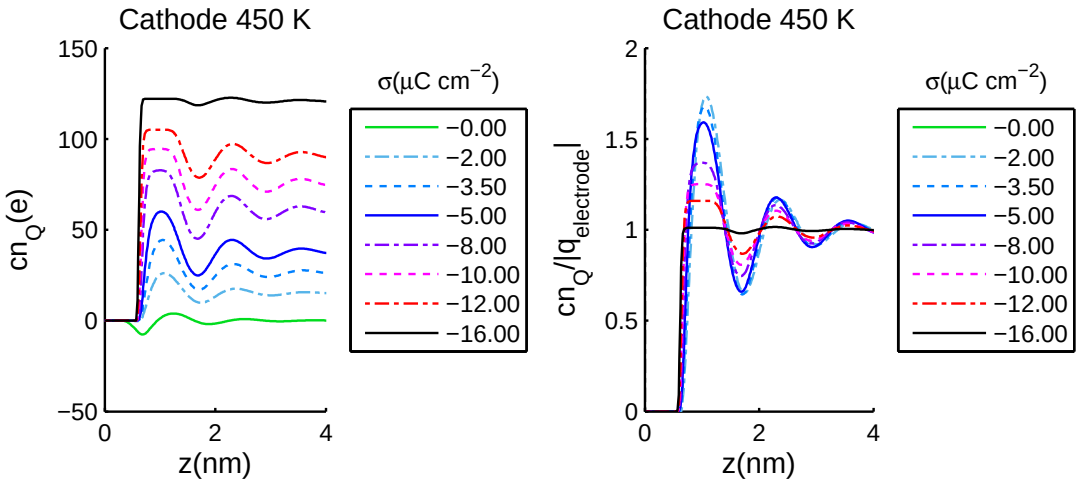

Figure B.40: Cumulative charge $cn_Q(z) = \int_0^z \rho_N(z')\mathrm{d}z'$ at the Cathode for different surface charges at $T = 450\,\mathrm{K}$. The centre of mass of the electrode atoms are situated on the xy-plane with $z = 0$. (LEFT) Cumulative charge for different surface charges, (RIGHT) Cumulative charge normalized by the number of elementary charges on the electrode. The charge normalization is identical to the concept of dividing the local charge density in the solution side of the electric double layer by the absolute surface charge density of the electrode.

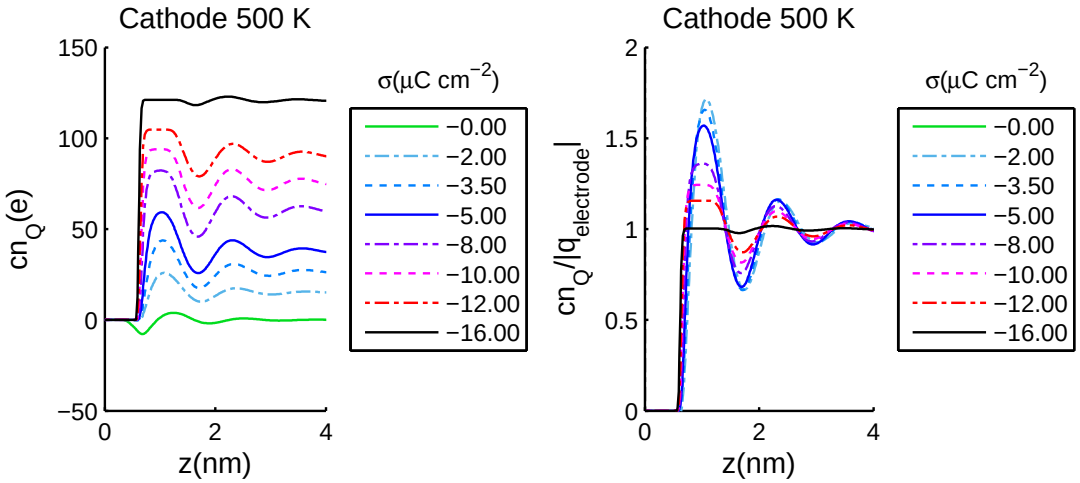

Figure B.41: Cumulative charge $cn_Q(z) = \int_0^z \rho_N(z')\mathrm{d}z'$ at the Cathode for different surface charges at $T = 500\,\mathrm{K}$. The centre of mass of the electrode atoms are situated on the xy-plane with $z = 0$. (LEFT) Cumulative charge for different surface charges, (RIGHT) Cumulative charge normalized by the number of elementary charges on the electrode. The charge normalization is identical to the concept of dividing the local charge density in the solution side of the electric double layer by the absolute surface charge density of the electrode.

B.5 Snapshots: Herring-bone structure

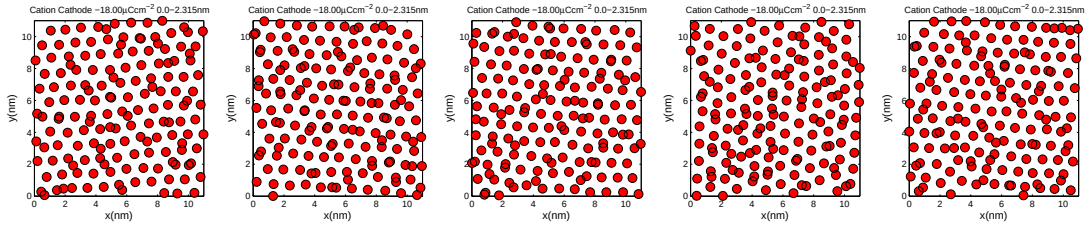

Figure B.42: Snapshots of the superposition of first and second interfacial layer of cations at the cathode at $T = 450\,\mathrm{K}$ and $\sigma = -18.00\,\mu\mathrm{C/cm^2}$. From left to right the configurations of five different replicas are shown.

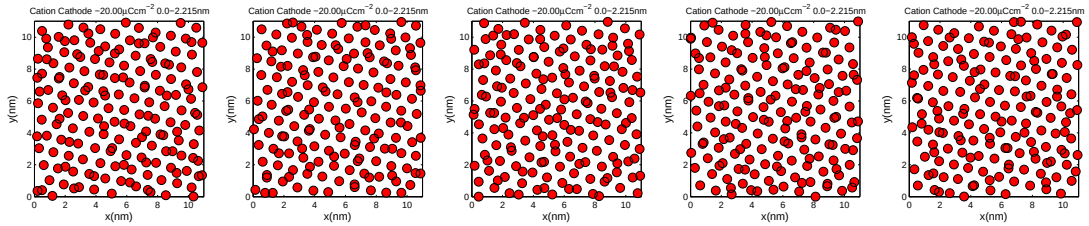

Figure B.43: Snapshots of the superposition of first and second interfacial layer of cations at the cathode at $T = 450\,\mathrm{K}$ and $\sigma = -20.00\,\mu\mathrm{C/cm^2}$. From left to right the configurations of five different replicas are shown.

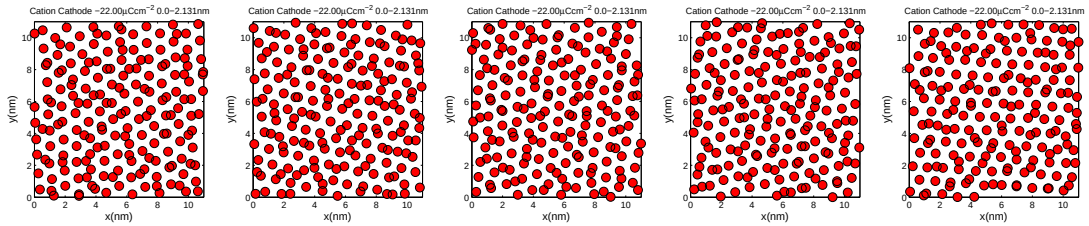

Figure B.44: Snapshots of the superposition of first and second interfacial layer of cations at the cathode at $T = 450\,\mathrm{K}$ and $\sigma = -22.00\,\mu\mathrm{C/cm^2}$. From left to right the configurations of five different replicas are shown.

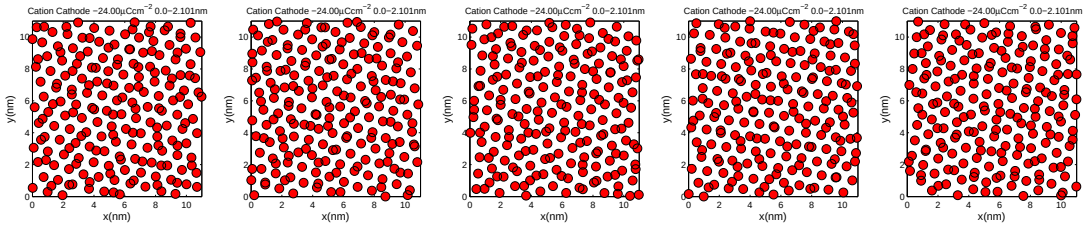

Figure B.45: Snapshots of the superposition of first and second interfacial layer of cations at the cathode at $T = 450\,\mathrm{K}$ and $\sigma = -24.00\,\mu\mathrm{C/cm^2}$. From left to right the configurations of five different replicas are shown.

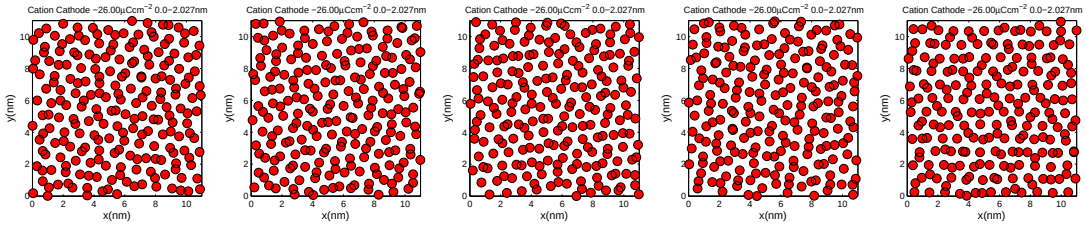

Figure B.46: Snapshots of the superposition of first and second interfacial layer of cations at the cathode at $T = 450\,\mathrm{K}$ and $\sigma = -26.00\,\mu\mathrm{C/cm^2}$. From left to right the configurations of five different replicas are shown.

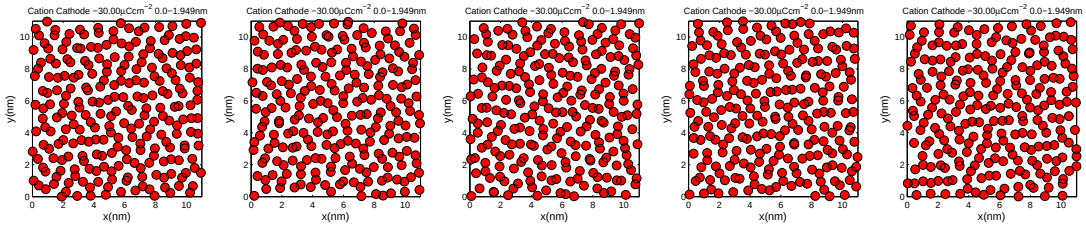

Figure B.47: Snapshots of the superposition of first and second interfacial layer of cations at the cathode at $T = 450\,\mathrm{K}$ and $\sigma = -30.00\,\mu\mathrm{C/cm^2}$. From left to right the configurations of five different replicas are shown.

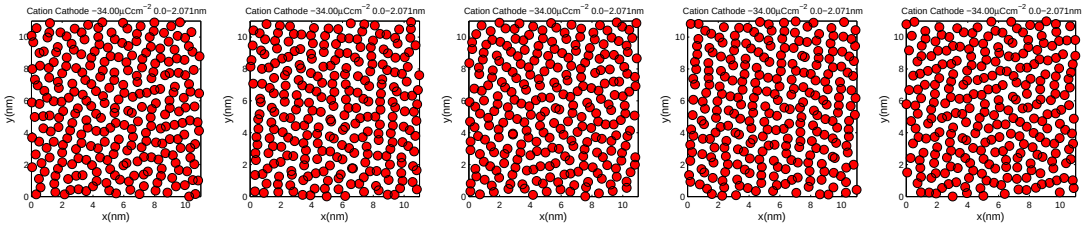

Figure B.48: Snapshots of the superposition of first and second interfacial layer of cations at the cathode at $T = 450\,\mathrm{K}$ and $\sigma = -34.00\,\mu\mathrm{C/cm^2}$. From left to right the configurations of five different replicas are shown.

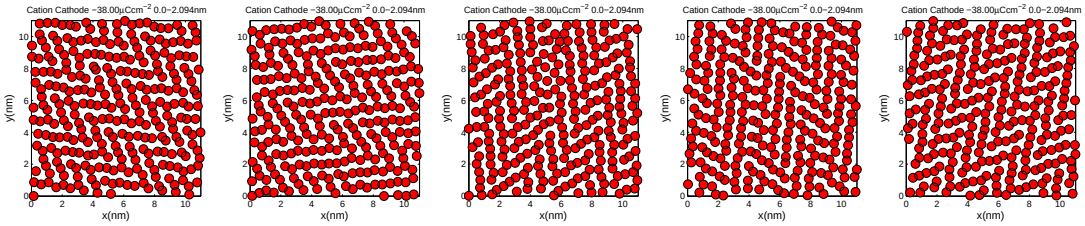

Figure B.49: Snapshots of the superposition of first and second interfacial layer of cations at the cathode at $T = 450\,\mathrm{K}$ and $\sigma = -38.00\,\mu\mathrm{C/cm^2}$. From left to right the configurations of five different replicas are shown.

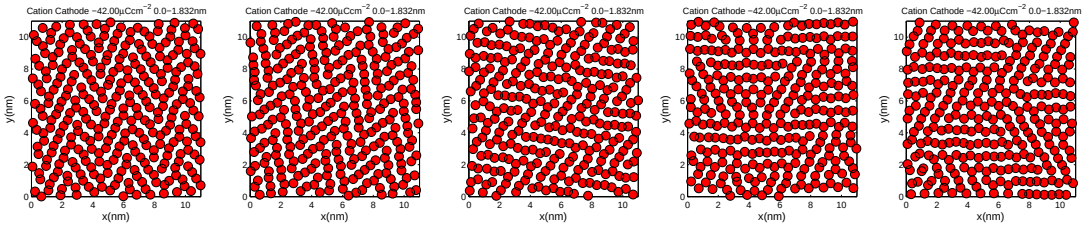

Figure B.50: Snapshots of the superposition of first and second interfacial layer of cations at the cathode at $T = 450\,\mathrm{K}$ and $\sigma = -42.00\,\mu\mathrm{C/cm^2}$. From left to right the configurations of five different replicas are shown.

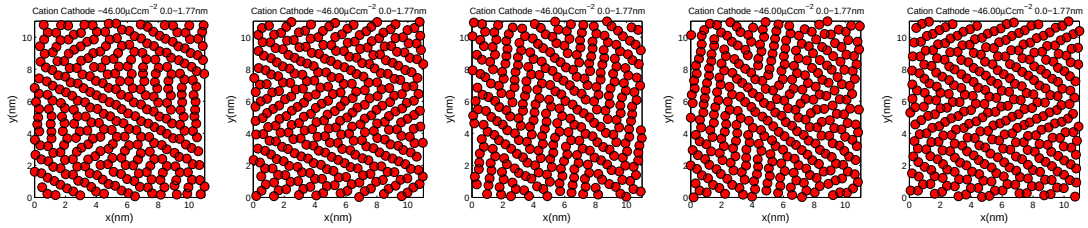

Figure B.51: Snapshots of the superposition of first and second interfacial layer of cations at the cathode at $T = 450\,\mathrm{K}$ and $\sigma = -46.00\,\mu\mathrm{C/cm^2}$. From left to right the configurations of five different replicas are shown.

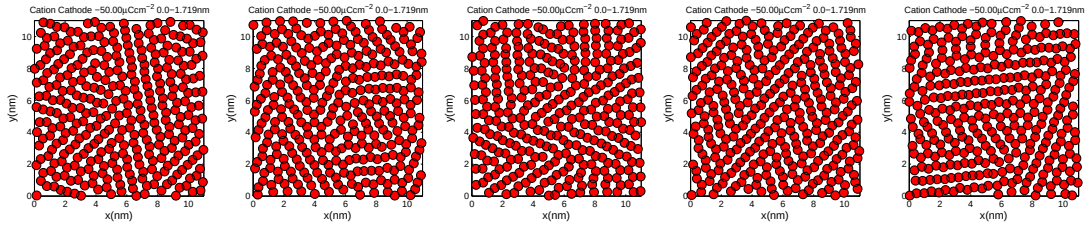

Figure B.52: Snapshots of the superposition of first and second interfacial layer of cations at the cathode at $T = 450\,\mathrm{K}$ and $\sigma = -50.00\,\mu\mathrm{C/cm^2}$. From left to right the configurations of five different replicas are shown.

Appendix C

NaRIBaS

C.1 Introduction

In times of steadily increasing performance of computing facility and enhanced data accessibility the bottleneck for increasing the scientific productivity lies in the mere productivity of the scientist. When the question is asked, how to increase someone's productivity, one has to find out what the person does and how many time is spend on each step.

A computer scientist ought to think, to read, to create data by numerical calculations or simulations, to analyse the data again by numerical methods and to read/write and think again. Usually a large amount of the whole working time is used for using scientific software, writing scripts to automatize the usage, to perform analysis steps and to visualize the results. Every day, every week,

every month, the whole year. When it comes to coding for a scientists, he usually makes a quick check if someone else already wrote a tool, and commonly he starts coding on his own. Because his main task is to produce results, he does not care much on the code but uses it as a means to an end ("quick and dirty"). When a task has to be repeated (by the same person or someone else) the code is in most cases rewritten, as the old version lies undocumented and broken in some old directory, if it can be found at all. The common practice and good habits of software engineers seem to have never put a feet into a labs door.

> Writing software for a research lab myself, I can def[initely] say that it is not a safe assumption that the "get it done quick" attitude is an indication that the scope of the software is small or "script-level". Principle scientific researchers often view the software created for their research as a means to an end and do not care about the quality the software produced, only it's end results. This often results poor software design due to pressure to get things done in the short run as well as duplicated efforts across projects due to a lack of modular implementations.[1]

What is given here as a quote from just one scientist is put on a more sophisticated basis by a few researchers:

Sletholt et al [50, 51] made a survey on the question "How well do current scientific software-development processes match the practices found in agile development methods, and what are the effects of using agile practices in such processes" in their recent work (2012) "What Do We Know about Scientific Software Developments Agile Practices?'. They analysed different projects according to their usage of a defined list of agile development methods and found that most methods are not present or used only occasionally by some developers. Furthermore the researchers conclude, that mostly technology driven methods, which are used by professional software developers, are unknown to the scientists. Finally they observed from case studies that the usage of agile techniques generally had positive effects in the projects and none of the studies displayed any particular negative side effects of using agile practices.

Another survey by Pitt-Francis et al [52] reports on the usage of "agile programming techniques to develop computational biology software". The researchers discuss software development methods used in biology software, describe test-driven agile methods and argue that such methods are more suitable for scientific software development than the traditional academic approaches. They also

[1] Taken from `http://stackoverflow.com/questions/1178786`.

present their experiences with a review of the progress of the Chaste (Cancer, Heart And Soft Tissue Environment) project, which is a library of computational biology software. Their main conclusion about using agile approaches is that the work results in a solid foundation of scientific code that allows coping with the fast changing requirements that scientific researchers have to focus on during their project.

Taking these positive documentations into account as well the own experiences when it comes to using scientific software (whether it is self written or delivered from someone else), we all are in duty to use the existing set of methods and literally leave the swamp of dirty programming. To move ourselves to deliver flexible, reusable, maintainable and well documented scientific software will not only allow us to produce results, but makes results reproducible, allows to refine results and will be beneficial for the whole scientific community.

C.2 A scripting framework for iterative repetition of tasks

NaRIBaS provides a framework that decouples user input parameter and terminal based command lines. NaRIBaS does not replace a simulation software and specific analysis tools like Gromacs, but it allows iterative repetition of tasks while changing specific input parameter. Mind the following example:

> A scientist performs a molecular dynamics simulation of substance A dissolved in substance B. For this tasks he prepares the initial configuration (e.g. 10 molecules A, 990 molecules B, cubic box of 10 nm box length in each direction), modifies run parameter (e.g. temperature) and runs the simulation. After doing some analysis, he finds out that he needs to perform the same simulation, but (a) at different temperatures and (b) with a third substance C at different concentrations added to the simulation [2]. Now the scientist starts creating an initial configuration, modifies run parameter (e.g. temperature) and runs the simulation, run the next simulation... Assuming 5 different temperatures under study and 10 different concentrations, the scientist is doing the same set of tasks $5 \times 10 = 50$ times [3].

[2] Task (a) differs from task (b) because in task (b) a new quantity not considered yet ('impurity, concentration') is introduced.

[3] How long the analysis takes when the scientist needs to calculate and plot the radial distribution functions between substances A and B, A and C, B and C, respectively, and compare

At this stage NaRIBaS steps in and allows a fast adjustment or extension of the former procedure the scientist followed for producing his first simulation.

> Assuming that the scientist stored every terminal line he used for performing his calculations (and he used bash commands like sed or awk for editing any text file), he can simply copy those lines to a text file. The parameter to change for task (a) are stored in a list in a combined folder. For task (b) a few lines are added to the text file that contains the terminal lines to account for the new quantity. With a simple `./NaRIBaS.sh` in the terminal the simulations are running and the analysis is done the next day.

Probably this is sounding to simplified, but it is exactly what NaRIBaS can do (with a little effort by the scientist). In other words: NaRIBaS provides a scripting framework, where data input (like a list of temperatures) and algorithms (e.g. modifying a run parameter file and running a simulation) are decoupled from each other. Figure C.1 gives a graphical idea, what NaRIBaS is supposed to do.

In addition to the basic framework, a comprehensive collection of terminal lines, we will call them 'task lists', and software specific input files for preparation and analysis of common MD simulations in the field of bulk and slab simulations of ionic liquids are provided [4].

C.3 Algorithms and building blocks - The link between data sets and algorithms

A large number of scientific software allows automation of tasks by using relatively simple bash commands for invoking the tools and providing a reasonable amount of user input. Also input files with specific system definition show up as templates in the community. Doing a simulation or calculation ones is thus something that requires a good physical and chemical knowledge and some very basic programming knowledge. However extensive research of a property requires mostly not characterizing only one single simulation but varying the simulation as often as possible. In other terms, specific command lines or input files -algorithms - need to be varied according to a specific physical setup - a set of data - under study.

for the 50 temperature-concentration combinations, is left as a task to the reader

[4]The author worked mainly with Gromacs for molecular dynamics simulations and Matlab for mathematical calculations and advanced plotting. Thus Gromacs topologies and input files as well as numerous Matlab functions are provided.

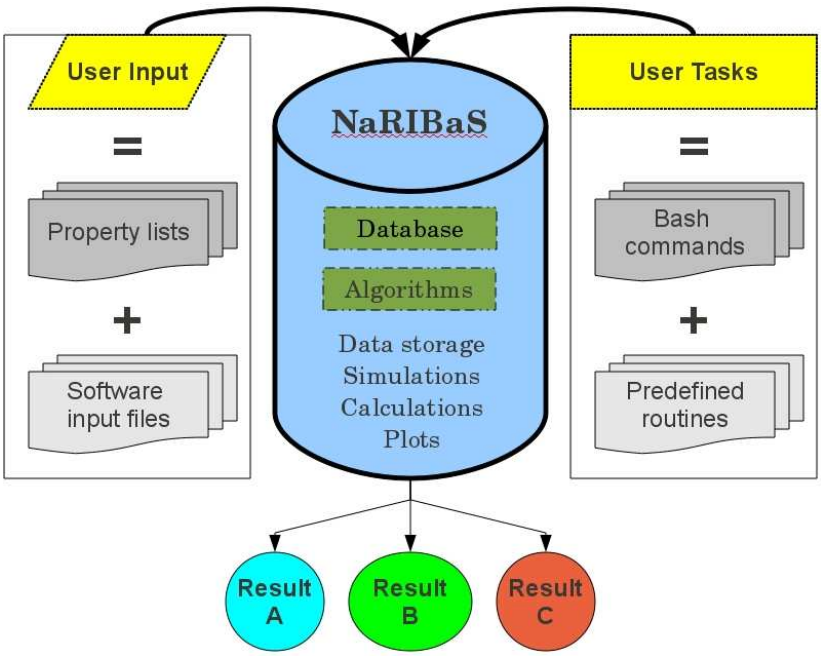

Figure C.1: General composition of NaRIBaS scripting framework.

Accessing an *extendible* - in both directions, more entries per variable but also more variables itself - set of data and post-processing the data for usage in several algorithms seems to be an unaccomplishable task. However, this task is well known - and solved - for a programmer. Solutions for such 'basic' problems are called design patterns, as they provide design ideas that can be implemented in most programming languages. The design pattern that solves the problem considered here is called iterator pattern. Basic understanding and implementation in NaRIBaS will be explained below.

C.3.1 Design pattern: Iterator pattern

Figure C.2 shows a general work flow of a program that uses the iterator pattern. User input may be provided in several way, as a data base or list. The data is read in once and processed to the iterator algorithm. The iterator or cursor traverse a data base and access all elements of the data base. At first iteration, the first combination of all data base elements, also called configuration, is accessed. The configuration changed from nothing to initial configuration. The iterator or cursor contains now links to all "first elements" of the data base.

A loop is started to question, whether a new configuration has been found by the iterator. This configuration is used to perform user tasks or algorithms. Finally The iterator tries to find the next configuration, which might work or not.

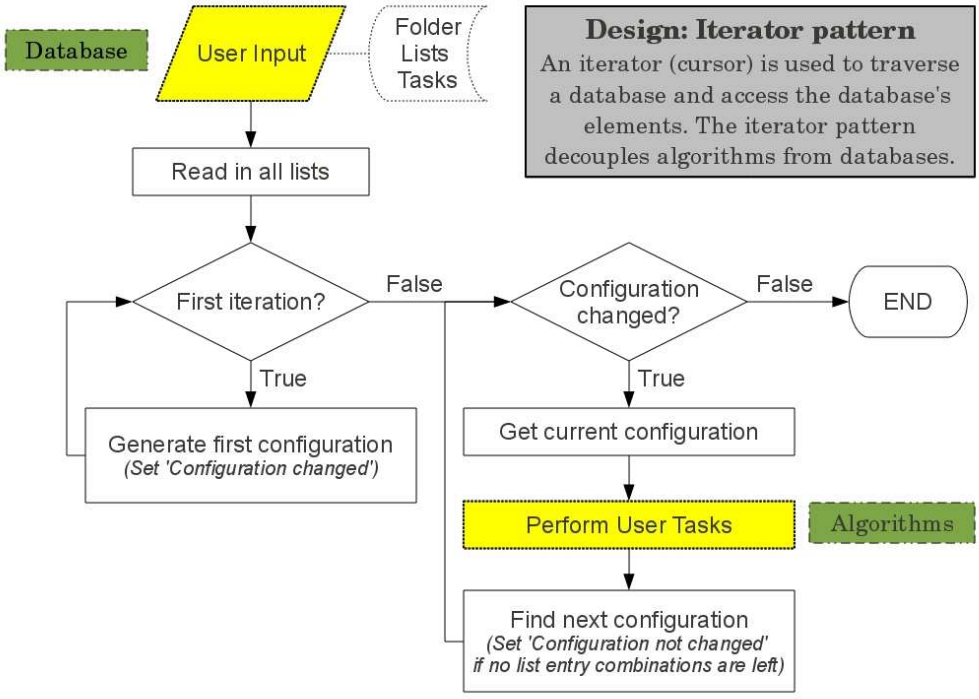

Figure C.2: General chart flow of the Iterator pattern: a programming design pattern for decoupling algorithms from database and accessing all database's elements.

C.3.2 Implementation in this work

General appearance of the iterator pattern can in principle be implemented in most programming languages. Several languages such as python have this pattern build in, however for bash this is not the case. Fig. C.3 shows a implementation of the design pattern in NaRIBaS. The basic algorithms (provided in the `source` folder as `basicfunction_read.sh` and `basicfunction_iterator.sh`) are the algorithms to read in all input lists and the iterator itself with the functions `hasnext()`, `next()` and `loop_through_all_elements()`, that uses `hasnext()` and `next()` to traverse through the database.

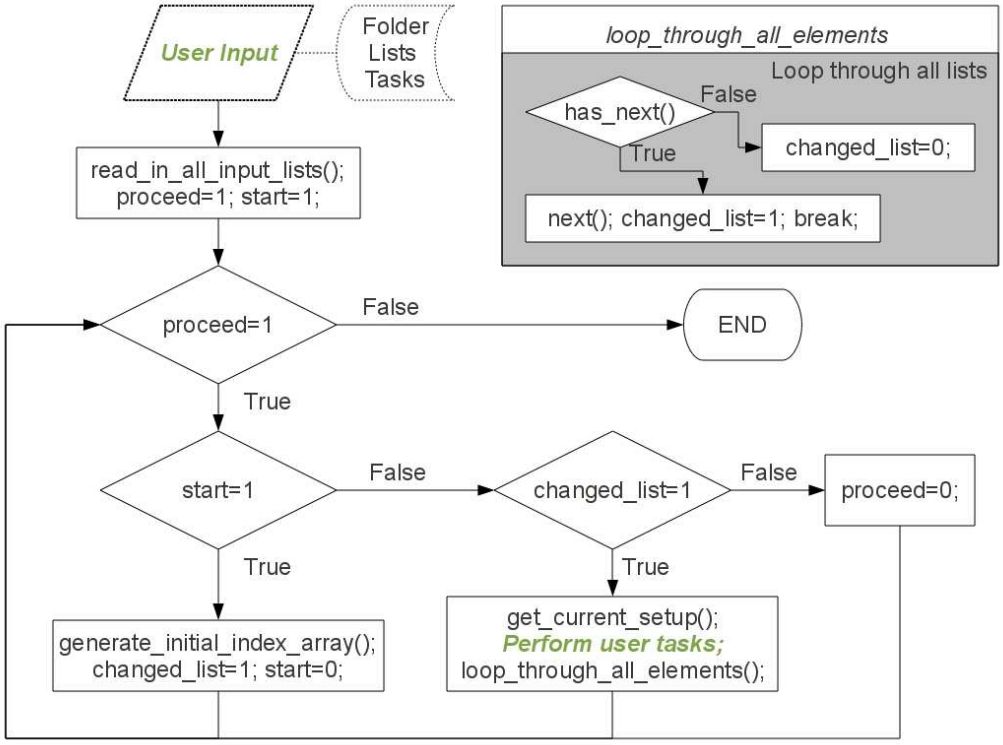

Figure C.3: Implementation of the iterator pattern in NaRIBaS.

C.4 Source code

Whereas design patterns are well known in the programming community and several programming languages like python contain implementations of common patterns, we found no free available implementation of the iterator pattern in the scripting language bash. Thus, the main source code lines are provided in this section.

C.4.1 NaRIBaS.sh

```
#!/bin/bash

./_main.sh user-input.sh
```

C.4.2 _main.sh

```
#!/bin/bash

starttime=$(date +%s.%N)

currentdir=$(pwd)

####### User input will be read in here. The file
   should contain variable definition of '
   inputlists_folder', 'inputlists', 'tasks'
source $currentdir/$1
#######

Which_dir_to_read_in=$currentdir/$inputlists_folder

source $currentdir/source/basicfunction_read.sh
source $currentdir/source/basicfunction_iterator.sh

# Reading in all data, done by a function stored in
   basicfunction_read.sh
read_in_all_input_lists
#read -p "Press enter to continue..." # allows to
   generate a break (e.g. to check the output of a
```

```
   former step) and proceed after enter is pressed).
19
20 # Now use the iterator pattern to access all elements
   of all lists, the basic functions are stored in the
   file basicfunction_iterator.sh
21
22 proceed=1
23 start=1
24
25 while [ $proceed -eq 1 ]; do
26 if [ $start -eq 1 ]; then
27   start=0
28 # Initialize the array that holds for every list the
   index
29   generate_initial_index_array
30   generate_max_index_array
31   totalnumberofsetups=0
32   changed_list=1
33   listcount=0
34 else
35   if [ $changed_list -eq 1 ]; then
36     totalnumberofsetups=$((totalnumberofsetups+1))
37 #    echo 'Next setup is'
38 #    print_current_setup $variablename
   $current_index_all
39 #    echo '------'
40
41     get_current_setup
42
43 ##############
44     eval source $currentdir/$tasks
45 ##############
46
47     loop_through_all_elements
48   else
49     proceed=0
50   fi
```

```
fi
done

echo ''
echo 'Total number of setups equals '
   $totalnumberofsetups '.'

stoptime=$(date +%s.%N)
echo ''
printf "Script finished after:    %.3F seconds.\n"  $(
   echo "$stoptime - $starttime"|bc )

exit
```

C.4.3 basicfunction_read.sh

```
#!/bin/bash

function read_sinlge_list()
{
   local  _resultvar=$1
   local  numofrows=$(cat $2 | wc -l)
   local  numofcolumns=$(awk '{print NF}' $2 | sort -nu
       | tail -n 1)
  local  row=$3
  local  column=0
  while [ $column -lt $numofcolumns ]; do
    column=$((column + 1))
     local myresult[$column]=$(sed -n "$row p" $2 | cut
         -d' ' -f$column)
  done
   eval $_resultvar="'${myresult[*]}'"
}

function read_in_all_input_lists()
{
#   echo ${inputlists[*]}
```

```
20
21 #    input=${inputlists[*]}
22 #    path_to_lists=$Which_dir_to_read_in
23
24     echo ''
25     echo 'Starting the read in of the input data ...'
26     echo ''
27     echo 'Accessing lists in '$Which_dir_to_read_in
28     echo 'Reading in the following lists:'
29     echo ''
30
31     listcount=0
32     while [ $listcount -lt ${#inputlists[@]} ]; do
33        variablename=${inputlists[$listcount]%.list}
34        numrow=1
35        while [ $numrow -le $(cat $Which_dir_to_read_in/$
             {inputlists[$listcount]} | wc -l) ]; do
36           read_sinlge_list $variablename[$((numrow-1))]
                $Which_dir_to_read_in/${inputlists[
                $listcount]} $numrow
37           numrow=$((numrow+1))
38        done
39
40        eval numberofitems=\${#$variablename[*]}
41        echo $variablename.list 'containing '
             $numberofitems ' item(s).'
42
43        listcount=$((listcount+1))
44     done
45
46     echo ''
47     echo 'Finished data input.'
48 }
```

C.4.4 basicfunction_iterator.sh

```
#!/bin/bash

function generate_initial_index_array()
{
  count=0
  while [ $count -lt ${#inputlists[@]} ]; do
    current_index_all[$count]=0
    count=$((count+1))
  done

# echo ${current_index_all[*]}
}


function generate_max_index_array()
{
  count=0
  while [ $count -lt ${#inputlists[@]} ]; do
    variablename=${inputlists[$count]%.list}
    eval numberofitems=\${#$variablename[*]}
    max_index_all[$count]=$numberofitems
    count=$((count+1))
  done

# echo ${max_index_all[*]}
}

function print_current_setup()
{
   local  variable=$1
   local  listindex_all=$2

  count=0

  while [ $count -lt ${#inputlists[@]} ]; do
    variablename=${inputlists[$count]%.list}
```

```
37      i=${current_index_all[$count]}
38
39  #   test=$(eval echo \${$variablename[$i]})
40  #   echo $variablename $i $(eval echo \${$variablename[
        $i]}) #${!variablename[$i]}
41      eval echo \${$variablename[$i]}
42
43      count=$((count+1))
44    done
45  }
46
47  function get_current_setup()
48  {
49    count=0
50
51    while [ $count -lt ${#inputlists[@]} ]; do
52      variablename=${inputlists[$count]%.list}
53      i=${current_index_all[$count]}
54
55  #   test=$(eval echo \${$variablename[$i]})
56  #   echo $variablename $i $(eval echo \${$variablename[
        $i]}) #${!variablename[$i]}
57      eval current_$variablename=\${$variablename[$i]}
58  #   eval echo \$current_$variablename
59      count=$((count+1))
60    done
61  #   echo $variablename $i $(eval echo \${$variablename[
        $i]}) #${!variablename[$i]}
62  }
63
64  function hasnext()
65  {
66     local  variable=$1
67     local  listindex=$2
68
69     eval numberofitems=\${#$variable[*]}
70  #   echo $numberofitems
```

```
71
72      if [ $((listindex+1)) -lt $numberofitems ]; then
73          echo 1
74      else
75          echo 0
76      fi
77  }
78
79  function next()
80  {
81      local  variable=$1
82      local  listindex=$2
83
84      echo $((listindex+1))
85  }
86
87
88  function loop_through_all_elements()
89  {
90  listcount=0
91  while [ $listcount -lt ${#inputlists[@]} ]; do
92      variablename=${inputlists[$listcount]%.list}
93      current_index=${current_index_all[$listcount]}
94
95      if [ $(hasnext $variablename $current_index) -eq 1
            ]; then
96       current_index_all[$listcount]=$(next $variablename
            $current_index)
97       current_index=${current_index_all[$listcount]}
98       changed_list=1
99       break
100     elif [ $(hasnext $variablename $current_index) -eq 0
            ]; then
101      changed_list=0
102      current_index_all[$listcount]=0
103 #    echo ${current_index_all[$listcount]}
104 #    listcount=$((listcount-1))
```

```
105     fi
106     listcount=$((listcount+1))
107 done
108 }
```